

Characterisation, Modelling and Tribological Investigations of Nano-structured TiC-based Electrical Discharge Coatings

Samer Jasim Mahmood Algodi
(B.Sc., M.Sc.)

Faculty of Engineering
Department of Mechanical, Materials and Manufacturing Engineering

Thesis submitted to the University of Nottingham for the degree of Doctor of Philosophy

September 2018

Abstract

Electrical discharge coating (EDC) is a surface modification process used to produce hard coatings from a sacrificial powder metallurgy (PM) tool electrode onto a target workpiece. However, the integrity of as-processed EDC surfaces, as reported on in literature, is generally poor, with limited understanding of the fundamental interactions between energy source and workpiece material, and the microstructural development of the surfaces created.

This thesis explores, at the nano-scale, the deposition and microstructural development of ED processed cermet coatings. Emphasis is given to TiC-based ED coatings, prepared using a semi-sintered TiC tool electrode. A comprehensive study of TiC/Fe cermet coating microstructural development, as a function of ED processing conditions (current 2 - 19 A; pulse-on time 2 - 64 μs) is presented, using the combined characterisation techniques of scanning electron microscopy (SEM) / energy dispersive X-ray spectroscopy (EDS), X-ray diffractometry (XRD) and cross-sectional transmission electron microscopy (TEM). The ED coatings were composites in nature, with complex banded nanostructures of TiC grains within an Fe matrix. Preferred TiC/Fe ED coatings on 304-SS, achieved under conditions of low processing energy (10 A current and 8 μs pulse-on time), exhibited low levels of cracks and porosity, with hardness values of ~ 1800 HV.

The fraction of energy transferred to the workpiece, F_v, as a consequence of ED sparking, is an important parameter which affects directly individual crater geometry and the microstructural development of the near surface modified layer. Hence, a 2D transient heat transfer model is presented, using finite difference methods, and used to estimate effective values for F_v as a function of processing conditions, and thereby to predict coating layer thicknesses of developed microstructures through appropriate

consideration of heat flow into the system. The model is validated against previous work in literature and with experimental observations. The modelling demonstrated a variation of energy transferred to the workpiece, of 17 - 23% for increasing current from 2 - 19 A at fixed pulse-on time of 8 μs; and 7 - 53% for increasing pulse-on time from 2 - 64 μs at fixed current of 10 A. Predictions for heat transfer and the cooling of melt pools, arising from single spark events, compared well with experimental observations for the development of these TiC/Fe cermet microstructures. The cooling phase had two distinct stages, with initial rapid non-uniform cooling within the first ~ 10 - 20 μs leading up to the onset of TiC crystallisation, followed by a more uniform stage of heat loss up to ~ 100 μs, leading up to the onset of Fe matrix solidification.

The tribological behaviours of TiC/Fe ED cermet coatings on both HSS and 304-SS substrates were investigated, with reference Cu EDM surfaces. The wear resistance of these cermet coatings, on both substrate types, yielded dry sliding wear resistances up to two orders of magnitude greater than that of the substrate. Further, EDC cermet coatings on HSS were typically 2 - 4 times more wear resistant, depending on loading, than those deposited on 304-SS, with wear performances reflecting the composite nature of the coatings coupled with the mechanical properties of the substrates.

Laser surface treatments, used to improve the surface integrity of the as-deposited coatings, through the elimination of cracks and porosity, acted to increase the wear rate for all samples, with the exception of coatings on HSS under conditions of high loading. The general increase in wear rate was attributed to a significant reduction in the proportion of TiC within the ED coatings, after laser treatment, combined with an increase in grain size; whilst improvements to the wear performance of laser treated, cermet coated HSS, under high loading, was attributed to the avoidance of an abrasive wear mechanism.

Publication

Journals

- Samer J. Algodi, James W. Murray, Paul D. Brown, Adam T. Clare. "Wear performance of TiC/Fe cermet electrical discharge coatings." **Wear** 402 (2018): 109-123.
- Algodi, Samer J., Adam T. Clare, and Paul D. Brown. "Modelling of single spark interactions during electrical discharge coating." **Journal of Materials Processing Technology** 252 (2018): 760-772.
- Samer J Algodi, James W Murray, Michael W Fay, Adam T Clare, Paul D Brown. "Electrical discharge coating of nanostructured TiC-Fe cermets on 304 stainless steel." **Surface and Coatings Technology** 307 (2016): 639-649.
- J.W. Murray, Samer. J. Algodi, M.W. Fay, P.D. Brown, A.T. Clare. "Formation mechanism of electrical discharge TiC-Fe composite coatings." **Journal of Materials Processing Technology** 243 (2017): 143-151

Conferences

- Algodi, S.J., Murray, J. W., Clare, A. T., & Brown, P. D. "Modelling and Characterisation of Electrical Discharge TiC-Fe Cermet Coatings." **19th CIRP Conference on Electro Physical and Chemical Machining**, 23-27 April 2018, Bilbao, Spain. Procedia CIRP. 68: p. 28-33
- Algodi, S. J., Murray, J. W., Clare, A. T., & Brown, P. D. "Characterisation of TiC layers deposited using an electrical discharge coating process." In Journal of Physics: Conference Series (Vol. 644, No. 1, p. 012008). **EMAG 2015**, Manchester, United Kingdom. IOP Publishing.

Acknowledgements

Firstly, I would like to express my deepest gratitude to my supervisors Professor Paul D. Brown and Professor Adam T. Clare for their continuous support, professional advice and guidance during all stages of my PhD. I've had the opportunity to access a wide range of novel processes and technologies. Thanks for the careful reviews of my written papers and thesis chapters which have made it possible for me to reach this stage. I also extend my gratitude to Dr James Murray for his support during my work. In addition, I also acknowledge the technical assistance of Dr Nigel Neate, Martin Roe, Stuart Branston and Tom Buss. I also would like to offer thanks to Dr Mike Fay in preparation of excellent FIB TEM samples which were critical to this thesis.

Special thanks go to my sponsor, The Ministry of Higher Education & Scientific Research in Iraq and the Iraqi Cultural Attaché in London for their kindness in providing the necessary financial support for the completion of my study. I also extend my thanks to the Al-Nahrain University, Baghdad, Iraq, and especially the Department of Mechanical Engineering, College of Engineering, for their support and encouragement in every way.

Thanks to the spirit of my father you will always be with me. Thanks to my mother who always said that the largest goal can be achieved with continuous determination and faith. Also, thanks to my brothers and sister for their unlimited and sincere support, and encouragement over the years. A special thanks to my wife who does not spare any effort to support me, and to my beloved children, Hamzah, Sama and Aya for their unconditional love. Finally, I would like to thank all of those whose names do not appear here, who have contributed to the successful completion of my study.

Table of content

Abstract i
Publication iii
Acknowledgements iv
Table of content v
List of figures x
List of tables xviii
List of abbreviations xix
1 Introduction 1
1.1 Aims and objectives 3
1.2 Thesis overview 4
2 Context and Literature Review 6
2.1 Introduction 6
2.2 Overview of hard-coating processing techniques 6
2.3 The fundamentals EDM/EDC 8
2.3.1 EDM discharge location and gap debris 11
2.3.2 ED processing using PM electrodes 12
2.3.3 ED processing using powder particles suspended in dielectric fluid 16
2.3.4 ED processed surface nanostructures 18
2.3.5 Effects of ED processing parameters on material deposition 19
2.3.6 TiC-based coating using ED process 21
2.4 ED process modelling 25
2.4.1 Single spark events 25
2.4.2 ED energy distribution between anode and cathode 27
2.4.3 Plasma channel characteristics 31
2.5 Overview of wear 33
2.5.1 Fundamental of wear mechanisms 33
2.5.1.1 Adhesive wear 34
2.5.1.2 Abrasive wear 34
2.5.1.3 Fatigue wear 35
2.5.1.4 Chemical wear 35
2.5.2 Contact condition 35
2.5.3 Wear under practical conditions 37

2.5.4 Wear performance of TiC-based materials 38
2.5.4.1 TiC-based coatings 38
2.5.4.2 TiC-based cermets 40
2.5.5 Sliding wear behaviour of EDC coatings 40
2.5.6 Wear behaviour of TiC-based ED coatings 42
2.6 Laser re-melting process 44
2.7 Summary of literature review and the research gap 45
2.7.1 Development of ED processes for surface modification 45
2.7.2 Process modelling in support of ED processing 46
2.7.3 Tribological performance 47
2.7.4 Laser surface melting (LSM) 47
3 Materials and Methodology 49
3.1 Introduction 49
3.2 Tool electrode materials 49
3.2.1 Solid copper (Cu) 49
3.2.2 Semi-sintered titanium carbide (TiC) 50
3.3 Workpiece materials 51
3.3.1 Austenitic stainless steel 51
3.3.2 High speed steel (HSS) 52
3.4 Surface modification equipment 54
3.4.1 The electrical discharge machine (for EDM & EDC) 54
3.4.2 Laser surface melting (LSM) 56
3.5 Sample preparation 58
3.5.1 Substrate preparation for coating 58
3.5.2 Cross-sectional sample preparation for SEM, optical microscopy and microhardness testing 58
3.6 Sample characterisation 59
3.6.1 Surface roughness 59
3.6.2 Microhardness 60
3.6.3 Optical microscopy 60
3.6.4 Scanning electron microscopy (SEM) and energy dispersive X-ray spectroscopy (EDS) 61
3.6.5 Structure determination 63
3.6.5.1 X-ray diffractometry (XRD) 63
3.6.5.2 Grain size determination 65
3.6.6 Transition electron microscopy (TEM) 65

3.6.6.1 TEM sample preparation 67
3.6.7 Spark emission spectrophotometry 68
3.7 Thermal conductivity measurements 69
3.8 Gap voltage measurement during ED processing 69
3.9 Tribology 70
3.9.1 Reciprocating wear testing 70
3.9.2 Linear voltage displacement transducer (LVDT) calibration 72
3.9.3 Wear scar measurement 73
3.9.4 Ball wear scar measurements 74
3.10 Summary 75
4 EDC TiC/Fe cermet coatings 76
4.1 Introduction 76
4.2 Starting material morphologies 76
4.3 Effect of current and pulse-on time on ED coating morphology 80
4.3.1 Surface topography of ED processed coatings 80
4.3.2 Microstructure of ED processed coatings 84
4.3.3 Cross-sectional TEM of a continuum cermet coating 86
4.3.4 Coating thickness 89
4.3.5 Hardness 92
4.4 Comparison of EDC & EDM processed samples on 304-SS and HSS substrates 93
4.4.1 Microscopy of processed surfaces and coating cross-sections 93
4.4.2 Processed surface microstructures 97
4.5 Discussion 99
4.6 Summary 105
5 Modelling and characterisation of single spark interactions .. 107
5.1 Introduction 107
5.2 Process modelling and simulation 108
5.2.1 Heating phase 108
5.2.1.1 Governing equations and boundary conditions 108
5.2.1.2 Heat source 110
5.2.1.3 Plasma channel 111
5.2.2 Cooling phase 112
5.2.3 Workpiece and tool electrode material properties 114
5.2.4 Program flow chart 114

5.3 Results 115
5.3.1 Gap voltage measurement 115
5.3.2 Code validity and fraction of energy transferred to the workpiece 117
5.3.3 Heat distribution 119
5.3.4 Crater diameter 122
5.3.5 TiC distribution and cermet layer thickness 125
5.3.6 Cooling phase and coating microstructure development 128
5.3.7 Cross-section TEM of single crater 133
5.4 Discussion 135
5.5 Summary 138
6 Laser surface melt processing and tribological behaviour of EDC TiC/Fe cermet coatings 140
6.1 Introduction 140
6.2 Laser surface melting (LSM) of EDC TiC/Fe coatings 141
6.2.1 Surface topography of as-deposited and LSM processed coatings 141
6.2.2 Microstructure of as-deposited and LSM processed coatings 143
6.2.3 Crystal structure of LSM processed coatings 146
6.3 Reciprocating wear testing of EDC TiC/Fe coated and EDM processed steel surfaces 148
6.3.1 Specific wear rates and wear scar profiles 148
6.3.2 Wear scar characterisation 151
6.3.3 Counterbody wear rate 157
6.3.4 Coefficient of friction (CoF) 160
6.4 Reciprocating wear testing of LSM processed EDC TiC/Fe 163
6.4.1 Specific wear rates 163
6.4.2 Wear scar characterisation 165
6.4.3 Coefficient of friction (CoF) 167
6.5 Discussion 168
6.6 Summary 174
7 Discussion 175
7.1 Introduction 175
7.2 Surface topography and microstructure 176
7.3 Coating hardness 178
7.4 Modelling of single spark event 180
7.5 Formation mechanism of TiC/Fe composite coatings 182

7.6 Wear behaviour of TiC/Fe cermet ED coatings 185
7.7 Laser processed TiC/Fe cermet ED coating 187
8 Conclusions and Future work 190
8.1 General conclusions 190
8.2 Future work 194
References 196
Appendix 1 TEM image of 304-SS 208
Appendix 2 Heat transfer equations 209
Appendix 3 MATLAB code 215
Appendix 4 SE images of the wear tracks 225
Appendix 5 SE images of the LSM wear track 230

List of figures

Figure 2-1 Schematic representation of: a) EDM mechanism with a solid tool electrode and positive polarity; and b) EDC mechanism with sacrificial semi-sintered tool electrode and reverse polarity 9

Figure 2-2 Voltage and current waveforms during the electrical discharge process (adapted from [16]) 10

Figure 2-3 Electrical discharge location determination [16] 11

Figure 2-4 Illustrations of EDC conducted under environments of: a) kerosene dielectric fluid (wet); and b) nitrogen gas (dry) [21] 15

Figure 2-5 Illustration of EDM, with powder suspension in the dielectric fluid 16

Figure 2-6 Microcrack density/unit area for EDM & EDC tungsten carbide processed surfaces [33] 18

Figure 2-7 HAADF STEM image of a W impregnated Si recast layer, following EDM, with EDS mapping showing regions of W, Si and C [36] 19

Figure 2-8 Ishikawa (cause and effect) diagram for ED process parameters (adapted from [37-39]) 19

Figure 2-9 Plot of pulse duration against discharge current, outlining conditions for material removal or TiC deposition [42] 21

Figure 2-10 Average Vickers hardness, for EDC deposited TiC, measured with 200gf as a function of increasing current and pulse-on time [1] 22

Figure 2-11 Schematic illustration of the EDC TiC adhesion process: For the case of: a) constant voltage; and b) a temporary voltage drop [44] 23

Figure 2-12 XRD patterns for TiC coatings: EDC processed with (a) graphite mixed within the dielectric fluid; and b) without graphite [45] 24

Figure 2-13 a) Temperature distribution; and b) simulation and experimental data for a crater boundary (90 V and positive polarity) [56] 26

Figure 2-14 Experimental set-up for anode temperature measurement and the model used for temperature calculation [66] 29

Figure 2-15 Comparison of energy distribution into the workpiece, from needle and disk-shaped electrodes [67] 30

Figure 2-16 High-speed video frames of arc plasma during EDM (23 A, 80 μs pulse-on time and 280 V) [71] 32

Figure 2-17 Basic of mechanisms of wear: a) adhesive, b) abrasive, c) fatigue and d) chemical [6] 34

Figure 2-18 Macromechanical contact conditions as a hard spherical slider moves over a coated surface [82] 36

Figure 2-19 Wear rate of TiC coated and uncoated 303-SS for sliding speed conditions of: a) 3 $cm.s^{-1}$, b) 7 $cm.s^{-1}$, c) 11 $cm.s^{-1}$ and d) 15 $cm.s^{-1}$, under various normal loads [88] 39

Figure 2-20 Wear behaviour of Ni-W EDC coatings on die steel substrates, as a function of temperature: a) RT; b) 100˚C; c) 200˚C; d) 300˚C and e) 400˚C (total sliding distance 1000 m, 2 m/s sliding speed, 80 N load) [13] 41

Figure 3-1 Titanium-Carbon binary phase diagram [105] 50

Figure 3-2 Equilibrium Fe-Ni phase diagram [107] 52

Figure 3-3 Volume fraction of undissolved carbides in M2 HSS [114] 53

Figure 3-4 a) Experimental set-up of ED machine used to perform EDC; and b) tool electrode & workpiece arrangement 55

Figure 3-5 Experimental set-up for the laser surface melting of ED coatings 57

Figure 3-6 a) Surface profilometer (Talysurf CLI 1000); b) inductive contact stylus (75.6 mm length); c) reference specimen for calibration (59.6 mm x 29.6 mm) 59

Figure 3-7 (a) Signals produced following interaction of a highly energetic electron beam with a sample; and (b) depiction of the electron beam / material interaction volume 61

Figure 3-8 Production of a characteristic X-ray, as used for EDS 62

Figure 3-9 Illustration of the geometric conditions for X-ray diffraction (Bragg's law) 64

Figure 3-10 a) Bright-field; and b) Dark-field diffraction contrast imaging in TEM (parallel illumination); and c) bright-field and annular dark-field imaging in STEM (converged electron probe) 66

Figure 3-11 Schematic of experimental set-up for voltage waveform measurement 69

Figure 3-12 Experimental set-up of the wear test rig 70

Figure 3-13 Schematic of the ball-on-flat wear testing configuration 71

Figure 3-14 Schematic representation of the wear scar profilometry measurements 73

Figure 3-15 Wear of the reciprocating ball (spherical cap) 74

Figure 4-1 SE image of the starting TiC tool electrode 77

Figure 4-2 X-ray diffraction data for the starting tool electrodes: a) TiC; and b) Cu 78

Figure 4-3 X-ray diffraction patterns for the starting: a) 304-stainless steel; and b) high speed steel substrates..... 79

Figure 4-4 SE images of: (a) as-polished 304 stainless steel; and (b-f) TiC-based coatings deposited as a function of increasing current: 2, 6, 10, 14 and 19 A, respectively, for 1 h processing time and 8 μs pulse-on time 82

Figure 4-5 SE images of: (a-f) Coatings deposited as a function of increasing pulse-on time: 2, 4, 8, 16, 32 and 64 μs, respectively, for 1 h processing time and a fixed current of 10 A 83

Figure 4-6 High magnification SE images showing details of: (a) A pore formed under conditions of 19 A current (fixed pulse-on time of 8 μs); and b) a large surface particle formed under conditions of 32 μs pulse-on time (fixed current of 10 A) 84

Figure 4-7 XRD patterns of coatings produced under conditions of 8 μs pulse-on time and increasing current: a) 2 A, b) 6 A, c) 10 A, d) 14 A, and e) 19 A, respectively..... 85

Figure 4-8 XRD patterns of coatings produced under conditions of 10 A and increasing pulse-on times: a) 2 μs, b) 4 μs, c) 8 μs, d) 16 μs, e) 32 μs, and f) 64 μs, respectively 85

Figure 4-9 Cross-sectional TEM micrographs of an EDC layer processed under conditions of 10 A and 8 μs: (a) Bright field image, large field of view; (b,c) near surface region at increasing levels of magnification (boxed regions in each respective images); (d,e) high magnification dark field images of boxed regions showing transitional band and columnar growth microstructures..... 87

Figure 4-10 ADF-STEM image with associated EDS elemental maps showing the dispersion of Ti, Fe, C and Cr 88

Figure 4-11 ADF-STEM image of the near surface grain structure; with associated CBED patterns from the specified locations consistent with (1, 2) TiC; (3) Fe and (4) amorphous C 89

Figure 4-12 SE image of a coating, viewed in cross-section, EDC processed with 6 A current and 8 μs pulse-on time 90

Figure 4-13 Variation of coating layer thickness (μm) as a function of current (A) and fixed pulse-on time of 8 μs (n=40)..... 91

Figure 4-14 Variation of coating layer thickness (μm) as a function of pulse-on time (μs) and fixed current of 10 A (n=40)..... 91

Figure 4-15 Vickers hardness and Ti wt% values, as a function of: a) current (A) and b) pulse-on time (μs); error bars are the standard deviations of 8 measurements 93

Figure 4-16 SE images of (a,c) EDC cermet coatings (10 A current and 8 μs pulse-on); and (b,d) EDM Cu reference samples (10 A current and 8 μs pulse-on), on (a,b) 304-SS; and (c,d) HSS substrates, respectively..... 94

Figure 4-17 Cross-sectional BSE images of a TiC/Fe cermet EDC coating on 304-SS (TiC deposited under conditions of 10 A current and 8 μs pulse-on time), showing the development of a banded, composite microstructure. (a) Low magnification image with inset magnified in (b), and further magnified in (c,d)..... 95

Figure 4-18 Cross-sectional BSE images of a TiC/Fe cermet ED coating on HSS (TiC deposited under conditions of 10 A current and 8 μs pulse-on time), showing the development of a similar, variable, composite microstructure. (a) Low magnification image with inset magnified in (b), and further magnified in (c,d)..... 96

Figure 4-19 XRD patterns for ED processed TiC/Fe cermet coatings on: (a) 304-SS and (b) HSS substrates, along with a reference Cu machined surface 98

Figure 4-20 Calculated input energy as a function of: a) current (A); and b) pulse-on time (μs) 102

Figure 4-21 Schematic of the resultant TiC/Fe ED coating microstructure, under conditions of 10 A current and 8 μs pulse-on 104

Figure 5-1 Gaussian profile heat source and boundary conditions with the workpiece, including interior node and expanded view of a top surface boundary node 109

Figure 5-2 Crater radius as a function of current and pulse-on time obtained experimentally (Table 4-2)..... 112

Figure 5-3 Schematic illustrations of fluid flow over a flat plate 113

Figure 5-4 Process flow, highlighting the 2D transient heat transfer model 115

Figure 5-5 Waveforms associated with EDC coatings produced using a TiC tool electrode and a 304 stainless steel workpiece, with negative polarity for pulse-on times of: a) 8 μs, b) 32 μs and c) 64 μs (fixed 10 A current) 116

Figure 5-6 Fraction of energy transferred to the workpiece as function of increasing current, compared to literature (Singh, 2012 [64]) and (Shabgard and Akhbari, 2016 [136])..... 118

Figure 5-7 Fraction of energy transferred to the workpiece as function of increasing pulse-on time, compared to literature (Singh, 2012 [64]) and (Shabgard and Akhbari, 2016 [136]) 118

Figure 5-8 MATLAB simulations showing heat distribution into the workpiece at the end of the 'pulse-on' stage; along with the temperature distribution across the top surface (dotted white line) and the boundary of molten material with the bulk substrate (dashed white line) 120

Figure 5-9 Radial temperature profiles along the top surface of the workpiece as functions of: a) increasing current; and b) pulse-on time 121

Figure 5-10 Plan view SE images of craters created from single spark events, at the start of template coating. Average crater sizes increased with increasing discharge energy 123

Figure 5-11 Simulated crater boundaries into the workpiece as a function of increasing a) current; and b) pulse-on time 124

Figure 5-12 SE images of EDC processed coatings, viewed in cross-section: (a,c,e,g) for fixed pulse-on time of 8 µs as a function of increasing current; and (b,d,f,h) for fixed current of 10 A as a function of increasing pulse-on time. (b:1-3; and e:4-6) Representative regions for localised composition, determined by EDS, as summarised in Table 5-3. 126

Figure 5-13 Comparison of simulated crater depth from a single spark event with experimentally determined EDC layer thicknesses, as function of increasing current and pulse-on time 128

Figure 5-14 BSE images of the developed cermet coating microstructures in cross-section geometry, processed under conditions of: a-d) 10 A current and 8 µs pulse-on time 129

Figure 5-15 BSE images of the developed cermet coating microstructures in cross-section geometry, processed under conditions of: a-d) 10 A current and 64 µs pulse-on time 129

Figure 5-16 Average surface simulated cooling rate for a single TiC crater deposit as a function of: a) Current (fixed pulse-on time of 8 µs) and b) Pulse-on time (fixed current of 10 A) 131

Figure 5-17 Cooling profiles as a function of increasing time (pulse-off), with each line representing a node located at the crater centre (a-l) from the oil-flow/surface interface to the melt/solid interface, with 1 µm pitch. 132

Figure 5-18 Single deposit sample used for TEM sectioning: (a,b) SE and BSE images showing individual craters/deposits, EDC processed on 304-SS; (c) magnified SE image of the boxed region in (b) showing location selected for sectioning; (d) SE image of FIB milled, electron transparent sample foil (arrowed). 133

Figure 5-19 (a,b) Cross-sectional TEM micrographs of a single EDC deposit processed under conditions of 10 A and 8μs; and (c) associated EDS maps for Ti, Fe and C 134

Figure 6-1 SE images of (a,b) as-deposted TiC/Fe on 304-SS and HSS, (c-f) laser surface treated TiC/Fe cermet coatings on: (c,e) 304-SS and (d,f) HSS substrates, as a function of power: (c,d) 240 W and (e,f) 280 W, respectively (1600 mm/minute scan speed; Ar environment)..... 142

Figure 6-2 High resolution cross-sectional BSE images of: (a,b) as-deposted TiC/Fe on 304-SS; and laser surface treated TiC/Fe cermet coatings as a function of power: (c,d) 240 W and (e,f) 280 W, respectively (1600 mm/minute scan speed; Ar environment) 144

Figure 6-3 High resolution cross-sectional BSE images of (a,b) as-deposted TiC/Fe on HSS; and laser surface treated TiC/Fe cermet coatings, as a function of power: (c,d) 240 W and (e,f) 280 W, respectively (1600 mm/minute scan speed; Ar environment) 145

Figure 6-4 XRD patterns for as-deposited TiC/Fe on (a) 304-SS; and (b) HSS; and LSM processed under conditions of 240 and 280 W, respectively (1600 mm/minute scan speed; Ar environment) 147

Figure 6-5 Specific wear rates (logarithmic scale) for samples based on: a) HSS and b) 304-SS substrates (as-polished substrate; EDM Cu reference surface; and EDC TiC/Fe cermet coating) under loads of 10 N and 50 N, respectively..... 148

Figure 6-6 Cross-sectional wear scars profiles for the as-polished substrates, EDM Cu reference samples, and EDC TiC/Fe cermet on HSS samples under conditions of a) 10 and b) 50 N, respectively 150

Figure 6-7 Cross-sectional wear scars profiles for the as-polished substrates, EDM Cu reference samples, and EDC TiC/Fe cermet on 304-SS samples under conditions of a) 10 and b) 50 N, respectively 150

Figure 6-8 Low magnification SEM images showing: (a) the extent of a wear scar (mixed SE & BSE image); and (b,c) representative details of a wear scar on an as-polished HSS substrate, under loading conditions of 10 N, indicative of abrasive wear..... 152

Figure 6-9 Low magnification SE images showing: (a) the extent of a wear scar; and (b,c) representative details of a wear scar on a cermet coated HSS sample, under loading conditions of 10 N, indicative of greatly improved wear performance..... 152

Figure 6-10 a) SE and b) BSE images of TiC/Fe coated HSS, under loading conditions of 10 N 153

Figure 6-11 High magnification SE images of wear tracks of: (a,c,e) HSS; and (b,d,f) 304-SS, under conditions of 10 N loading. (a,b) as-polished

substrates; (c,d) EDM Cu reference samples; and (e,f) EDC cermet coatings..... 154

Figure 6-12 High magnification SE images of wear tracks of: (a,c,e) HSS; and (b,d,f) 304-SS, under conditions of 50 N loading. (a,b) as-polished substrates; (c,d) EDM Cu reference samples; and (e,f) ED cermet coatings..... 155

Figure 6-13 Low magnification SE images showing (a) the extent and (b,c) representative details of a wear scar on a cermet coated HSS sample, under loading conditions of 50 N, again indicative a greatly improved wear performance..... 156

Figure 6-14 Low magnification SE images showing: (a) the extent; and (b,c) representative details of a wear scar on cermet coated 304-SS, under loading conditions of 50 N, again indicative a greatly improved wear performance..... 157

Figure 6-15 Specific wear rates of the counterbody Al_2O_3 ball after sliding test against TiC/Fe cermet coating on a) HSS and b) 304-SS, both under loading conditions of 10 and 50 N 158

Figure 6-16 Optical microscope images of Al_2O_3 ball wear scars, after sliding wear testing against TiC/Fe cermet coatings on: (a,b) HSS; and (c,d) 304-SS, both under conditions of (a,c) 10 N and (b,d) 50 N 159

Figure 6-17 SE images and associated EDS analyses of: (a) a new Al_2O_3 ball; and (b) a ball after sliding testing against a TiC/Fe cermet coating on HSS 160

Figure 6-18 Time dependent CoF profiles for as-polished substrates, EDM Cu reference samples, and EDC TiC/Fe cermets on HSS, under conditions of: (a) 10 N; and (b) 50 N, respectively..... 162

Figure 6-19 Time dependent CoF profiles for as-polished substrates, EDM Cu reference samples, and EDC TiC/Fe cermets on 304-SS, under conditions of: (a) 10 N; and (b) 50 N, respectively..... 162

Figure 6-20 Specific wear rates of as-deposited and laser treated TiC/Fe cermet coatings as a function of power, 240 W and 280 W, under loading conditions of 10 N and 50 N on: (a) HSS and (b) 304-SS substrates, respectively..... 164

Figure 6-21 SE micrographs of wear scar details following: (a,b) 240 W and (c,d) 280 W laser surface treatment of TiC/Fe cermet coated HSS under loading conditions of: (a,c) 10 N; and (b,d) 50N, respectively (1600 mm/minute scan speed; Ar environment) 165

Figure 6-22 SE micrographs of wear scar details following: (a,b) 240 W and (c,d) 280 W laser surface treatment of TiC/Fe cermet coated 304-SS under loading conditions of: (a,c) 10 N; and (b,d) 50 N, respectively (1600 mm/minute scan speed; Ar environment) 166

Figure 6-23 Time dependent CoF profiles for as-deposited and LSM treated TiC/Fe cermet coatings on HSS, as a function of power, 240 W and 280 W, under loading conditions of a) 10 N and b) 50 N 167

Figure 6-24 Time dependent CoF profiles for as-deposited and laser treated TiC/Fe cermet coatings on 304-SS, as a function of power, 240 W and 280 W, under loading conditions of: (a) 10 N and (b) 50 N 168

Figure 6-25 Schematic illustrations of the wear mechanisms of TiC/Fe cermet coated: (a,b) HSS and (c,d) 304-SS, under conditions of 10 N and 50 N loading, respectively..... 171

Figure 7-1 Depiction of initial TiC deposition/metal intermixing during the ED coating process 182

Figure 7-2 Liquidus projections for the Fe-Ti-C ternary system a) over whole composition range; and b) the Fe-rich corner [128]..... 183

List of tables

Table 2-1 Example ED investigations using various PM tool electrodes 12

Table 3-1 EDC processing parameters 55

Table 3-2 EDC processing parameters for the wear test samples 56

Table 3-3 Substrate sizes 58

Table 4-1 Chemical composition of the starting 304-SS and HSS substrates 77

Table 4-2 Summary of individual crater sizes (n = 30), continuum layer surface roughness values (n = 5), cermet layer thicknesses and coating Ti wt% values, as a function of increasing current and pulse-on time 81

Table 4-3 Estimate of the total number of sparks experienced by each location during the EDC process (1 h), emphasising that every location undergoes repeated melt pool formation and solidification, to create each continuum TiC/Fe cermet coating 100

Table 5-1 Material properties of the workpiece and tool electrode (Granta CES 2009 EduPack data base software) 114

Table 5-2 Average crater sizes (n = 30) as a function of processing conditions 123

Table 5-3 Localised cermet coating compositions as determined by EDS (Figures 5-12b,e) 127

Table 6-1 Summary of the reciprocating ball-on-flat wear tests, to be investigated 141

Table 6-2 TiC/Fe cermet coating compositions before and after LSM treatment, based on EDS area analyses 143

List of abbreviations

Symbols

AISI	American Iron and Steel Institute
ADF	Annular dark-field
ADF-STEM	High magnification annular dark field scanning TEM
Ar	Argon
a	Constant
B	Full width at half maximum
BSE	Backscattered electron
BF	Bright-field
CBED	Convergent beam electron diffraction
CVD	Chemical vapour deposition
CoF	Coefficient of friction
CW	Continuous-wave
C_p	Specific heat capacity (J/kg.K)
D	Grain size (nm)
DF	Dark-field
d	Laser beam diameter (mm)
d_s	Sliding distance (m)
d_{hkl}	Spacing between lattice planes
DF-STEM	Dark-field scanning transition electron microscopy
d_{fiber}	Delivery fibre
d_f	Focused spot size diameter
ED	Electrical discharge
EDC	Electrical discharge coating
EDM	Electrical discharge machining
EDT	Electrical discharge texturing
EDS	Energy dispersive spectroscopy
F	Applied force (kg)
FIB	Focused ion beam
FWHM	Full width at half maximum
F_{coll}	Collimation lenses
FEM	Finite element method
F_l	Focal length
F_v	Fraction of energy transferred to the workpiece
GIS	Gas-injection system
HRTEM	High-resolution transmission electron microscopy
HVOF	High velocity oxy fuel
HSS	High speed steel
h_s	Height of the spherical cap (mm)
HSFC	High speed framing camera

h	Convection heat transfer coefficient ($W/m^2.K$)
I	Current (A)
K	Constant
k	Thermal conductivity (W/m.K)
L	Workpiece length (m)
L_a	Applied load (N)
LSM	Laser surface melting
LVDT	Linear voltage displacement transducer
L_m	Latent heat of melting (J/kg)
MRR	Metal removal rate
MMC	Metal matrix composite
m	Constant
N	Applied load
N_r	Total number of reciprocations
Nd: Yag	Neodymium-doped yttrium aluminium garnet
Nu_x	Nusselt number (-)
n	Constant
P	Laser power (W)
PEB	Pulsed electron beam
PM	Powder metallurgy
PVD	Physical vapour deposition
PCR	Percentage contribution ratios
Pr	Prandtl number (-)
q	Convection heat flux (W/m^2)
$q_\circ$	Maximum heat flux (W/m^2)
R	Ball radius (mm)
Re	Reynolds number (-)
R_p	Empirical constant
Rpc	Plasma channel radius (μm)
r	Radial distance (m)
r_w	Radius of the wear scar (mm)
S	Stroke length (mm)
SAED	Selected area electron diffraction
SEM	Scanning electron microscopy
SE	Secondary electron
STEM	Scanning transition electron microscopy
T	Temperature (K)
TEM	Transmission electron microscopy
TIG	Tungsten inert gas
T_m	Melting temperature (K)
T_s	Initial temperature (K)
T_∞	Dielectric fluid temperature (K)
t	Time (s)
ton	Pulse-on time (μs)

u_∞	Velocity of the fluid (m^2/s)
V	Voltage (V)
V_0	Voltage when the stage is stationary (V)
V_c	Cup volume (mm^3)
V_m	Measured voltage
V_w	Volume loss (mm^3)
W	Specific wear rate W (mm^3/Nm)
XRD	X-ray diffractometry
x & y	Cartesian coordinates
2D	Two dimensions
304-SS	304-Stainless steel

Greek letters

α	Thermal diffusivity (m^2/s)
α'	Modified thermal diffusivity (m^2/s)
θ	Scattering angle
μ	Dynamic viscosity of the fluid (kg/m.s)
μ_f	Coefficient of friction
ρ	Density (kg/m^3)
σ	Standard deviation
$\boldsymbol{v}$	Laser scan speed (mm/s)
λ	Wavelength

Subscripts

i & j	Iteration in x & y direction

1 Introduction

Electrical discharge coating (EDC), an adaptation of electrical discharge machining (EDM), is of interest as a technique for the deposition of high melting point materials onto a metallic workpiece. The coating material originates either directly from a sacrificial tool electrode [1], or through the addition of powder to the system, suspended within a dielectric fluid [2].

EDM is essentially a non-contact process that can be used to machine electrically conductive materials, regardless of their mechanical properties of hardness, toughness or strength [3]. The first reported use of EDM was recorded in the late 1940s [4] and it is still considered a non-conventional machining process when compared to more conventional, shear-based machining methods. During EDM, the removal of material relies on the conversion of electrical energy into thermal energy, which generates a plasma channel in the working gap between two electrodes (*i.e.* tool electrode and workpiece) immersed in a medium of dielectric fluid. As a result of the discharge, the workpiece, and to a lesser extent tool electrode, are locally melted and/or vaporised and subsequently ejected upon the end of discharge. This forms the basis of material removal. Hence, the energy distribution into the workpiece and tool electrode material is an important factor, to determine the amount of material removed, crater geometry and associated microstructural developments.

Electrical discharge (ED) processing has advantages over competing surface modification techniques, including the ability to machine a material and apply a coating using the same machine tool (by reversing the polarity), removing the need for post-processing, combined with the ability of EDM to create highly complex shapes using a shaped tool electrode, with applicability to conformal surfaces. The high

temperatures associated with sparking allow a large range of difficult to process materials, including ceramics, to be deposited, whilst rapid quenching facilitates the production of very hard coatings, and hence the technique has good potential for the production of hard-wearing coatings to enhance the lifetime of components, with the added benefits of easy set-up and low operational costs. Hence, EDC has excellent potential across a range of industrial applications, in areas requiring improvements in the performance of surfaces subjected to EDM, *e.g.* cutting tools, chip-less shaping applications such as blanking, extrusion, injection moulding and dies, along with punching tools, and hot and cold roll manufacturing.

However, one of the most critical limitations of EDC, at present, is poor surface integrity, characterised by the presence of cracks and voids, with high surface roughness. These features arise partly as a consequence of rapid cool down, with thermal properties, such as melting points and differential thermal contraction, leading to defect formation and coating disruption.

For many industrial applications, the mechanical and chemical properties of a component surface are critical, necessitating, for example, the development of coated or surface modified materials to withstand specific wear conditions. However, high performance materials might be difficult to deposit, or have high cost. Hence, the development of protective coatings, at low expense, using easy to apply methods, becomes commercially interesting.

The main theme of this thesis is to improve upon present, state-of-the-art EDC processing, by gaining improved understanding of the fundamental principles of materials deposition, through a combination of experimentation and numerical modelling of singe spark interactions. Emphasis is given to the ED processing of TiC/Fe cermet coatings and their microstructural development. Particular attention is

given to the mechanical properties of hardness, and wear resistance is investigated using a linear reciprocating ball-on-flat configuration. The potential of post-deposition, laser surface melting (LSM) treatment, to improve surface quality, is also appraised.

1.1 Aims and objectives

The scope of this investigation is partitioned into four areas:

Characterisation of TiC/Fe ED cermet coatings: In this section, a candidate TiC-based model system is investigated for the ED coating of two types of steel 304 stainless steel (304-SS) and high speed steel (HSS). A comprehensive study of coating development is reported, with emphasis on the fundamental principles of material deposition, down to the nano-scale. Particular attention is given to the interrelationship between microhardness and microstructural development, as a function of processing parameters (*i.e.* process-mapping), through determination of the shape, size and distribution of TiC within the Fe matrix.

Modelling of single spark interactions during EDC: There is a lack of modelling effort to understand the fundamental interactions between energy source and material during EDC processing, hence, a novel of 2D transient heat transfer model for single spark events has been developed. The model is capable of estimating the effective amount of energy transferred into the workpiece, through calculation of the temperature distribution, in turn providing for estimates of crater geometry and coating layer thicknesses. Further, modelling of the cooling phase of molten deposits allow for the prediction of microstructural developments.

Laser surface melting (LSM) of TiC/Fe ED coatings: This is a novel surface treatment, capable of re-melting surfaces, by use of a continuous wave laser within an argon environment. Characterisation of developed microstructures provided for detailed understanding of LSM at the fundamental level, towards establishing a simple method for improving ED processed material surfaces, *i.e.* reducing surface roughness and minimising crack density.

Wear performance of TiC/Fe cermet electrical discharge coatings: Combined with EDC process optimisation and LSM modification, a systematic study of the wear behaviour of TiC/Fe ED coatings was performed. Two different types of EDC cermet coated steel substrate were investigated, benchmarked against reference EDM surfaces prepared using an ordinary Cu electrode. Surfaces were subjected to wear testing, to appraise the tribological behaviour of EDC coatings, correlated with the near surface microstructure.

1.2 Thesis overview

This thesis comprises of eight chapters:

Chapter 1 provides a brief introduction to EDM and EDC processing technologies, emphasising the potential of EDC over more conventional coating techniques.

Chapter 2 is concerned with the context to ED processing, including literature review. This chapter comprises four main sections, including the fundamentals of ED processing and material deposition mechanisms; the modelling of single spark events during ED processing; an overview of the wear behaviour of ED processed TiC and the potential of LSM. The chapter ends with the identification of research gaps, leading to the defined aims of the research programme presented here.

Chapter 3 provides a description of the research methodology, the materials investigated and the equipment utilised, covering the themes of sample preparation, processing and characterisation. The physical principles underpinning the process and characterisation techniques applied are described.

Chapter 4 presents a fundamental study, down to the nano-scale, of the microstructural development of TiC/Fe cermet ED coatings, with emphasis on the effect of process parameters on surface topography, microstructure, layer thickness and microhardness. The results presented here allow for ED process optimisation and impact on the following experimental chapters.

Chapter 5 describes the development of a 2D transient heat transfer model for a single spark event during EDC, to predict the amount of energy transferred into the workpiece, as validated against previous work and experimental observations. In addition, a correlation of nano-scale microstructure development within a crater and cooling profiles is demonstrated, along with predictions for crater profiles and layer thicknesses.

Chapter 6 builds upon the findings in chapters 4 and 5, and presents a systematic investigation of the tribological behaviour of TiC/Fe cermet coatings, prepared under favourable EDC processing conditions. This chapter also describes the effects of the additional novel LSM surface treatment technique on the as-deposited ED cermet coatings, to improve surface integrity. The repair mechanism the surface cracks is also described.

Chapter 7 presents a general discussion of the main findings presented in the results chapters, in the context of established literature.

Chapter 8 presents a summary of the main contributions of this research, along with an outline of possible strategies for future work.

2 Context and Literature Review

2.1 Introduction

This chapter presents a review and discussion of the background and literature relevant to the main themes of this thesis, covering the main topics: Section 2.2 presents a general overview of hard-coating processing techniques. Section 2.3 concerns the background of electrical discharge machining (EDM) and electrical discharge coating (EDC), with emphasis on the fundamental principles of ED processing for cermet layer formation and their potential applications. Section 2.4 is concerned with the modelling of single spark events during ED processing, including energy and heat distribution, and associated microstructural developments. Section 2.5 presents a brief description of friction and wear mechanisms, with emphasis on the performance of TiC-based materials and ED coatings. Section 2.6 presents an overview of the technique of laser surface melting (LSM) for coating modification. Section 2.7 summarises the main research challenges for EDM/EDC processing.

2.2 Overview of hard-coating processing techniques

The surface modification and/or coating of materials has maintained interest in recent years, driven by the industrial requirements of wear and corrosion resistance. Applications include tooling implements, with a view towards increasing the life span of the workpiece whilst reducing manufacturing costs, along with the repair of worn components. For example, the generic techniques of physical vapour deposition (PVD) and chemical vapour deposition (CVD) are used frequently to produce hard coatings, *e.g.* to improve friction and the wear resistance of contact surfaces [5].

Coating techniques may be categorised according to the means of source material atomisation, such as resistance evaporation, induction heating, electron beam evaporation, cathode arc evaporation and cathode sputtering. For example, the PVD process involves the atomization or vaporization of a target material, to deposit a coating (~ 0.1 - 1000 μm thick) on a substrate surface. PVD methods are often divided into evaporation and sputtering. Evaporation involves the thermal vaporisation of target material, whilst sputtering is a kinetically controlled process in which the target is made cathodic and bombarded with ions, usually of an inert gas. PVD is used for the deposition of metallic elements, alloys and ceramics, with the latter being achieved either by direct use of a ceramic source or by using a pure metal source in combination with a reactive gas such as nitrogen, oxygen or methane, to produce, *e.g.,* nitrides, oxides or carbides [6].

The basic principle of the CVD process is that of solid material deposition on a surface by introducing a flow of gases into a chamber which condense material on to a heated substrate to form a coating (~ 0.5 - 2000 μm thick). Enhanced CVD processes involve the use of lasers, ions, plasmas, photons or hot-filaments to produce a wide range of wear resistance materials such as borides, nitrides, carbides, carbo-nitrides, oxides and oxy-nitrides, of almost all the transition metals. One of the main limitations of the CVD process is that it is very slow, and sometimes involving incomplete reactions [6, 7].

Hard coatings with good mechanical properties may be produced using CVD [8, 9] or PVD [10, 11]. However, CVD coatings are deposited usually at high temperatures (150 - 12000°C) [6], which may affect the mechanical properties of the substrate. PVD may be performed at lower temperatures (50 - 500°C), but coatings deposited by thermal evaporation or ion plating, for example, tend to suffer from poor adhesion

[12]. Also, PVD and CVD coatings may require the application of initial surface preparation techniques, in addition to ultrasonic cleaning, such as laser shock peening, sputtering, grit-blasting or other surface mechanical attrition treatment [13]. They are also relatively expensive techniques, requiring vacuum chambers and complex operational procedures [14]. Conversely, surface modification using the method of electrical discharge coating (EDC), being a modification of electrical discharge machining (EDM), has gained attention due to its simplicity of operation, with only a powder metallurgy (PM) electrode required to create a hard cermet coating [1].

2.3 The fundamentals EDM/EDC

EDM is a process for machining hard electrical conductive materials, by use of precisely controlled sparks, between a tool electrode and workpiece in the presence of dielectric media [15]. Essentially, the EDC process exploits the principle of sparking, being an adaptation of EDM, to deposit functionally significant amounts of material onto a surface, as part of an integrated manufacturing process. In particular, EDC requires the use of reversed polarity, compared to EDM, to promote material deposition. EDM, as used for sink-machining, normally utilises an anodic, solid tool electrode and a cathodic workpiece (Figure 2-1a), however in some cases a reverse polarity is employed, depending on the desired energy distribution, for finishing machining in particular [16]. Whilst EDC employs a cathodic powder metallurgy tool electrode and an anodic workpiece (Figure 2-1b). This polarity reversal, combined with optimised processing parameters and sacrificial tool electrode materials, provides for maximised incorporation of material from the tool electrode into the workpiece surface. Conveniently, the EDC technique is integrated easily within widely available EDM hardware.

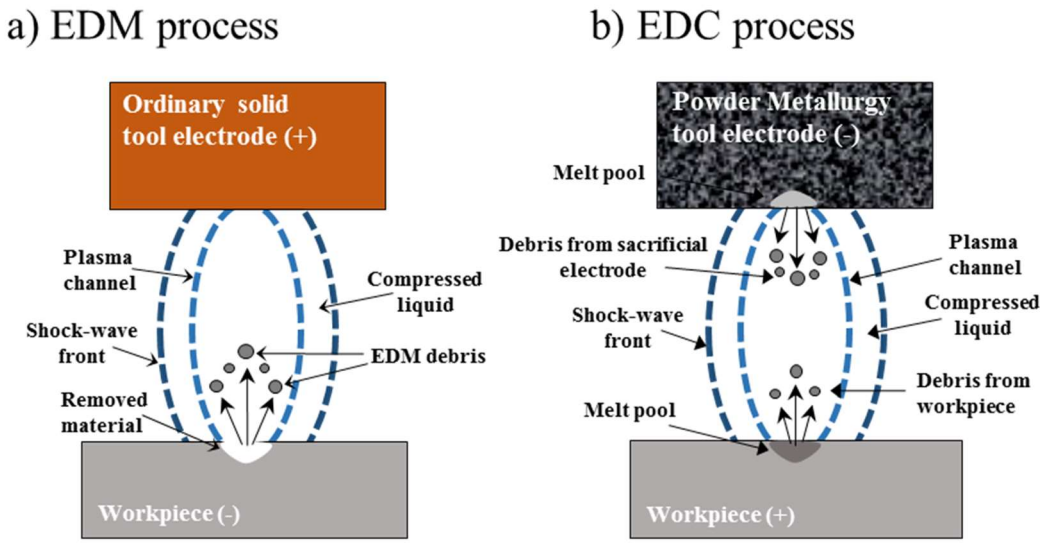

Figure 2-1 Schematic representation of: a) EDM mechanism with a solid tool electrode and positive polarity; and b) EDC mechanism with sacrificial semi-sintered tool electrode and reverse polarity

During conventional EDM, the removal of material is achieved through the conversion of electrical energy into thermal energy through a series of high frequency, 10^3 - 10^6 Hz, discrete electrical discharges between the two electrodes, separated by a small gap distance of 10 - 100 µm, immersed in a medium of dielectric fluid [16]. Prior to discharge, an open voltage is applied between the two electrodes, after which an ignition delay-time occurs for dielectric breakdown, constituting the statistical time-lag required for the generation of initial electrons and the time for dielectric ionisation. This delay-time varies (Figure 2-2) [16], and depends upon the localised conditions within the gap. Breakdown develops from the acceleration of electrons towards the anode, with the source of electrons being either from the cathode under the applied field, or from stray electrons present within the gap. The electrons impact with neutral atoms and particles present in the dielectric fluid, creating positive ions and additional electrons which accelerate towards cathode and anode, respectively. Each spark generates a localised plasma channel with very high temperature, estimated to be in the range ~ 8,000 - 12,000˚C, which induces a large localised pressure on the scale of

~ 200 atmospheres [17]. Material at both electrodes becomes superheated and form melt pools at their surfaces, whilst boiling is suppressed due to the high pressure exerted from the plasma. However, ejection of some molten material from the melt pools is thought to occur at the end of each discharge, promoted by a rapid drop in pressure [18]. The anode is melted first due to absorption of electrons at the start of the pulse-on time, whilst melting of the cathode is delayed, by a time one or two orders of magnitude beyond that of anode, because it emits electrons and absorbs positive ions [19]. Further, the size of the plasma radius at the cathode is smaller as compared with the anode, again because it emits electrons [20]. Accordingly, for EDC processing, the tool electrode is selected to hold a negative polarity whilst the workpiece is held at positive polarity [21].

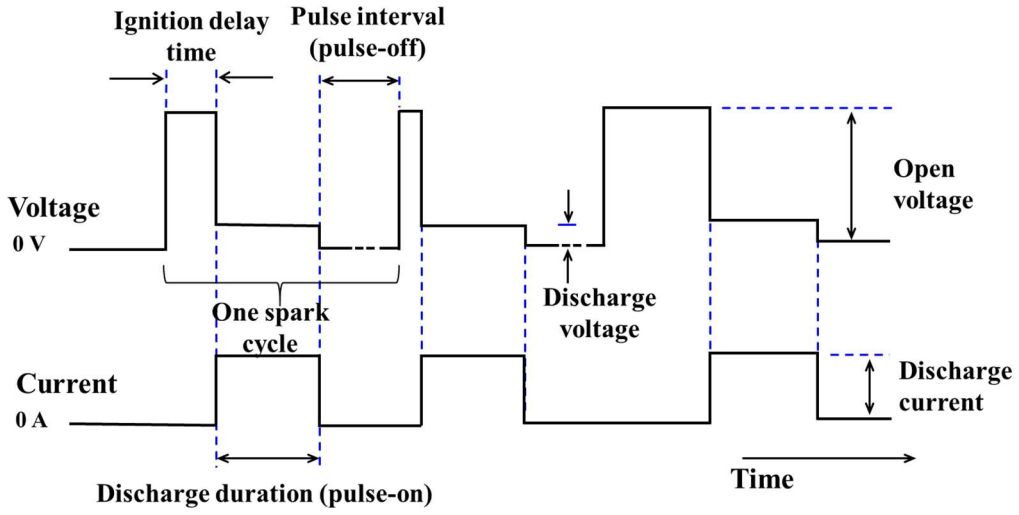

Figure 2-2 Voltage and current waveforms during the electrical discharge process (adapted from [16])

Figure 2-1b presents an adaption of the EDM process with reference to EDC, with workpiece and tool electrode held at positive and negative potentials, respectively. Sparking leads to the development of localised melt pools on the surface of the workpiece which, when combined with the transferred tool electrode material, cools

rapidly to form localised cermet deposits. Multiple sparking events then allow multiple, overlapping craters to form a continuum coating across the workpiece.

2.3.1 EDM discharge location and gap debris

In principle, discharges during EDM occur at the location of the shortest gap-width, and this can assist with EDM process reproducibility. However, the presence of electrically conductive debris can lead to a significant increase in the localised gap-width, and this can have both a negative and positive effect during EDM processing, *i.e.* by reducing replicating accuracy due to non-uniform debris distribution, whilst making the servo-gap control easier due to the extended gap width, respectively. In practice, it is difficult to maintain the gap width constant at several μm [16]. For example, Luo [22] reported that in pure kerosene dielectric fluid discharges occur at a small gap width not exceeding several μm, and that this can be a cause of failure to evacuate excess debris, resulting in an unstable arcing process. Hence, improved control requires a system with increased gap size, to overcome this arcing problem through improve debris evacuation, but this in turn can reduce the control over surface irregularities.

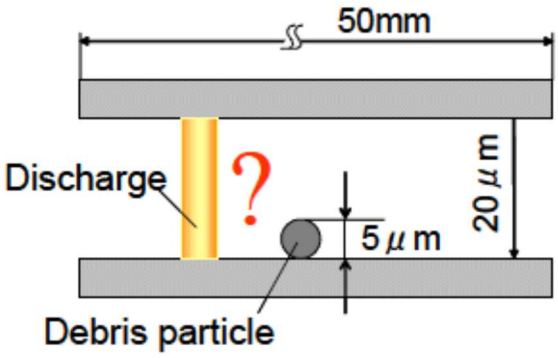

Figure 2-3 Electrical discharge location determination [16]

In order to clarify the influence of debris particles on discharge location, Kunieda and Takanobu [23] investigated the effect of placing debris particles of 5 μm diameter in

a 20 μm gap width, filled with clean EDM dielectric fluid (Figure 2-3). The data showed that, in most cases, discharge craters developed at different places, away from where the debris was placed. Hence, discharge occurrence is considered a probabilistic phenomenon, whereby the probability of discharge occurrence is determined simply by the product between probabilities of discharge occurrence per unit area and its surface area. Since the projected area of debris in the direction normal to the electrode surface is negligible, compared to the typical electrode surface area, the suggestion of determination of discharge location in a probabilistic rather than deterministic way implies a shorter gap width and higher debris density will increase the probability of discharge at that point [16, 23].

2.3.2 ED processing using PM electrodes

EDM allows for surface modification by employing a powder metallurgy (PM) tool electrode with reversed polarity. Table 2-1 broadly illustrates the progression of this technique for coating fabrication, using different powder metallurgy tool electrodes, over the years.

Table 2-1 Example ED investigations using various PM tool electrodes

Ref	Tool electrode	Substrate	Investigation	Comment
[24]	Cu, Al, WC, Ti/Al, WC/Co	Carbon steel, Aluminium	The availability of using powder metallurgy tool electrode for surface modification	A remarkably changed in the workpiece surface with transfer of tool electrode material
[25]	TiC/WC/Co WC/Co	AISI D2 Sendzimir rolls	Effects of compacting and sintering conditions, in addition to other operational conditions such as current and pulse on time	Ti and W, with C decomposed from the dielectric fluid, were transferred to the workpiece surface
[26]	Cu-W	Low carbon steel	Variation of the material removal rate, surface deposit rate and electrode wear rate, with processing parameters for surface modification, using a semi-sintered tool electrode	ED process is feasible for surface modification. Deposition was found at the processed surface, when the no-load voltage and the current were set to a low level
[1]	Ti	Carbon steel	Principles of EDC using a green compact electrode	A TiC ceramic layer was formed easily on the workpiece surface. Hardness varied with the current and pulse-on time

[27]	Cu	Ti–6Al–4V	The effects of using solid and powder compacted Cu electrodes with negative and positive polarity	A significantly higher amount of Cu was transferred from the powder compact electrodes to the workpiece surface, and more uniform layers produced with reverse polarity
[28]	Cu-W	Hot die steel H11	The effects of using powder metallurgy tool electrodes, with suitable machining conditions, to facilitate transfer of desirable alloying elements to the machined surface	Cu–W PM tool electrode found capable of surface alloying under favourable processing conditions, with high microhardness and significant amounts of surface alloying, with the formation of Fe_3C and W_3C
[21]	Ti	6061-T6 Aluminium	The effects of using sintered tool electrodes with wet (TiN powder to kerosene) and dry (N_2) EDC	TiC was formed, with no TiN layer, during wet EDC processing. A 20 μm layer thickness of pure TiN formed during dry EDC
[29]	Ti	Carbon steel	The preparation of ternary TiCN coatings by EDM, with a dielectric medium of ethanolamine, containing carbon and nitrogen	A 15 μm TiCN layer thickness, comprising mainly $TiC_{0.3}N_{0.7}$ with fine-grain structure

For example, Mohri *et al.* [24] initially demonstrated the benefits of using green compact composite tool-electrodes of Cu, Al, WC, Ti or Co to modify a carbon steel and Al substrate, and reported high wear of the green compact or sintered electrodes due to the low thermal conductivity of composite material, as compared to the raw material, along with a remarkable change of the machined surfaces with improved corrosion and wear resistance. Further, Simão *et al.* [25] reported on the effect of using green compact and sintered tool electrodes of TiC/WC/Co and WC/Co during the surface modification of AISI D2 Sendzimir rolls, using an electrical discharge texturing (EDT) process. The data demonstrated that Ti and/or W from the PM electrode had made its way into the processed surface, along with C decomposed from the dielectric fluid during sparking, with high concentrations observed for the case of negative polarity. However, the processing variables associated with the production of PM electrodes, such as compacting pressure and sintering conditions, were found to have a critical effect on this EDT process, with reduced material transfer for increasing compact pressure and sintering temperature, whilst the hardness of the recast layer

increased up to 950 HK (0.025) using a sintered TiC/WC/Co tool electrode, resulting in reduced roll wear. Similarly, Chen *et al.* [26] reported on the development of semi-sintered Cu-W tool electrodes (powder size < 45 μm, blended for 10 h and then semi-sintered under 770 MPa at 600˚C for 20 minutes), for ED surface modification of low carbon steel. The results confirmed that tool electrode material was effectively transferred during EDM processing, with the authors proposing that the bonding strength of the semi-sintered tool electrode was too low to withstand thermal erosion during the discharge. Further, Wang *et al.* [1] reported the development of a ~ 20 μm TiC ceramic layer thickness in a few minutes, using a Ti powder green compact tool electrode, following reaction with cracked C from the dielectric oil, with coating hardness being more than three times than that of the substrate.

Ho *et al.* [27] reported on the use of solid and PM Cu electrodes, with positive and negative polarity, during the surface modification of Ti-6Al-4V alloy, with the recast layers varying between ~ 4 - 11 μm. Use of a positive tool electrode polarity produced thicker but rougher layers, whilst more uniform layers resulted from the use of a negative tool polarity. Higher material transfer was found for surfaces processed with a powder compact tool electrode.

Gill and Kumar [28] report an 83% improvement in microhardness of H11 die steel processed using a Cu-W powder metallurgy electrode, with XRD indicating the presence of Fe_3C and W_3C as being responsible for the increased hardness. Further, Chen *et al.* [21] EDC surface modified an 6060-T6 Al alloy using a Ti sintered electrode, under wet and dry environments, with TiN powder mixed in kerosene dielectic fluid or high purity N_2 gas (Figure 2-4). The results demonstrated a TiC layer deposited on the workpiece surface, whilst dispersed TiN powder in the dielectric enhanced the plasma column under conditions of low discharge energy. No TiN was

found in the coated surface, under wet processing conditions, whilst a ~ 20 µm TiN layer was formed under dry processing conditions. Xiao *et al.* [29] attempted to deposit a ternary TiCN layer on 45# carbon steel, using a Ti electrode combined with a novel dielectric fluid of ethanolamine aqueous solution containing carbon and nitrogen. The development of layers of ~ 15 µm thickness was reported, comprising fine-grained structures of nitrogen-rich $TiC_{0.3}N_{0.7}$, with hardness of 1780 HV, metallurgically bonded to the steel substrate.

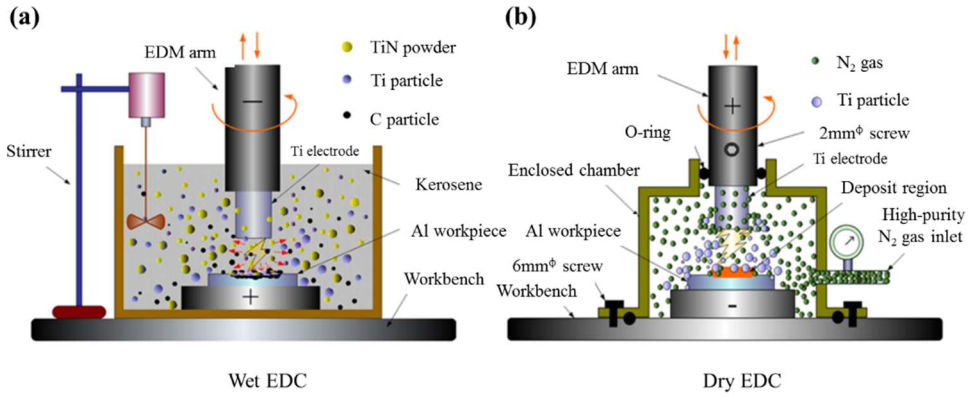

Figure 2-4 Illustrations of EDC conducted under environments of: a) kerosene dielectric fluid (wet); and b) nitrogen gas (dry) [21]

Researchers to date have done successful work, investigating the role of powder metallurgy tool electrodes, with appropriate processing conditions, to enhance material transformation to improve the surface performance of components, thereby extending the applicability of EDM. However, no in-depth work has been done so far to analyse the fundamental material transfer mechanisms, the nature of the resultant coatings, and the effects of processing parameters on the elemental distributions and coating performance.

2.3.3 ED processing using powder particles suspended in dielectric fluid

One variant EDM technique uses powder mixed within the dielectric fluid, proposed to improve the surface finish as a result of reducing the spark energy, effectively by enlarging the discharge gap distance combined with homogenisation of the discharge conditions throughout the processed surface [30]. The material transformation from both tool electrode and/or suspended powder helps to improve the surface performance. Figure 2-5 presents a schematic illustration of the EDM surface modification process, using a powder suspension in dielectric fluid. The suspended powder may become deposited directly, in its original state, or after reacting with carbon decomposed from the hydrocarbon dielectric fluid.

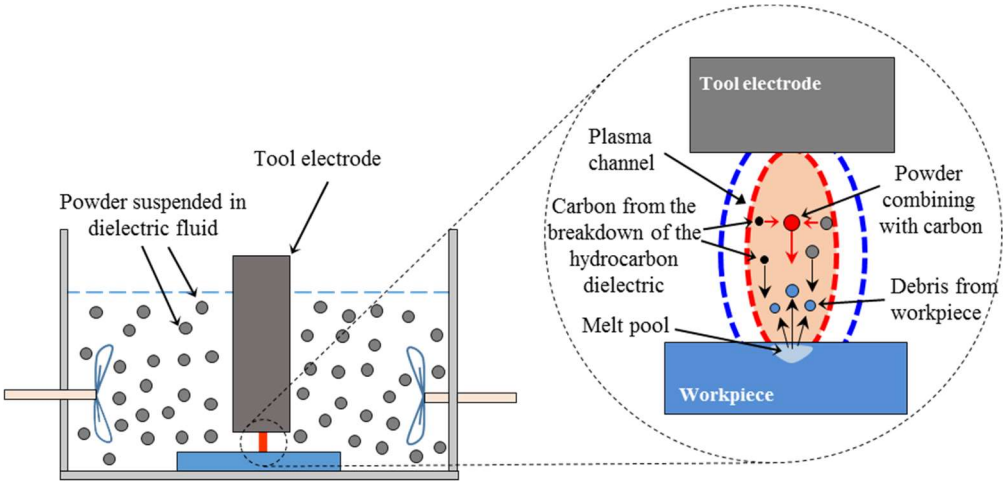

Figure 2-5 Illustration of EDM, with powder suspension in the dielectric fluid

For example, Batish *et al*. [31] reported an increase in microhardness, up to 80%, for three types of die steels (EN31, H11, and High Carbon High Chromium (HCHCr)) after EDM with a powder mixed dielectric fluid (no add powder to dielectric fluid compared to adding graphite and Al powder) using two types of tool electrode (Cu and W-Cu). It was reported that graphite powder had more benefit in improving microhardness compared to Al, in all cases, with the dominant deposited phase being

that of the suspended powder particles, in addition to trace deposition of material from the electrode.

In order to obtain high performance modified surfaces, the powder particles should be distributed uniformly within the working fluid. For example, Furutania *et al.* [2] reported on two ways to keep the Ti powder concentration at high levels within the dielectric fluid between workpiece and electrode, *i.e.* by a rotating thin electrode or disk electrode. The experimental results indicated that a TiC layer can be obtained using both electrode shapes, with wider area of coating and uniform thickness obtained with a gear shaped rotating electrode. Further, Yih-Fong and Fu-Chen [32] examined the effects of particle size within the dielectric fluid on the EDM process. They reported that the thickest recast layer, with best surface finish, was produced using the smallest particles (~ 70 - 80 nm), whilst larger particle sizes were associated with the development of rougher surfaces and a thinner recast layer at the machined surface. The authors also reported that Al powder produced the best surface finish, but with the thinnest recast layer, followed by Cr, SiC and Cu powders the worst. Janmanee and Muttamara [33] reported significant improvement in surface quality of a tungsten carbide workpiece, *i.e.* by eliminating microcracks, when using EDC (with 36 μm Ti powder suspended in the dielectric fluid and a 5 mm Cu electrode), as compared to conventional EDM surfaces (Figure 2-6). The hardness of the coated layer was reported to increase from 990 HV to 1750 HV or by 76.76%, due to the formation of TiC. Further, Chen *et al.* [34] succeeded in producing TiO on a Grade 4 pure Ti workpiece surface, using micro-current EDM with deionized water mixed with Ti powder. The recast layer thickness increased with increasing current, pulse-on time and powder concentration, with a significant decrease in cracking observed using a suitable concentration of 6 g/l Ti powder in the dielectric fluid.

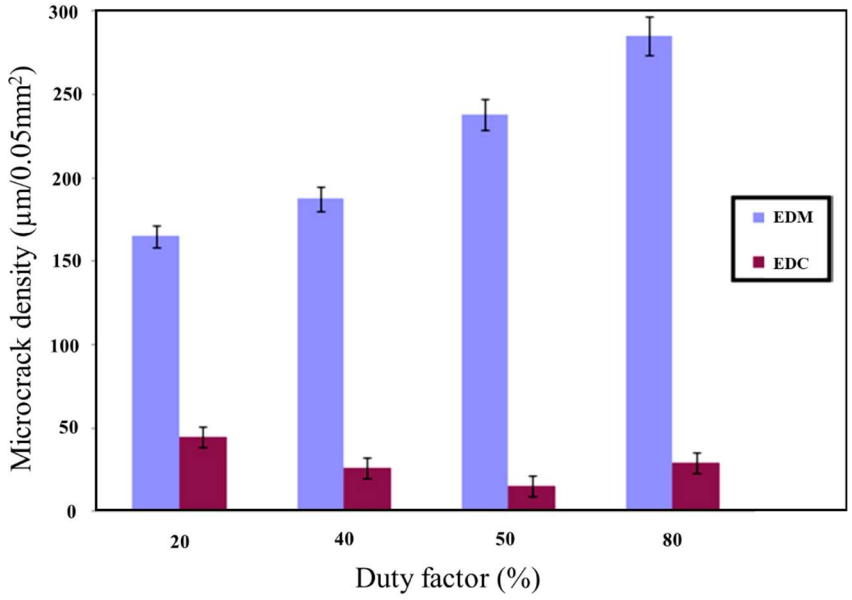

Figure 2-6 Microcrack density/unit area for EDM & EDC tungsten carbide processed surfaces [33]

2.3.4 ED processed surface nanostructures

Improvement in the mechanical properties of coatings may be achieved effectively through control of the shape, size and distribution of phases. To date, however, the nanostructures of ED processed surfaces have not been widely investigated by researchers. For example, Chen *et al.* [35] reported on the development of nanostructured ɣ-phase and $Fe_{0.6}Mn_{5.4}C_2$ on the recast layer of EDM Fe-Al-Mn alloys. Further, Murray *et al*. [36] used TEM to investigate EDM single-crystal Si using W tool electrode, identifying nano-sized W-particles within the recast layer (Figure 2-7). Similarly, Xiao *et al*. [29] observed fine grain structures within TiCN coatings, ED processed using a Ti tool electrode, with C and N in a dielectric fluid of ethanolamine.

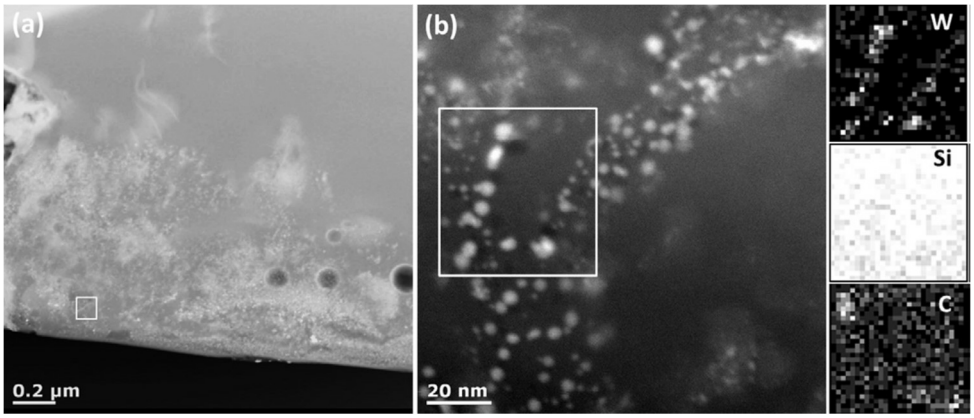

Figure 2-7 HAADF STEM image of a W impregnated Si recast layer, following EDM, with EDS mapping showing regions of W, Si and C [36]

2.3.5 Effects of ED processing parameters on material deposition

ED process variables can be classified according to literature [37-39] into four main categories, as shown in cause and effect diagram of Figure 2-8.

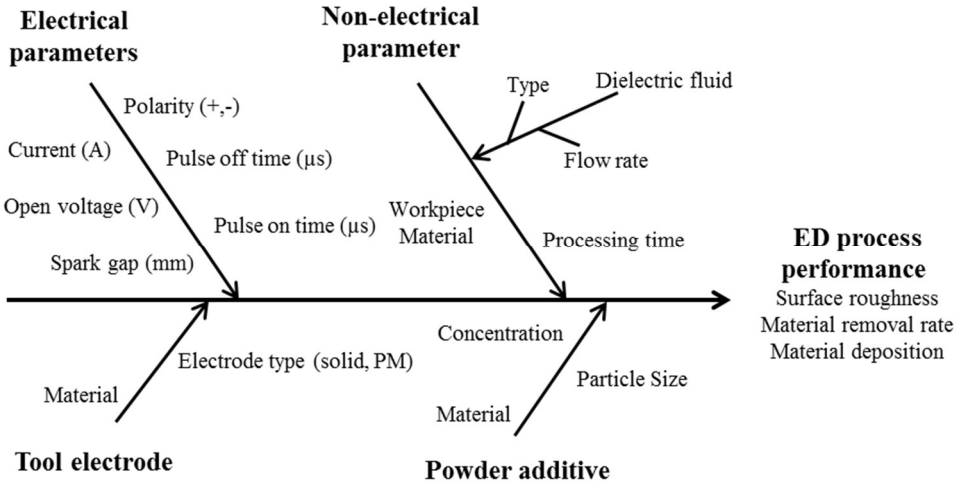

Figure 2-8 Ishikawa (cause and effect) diagram for ED process parameters (adapted from [37-39])

The performance of ED processed surfaces correlates directly with electrical discharge machining parameters such as current, pulse-on/off time *etc*. For example, Simao *et al.* [40] used statistical analyses (L8 fractional factorial Taguchi design) to identify the effect of key operational factors on H13 hot worked tool steels coated via

a PM WC-Co tool electrode. The development of a ~ 30 µm uniform hard layer with relatively few microcracks was demonstrated, with microhardness increasing from ~ 640 HK to ~ 1319 HK; with percentage contribution ratios for discharge current, polarity and pulse on time being ~ 24, 20 and 19%, respectively, whilst the open gap voltage was shown to have a small effect. Further, Chen *et al.* [26] investigated the surface modification of low carbon steel processed using a semi-sintered Cu-W tool electrode, and showed a deposition effect at low current (3 and 5 A), with the highest deposition rate at 5 A and short pulse-on times, The process was reported to turn to a material removal process with increasing current (10 A, 16 A). Similarly, Chen *et al.* [21] reported optimised processing conditions for wet EDC processing, using a Ti sintered tool electrode and kerosene dielectric fluid, at $1 > I_p > 8$ A current and $9 < T_{on} < 100$ µs pulse-on time, at 27% duty factor. However, replacing kerosene with high purity N_2 gas led to the formation of a pure TiN layer on the processed surface, with optimised parameters of $1 > I_p > 30$ A current and $6 < T_{on} < 72$ µs pulse-on time, at 16% duty factor.

Kumar and Batra [41] used W powder in hydrocarbon dielectric fluid and demonstrated the deposition of tungsten carbide on three types of die steel. The presence of WC and W_2C, with high percentage of carbon, in the processed surface indicated a reaction between W powder and pyrolytic carbon under the high temperature conditions of the plasma channel. Favourable machining conditions were reported for material transfer; *i.e.* a low discharge current < 5 A, a short pulse-on time < 10 µs, and a long pulse-off time > 50 µs, with negative tool electrode polarity, leading to > 100% improvement in the microhardness of all workpiece materials. Similarly, Furutani *et al.* [42] investigated the influence of processing parameters (current and pulse-on time) on TiC deposition and the EDM removal process, using a 1 mm

diameter Cu tool electrode and Ti powder suspension within the dielectric fluid. The favourable range of electrical conditions for the deposition of material is summarised in Figure 2-9.

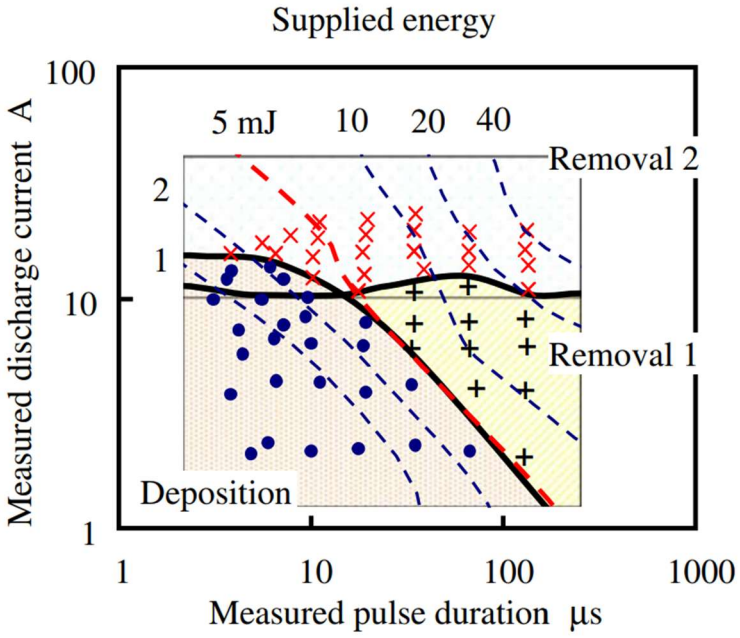

Figure 2-9 Plot of pulse duration against discharge current, outlining conditions for material removal or TiC deposition [42]

The solid blue circles indicate deposition conditions providing for maximum hardness of 2000 HV. Material removal was classified into two regions: Region 1 relates to cracks observed within Ti-rich surfaces, whilst Region 2 relates to the simple removal of material.

2.3.6 TiC-based coating using ED process

ED processing may employ both a PM tool electrode and/or suspended powder to form a TiC/Fe coating on steel. For example, Wang *et al.* [1] reported on the deposition of TiC onto a carbon steel workpiece using a Ti green compact electrode. The authors proposed a chemical reaction between cracked carbon from the dielectric fluid and the Ti powder to form the TiC deposited onto the workpiece surface, as confirmed by

XRD, with variable hardness depending on the processing condition (Figure 2-10). In particular, these coatings exhibited hardness levels more than four or five times that of the substrate. Similarly, Hwang *et al.* [43] demonstrated that EDC using a multi-layered Ti/graphite electrode facilitated the development of TiC coatings on a Ni workpiece with reduced micro-crack formation. The maximum hardness achieved was ~ 1710 HV. The authors also reported that the presence of a graphite layer on the electrode enhanced the carbon concentration, resulting in increasing combinations of Ti and C.

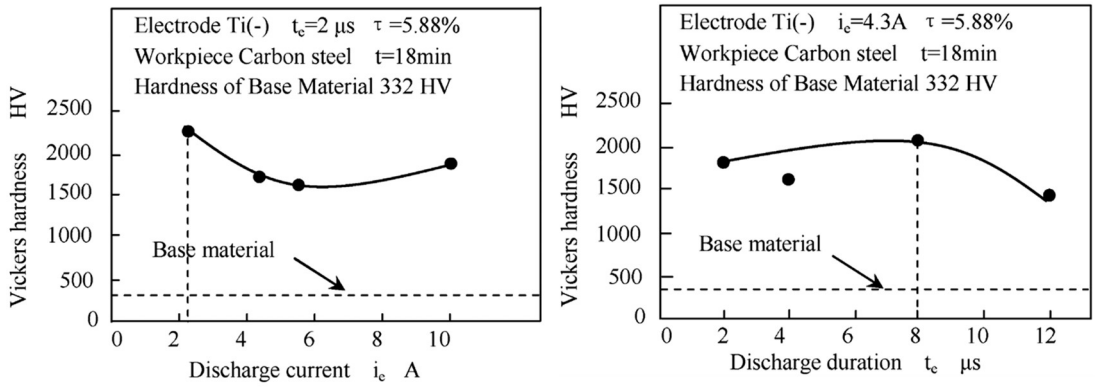

Figure 2-10 Average Vickers hardness, for EDC deposited TiC, measured with 200gf as a function of increasing current and pulse-on time [1]

Suzuki and Kobayashi [44] investigated the EDC formation mechanisms of TiC on high speed steel, processed using a semi-sintered TiC tool electrode with reversed polarity. It was reported that TiC particles migrated directly from the TiC electrode to the workpiece surface, without their prior presence in the gap between the electrodes. Melted and re-solidified TiC was found in the processed surface, in the form of craters for conditions of constant voltage; however, a temporary voltage drop during discharge resulted in the presence of TiC powder within the crater (Figure 2-11). The temporary voltage drop was attributed to large TiC clusters within the gap.

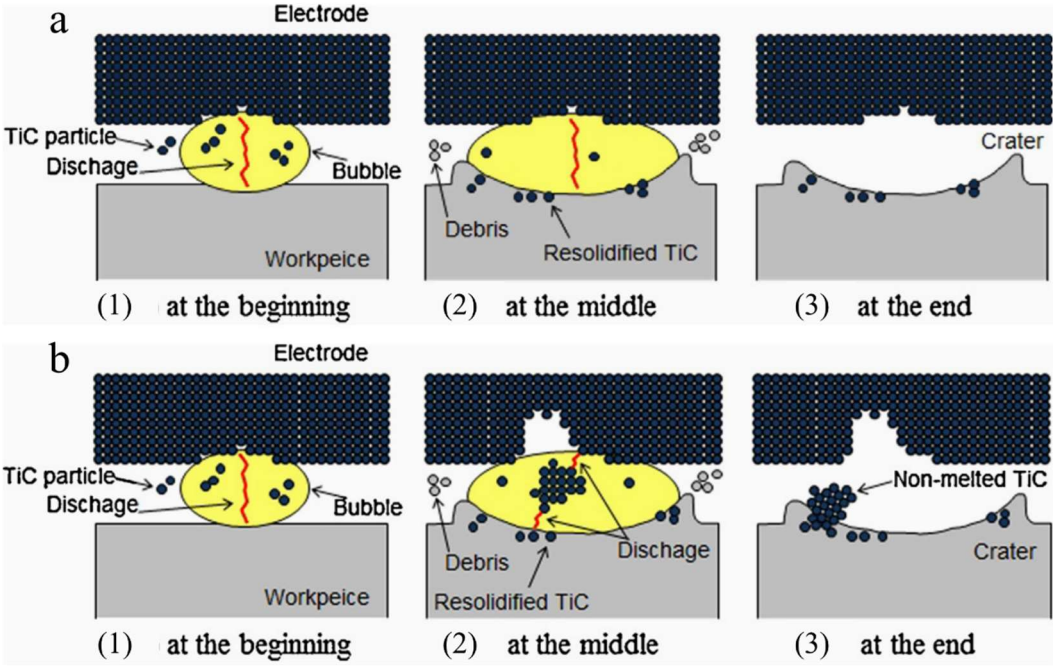

Figure 2-11 Schematic illustration of the EDC TiC adhesion process: For the case of: a) constant voltage; and b) a temporary voltage drop [44]

Xie *et al.* [45] compared EDC TiC coatings prepared using a semi-sintered Ti tool electrode, with and without added graphite powder to the dielectric fluid. Again, it was suggested that the additional graphite source acted to enhance the combination of Ti from the tool electrode with carbon, for TiC deposition onto 45# carbon steel, as confirmed by XRD (Figure 2-12). The presence of graphite powder serves as an additional carbon source, and led to an increase in the reaction and transition of Ti from the tool electrode to TiC phases, thereby increasing the coating microhardness. It also acted to reduce coating inhomogeneities, such as non-uniform layer thickness, and to reduce micro-cracks by dispersing the discharge energy more randomly throughout the surface.

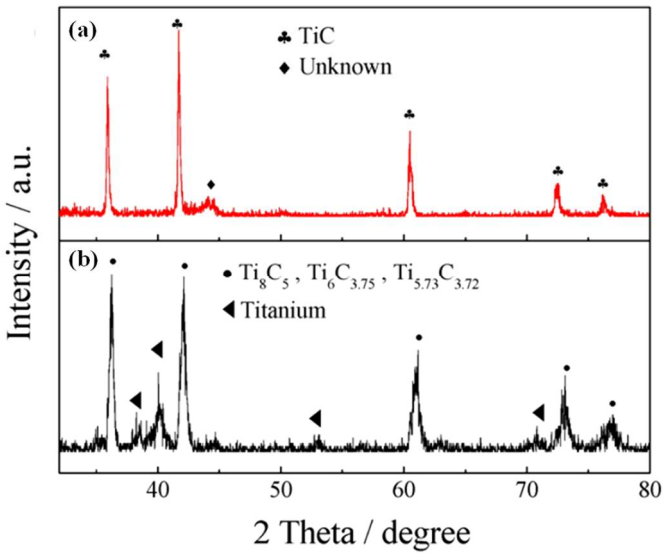

Figure 2-12 XRD patterns for TiC coatings: EDC processed with (a) graphite mixed within the dielectric fluid; and b) without graphite [45]

Ueno *et al.* [46] performed EDC using a TiC sintered electrode and a kerosene-based dielectric fluid to improving the wear resistance of the roll surface of 2% Cr steel, in laboratory skin-pass rolling. The results showed a large variation of hardness as a function of processing parameters (current and pulse-on time), with more than 1500 HV can be secured, whilst additional machining time did not affect the hardness or layer thickness. The wear resistance of the TiC coated rolls produced by EDC were superior to that of conventional chrome plated rolls.

With regard to the use of Ti powder mixed within the dielectric fluid, Furutania *et al.* [2] demonstrated an EDC method to accrete TiC layers with hardness of ~ 1600 HV onto carbon steel workpiece surfaces, using Ti powder mixed with kerosene dielectric fluid, thereby avoiding the need for using a semi-sintered tool electrode. A thin ~ 1 mm diameter rotation disk was used to keep the powder concentration high between the tool electrode and the workpiece. Likewise, Janmanee and Muttamara [33] obtained a ~ 5 μm coating thickness for EDC processed TiC, using a tungsten carbide substrate and an ordinary Cu tool electrode, with < 36 μm sized Ti powder

suspended in the dielectric fluid. EDS analyses confirmed that the coating contained Ti and C with hardness of ~ 1750 HV.

This section has presented a wide overview of the fundamentals of EDC processing, with reference to EDM. The next section will cover the basics of EDM and process modelling for better understanding the interaction caused by single discharge incidents and the consequent energy distributions.

2.4 ED process modelling

2.4.1 Single spark events

The ED process involves a complex combination of physical phenomena [47] including electrodynamics, thermodynamics and hydrodynamics [48], necessitating transition between solid, liquid and gas/plasma phases, with chemical reactions leading to mass transfer and boundary displacement [16], making it difficult to express a simple and comprehensive model.

During ED processing, material is removed by a series of discrete electrical discharges between two electrodes immersed in a medium of dielectric fluid, through conversion of electrical energy into thermal energy [49]. The energy distribution into the workpiece material may be estimated with reference to the physical properties of the electrodes in question, by assuming either all the electrical energy is converted into heat [50]; or by using refined process models, using either analytical [20] or numerical approaches [51, 52] based on underpinning electro-thermal and electro-mechanical mechanisms of material removal [53]. However, there is variability in the bases of these modelling approaches, for single spark events, which consider a variety of heat sources (*e.g.* point, cylindrical or Gaussian) and assume different levels of energy transfer, in order to calculate temperature distributions, crater geometries and the

volume of material removed. For example, Joshi and Pande [54] developed a thermal-physical model for the die-sinking EDM process, using finite element methods (FEM), and considered a 2D axi-symmetric model based on realistic assumptions, such as Gaussian distribution heat source, spark radius based on current and pulse-on time, and latent heat of melting, to estimate crater geometry and the material removal rate. They reported that the metal removal rate (MRR) values and crater cavity shapes predicted in their analytical models were very close to experimental results during actual machining. Further, Zhang *et al.* [55] reported that a Gaussian distribution heat source is much more consistent with actual EDM, as compared with point and circular heat sources.

Shao and Rajurkar [56] simulated single crater formation for 304-SS using micro-EDM, this electro-thermal model considered a realistic assumption for the Gaussian distribution of heat flux, expanding plasma radius and temperature dependent thermal properties. It was reported that the molten isothermal profile was deeper inside and shallower outside due to expansion of the heat source. At the beginning of the pulse-on time, the energy is more concentrated when the radius is small so it is deeper inside, whilst the outside surface experiences less heating time. The simulated crater radius was closer to experimental results, but the simulation over-estimated crater depth (Figure 2-13b), being attributed to the re-solidification of unremoved molten material.

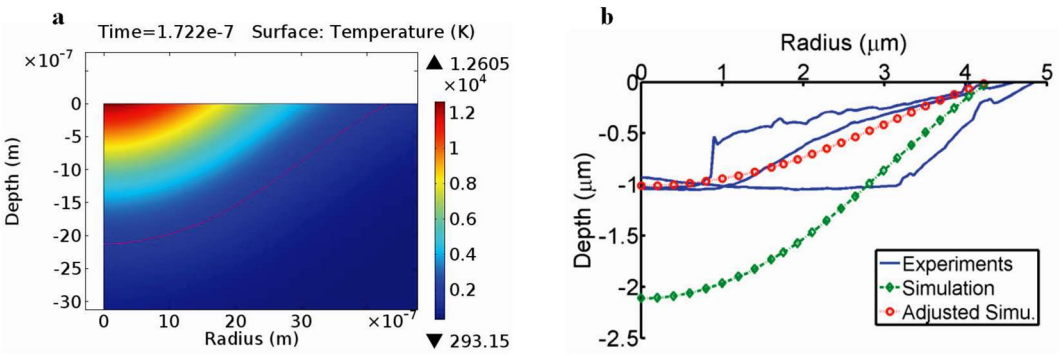

Figure 2-13 a) Temperature distribution; and b) simulation and experimental data for a crater boundary (90 V and positive polarity) [56]

A model based on thermo-hydraulic coupling was developed by Tang and Yang [57] to predict the temperature distribution of the workpiece, and crater formation, from the perspective of the hydrodynamic characteristics of the molten material. The simulation data indicated that the crater appeared shortly after the ignition time, and reached a maximum size at the end of the discharge duration. Molten material was removed by evaporation during the initial stage, then by splashing. It was reported that ~ 7.6% of the molten material was removed, whilst the rest re-solidified on the crater surface, for the conditions studied.

2.4.2 ED energy distribution between anode and cathode

During EDM, the anode and cathode removal amounts are dependent on the discharge conditions, and are quite different even when the same material is used for both electrodes. This phenomenon is related to variations in the energy distribution into the anode and cathode, as a function of processing parameters [16]. In general, the discharge energy is distributed mainly between the tool electrode, workpiece and dielectric fluid. The energy is consumed by a number of physical process, such as explosion, radiation, conduction, evaporation, melting and ignition [58]. Researchers such as Snoeys and Van Dijck [59], Van Dijck and Dutre [60], Beck [61], and Jilani and Pandey [62] all assumed a constant percentage of energy, $F_v = 0.5$, transferred to the anode and cathode under different machining conditions. Later DiBitonto *et al*. [19] assumed only $F_v = 0.183$ of discharge energy was transferred for cathode erosion. Similarly, Eubank *et al.* [63] assumed 18% and 8% of the total energy contributed to the melting of the cathode and anode, respectively. Indeed, the assumption of a constant fraction of energy transferred to the workpiece is considered one of the main reasons for the variability between modelling and experimental data [64]. A

comprehensive comparison by Yeo *et al.* [48] of five different EDM electro-thermal models, in terms of temperature distribution, material removal and crater geometry, demonstrated that the model of Di Bitonto *et al.* [19], based on 18.3% of the available energy transferred to the cathode, showed better agreement with experimental data than other models. Models which assumed 50% energy transfer led to an overestimate of workpiece temperature and the resultant crater size.

The traditional method for the determination of energy distribution between anode, cathode and dielectric fluid, during EDM, was done by comparing measured temperatures with calculated results. For example, Okada *et al.* [65] investigated energy distributions by measuring the temperature of both workpiece and electrode temperature using a simple thermocouple approach. Further, Xia *et al.* [66] determined the energy distribution to anode and cathode by comparing measured and calculated electrode temperatures as a function of position. In this case, a finite difference method was used iteratively, with the experimental set-up shown in Figure 2-14. It was reported that the energy distribution converged towards ~ 40 - 48% and ~ 25 - 34% into the anode and cathode, respectively, as the temperatures coincided.

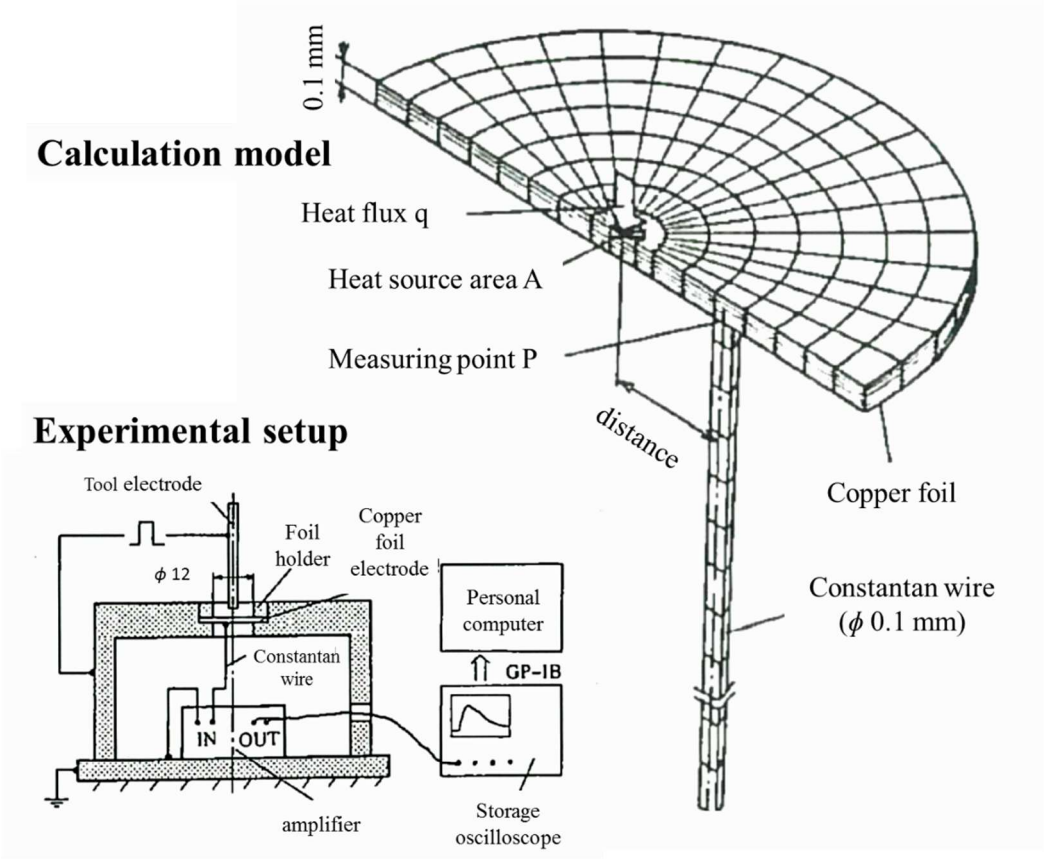

Figure 2-14 Experimental set-up for anode temperature measurement and the model used for temperature calculation [66]

Similarly, Singh [64] performed an experiment to consider the fraction of energy transferred to the cathode, for different discharge parameters, utilising heat transfer principles. The experiment was performed using a Cu tool electrode and a WC workpiece. The temperature was measured using J-type Iron/Constantan thermocouples inserted in the Teflon insulation around the tool electrode and the workpiece at known positions. The results showed that the fraction of energy transferred varied, from 6.1% to 26.8%, with increasing current and pulse-on time (total energy per discharge event).

Alternatively, Shen *et al*. [67] proposed a new method to determine the energy distribution into Ti-6Al-4V during EDM, by comparing the boundary of melted material from experiment work with the calculated boundary. The model considered

pulse-on time, inter-electrode distance, electrode shape and polarity. It was found that the energy distribution characteristics were affected highly by the power density applied. For example, the electrode shape had a significant effect on the energy distribution, with a needle-shaped tool electrode distributing more energy into the workpiece surface, being attributed to plasma diameter (Figure 2-15). It was also reported that increasing the inter-electrode distance led to a decreased energy distribution ratio. Similarly, Zhang *et al.* [58] determined the plasma diameter and energy distribution during EDM, by comparing the experimentally determined boundaries of molten material (*i.e.* crater morphologies) with data from a finite element method (FEM) thermo-physical model. It was shown that the power density is an important factor when considering material removal and energy efficiency. For conditions of short pulse-on time, material removal and energy efficiency are much higher, than for long pulse-on times, due to the higher power density. Also, for consistency, the expansion of plasma diameter should be taken into consideration, under conditions of fixed current.

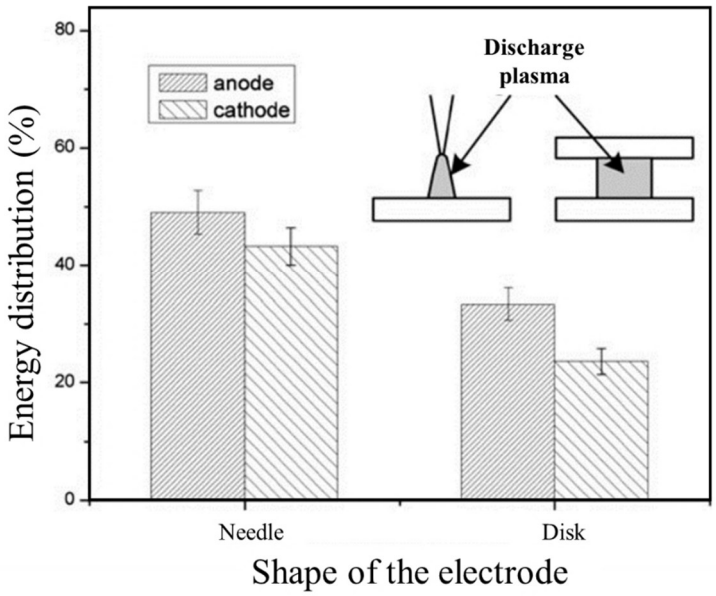

Figure 2-15 Comparison of energy distribution into the workpiece, from needle and disk-shaped electrodes [67]

2.4.3 Plasma channel characteristics

There are inherent difficulties in measuring the plasma channel radius R_{pc} due to the very small distance between the two electrodes (~ 10 - 100 μm [16]), with the plasma occurring only for very short pulse-on times (few microseconds). Further, gap pollution, in the form of debris and bubbles, acts to obscure the spark gap, making it difficult to analyse the light emission [68].

However, recent high speed camera developments have facilitated characterisation of the EDM plasma diameter. For examples, Descoeudres *et al.* [69] used spatially-resolved optical emission spectroscopy to investigate the plasma created during EDM and reported very fast development of the plasma, with formation < 50 ns after dielectric breakdown. The plasma excited a broad volume between ~ 50 and 400 μm around the electrode, for increasing current from 6 to 48 A, with light originating mostly from a region broader than the gap itself. The light emission was strongest in the central region, and light was still emitted after the discharge from incandescent metallic debris arising from erosion of the workpiece.

Natsu *et al.* [70] used a high speed camera to determine the plasma diameter of single discharge in air (20 A, 300 μs pulse-on time and 500 V open circuit voltage). The results showed that expansion of the plasma was complete within a few μs after dielectric breakdown, with the light emitting zone expanded to ~ 0.6 - 0.7 mm, being several times larger than the resultant discharge crater. Similarly, Kojima *et al.* [71] used a high speed camera to show that expansion of the plasma was complete within ~ 2 μs after dielectric breakdown (Figure 2-16), whilst the diameter of the crater grew slowly in comparison to the plasma, leading to the suggestion that plasma diameter was ~ five times larger than the crater diameter under certain conditions. This was distinct from more conventional plasma expansion models, which suggested that the

plasma channel continued to expand, even several dozen of microseconds after dielectric breakdown.

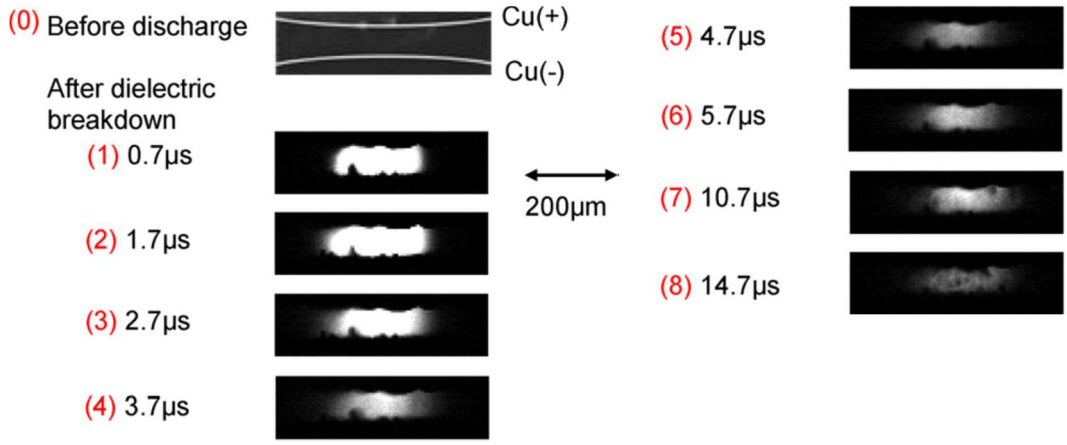

Figure 2-16 High-speed video frames of arc plasma during EDM (23 A, 80 μs pulse-on time and 280 V) [71]

There have been a variety of approaches to express plasma channel radius in the literature, but with no clear consensus. For example, the time dependent plasma radius equation may be taken as:

$$\boldsymbol{R_{plasma} = R_p\, t^n} \qquad (2\text{-}1)$$

Where $\boldsymbol{R_p}$ is an empirical constant, and exponent n depends on the experimental conditions. Eubank *et al.* [63] suggest n = 0.75, whilst Revaz *et al.* [72] determined the exponent for the plasma channel to be n = 0.2. Similarly Izquierdo *et al.* [73] suggested n = 0.2. Alternatively, the time-dependent plasma channel radius equation may be expressed as:

$$\boldsymbol{R_{pc} = a\, I^m t_{on}^n} \qquad (2\text{-}2)$$

Where t_{on} is the pulse-on time; I is current, and a, n and m are empirical constants. Ikai and Hashiguchi [74] used experimental values for crater radii from single pulse

interactions to determine the following empirical relationship, based on pulse width the discharge current profiles:

$$R_{pc} = 2.04\ x\ 10^{-3}\ I^{0.43}\ t_{on}^{0.44} \qquad (2\text{-}3)$$

Accordingly, it is recognised that different processing conditions can lead to significant differences in the plasma channel radius [58].

2.5 Overview of wear

2.5.1 Fundamental of wear mechanisms

Wear can be defined as a progression of material removal from one or both surfaces in contact motion relative to each other [75]. The wear mode refers to the type of contact defined by movement, geometry and environment, *e.g.* rolling wear, sliding wear, fretting wear, erosion wear, impact wear and cavitation [6]. Further, a number of classifications have been suggested to describe the mechanisms of wear. Initially, wear was classified based on surface appearance after a contact event, *e.g.* pitting, gouging, scuffing, spalling, scoring, fretting and galling, as related to certain applications such as gear contact [76]. The most common classification of the wear is based on the fundamentals of material removal from the surface under contact, divided into adhesive wear, abrasive wear, fatigue wear and chemical wear [6, 76, 77] (Figure 2-17). However, wear may involve a complex combination with more than one wear mechanism.

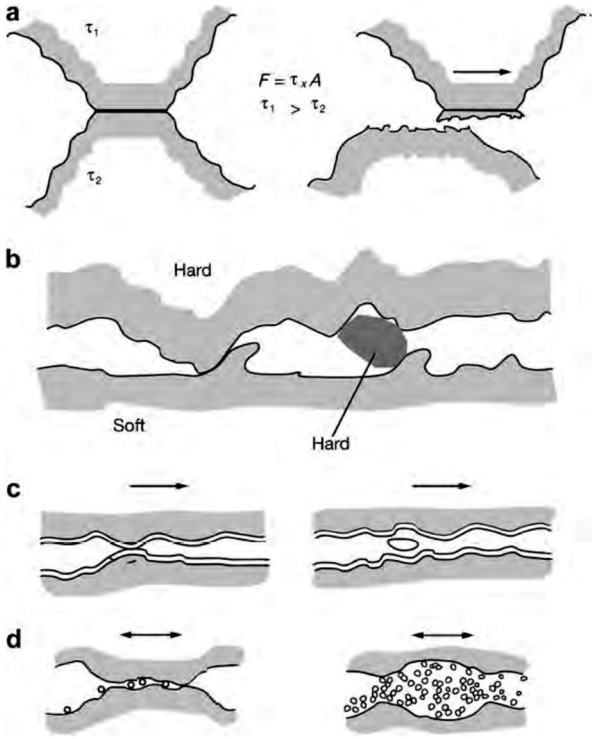

Figure 2-17 Basic of mechanisms of wear: a) adhesive, b) abrasive, c) fatigue and d) chemical [6]

2.5.1.1 Adhesive wear

Briefly, adhesive wear occurs when the asperities of two contacting surfaces slide over each other, with tangential motion causing a separation of softer material which adheres to the opposing surface. Material properties combined with a possible protective layer or contamination play important roles in adhesive wear. Reciprocating sliding geometries are associated with higher wear rates than unidirectional sliding geometries under identical loading conditions [6, 78].

2.5.1.2 Abrasive wear

Abrasive wear is the most common type of wear, constituting ~ 50% of total wear in industrial applications [79]. For this type of wear, material is removed or detached from a solid surface by the passage of hard/sharp particles between two solid surfaces in relative motion [80]. The early stages of abrasive wear is concerned with two-body

abrasion, where cutting and plowing occurs by hard particles fixed on opposite surfaces. The later stage is concerned with three-body abrasion, whereby hard particles are free to tumble and change their angles of approach, penetrating into the solid surface [77, 81].

2.5.1.3 Fatigue wear

Fatigue wear occurs when surfaces in contact undergo repeated motion, with the cycle of loading and unloading resulting in the development of surface or sub-surface cracks. Eventually, material breaks up and forms large fragments, in turn leaving large pits in the surface. This type of wear is a lifetime limiting failure mechanism, *e.g.* in ball, roller bearings and gears [6, 78].

2.5.1.4 Chemical wear

Chemical or corrosive wear occurs due to chemical reactions initiated by the effect of surrounding environmental conditions, in combination with chemical contact mechanisms. A chemical change in the composition and mechanical properties of the surface results influences both friction and wear. Oxidation is the most common chemical process affecting wear. For example, a very thin oxidation layer can act as a protection layer, reducing friction and wear in metal contact [6, 77].

2.5.2 Contact condition

The tribological process of two solid surfaces in contact with relative motion is a complex mix of friction, wear and deformation mechanisms. With respect to a coated surface, four main parameters have been identified to help control the contact

condition and hence friction behaviour; *i.e.* the coating/substrate hardness relationship, coating thickness, surface roughness and the size and hardness of contacting debris. The interrelationships between these parameters result in different contact conditions. Figure 2-18 presents a schematic overview of twelve typical contact modes, as a hard spherical slider moves over a coated flat surface [82].

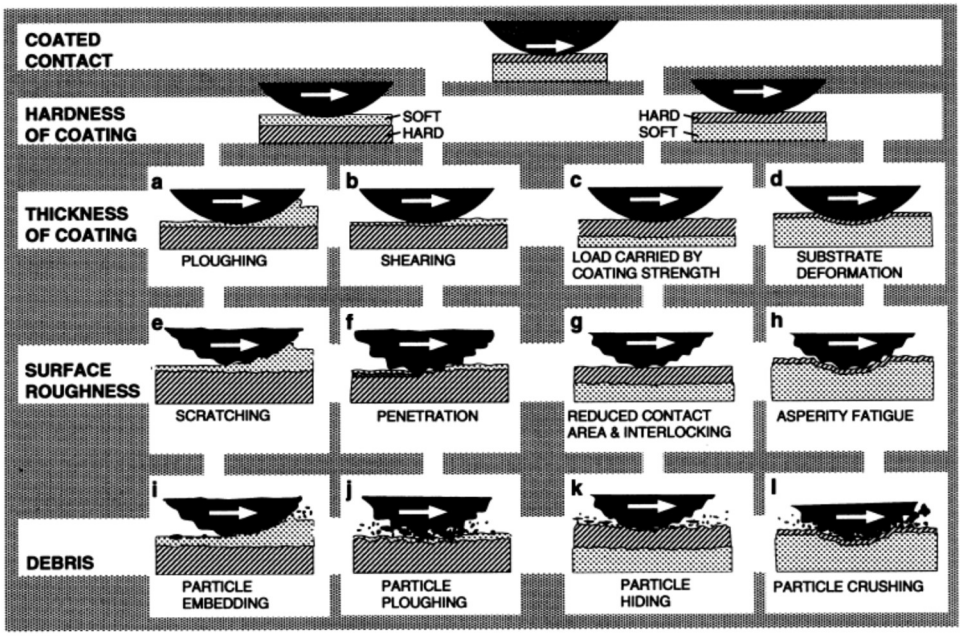

Figure 2-18 Macromechanical contact conditions as a hard spherical slider moves over a coated surface [82]

The relationship between coating and substrate hardness is considered a primary factor. A hard coating on a soft substrate can prevent ploughing and thereby reduce friction and wear. This can be decreased further by improving the load support, which can be achieved by increasing substrate hardness.

Further, a thin hard coating on a softer substrate can result in elastic or plastic deformation of the substrate and coating fracture (Figure 2-18d), whilst a thicker hard coating on soft substrate can assist a softer substrate in carrying the load, resulting in a reduction in contact area (Figure 2-18c). Further, a rough surface can reduce the

contact area for a hard coating, although the asperities may be subjected to abrasive or fatigue wear (Figures 2-18g,h).

For a soft coating on a hard substrate, coating thickness can influence the ploughing behaviour (Figures 2-18a,b), whilst surface roughness affects the degree of asperity penetration through the coating into the substrate (Figures 2-18e,f). Wear debris related mechanisms relate to entrapping, embedding, crushing and particle hiding, depending on the contact conditions involved (Figures 2-18:i-l) [6, 82].

2.5.3 Wear under practical conditions

The four wear mechanisms outlined above (Section 2.5.1) relate to the removal of material from the surface. However, these mechanisms can give rise to mild or severe wear regimes. For example, in 1956, Archard and Hirst [83] classified the unlubricated sliding wear of metal into two modes of mild and severe wear. In general, mild wear is characterised by a smooth surface with a strongly oxidised worn surface. The wear progresses in a steady state with low wear rate [84, 85]. In particular, the tribo-oxide layer formed on the steel surface, in air conditions, prevents metal to metal adhesion and hence acts to reduce the wear rate [86]. Conversely, the severe wear regime is characterised by a rough wear surface and an unsteady, high wear rate [87]. The role of the tribo-oxide layer has not been clarified for such severe wear conditions [86]. Accordingly, the mild wear regime constitutes the safer option for engineering applications.

2.5.4 Wear performance of TiC-based materials

2.5.4.1 TiC-based coatings

There is much interest in the use of TiC-based coatings for the tribological protection of components. During wear testing, different tribological processes can occur, depending on the coating/substrate properties (*i.e.* hardness, roughness, thickness and internal stress), combined with the wear test conditions (*i.e.* applied load, sliding speed, counterbody material and testing environment). For examples, Rasool and Stack [88] reported on the sliding wear performance of TiC composite based coatings on 303 stainless steel against a 3 mm diameter alumina ball. The TiC was mixed with binder and spread onto the substrate. After drying, the sample was melted via Tungsten inert gas (TIG). The wear test was performed using a pin-on-disc test geometry, under 2 and 10 N loads, and 500 m total sliding distance. The results showed that the wear rate of the TiC composite coating varied with sliding speed and the loading conditions, with high wear resistance of the TiC coating compared to the 303 stainless steel substrate (Figure 2-19). In addition, different wear mechanisms were reported, *i.e.* adhesive, adhesive-oxidative, oxidative-adhesive, oxidative-abrasive and abrasive-oxidative wear, for these coated and uncoated substrates, for different testing conditions.

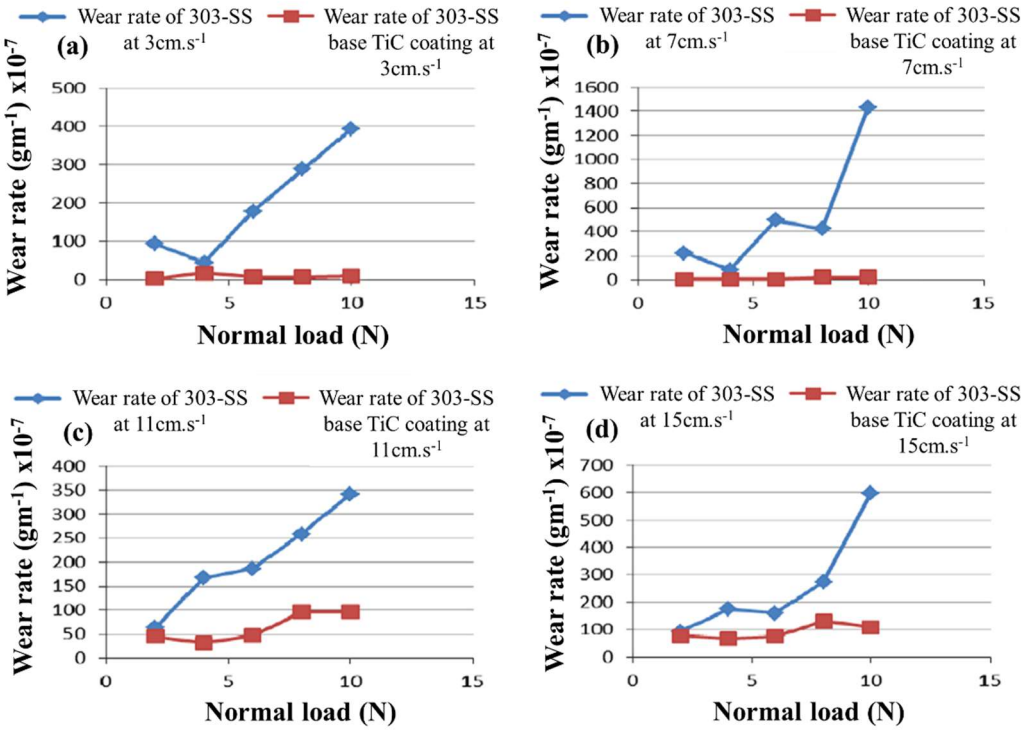

Figure 2-19 Wear rate of TiC coated and uncoated 303-SS for sliding speed conditions of: a) 3 cm.s^{-1}, b) 7 cm.s^{-1}, c) 11 cm.s^{-1} and d) 15 cm.s^{-1}, under various normal loads [88]

High wear performance of TiC coatings was reported also by Md Idriss *et al.* [89]. TiC coatings, processed using the TIG melt method, exhibited hardness values 2.6 times greater and wear rates 21 times lower than that of uncoated low alloy steel. The wear tests were performed using a ball-on disc test configuration, with an alumina ball, 10 N load, and 500 m total traveling distance. Further, Souček *et al*. [90] reported on the tribological behaviour of nano-composite TiC-coatings produced using magnetron sputtering, under conditions of low and high ion bombardment. Samples were tested against a 100Cr6 steel ball counterpart, at ambient temperature, and a silicon nitride ball at ambient and elevated temperatures of 300°C and 500°C. The results showed high levels of oxidation promoted gradual failure during elevated temperature testing, with significant delamination of the whole thickness of the coating being observed.

2.5.4.2 TiC-based cermets

The sliding wear behaviour of TiC-based cermets has also been investigated, having particular relevance to the applicability of ED processed coatings, with different wear mechanisms being reported. For example, Stewart and Plucknett [91] investigated the sliding wear of TiC and TiCN cermets against a WC-6 wt% Co ball, using a ball-on flat geometry, under 20 to 60 N loads. It was suggested that a two-body abrasive wear mechanism occurred during the initial stages, transitioning to a three-body abrasive mechanism following the formation of debris. A further transition to an adhesive wear mechanism was confirmed by the formation a thin tribo-layer with high oxygen content.

Further, Onuoha *et al.* [92] studied the influence of TiC grain size and binder content on the wear behaviour of TiC-stainless steel. Wear tests were performed using reciprocating geometry with a WC-Co ball. The results indicated that fine grained cermets exhibited a higher hardness and superior wear resistance as compared to coarse grained cermets, with specific wear rates in the range ~ 10^{-7} mm^3/Nm. The presence of binder extrusion and TiC grain fragments was indicative of a transition from two-body to three-body abrasive wear during the sliding wear process.

2.5.5 Sliding wear behaviour of EDC coatings

Similarly, the wear mechanisms of EDC coatings depend on many variables, including the physical properties of the coating/substrate material system, the ED processing parameters and the wear testing conditions applied (*i.e.* sliding speed, applied load, counterbody, temperature and environment). For example, Arun *et al.* [13] reported three wear mechanisms of ploughing, oxidation and delamination (Figure 2-20) operative at different temperatures (*i.e.* room temp up to 400˚C), during the wear

testing of Ni-W coatings on AISI-D2 die steel substrates (in pin form, with 10 mm diameter and 31 mm length), formed using an ED process with 50 wt% Ni and 50 wt% W powder suspended in the dielectric fluid. Pin-on-disk wear tests were carried out against AISI-D2 steel disc of diameter 60 mm, and sliding speeds of 2 m/s for a 1000 m total sliding distance under 80 N load. In addition, the alloy showed lower specific wear rates and a higher coefficient of friction at room temperature. The wear rate increased in combination with a lower coefficient of friction at high temperature.

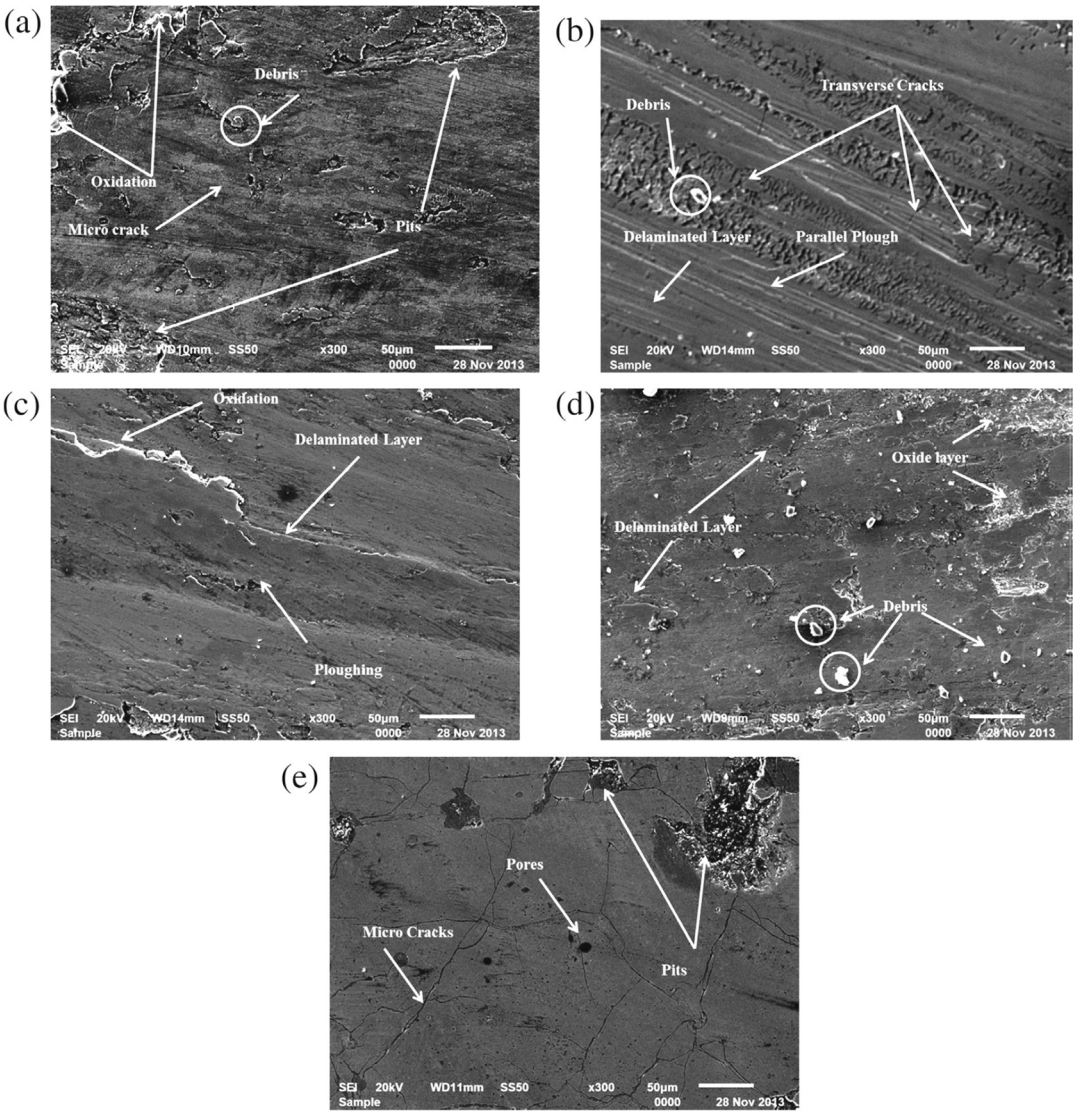

Figure 2-20 Wear behaviour of Ni-W EDC coatings on die steel substrates, as a function of temperature: a) RT; b) 100˚C; c) 200˚C; d) 300˚C and e) 400˚C (total sliding distance 1000 m, 2 m/s sliding speed, 80 N load) [13]

Tijo and Masanta [93] investigated the effect of current and duty factor on the formation and tribological behaviour of TiC-TiB_2 coatings on Ti-6Al-4V alloy, produced using a Ti and B_4C powder mixed dielectric EDC process. Ball on disc sliding tests were carried out using 10 mm WC-Co ball under 20 N normal load. The coatings exhibited up to seven times improvement in wear resistance as compared with the uncoated substrate. Further, Zeng *et al.* [94] reported improved wear performance for an ED processed TiC-N coating, as compared with a TiN PVD coating, for applied loads exceeding 30 N. The crater edges played a role as rolling balls, leading to a lower coefficient of friction during the initial stages of testing of these EDC surfaces. As the wear progressed, the actual contact area increased, resulting in a gradual increase of the coefficient of friction to a stable value.

2.5.6 Wear behaviour of TiC-based ED coatings

TiC is a hard ceramic material that can be applied as a coating material to modify the mechanical properties of a component surface, in particular for wear applications, due to its high hardness, high wear resistance, low coefficient of friction, and good chemical and thermal stability [95, 96]. There have been various reports on the formation and performance of ED TiC-based cermet coatings, however the wear behaviour of such coatings is not well understood. For example, Hwang *et al.* [43] investigated coating development using a multi-layered Ti and graphite electrode, on a Ni substrate, showing that the presence of graphite enhanced TiC layer formation, with the coating exhibiting good abrasive resistance up to ~ 400°C, but degrading under high load conditions. Xie *et al.* [45] reported on the wear behaviour of ED coatings formed from a sacrificial Ti electrode reacting with the dielectric oil, with and without addition of graphite powder, wear tests carried out using a ball-on-disk configuration,

with 6 mm diameter Si_3N_4 ball under two loading conditions of 20 N and 50 N for 15 minutes returned wear rates of 5.8 x 10^{-6} to 8 x 10^{-6} mm^3/Nm and 24.6 x 10^{-6} to 150 x 10^{-6} mm^3/Nm for coatings produced using semi-sintered Ti tool electrode, with and without graphite mixed dielectric fluid, at 20 N and 50 N loads, respectively. A reduction in both coefficient of friction and wear rate for coatings made in the presence of graphite was also reported, being attributed to increased TiC formation and the introduction of amorphous carbon into the coatings. This amorphous carbon acts as a continuous lubricant supply at the contact, helping to accommodate sliding motion and reduce mechanical wear and oxidation. It was suggested the abrasive, adhesive and oxidation were the main wear mechanisms of the coatings created with graphite mixed within the dielectric fluid, whilst only mild abrasive wear was associated with the coatings formed without graphite mixed within the dielectric. Further, Tijo *et al.* [97] investigated the wear behaviour of TiC composite coatings on AISI 1020 mild steel produced using a PM TiC-Cu tool electrode. Ball-on-disc sliding wear tests were conducted against 8 mm diameter WC-Co counterbody, at 20 N normal load and 126 mm/s sliding speed for 30 minutes. It was found that the wear rate varied with the ED processing conditions of current and pulse-on time, in the range of 2.6 x 10^{-5} - 4.33 x 10^{-5} g/minute, being two to four times lower than that of the substrate only. Such improvement was attributed to the high oxidation resistance of the TiC-composite coating and the different wear mechanisms compared to the substrate. In addition, the TiC-composite coating exhibited some evidence for brittle fracture, indicative of the initiation and propagation of cracks during the test.

2.6 Laser re-melting process

Various coating materials and deposition methods have been investigated, to help improve surface properties. However, problems resulting in the development of coating defects, such as cracks, porosity *etc.* can deleteriously affect component performance. One suggested approach to address this issue is to laser re-melt the coatings. For example, Sova *et al.* [98] reported a reduction in the porosity of ~ 1 - 3 mm thick cold-spray stainless steel coatings, from ~ 8% to ~ 1%, using laser re-melting. The laser treatment was done using Nd: YAG (neodymium-doped yttrium aluminum garnet) at 500 W power, 100 mm/s scanning speed and 1.4 mm spot size diameter, which produced ~ 200 μm of melting depth, without a significant heat effect on the Al substrate. Further, Afzal *et al.* [99] reported the production of plasma sprayed WC:12%Co coatings, free of gross defects after laser melting, but with variable thickness and wear resistance as a function of the laser input energy. It was reported that hardness can be controlled by optimising the laser scan speed, with the laser melting process enhancing the wear performance significantly at a scan speed of 100 mm/minute, but with a decrease in performance at an increased speed to 250 mm/minute. Laser surface melting has also been shown to improve the microstructure and increase the coating adhesion of high velocity oxy fuel (HVOF)-sprayed stellite on martensitic stainless steel [100].

2.7 Summary of literature review and the research gap

2.7.1 Development of ED processes for surface modification

The electrical discharge coating (EDC) method, being an adaptation of electrical discharge machining (EDM), may be used to produce hard cermet coatings, using a sacrificial semi-sintered tool electrode.

The general consensus on the process of material deposition is through the development of localised melt pools on the workpiece surface, resulting from a series of sparking events, combined with the direct transfer of tool electrode material or powder suspension within the dielectric fluid, either in free form and/or after reacting with the carbon following hydrocarbon decomposition. The current and pulse-on time are considered critical process parameters, affecting the deposition of material from either the PM electrode or the powder mixed dielectric fluid.

From the literature reviewed, it is evident that there have been many successful attempts to deposit hard layer coatings on substrate surfaces using ED processes. However, the precise mechanisms of material transfer between the electrodes during ED processing is not well understood, nor is there a clear view of the details of coating development, and the dispersion of phases within the coating needs clarification. Further, the effects of the processing parameters, such as current and pulse-on time, on the mechanical properties such as hardness, and their correlation with the developed microstructure, needs clarification, through a process mapping approach for each materials system.

In particular, very little work has been reported to date on the use of semi-sintered TiC tool electrodes (for direct deposition), as distinct from using green compact Ti electrodes, or adding Ti powder to the dielectric fluid. In all cases, there is a variation

in the resultant microhardness, being attributable to effects of tool electrode/workpiece material system, the material distribution within the coating, and the processing conditions applied.

2.7.2 Process modelling in support of ED processing

Researchers have demonstrated effective simulation methods for determining temperature distributions and the developed crater geometries, and for estimating the amount of material removed during EDM, based on the consideration of single spark events. However, there has been a lack of modelling effort to understand the fundamental interactions between energy source and material during EDC processing.

From previous contributions to literature, it is clear that the proportion of energy transferred into the workpiece during EDM is a critically important factor in defining the model fidelity. Some researchers assumed a constant amount of energy, $F_v = 50\%$, transferred to the anode and cathode under different machining conditions [59-62], whilst others assumed only 18 % and 8% of total energy contributed to the melting of the cathode and anode, respectively [63]. Indeed, the assumption of a constant amount of energy transferred to the workpiece is recognised as the main reason for the variability between modelling and experimental data. A few attempts have been made to estimate the energy distribution between anode, cathode and dielectric fluid during EDM, but there is a lack of general method to determine F_v during EDC processing.

Precise measurement of the plasma channel radius is very difficult, due to the small distance between the two electrodes where the plasma occurs, and the very short pulse-on time. High speed cameras used to determine and analyse the plasma channel showed that the plasma expansion was completed within two microseconds after dielectric breakdown, whilst recognising that the light emitting region photographed

might not be the arc plasma region itself, with the camera settings such as frame rate, exposure time and diaphragm aperture affecting the images. Hence, many researchers have assumed the crater diameter to be equal to the plasma channel.

2.7.3 Tribological performance

Wear can be defined as the progression of material loss from one or both surfaces in contact, moving relative to each other, being broadly classified according to the wear mechanisms of adhesive wear, fatigue wear, abrasive wear and chemical wear, or combination thereof.

Some wear studies have focused on the performance of ED coatings in terms of coefficient of friction (CoF), and material abrasive, adhesive and oxidation removal mechanisms. In particular, ED TiC-based coatings have been prepared using a multi-layered Ti and graphite electrode, and a semi-sintered Ti electrode with or without graphite mixed within the dielectric, or by using Ti powder with an ordinary Cu electrode. However, there has been no systematic, tribological investigation of such ED coatings, and the impact of ceramic additions to wear performance of ED processed surfaces needs to be appraised and correlated with the developed coating microstructures.

2.7.4 Laser surface melting (LSM)

The laser surface melting (LSM) process is an engineering technique involving the melting of a pre-deposited layer. It has been shown to be an effective technique to improve surface quality and densify the coating layer. This process has been used successfully to improve various kinds of coating, such as cold-sprayed stainless steel, plasma sprayed WC:12% Co and HVOF-sprayed stellite.

EDC coatings are characterised generally by cracks, porosity and surface roughness, whilst LSM is one suggested approach to address this issue, through the reduction of surface defects and improvement of surface roughness. In particular, it is considered that the wear behaviour of ED processed coatings is likely to be affected strongly by the integrity of the surface.

In summary, this chapter has discussed the main literature related to the theme of this research project, include the fundamental processes of EDM/EDC and the basis of materials deposition and the impact on microstructural developments on coating properties, in particular hardness and wear. The chapter also identified significant research gaps and hence the aims of the following research work are defined. The next chapter will present an overview of the materials, methodologic approach and experimentation performed, including descriptions of the equipment utilised.

3 Materials and Methodology

3.1 Introduction

This chapter describes the experiments performed and provides details of the materials selected for processing, the EDM/EDC and laser surface melting equipment used, and the materials characterisation and testing techniques applied. The principles and practical aspects of the process machinery and instrumentation are explained along with their capabilities and limitations for the interpretation of results. Sections 3.2 and 3.3 describe the tool electrode and the workpiece materials. Section 3.4 describes the equipment used to create and post-process the coatings. Sections 3.5, and 3.6 outline the techniques used to analyse the coatings and substrates. Section 3.7 presents the thermal conductivity of the dielectric oil measurement. Section 3.8 describes the gap-voltage monitoring process, and Section 3.9 addresses the method of wear testing.

3.2 Tool electrode materials

3.2.1 Solid copper (Cu)

Typical tool electrode materials for EDM are graphite, copper, tungsten and copper-tungsten alloy. These material are chosen for their sufficient electrical conductivity in order to generate a spark [101], and their high thermal conductivities, since higher heat conduction results in a lower temperature at the electrode and hence reduced tool wear rate [16]. In this work, a reference Cu tool electrode with dimension 100×16×14 $(mm)^3$ was utilised, due to its low wear and ability to provide a good surface finish [4].

3.2.2 Semi-sintered titanium carbide (TiC)

Titanium carbide (TiC) is a hard, refractory ceramic material [102], widely used as a reinforcing phase in Cr-, Co-, Ni-, Mo- or Fe-based metallic alloys, to produce ceramic-metal (cermet) composites for a variety of applications [96, 103]. TiC coatings are commonly applied as a protective material to improve surface integrity and thereby extend part service life [104], owing to their excellent physical and chemical properties such as a high hardness, high wear resistance, low coefficient of friction, and high chemical and thermal stability [95]. TiC adopts a type B1-NaCl (fcc) crystal structure and exhibits a wide range of compositions depending on the percentage of carbon dissolved in the Ti phase [105]. Coating deposition technique and processing conditions have a significant effect on the properties of TiC coatings [106].

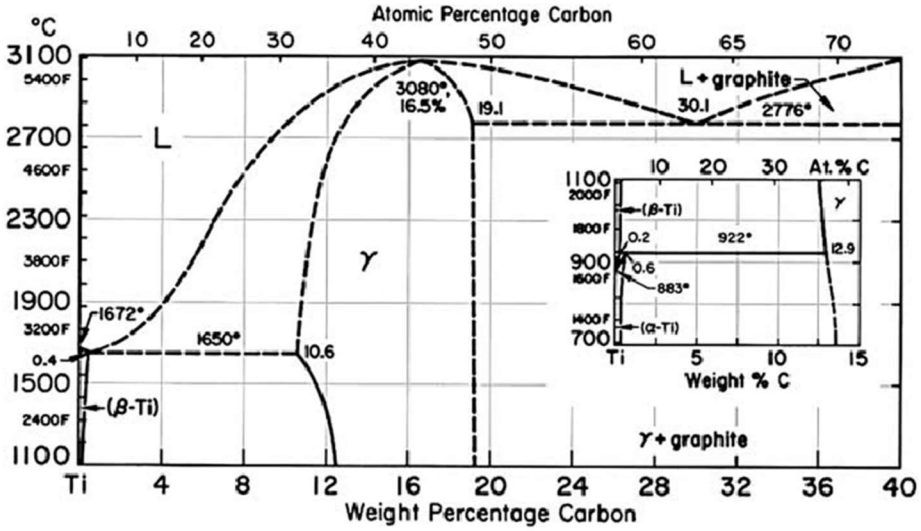

Figure 3-1 Titanium-Carbon binary phase diagram [105]

Figure 3-1 illustrates the binary phase diagram of Ti and C, the phase diagram consists of three solid terminals: α-Ti hexagonal close packed (hcp), ß-Ti body centred cubic

(bcc), and refractory monocarbide ɣ-TiC face centred cubic (fcc). Other phases present are liquid (L) and liquid plus graphite (L+ graphite) [105].

In this work, sacrificial semi-sintered TiC tool electrodes (Ryoden Koki Engineering Co., Ltd.) were prepared, with dimension 100×20×10 $(mm)^3$ and oriented with the 20x10 $(mm)^2$ surface facing the substrate, and used to produce coatings on each workpiece.

3.3 Workpiece materials

3.3.1 Austenitic stainless steel

Austenitic stainless steel is a non-magnetic metallic alloy, possessing excellent ductility, formability and high toughness, even at very low temperatures [107, 108]. It adopts an fcc structure which cannot be hardened by heat treatment. The addition of Ni strongly influences the design of stainless steel alloys, acting to stabilise the fcc phase of Fe and thereby expand the austenite phase field.

The equilibrium phase diagram of iron-nickel (Fe-Ni) Figure 3-2 shows that with sufficient Ni addition, austenite becomes stabilised at room temperature. Further, the addition of Cr in sufficient quantities leads to a reduction in the amount of Ni required to stabilise austenite. For example, Fe-alloys incorporating ~ 18 wt% Cr and ~ 8 wt% Ni are fully austenitic from room temperature to the melting point [107].

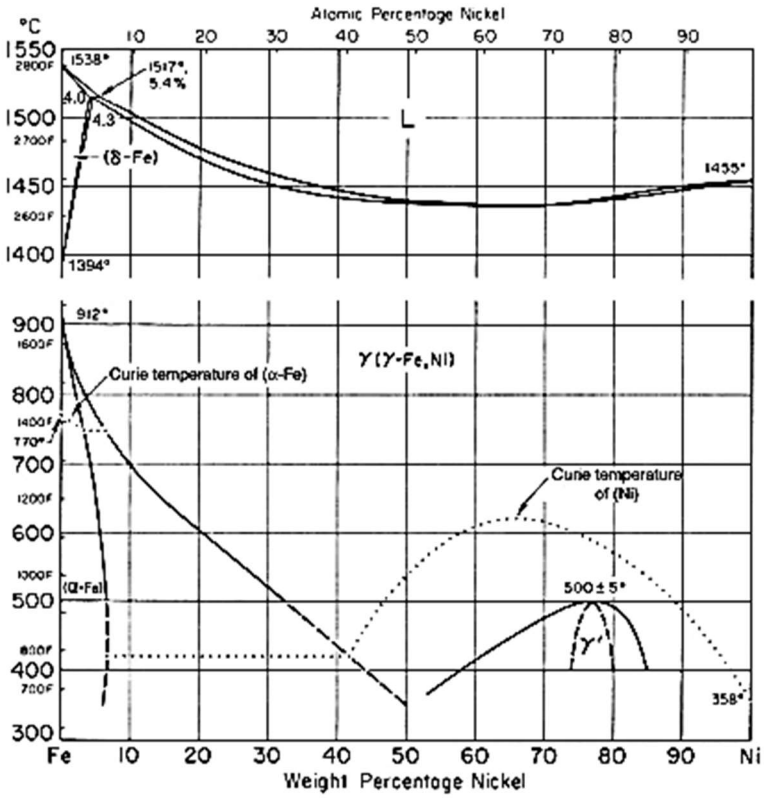

Figure 3-2 Equilibrium Fe-Ni phase diagram [107]

Austenitic alloys can be significantly hardened by cold working. The degree of work hardening depends on the alloy content, with the work hardening rate decreasing with increasing alloy content. Austenitic stainless steels with low alloy content, *e.g.* S20100, S20161, S30100 and S30400, transform generally to the martensitic structure and become magnetic when sufficiently cold worked or heavily deformed during forming or machining operation [108]. In the present work, 304 stainless steel, as commonly used across a range of engineering applications, was selected as an appropriate template for the appraisal of EDC processing phenomena.

3.3.2 High speed steel (HSS)

High speed steel (HSS) is one alloy group that is used widely in cutting tools [109]. In particular, it has gained attention in chip-less, shaping applications such as blanking, extrusion, moulding and punching [110] and in the field of hot-rolling manufacturing

[111]; owing to its excellent hardness which can be maintained at elevated temperature, combined with good wear resistance, good workability and high toughness [112]. Surface modification, such as coating, alloying or heat treatment, can enhance further the near surface properties of tool steel [113].

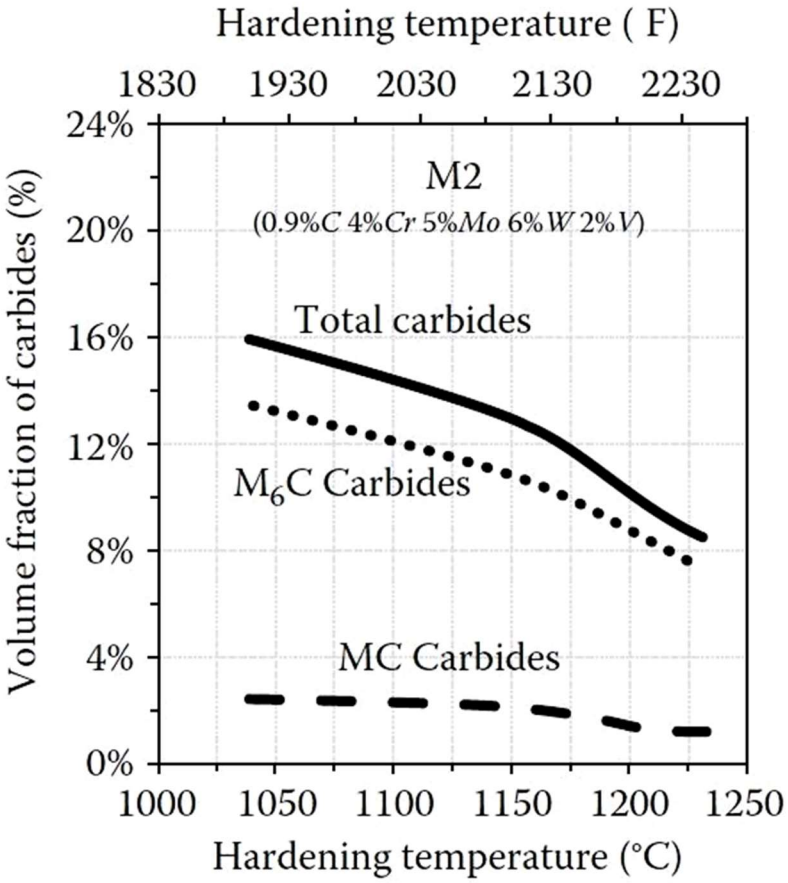

Figure 3-3 Volume fraction of undissolved carbides in M2 HSS [114]

The American Iron and Steel Institute (AISI) classifies HSS into two groups, according to its alloying elements, *i.e.* the tungsten T-group and molybdenum M-group. Generally, steels exhibit a wide range of properties depending on morphology, *i.e.* the phases and micro-constituents present, which in turn depend on the heat treatments applied. HSS generally contains M_6C (W- or Mo- rich carbide) and MC undissolved carbides (V-rich carbide, but not Cr-rich M_7C_3 carbides, because of the high amounts of W, Mo and V present). For example, Figure 3-3 indicates the volume

fraction of undissolved carbides in M2 HSS [114]. In this work, general purpose M2 HSS was used due to its wide range of industrial applications.

3.4 Surface modification equipment

3.4.1 The electrical discharge machine (for EDM & EDC)

The working principle of EDM is based on creating sparks between a workpiece and tool electrode separated by a specific small gap and immersed in dielectric fluid [115]. EDM consists of four main components, *i.e.* machine tool, power supply, servo control and dielectric unit. The machine tool positions the tool electrode; the power supply provides individual sparks to the sparking gap to promote material removal; the servo control identifies the gap conditions and accordingly retracts or maintains the position of the tool electrode with reference to the workpiece; and the peck cycle facility (selectable interval (one jump per second) and retraction distance (0.8 mm) of the tool electrode) acts to increase the effect of flushing. The dielectric unit is responsible for providing the dielectric fluid to the machine tank, for submersing the electrodes, in addition to cooling and removing EDM debris from the sparking gap [15].

A die sinking ED machine (Mitsubishi EA12V) (Figure 3-4) was used to process samples. A semi-sintered TiC tool electrode (Ryoden Koki Engineering Co., Ltd.), of dimension 100×20×10 $(mm)^3$, and an ordinary Cu electrode, of dimension 100x16x14 $(mm)^3$, were utilised to perform TiC-based ED coating (EDC) and ED machining (EDM) of workpiece surfaces, respectively. Shell Paraol 250 oil was used as the dielectric fluid.

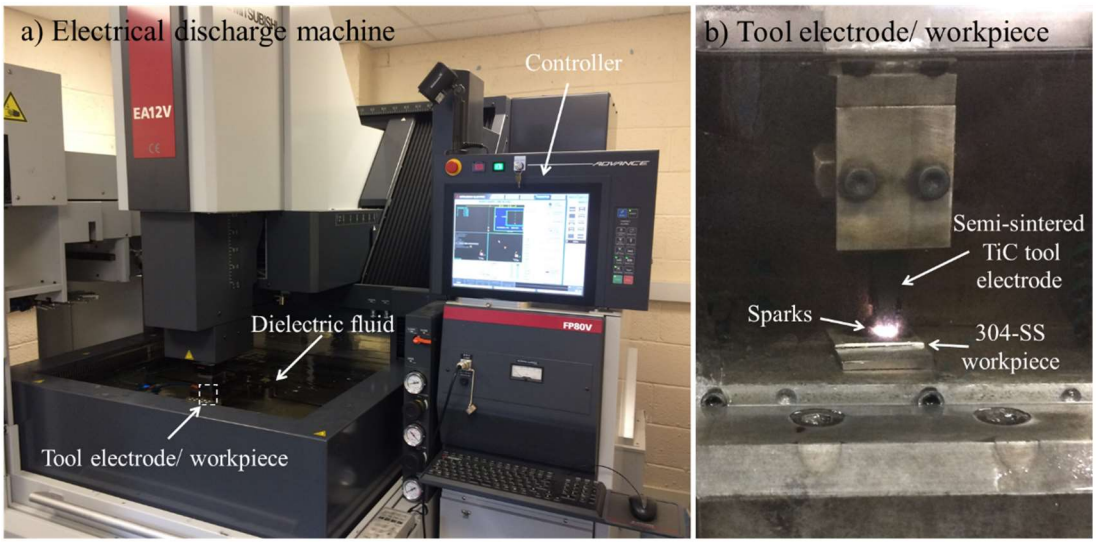

Figure 3-4 a) Experimental set-up of ED machine used to perform EDC; and b) tool electrode & workpiece arrangement

ED coatings were investigated systematically, as a function of current (A) and pulse-on time (µs), since these parameters are known to affect strongly the characteristics of processed surfaces [116]. The process parameters of electrode polarity, voltage, pulse-off time and total machining time were fixed, as summarised in Table 3-1. All samples were EDC processed for 60 minutes. For the purpose of determining spark diameters, the sample set was replicated, for ~ 30 seconds of machining time, using identical processing parameters. A long pulse-off time (256 µs) was chosen to ensure effective flushing of debris particles, in order to prevent the localization and concentration of discharge events.

Table 3-1 EDC processing parameters

Working parameters	Current / A (fixed pulse-on time of 8 µs)	Pulse-on / µs (fixed current of 10 A)	Pulse-off / µs	Open voltage / V	Tool electrode polarity	PM electrode	Machining time / minutes
Description	2,6,10,14,19	2,4,8,16,32,64	256	320	negative	TiC	~ 0.5 & 60

Processing was performed over a relatively large area of 2 cm^2, with significant impact on the required coating time. Accordingly, 60 minutes was used, to ensure uniform, complete coatings were produced.

For the wear test samples, all ED processing parameters, including electrode polarity, current, voltage, pulse-on/off time and total processing time were fixed, as summarised in Table 3-2.

Table 3-2 EDC processing parameters for the wear test samples

Working parameters	Current / A	Pulse-on / µs	Pulse-off / µs	Voltage / V	Tool electrode polarity	Machining time / minutes
Description	10	8	256	320	negative	~ 60

After clamping the workpiece on the machining table, the tip of the tool electrode was set to touch the top surface, as a reference point, and then retracted. The working oil filled the tank up to a specific level, ensuring that the electrodes were fully immersed in dielectric fluid. The electrode was then advanced towards the workpiece under servo-control, allowing the gap-voltage to rise until it became sufficient to ionise the dielectric oil, with short duration discharges in the electrode gap leading to localised material coating and alloying of the workpiece. The tool electrode surface was polished with P1200 grade paper after each coating, for consistency. Electrode and machined debris were removed by circulation of the dielectric fluid between the electrodes during processing.

3.4.2 Laser surface melting (LSM)

Laser surface melting (LSM) was performed using a 2 kW Ytterbium fibre laser (IPG Laser Company) (Figure 3-5) under continuous-wave (CW) mode operation (1.06 µm wavelength). A 600 µm diameter delivery fibre (d_{fiber}) was used, with 125 mm

collimation lenses (F_{coll}). The focal length (F_l) (distance between lens and workpiece surface) was set to 192 mm, giving a focused spot size diameter (d_f) on the workpiece surface of ~ 1 mm, according to the following equation [117]:

$$\mathbf{d_f = d_{fiber}\ \frac{F_l}{F_{coll}}} \qquad (3\text{-}1)$$

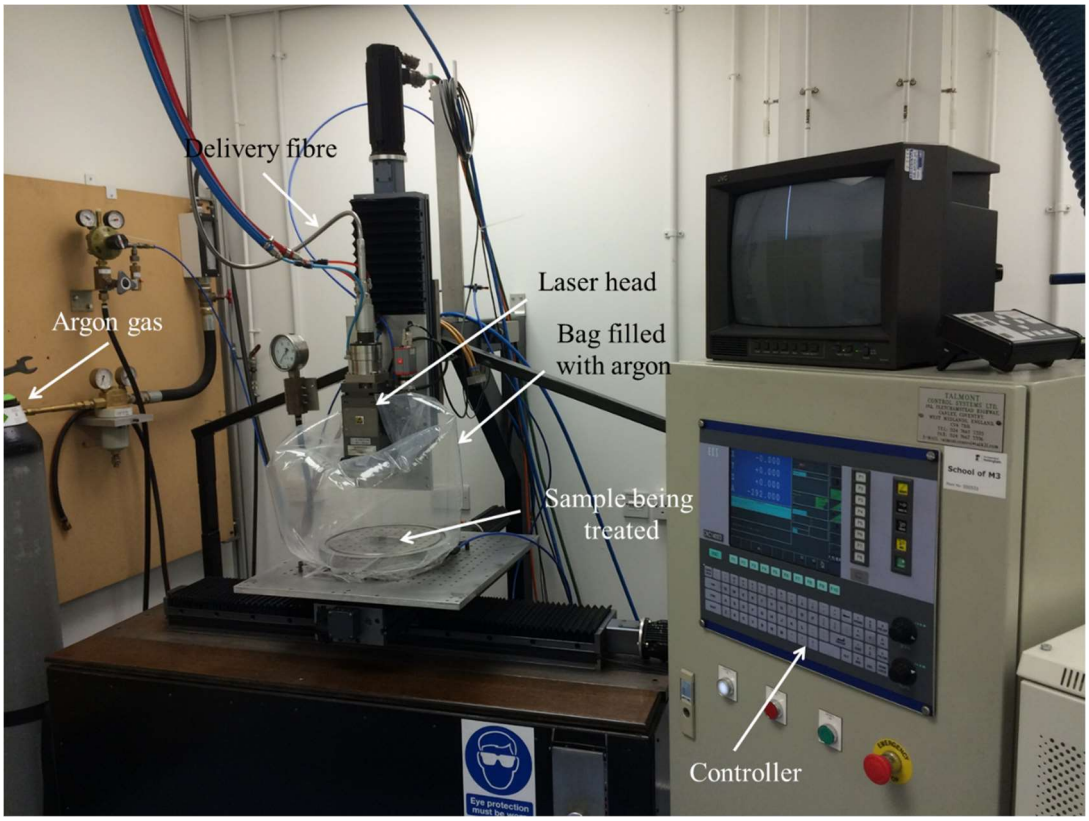

Figure 3-5 Experimental set-up for the laser surface melting of ED coatings

Process energy selection was based on preliminary experimentation, to determine the range of powers over which material melting took place. Consequently, powers of 240 and 280 W, corresponding to laser fluences of 9 and 10.5 J/mm^2, respectively, were chosen. Laser fluence, L_f (J/mm^2), is defined by the following equation [118]:

$$\mathbf{L_f = \frac{P}{v\,d}} \qquad (3\text{-}2)$$

Where P is laser power (W), $\boldsymbol{v}$ is laser scan speed (mm/s) and d is the laser beam diameter (mm). LSM was performed within a plastic chamber, under argon (Ar) inert

gas at a pressure of ~ 1 bar. The scan speed was fixed at 1600 mm/minute and scan performed line by line with 60% overlap to ensure the entirety of the surface was melted. After laser processing, samples were allowed to cool down slowly to ambient temperature.

3.5 Sample preparation

3.5.1 Substrate preparation for coating

Bulk samples were sectioned using an ATA Brillant 220 cutting machine. Sample sizes for characterisation and wear testing, respectively, are summarised in Table 3-3.

Table 3-3 Substrate sizes

Workpiece material	Size / mm (Length, Width and Height)	Purpose
304-SS	20 x 20 x 4	Characterisation
304-SS	100 x 20 x 4	Wear testing
HSS	20 x 10 x 10	Characterisation
HSS	100x 10 x 10	Wear testing

The workpiece materials were mechanically ground with SiC paper (sequential grade reduction: P240, P400, P800 and P1200), under flowing water, then polished with cloths coated with 6 and 1 μm diamond paste, with washing in water and acetone after each stage to remove debris and contamination, and then dried before coating.

3.5.2 Cross-sectional sample preparation for SEM, optical microscopy and microhardness testing

ED processed samples were cross-sectioned and mounted within conductive Bakelite. Samples were mechanically polished by sequential grinding on SiC paper (P240, P400, P800 and P1200 grades), under flowing water to keep the samples cool, then on polishing cloths coated with 6 and 1 μm diamond paste. Samples was washed with

water and acetone after each stage. Acetone was used as a final washing stage, before drying and etching with Glyceregia solution (15 ml hydrochloric acid HCl / 10 ml glycerol / 5 ml nitric acid HNO_3) for about ~ 45 - 60 second, to reveal the coating or surface modified layer. Krolls reagent (2 ml hydrofluoric acid HF / 3 ml nitric acid HNO_3 / 500 ml distilled water H_2O) was used also to delineate TiC distributions within the coatings.

3.6 Sample characterisation

3.6.1 Surface roughness

A Talysurf series CLI 1000 (Taylor Hobson) surface profilometer with inductive type contact stylus (Figure 3-6) was used to yield surface profiles and roughness Ra values. The principle of this test is to convert the vertical movement of a stylus as it travels across the peaks and valleys of a surface into an electrical signal, via an inductive gauge which, in turn, is converted into a 2D surface profile, depending on the dimensionality of table movement [119]. Subsequent to generating line and surface profiles, 'TalyMap Universal' software was used to analyse the scanned profiles.

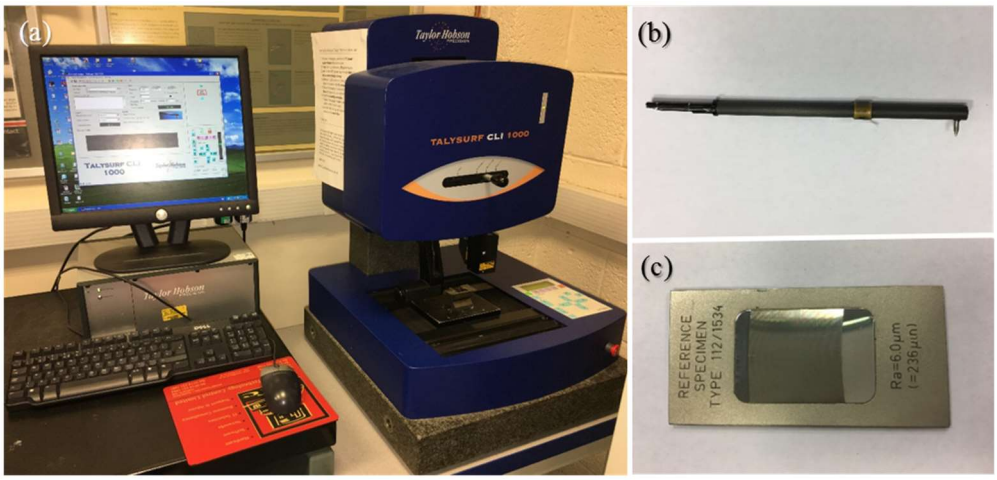

Figure 3-6 a) Surface profilometer (Talysurf CLI 1000); b) inductive contact stylus (75.6 mm length); c) reference specimen for calibration (59.6 mm x 29.6 mm)

In this work, a stylus with tip radius of 2.2 µm and 41.8˚ cone angle was used to measure surface roughness (Figure 3-6b). Five measurements of 2 mm length for each sample was evaluated at a scan speed of 100 µm/s, with lateral resolution of 0.5 µm. Calibration was carried out prior to each session using a Precision reference specimen with Ra value of 6 µm (Figure 3-6c).

3.6.2 Microhardness

Coating hardness is considered a critical factor for appraising the performance of a coated product. In this work, microhardness testing of both substrates and processed samples was performed using a Buehler model 1600 - 6400 tester with Vickers diamond indenter with pyramidal shape, square base and an angle of 136° between opposite faces. Vicker hardness is obtained by dividing load (N) in kgf by the square area (mm^2) of indentation (Equation 3-3):

$$\text{Vickers hardness } (\mathbf{HV}) = \frac{\mathbf{2\,N \sin\frac{136^{\circ}}{2}}}{\mathbf{d^2}} \qquad (3\text{-}3)$$

Where N (kgf) is the applied load and d (mm) is the mean diagonal length of the indentation. In order to enhance the accuracy of measurement, samples were mounted, polished and etched before testing; an indentation load of 10 gf with 15 s dwell time was used. Averages of eight indentations, with minimum distance between two adjacent indents of > 2.5 times the length of the indent diagonal, are reported along with standard deviation data.

3.6.3 Optical microscopy

Optical microscopy (Nikon Eclipse LV100ND equipped with a Nikon Digital Sight DS-Ri1 camera) was used for initial imaging of the developed coatings, to estimate

coating layer thickness. Open-source image processing software ImageJ was used for the measurement of layer thickness from the images.

3.6.4 Scanning electron microscopy (SEM) and energy dispersive X-ray spectroscopy (EDS)

Scanning electron microscopy (SEM) is a powerful technique used routinely for the characterisation of materials. Briefly, a focused beam of high energy electrons (~ 1 - 40 kV) bombards a sample, with signals produced as a result of a variety of interactions of the beam with atoms in the sample (Figure 3-7).

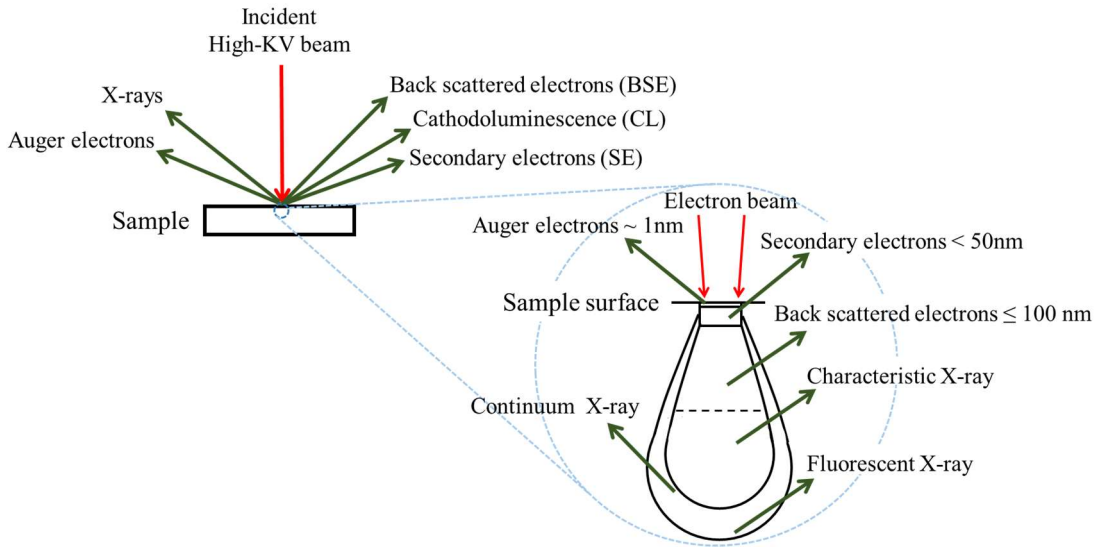

Figure 3-7 (a) Signals produced following interaction of a highly energetic electron beam with a sample; and (b) depiction of the electron beam / material interaction volume

Secondary electrons (SEs) provide for topographic imaging, whilst backscattered electrons (BSEs) provide images with compositional dependence. SEs are low energy (< 50 eV) electrons that have been ejected, following primary electron beam / material interactions. SEs are easily absorbed and only escape from the sample near surface, hence providing for a high resolution images of sample surface topography. BSEs are primary electrons that have undergone recoil interactions with atomic nuclei, and

enable different chemical compositions within a material to be distinguished. The higher the atomic number, the stronger (or the higher the probably) of interaction, hence the brighter the signal, hence images with locally averaged compositional dependence may be obtained.

In addition, SEMs are often equipped with energy-dispersive X-ray spectroscopy (EDS), which uses characteristic X-ray signals to perform compositional analysis of the sample near surface. When a highly energetic electron strikes an atom, a core shell electron may be excited and ejected from the atom, a process of ionisation. Subsequently, an electron from a higher energy shell jumps into the core level vacancy, with the emission of energy in the form of a characteristic X-ray (Figure 3-8). The X-ray energy (keV) has atomic number dependence.

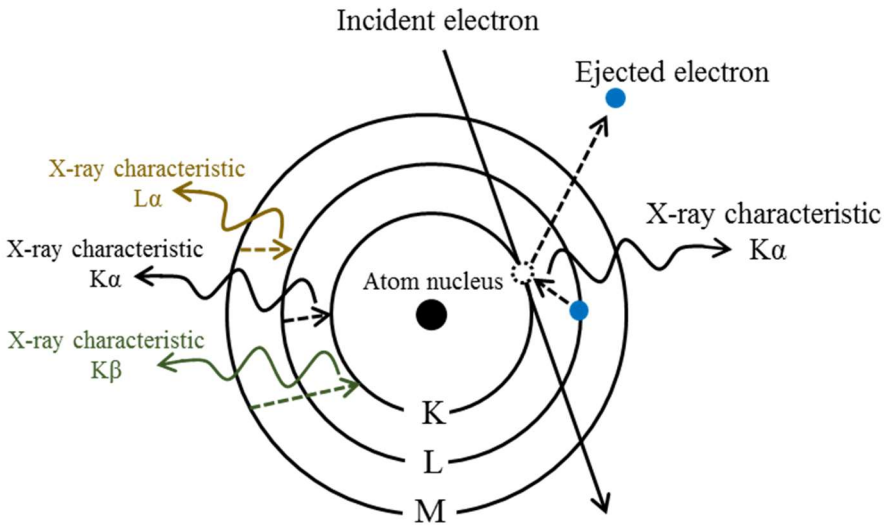

Figure 3-8 Production of a characteristic X-ray, as used for EDS

In this work, topography and composition of samples were investigated using an FEI XL30 SEM (W-electron gun; 20 kV; spot size 4) and a JEOL 7100F FEG-SEM (15 kV; spot size 8), both with 10 mm working distance, with images acquired using SE and BSE modes. EDS analysis was performed using an FEI XL30 SEM with

Oxford instruments X-max detector and associated INCA software (processing time 5; number of channels 10; and eV per channel 10).

3.6.5 Structure determination

3.6.5.1 X-ray diffractometry (XRD)

X-ray diffractometry (XRD) is a non-destructive characterisation technique used for identifying crystalline phases within materials. X-rays are a form of electromagnetic radiation with high energies and very short wavelengths on the order of atomic spacings within solid materials [120].

X-rays incident on a sample are scattered by outer shell electrons of the sample atoms. Constructive interference of the scattered X-rays is collected and used for structure determination. Figure 3-9 illustrates the diffraction process, with the angles of reconstructed wavefronts being related to crystalline spacings, via Bragg's law (θ/2θ diffraction geometry, Figure 3-9):

$$\mathbf{n\,\lambda = 2\,d_{hkl}\sin\theta} \qquad (3\text{-}4)$$

Where n is the order of diffraction, $\boldsymbol{\lambda}$ is wavelength of the source X-rays, d_{hkl} is the spacing between lattice planes and θ is the scattering angle.

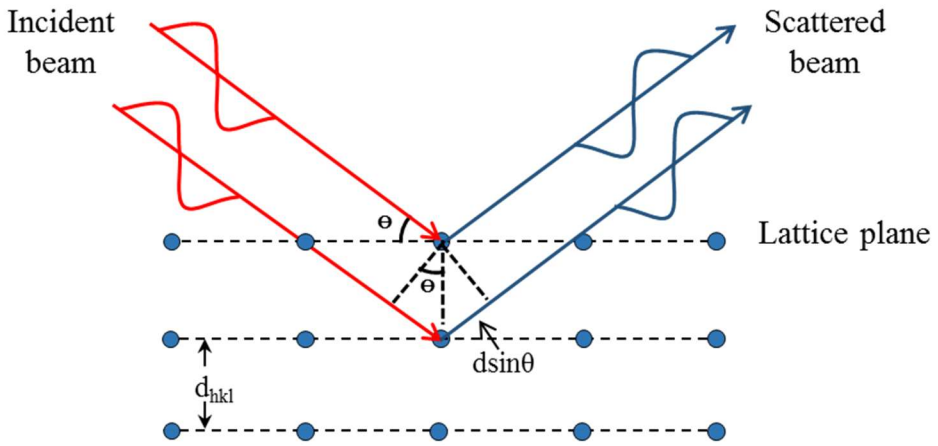

Figure 3-9 Illustration of the geometric conditions for X-ray diffraction (Bragg's law)

XRD data provide information on sample structure (and hence allows composition to be inferred) and grain orientation (texture) by comparison of the location and intensity of diffracted peaks with database values. In addition, the amount of a particular phase may can be identified by relative peak intensities, whilst peak widths reflect particle/grain sizes and the incorporation of defects.

In this work, the structures of starting materials and processed samples were investigated using a Siemens D500 X-ray diffractometer. The X-ray generator was operated at 40 kV and 25 mA, generating monochromatic Cu Kα radiation at a wavelength of $\lambda = 0.15406$ nm. Diffraction data were collected over a range of 2θ from 20° to 100°, with step size of 0.02° and 2 s dwell time per step, with EVA software being used for data analyses. Absorb DXV 1.14 software was used to calculate the X-ray penetration depth in TiC which showed that the penetration depth varied with 2θ (20, 40, 60, 80 and 100) to about 2.47, 4.86, 7.11, 9.14 and 10.9 μm, respectively.

3.6.5.2 Grain size determination

The Scherrer equation was used to determine the grain size of the TiC phase within the developed coatings, with peak width being inversely proportional to crystallite size (D). Assuming that peak broadening is a result of changes in grain size, and ignoring inhomogeneous strain:

$$\mathbf{D} = \frac{\mathbf{K}\,\boldsymbol{\lambda}}{\mathbf{B}\cos\boldsymbol{\theta}} \qquad (3\text{-}5)$$

Where, D is grain size (nm), B is full width at half maximum (FWHM) of the XRD peak, $\boldsymbol{\lambda}$ is X-ray wavelength ($\boldsymbol{\lambda}$ = 0.154060 nm), θ is the Bragg angle (rad) and K is the Scherrer constant which depends on several factors, such as how width is determined, crystal shape and size distribution, etc. In practice, K = 0.94 is commonly used (or K = 0.89 for integral breadth of spherical crystals). In this study, grain size was measured over a range of 2θ, typically from 30˚ to 40˚, with step size of 0.01˚ and 8 s dwell time per step. Diffraction peaks are background subtracted before taking Full width at half maximum (FWHM) measurements.

3.6.6 Transition electron microscopy (TEM)

Transmission electron microscopy (TEM) was used to examine materials at very high spatial resolution. A high energy electron beam (80 - 200 kV) passes through a very thin (< μm) sample, allowing a variety of morphological information to be gathered. Conventional imaging is performed using either directly transmitted or diffracted electrons, with contrast enhanced by inserting an aperture into the back focal plane of the objective lens (Figure 3-10). For the purpose of bright-field (BF) imaging in TEM, an objective aperture is used to select the transmitted beam and exclude scattered

beams (Figure 3-10a). In dark-field (DF) imaging, a specific diffracted beam is used to form an image (Figure 3-10b), *e.g.* to accentuate specific crystallographic phases and crystal defects.

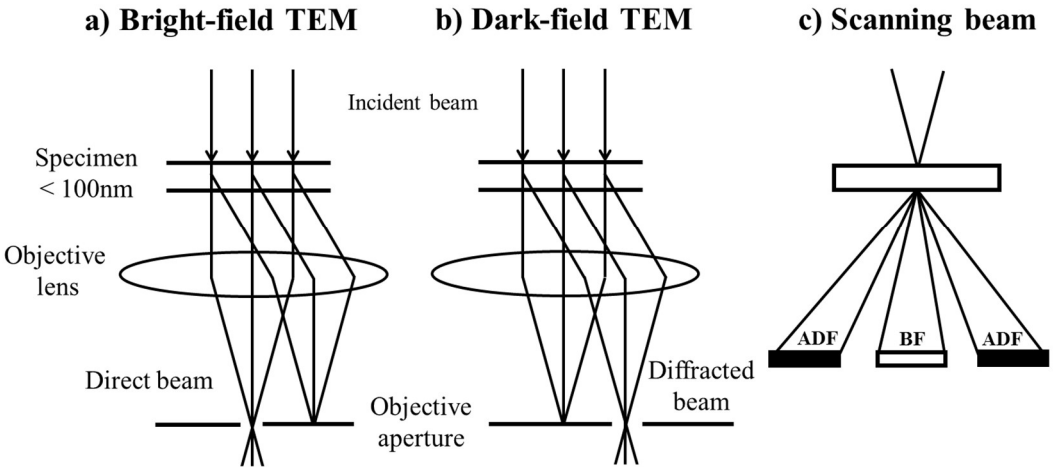

Figure 3-10 a) Bright-field; and b) Dark-field diffraction contrast imaging in TEM (parallel illumination); and c) bright-field and annular dark-field imaging in STEM (converged electron probe)

Conventional diffraction contrast imaging in TEM uses parallel electron beam illumination, whilst scanning transition electron microscopy (STEM) uses a converged electron probe which is scanned across a surface to minimise interactions with the specimen, whilst allowing for increased beam intensity. The STEM mode of operation uses annular detectors to select scattered electrons for imaging. Figure 3-10c illustrates the basic configuration for BF imaging, using a solid-state detector, and annular dark-field (ADF) imaging in STEM. Selected area electron diffraction (SAED) for structure determination in TEM uses parallel illumination and an aperture located in the first image plane to restrict the field of view. Convergent beam electron diffraction (CBED) may be performed in both TEM and STEM modes, using a converged beam (~ 10 - 100 nm diameter) for *e.g.* structure determination of small crystals [121]. In this work, coated samples and single craters were investigated in detail in cross-sectional

geometry using a JEOL 2100F FEG-TEM (200 kV), whilst starting material was investigated using a JEOL JEM-2000FX TEM.

3.6.6.1 TEM sample preparation

The preparation of electron transparent sample for TEM investigation is challenging, with approach depending on material type and the information content required. Conventional mechanical sectioning and ion milling techniques are relatively low cost but time consuming; as distinct from the rapid but high cost approach of site-specific sectioning using focused ion beam (FIB) milling (within a FIB-SEM).

Conventional mechanical sectioning

Thin slices (~ 1 mm thickness) were cut from bulk or coated samples using a disc cutting machine (ATA Brillant 220). Samples were then coarse ground to a thickness of ~ 500 μm using SiC paper (grade P400). A mechanical punch was used to cut 3 mm discs which were then ground to a thickness of ~ 200 μm (SiC paper, grade P1200). The discs were then fixed using thermal glue to a holder and mechanically dimpled (Fischione model 2000 Specimen prep system) using a small radius tool, down to a thickness of ~ 30 μm, using 6 μm and 1 μm diamond slurries. Samples were then Argon ion milled (Fischione model 1010; 4.5 keV; 8 mA; Ar 15˚ incident angle, with sample cooling and rotation), until electron transparent, as identified when a small hole appeared in the middle of the disc. Samples were then cleaned with acetone before examination. In this work, this approach was used to prepare starting 304-SS substrates for TEM investigation.

Focused ion beam (FIB) milling

Focused ion beam (FIB) milling, within a Dualbeam^{TM} FIB-SEM, is a powerful approach to prepare site-specific TEM samples. A very fine probe (< 10 nm diameter) of 30 keV Ga^{+} ions was applied, with the rastered beam used to sputter specific areas of the sample for sub-surface investigation, with sequential reduction in beam current density allowing for < 100 nm sections to be defined. A gas-injection system (GIS) allows protective Pt layers to be deposited over regions of interest prior to milling. A nano-manipulator was used to lift-out the sectioned lamellae which were then attached to a TEM support grid. In this work, electron transparent samples of representative TiC/Fe cermet coatings and single spark deposition events, ED processed under conditions of 10 A current and 8 μs pulse-on time, were prepared using an FEI Quanta 200 3D focused ion beam SEM (FIBSEM) operated at 30 kV. The transfer of electron transparent membranes to TEM support grids was achieved using a nano-manipulator (OmniProbe 100).

3.6.7 Spark emission spectrophotometry

The chemical composition of workpiece materials was analysed using spark emission spectrophotometry (Worldwide Analytical Systems AG, Foundry-Master). Samples were ground with P80 grade paper (median diameter 180 microns) and washed with acetone. The first two measurements were excluded, to avoid contamination issues, and an average across six different locations was taken.

3.7 Thermal conductivity measurements

The thermal conductivity of the dielectric fluid was measured directly using a C-Therm (TCi Technologies), averaged over six measurements, with the first measurement being excluded for accuracy. The machine was calibrated prior to testing using a standard reference material (*i.e.* distilled water).

3.8 Gap voltage measurement during ED processing

In order to measure gap voltage and record voltage waveforms for all the selected process parameters during ED processing, a data acquisition system (Figure 3-11) connected to PicoScope 6 software was used. Figure 3-11 presents the experimental set-up of the voltage waveform measurement system. The system comprised a high resolution PicoScope 4224 (PC USB Oscilloscope) with differential oscilloscope probes (TA041). The PicoScope (two-channels A and B; maximum input voltage 100 V) was set to a sampling rate of 80 Mega samples per second (MS/s) with 12.5 ns sampling intervals. The differential probe was set with 1:10 attenuation ratio and connected to the tool electrode (negative polarity) and workpiece (positive polarity) to record voltage profiles.

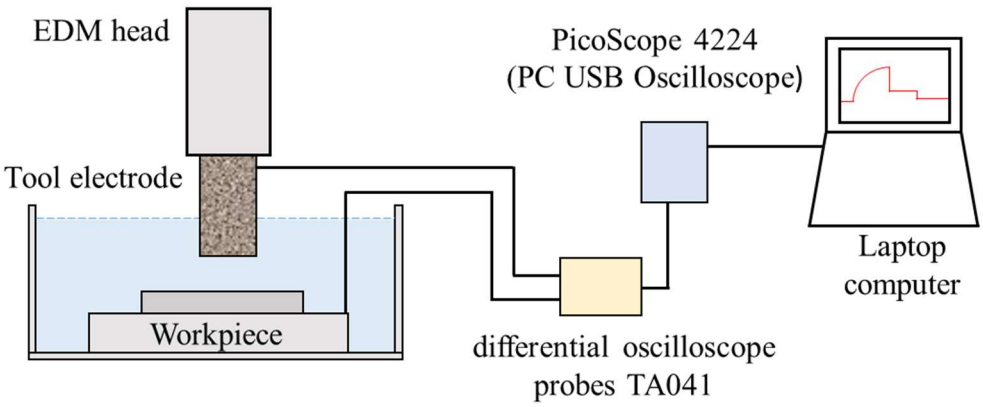

Figure 3-11 Schematic of experimental set-up for voltage waveform measurement

3.9 Tribology

3.9.1 Reciprocating wear testing

Wear testing was performed under dry sliding conditions using a linear reciprocating ball-on-flat approach (Figure 3-12). The apparatus consisted of a stationary ball sliding on a reciprocating plate fixed in a holder mounted on a sliding bed. The bed was driven by a crank mechanism and guided by two cylindrical bars to ensure motion remained rigid along the same axis. The load arm was balanced with a counterweight to ensure that applied weight only contributed to the applied load on the sample.

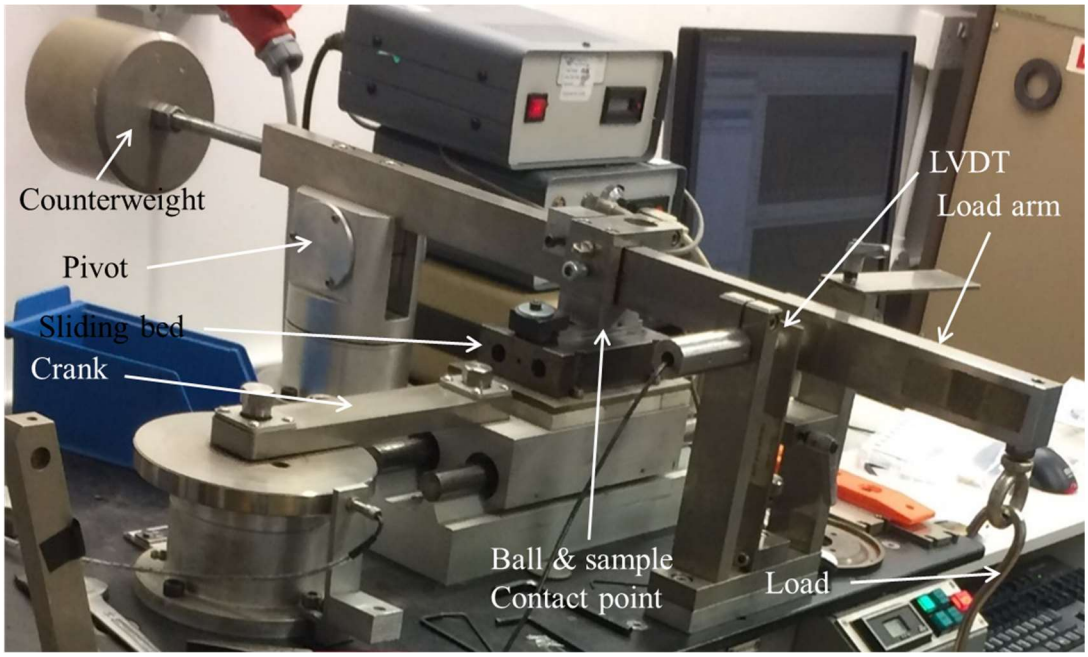

Figure 3-12 Experimental set-up of the wear test rig

The ball holder was positioned on the load arm at a distance L_1 = 424 mm from the pivot, to apply force (F) at the contact point on the sample (Figure 3-13). The force load (W) in (kg) may be calculated using equilibrium forces:

$$\textbf{Moment} = \textbf{Force x Distance} \qquad (3\text{-}6)$$

$$\mathbf{W \times 9.8 \times L = F \times L_1} \qquad (3\text{-}7)$$

$$\mathbf{W = \frac{F \times L_1}{9.8 \times L}} \qquad (3\text{-}8)$$

For an applied load of 10 N (with L = 586.5 mm and L_1 = 242 mm, respectively), the weight load required was:

$$\mathbf{W = \frac{10 \times 242}{9.8 \times 586} = 0.42\ kg}$$

Similarly, for an applied load of 50 N, the weight load required was:

$$\mathbf{W = \frac{50 \times 242}{9.8 \times 586} = 2.1\ kg}$$

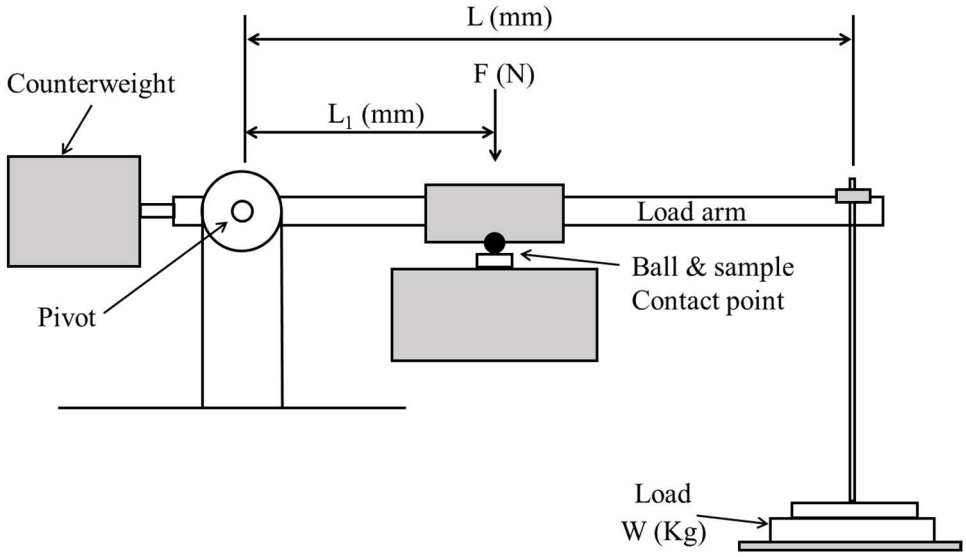

Figure 3-13 Schematic of the ball-on-flat wear testing configuration

The friction coefficient was measured using a linear voltage displacement transducer (LVDT) (labelled in Figure 3-12), connected to LabView software (Cyber-Sol). The coefficient of friction (CoF) was determined through conversion of recorded voltage into a lateral force, with rig calibration performed prior to tests under each loading condition.

Based on preliminary experimentation, wear test parameters identified for this study were 35,000 and 10,000 cycles, at a frequency of 2 Hz, with normal applied loads of 10 N and 50 N, respectively. The wear track length was kept constant at ~ 10 mm, and all experiments were conducted at room temperature (18 - 20˚C with relative humidity 20 - 30%). All wear tests were repeated three times, each using a new alumina (Al_2O_3) ball (9.525 mm) chosen to simulate aggressive wear conditions, because it exhibits higher hardness than the coating and it is easy to distinguish from the coating using EDS in the event of cross-transfer of material. Samples were washed with acetone prior to wear testing, to ensure that all debris and/or surface contamination was removed.

3.9.2 Linear voltage displacement transducer (LVDT) calibration

It is important to perform a LVDT wear rig calibration prior to measuring the coefficient of friction. Five weights of ~ 1 kg force loads (A, B, C, D and E) were weighed to determine their exact mass, and applied perpendicular to the arm load in stages, starting from the no load. The loads were then removed in reverse order, with output voltage recorded continually. Plotting the measured voltage against applied load gave a slope representing the system response (K). Equation (3-9) allows a measured voltage (V_m), at any point during testing, to be converted to coefficient of friction (μ_f):

$$\mu_f = \frac{(V_m - V_0)}{K w} \qquad (3\text{-}9)$$

Where V_0 is voltage when the stage is stationary and w (kg) is the applied load.

3.9.3 Wear scar measurement

Cross-sectional line profiles of the wear tracks were obtained using a Talysurf series CLI 1000 (Taylor Hobson) surface profilometer, with an inductive type contact stylus with lateral resolution of 0.5 µm (Figure 3-6). Five profiles were taken for each sample each separated by a distance of 2 mm (Figure 3-14). The profilometry was carried out over lengths of 2 and 5 mm for narrow and wide scars, with resolutions of 4001 points and 10001 points, respectively. The areas of the wear scars were calculated using 'TalyMap Universal' software. The average value of these measurements was taken as a final cross-sectional area for each sample. Based on the volume loss V_w (mm^3), the specific wear rate W (mm^3/Nm) was calculated according to the following equation:

$$\mathbf{W} = \frac{\mathbf{V_w}}{\mathbf{2\ L_a\ S\ N_r}} \qquad (3\text{-}10)$$

Where L_a (N) is applied load, S (mm) is the stroke length, and N_r is the total number of reciprocations.

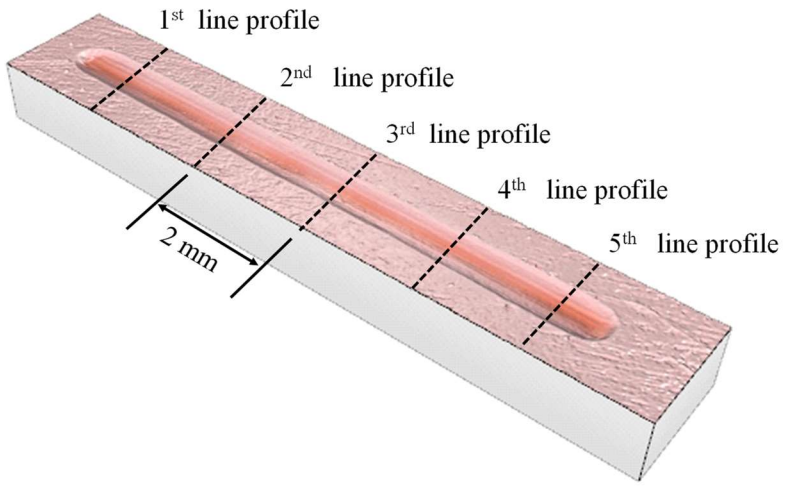

Figure 3-14 Schematic representation of the wear scar profilometry measurements

3.9.4 Ball wear scar measurements

The Al_2O_3 ball employed to perform wear testing also undergoes wear. Hence, an optical microscope (Nikon Eclipse LV100ND) attached with Nikon Digital Sight DS-Ri1 camera, was used to image the ball scars. The diameter of these scars was determined using ImageJ software and used to calculate the wear volume, assuming a spherical cap (Figure 3-15). The specific wear rate of the ball, W_b (mm^3/Nm), was then calculated using the following equation:

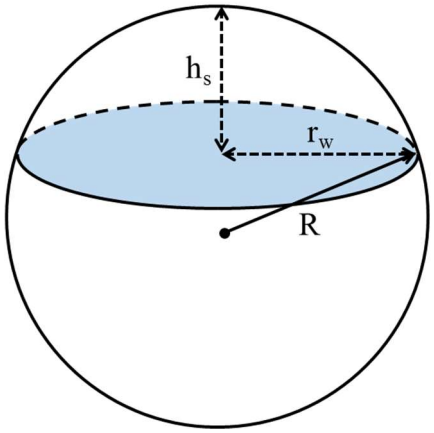

Figure 3-15 Wear of the reciprocating ball (spherical cap)

$$\mathbf{h_s = R - \sqrt{R^2 - r_w^2}} \qquad (3\text{-}11)$$

$$\mathbf{V_c = \pi\, h_s^2 \quad (R - \frac{h}{3})} \qquad (3\text{-}12)$$

$$\mathbf{W_b = \frac{V_c}{N\,d}} \qquad (3\text{-}13)$$

Where h_s is the height of the spherical cap (mm); R is the ball radius (mm); r_w is the radius of the wear scar (mm); V_c is the cup volume (mm^3); N is the normal load and d (m) is sliding distance.

$$\mathbf{d_s = 2\ x\ wear\ track\ x\ number\ of\ cycles} \qquad (3\text{-}14)$$

3.10 Summary

The chapter outlines the experimental design, based on the research gap in literature, as reviewed in chapter 2, followed by descriptions of procedures for sample preparation for coating, such as cutting, grinding and polishing, in advance of ED coating using semi-sintered TiC and solid Cu tool electrodes, and LSM processing. Protocols for monitoring and measuring the gap condition were also presented, providing input data for the modelling work. The results are now presented in chapters 4-6.

4 EDC TiC/Fe cermet coatings

4.1 Introduction

This chapter presents a process-map approach for the development of ED TiC/Fe cermet coatings on 304 stainless steel, as a function of increasing current (2 - 19 A) and pulse-on time (2 - 64 μs), and provides a fundamental description of the mechanisms of cermet layer formation. Optimised processing parameters for the production of cermet coatings on HSS substrates are also identified, and benchmarked against ED machined surfaces prepared using a conventional Cu electrode. A variety of characterisation techniques were used to appraise coating morphologies. The interrelationship between micro-hardness and developed coating microstructure is described.

The starting tool and workpiece materials are described initially, leading on to the investigation in to the development of TiC/Fe ED coatings, processed using a semi-sintered tool electrode, and characterised down to the nanometer-scale. Emphasis is given to the effects of current and pulse-on time on surface topography, microstructure, layer thickness and microhardness. Comparison of EDC and EDM processed samples on 304-SS and HSS substrates as made, leading to the construction of a comprehensive EDC process map.

4.2 Starting material morphologies

The chemical compositions of the 304-SS and HSS substrates used were obtained by spark emission spectrophotometry (Worldwide Analytical Systems AG, Foundry-Master; averaged over six different locations), as summarised in Table 4-1.

Table 4-1 Chemical composition of the starting 304-SS and HSS substrates

	C wt%	Si wt%	Mn wt%	Cr wt%	Mo wt%	Ni wt%	Al wt%	Co wt%	Cu wt%	V wt%	W wt%	Nb wt%	Fe wt%
HSS	0.87	0.39	0.30	4.26	4.21	0.17	0.03	0.23	0.07	2	5.35	0.06	bal.
304-SS	0.03	0.60	2.0	18.6	0.23	8.4	0.01	0.14	0.21	0.11	0.1	-	bal.

A secondary electron (SE) image of the starting, semi-sintered TiC tool electrode is presented in Figure 4-1, showing a coarse particle structure, up to ~ 5 μm in size. EDS data (79.4 wt% Ti and 20.6 wt% C) confirmed that the electrode mainly consisted of TiC particles (no other elements were detected at a level above 0.1 wt%). Electrical resistivity was measured to be ~ 258.7 μΩ.cm using a high accuracy Fluke 8845A multimeter.

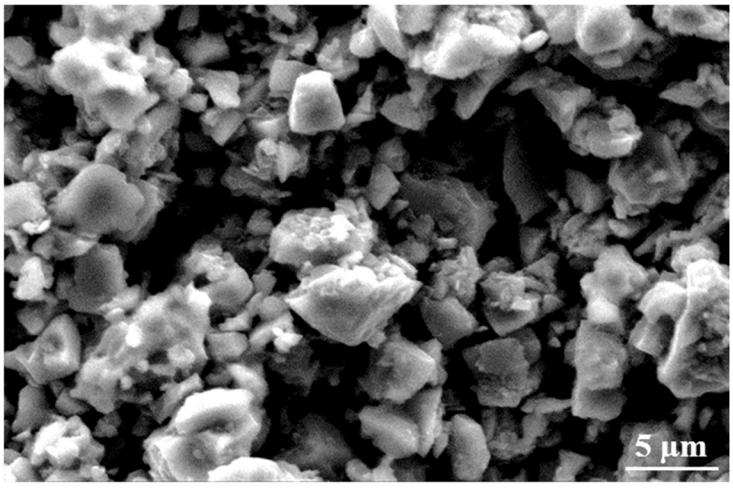

Figure 4-1 SE image of the starting TiC tool electrode

Further, XRD analyses were performed to appraise the crystal structures of the starting materials. XRD data for the TiC and Cu tool electrodes are presented in Figure 4-2. The diffraction pattern for the TiC electrode comprised six peaks which perfectly matched with TiC (fcc) (EVA software - card no 00-032-1383) (Figure 4-2a). Similarly, the diffraction pattern for the Cu electrode comprised five peaks which exactly matched with Cu (fcc) (card no 00-004-0836) (Figure 4-2b).

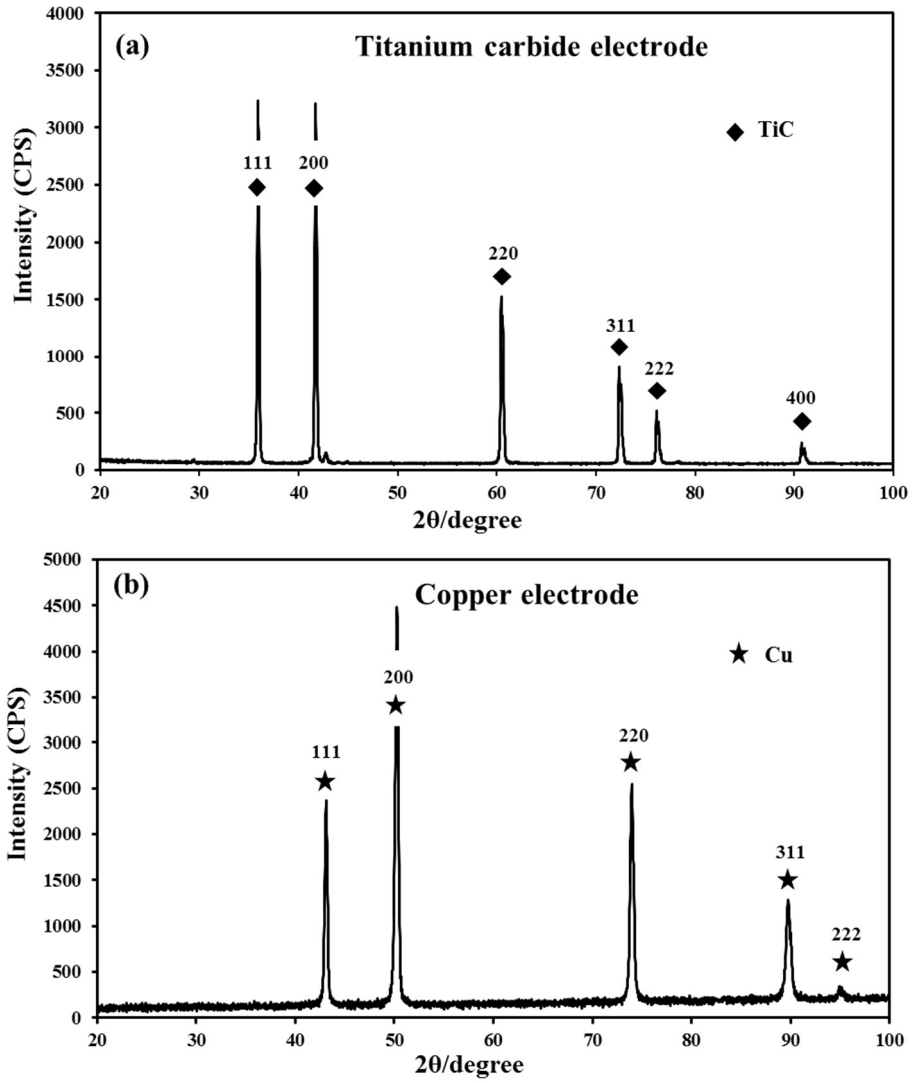

Figure 4-2 X-ray diffraction data for the starting tool electrodes: a) TiC; and b) Cu

Figure 4-3 presents XRD patterns for the as-polished steel substrates, prior to ED processing. The diffraction pattern for 304-SS was composed of austenite γ-Fe (fcc) (card no 00-033-0397) and martensite α`-Fe (bcc) phase (see Appendix 1 a complementary TEM image prepared using conventional mechanical sectioning), with the intensity for austenite γ-Fe being much higher than that for martensite α′-Fe, as expected (Figure 4-3a). It is recognised that there is a difficulty distinguishing between the ferrite α-Fe (bcc) and martensite α`-Fe phases using the XRD technique, since both possess the same diffraction peaks [122], however, the martensite α`-Fe phase within 304-SS is expected to develop after cold working [123]. XRD patterns for the HSS

substrate (Figure 4-3b) comprised mainly ferrite α-Fe (card no 00-006-0696) and M_6C carbide (Fe-Mo-C) (card no 00-047-1191), along with evidenced for MC vanadium rich carbide (V-C) (card no 00-035-0786).

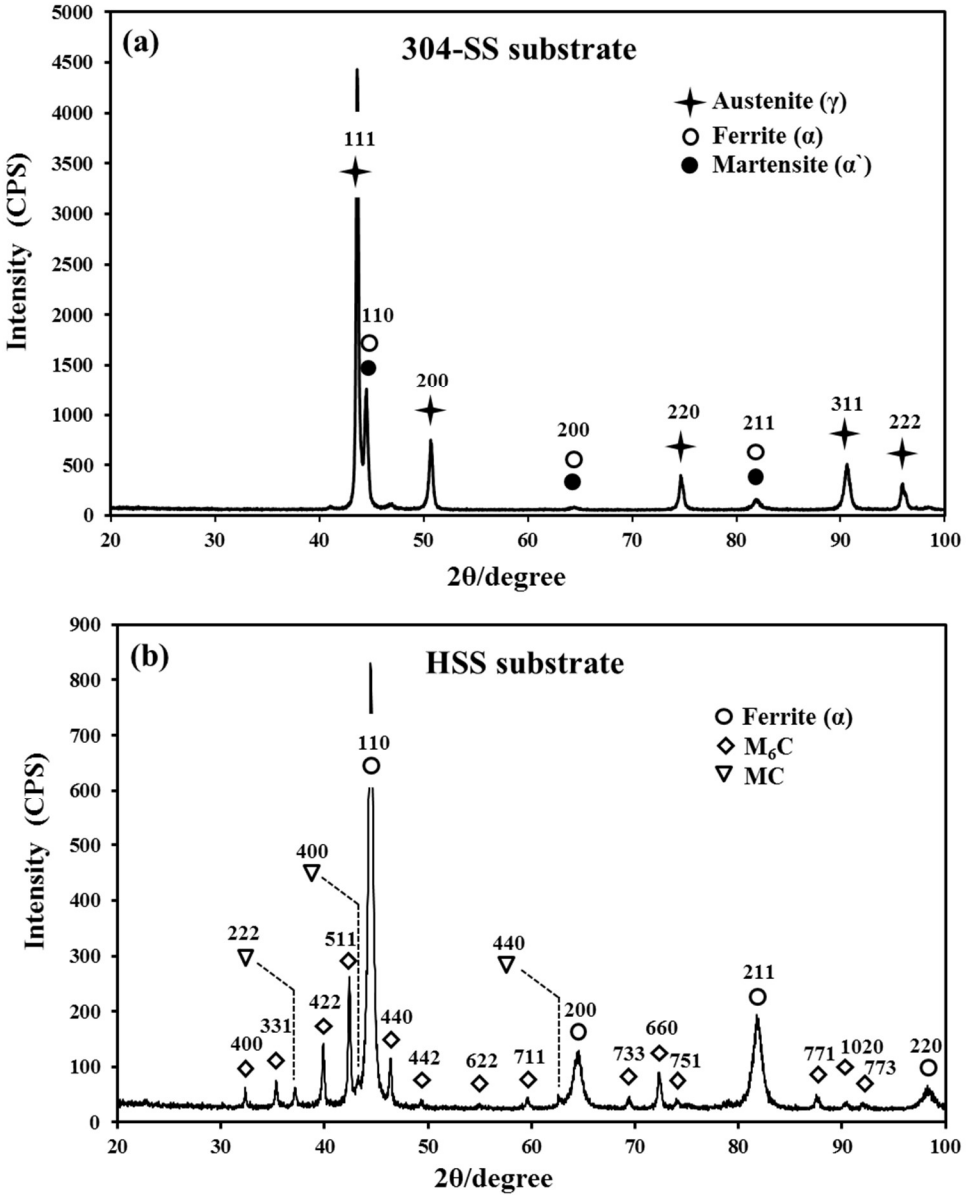

Figure 4-3 X-ray diffraction patterns for the starting: a) 304-stainless steel; and b) high speed steel substrates

4.3 Effect of current and pulse-on time on ED coating morphology

4.3.1 Surface topography of ED processed coatings

The surface quality and homogeneity of ED processed TiC-based coatings on 304-SS were found to be dependent strongly on discharge conditions. For example, Figures 4-4 and 4-5 present low magnification SE images of substrate and as-deposited coatings, as a function of increasing current (for a fixed pulse-on time of 8 μs) and increasing pulse-on time (for a fixed current of 10 A), respectively, showing significant changes in surface topography.

Figure 4-4b provides evidence for the development of individual TiC containing craters at the surface, when ED processed with a current of 2 A. This sample showed low levels of micro-cracking and micro-porosity, with surface roughness of Ra ~ 1.2 μm. Occasional TiC-rich surface particles, confirmed by EDS, were observed also on the surface of this sample, being attributed to larger particles transported from the tool electrode.

Figures 4-4c,d present ED coatings processed with higher discharge currents of 6 and 10 A, respectively, showing the onset and development of micro-cracks bounding the initially formed craters, with surface roughness values of ~ 1.2 and ~ 1.3 μm, respectively. With further increases of processing current to 14 and 19 A, void and micro-crack formation became even more pronounced, although the locations of individual craters could still be discerned. These samples showed slightly increased surface roughness values of ~ 1.8 and ~ 1.7 μm, respectively. It is noted that there was an increase in crater size with increasing processing current (Table 4-2).

Table 4-2 Summary of individual crater sizes (n = 30), continuum layer surface roughness values (n = 5), cermet layer thicknesses and coating Ti wt% values, as a function of increasing current and pulse-on time

	Current / A						**Pulse-on time / μs**					
	2	6	10	14	19		2	4	8	16	32	64
Mean crater size / μm	41	60	69	83	96		35	57	69	107	151	165
σ	*4.3*	*4.7*	*5.0*	*8.6*	*8.7*		*5.6*	*11.8*	*5.7*	*7.8*	*14.3*	*16.5*
Mean surface roughness Ra / μm	1.2	1.2	1.3	1.8	1.7		1	1.3	1.3	2.4	3.3	4.6
σ	*0.2*	*0.2*	*0.4*	*0.5*	*0.2*		*0.1*	*.02*	*0.4*	*0.2*	*1*	*0.7*
Mean cermet layer thickness / μm	7.0	8.0	10.4	11.6	10.0		3.6	7.9	10.4	11.9	16.0	34.0
Coating Ti content / wt%	30.6	28.5	40.3	42.8	46.5		26.7	42.9	40.3	36.3	22.9	20.4

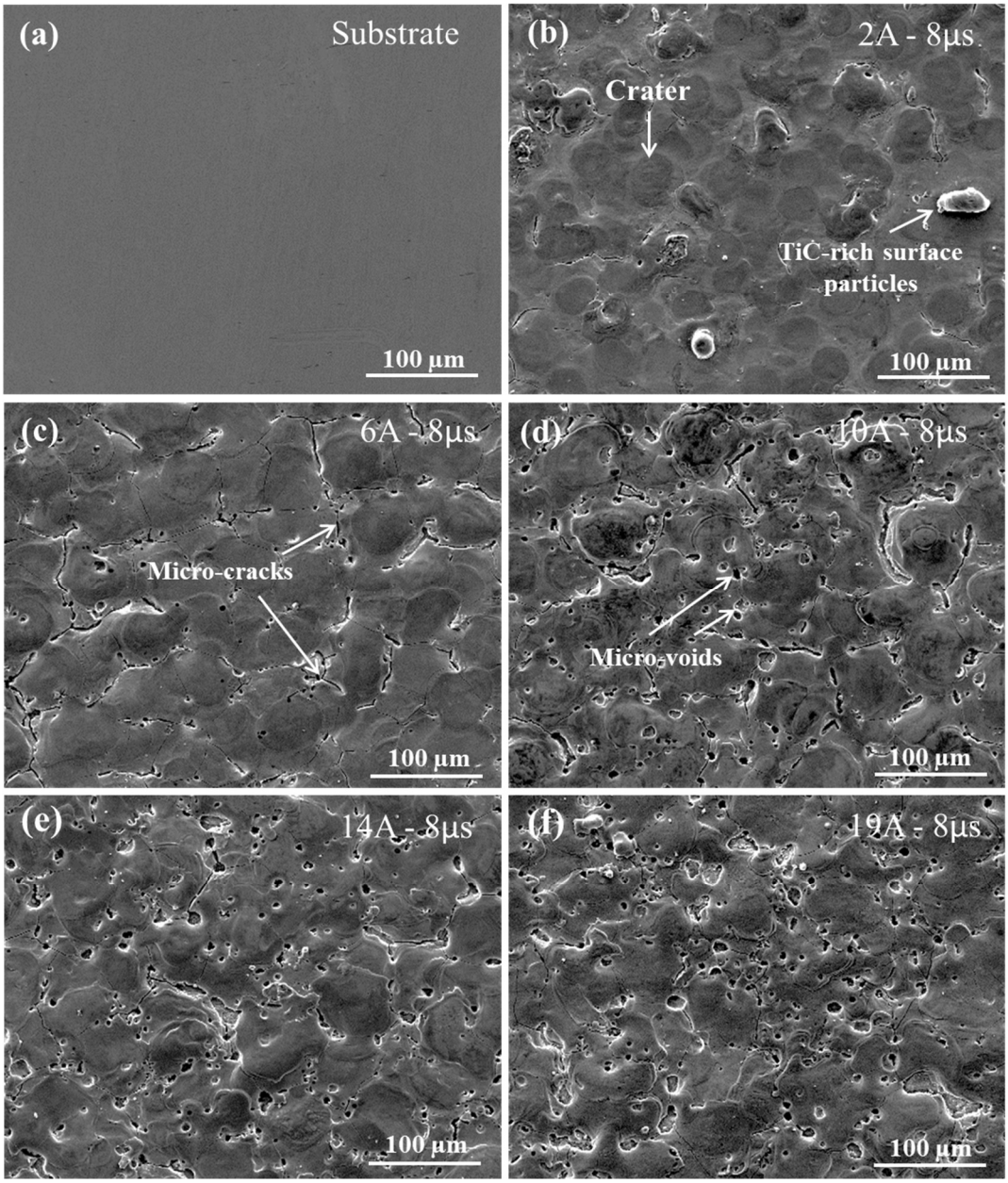

Figure 4-4 SE images of: (a) as-polished 304 stainless steel; and (b-f) TiC-based coatings deposited as a function of increasing current: 2, 6, 10, 14 and 19 A, respectively, for 1 h processing time and 8 µs pulse-on time

Figure 4-5 similarly illustrates the development of craters and surrounding micro-cracks for samples ED processed with increasing pulse-on time (fixed current of 10 A). For a short pulse duration of 2 µs, the processed surfaces showed low levels of void and crack formation (Figure 4-5a), and returned a surface roughness value of ~ 1 µm. Figures 4-5b,c demonstrate the onset and development of micro-crack formation bounding the craters with increasing pulse-on times, of 4 and 8 µs, respectively.

Increasing the pulse-on time further to 16, 32 and 64 µs, respectively, led to increased void formation, with cracks widening and becoming elongated, and voids becoming larger and denser, being instrumental in extended, interconnecting crack formation (Figures 4-5:d-f). It was found that surface roughness increased with increase pulse-on time, reaching ~ 4.6 µm at 64 µs pulse-on time.

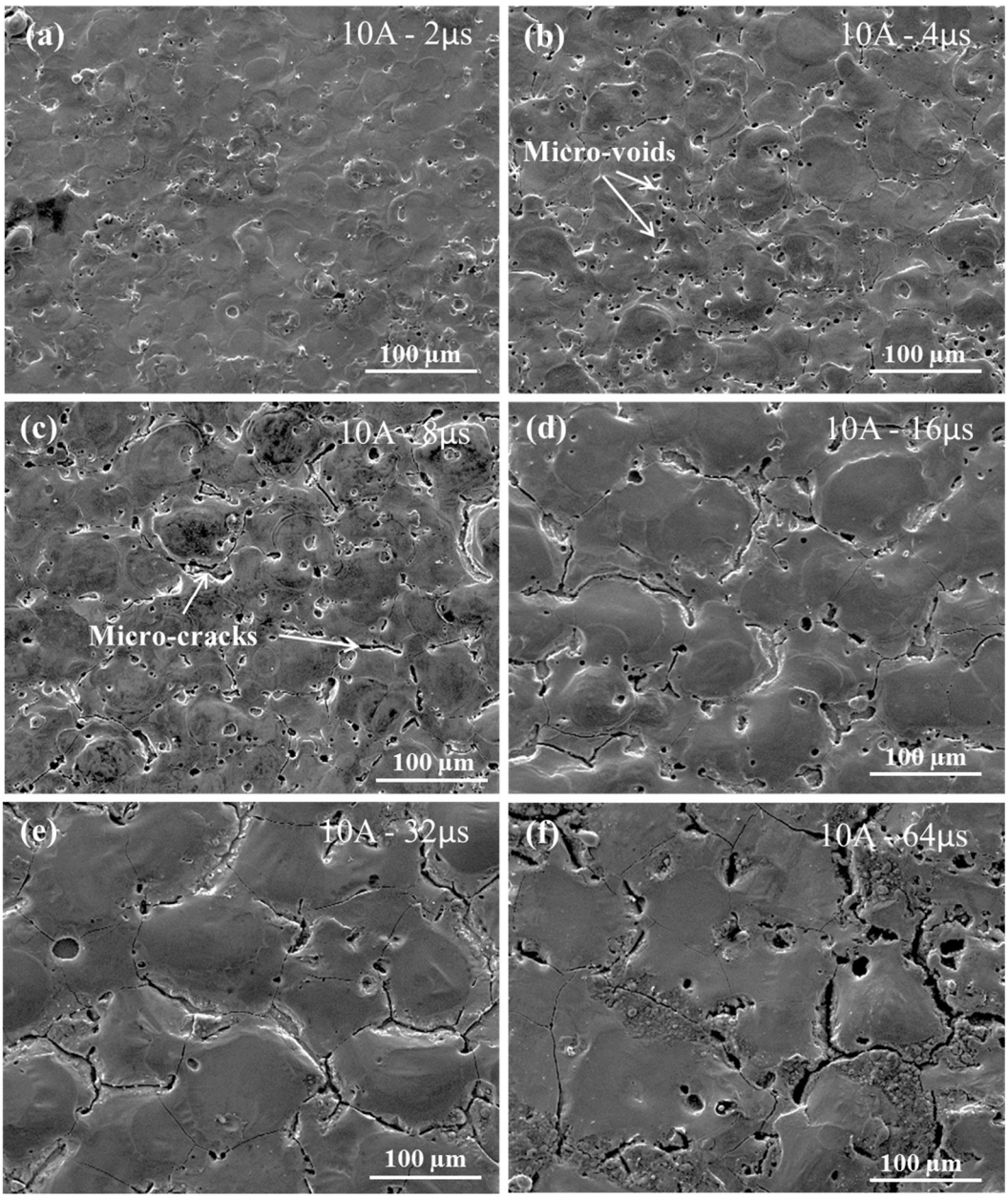

Figure 4-5 SE images of: (a-f) Coatings deposited as a function of increasing pulse-on time: 2, 4, 8, 16, 32 and 64 µs, respectively, for 1 h processing time and a fixed current of 10 A

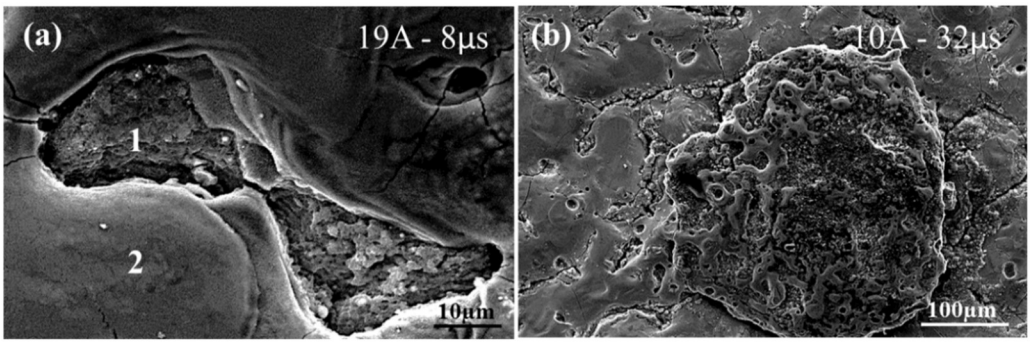

Figure 4-6 High magnification SE images showing details of: (a) A pore formed under conditions of 19 A current (fixed pulse-on time of 8 µs); and b) a large surface particle formed under conditions of 32 µs pulse-on time (fixed current of 10 A)

Figure 4-6 represent two characteristic features of these ED processed surfaces, *i.e.* a pore at the substrate, formed under conditions of 19 A current (fixed 8 µs pulse-on time); and a surface particle, formed under conditions of 32 µs pulse-on time (fixed current of 10 A). As the processing current increased, it was observed that pores and cracks opened-up (Figure 4-6a (1)), allowing the substrate to be detected by EDS, whilst the coating was found to be TiC-rich (Figure 4-6a (2)). Conversely, large surface particles (Figure 4-6b) were found to be carbon enriched TiC clusters, considered to originate from the PM tool electrode and reacting with carbon cracked from the dielectric fluid.

4.3.2 Microstructure of ED processed coatings

XRD analyses were performed to appraise the structural integrity of the coatings, as a function of process conditions. Figure 4-7 presents XRD patterns as a function of increasing current from 2 to 19 A (for fixed pulse-on time of 8 µs), confirming increasing incorporation of TiC in all the coatings with some slight preferred orientation. In addition, signatures for austenite γ-Fe and martensite ά-Fe phases were evident. A small peak attributable to amorphous carbon (card no 01-075-1621) was

found to develop with increasing current. Signatures due to low levels of Cr_3C_2 (card no 01-071-2287) and cementite Fe_3C (card no 00-035-0772) were detected also.

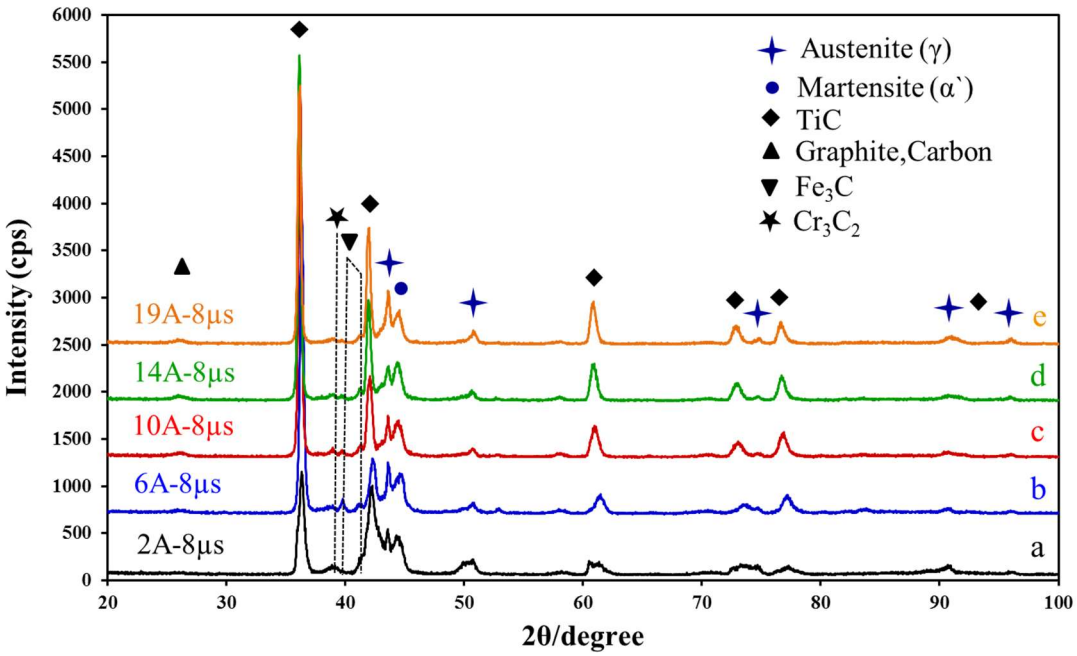

Figure 4-7 XRD patterns of coatings produced under conditions of 8 µs pulse-on time and increasing current: a) 2 A, b) 6 A, c) 10 A, d) 14 A, and e) 19 A, respectively

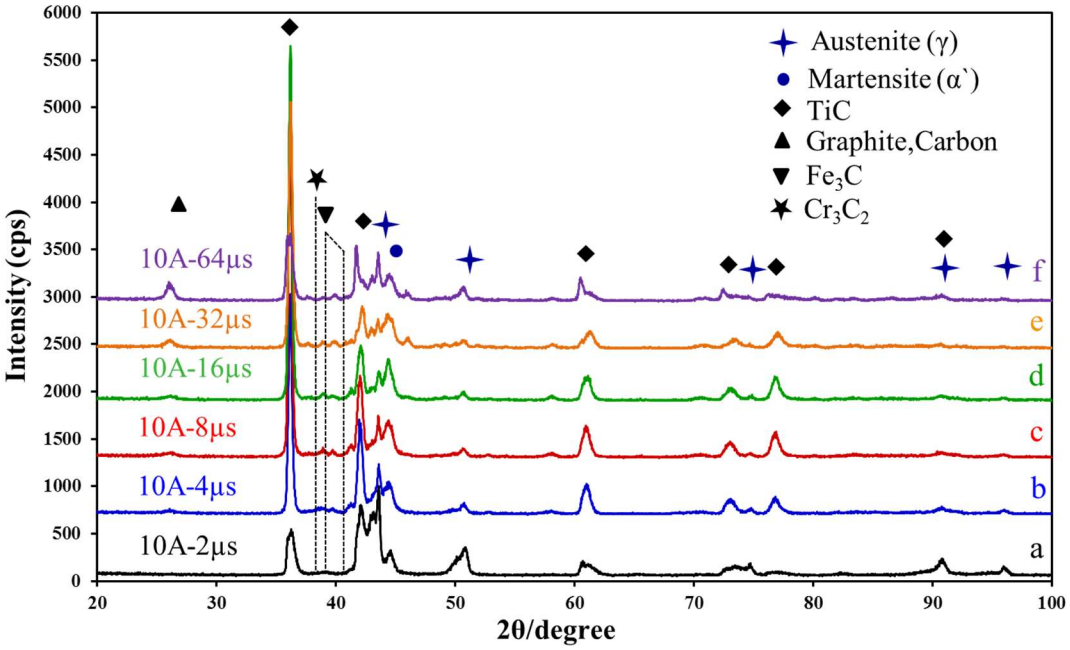

Figure 4-8 XRD patterns of coatings produced under conditions of 10 A and increasing pulse-on times: a) 2 µs, b) 4 µs, c) 8 µs, d) 16 µs, e) 32 µs, and f) 64 µs, respectively

Figure 4-8 presents XRD patterns for these coatings as a function of increasing pulse-on time from 2 to 64 μs (for fixed current of 10 A), again showing the increasing dominance of TiC with some slight preferred orientation. The crystalline peaks became more intense and sharp with increasing discharge duration from 2 to 16 μs, consistent with the development of higher levels of coating crystallinity. However, beyond 16 μs pulse-on time, the peak intensity due to TiC reduced, whilst the signature due to amorphous carbon increased, indicating the development of coatings with lower levels of crystallinity. Very small signals attributable to the presence of Cr_3C_2 and cementite Fe_3C again were detected.

4.3.3 Cross-sectional TEM of a continuum cermet coating

In order to gain insight into the fine-scale microstructure, Figure 4-9 presents a TEM cross-section, showing the variability of cermet structure into the depth of the coating. Figure 4-9a presents a bright field diffraction contrast TEM image showing the near-surface grain structure of the continuum TiC/Fe cermet coating, with boxed regions magnified (Figures 4-9b,d,e). It is evident that there are several broad bands of coating material, with small, ~ 20 - 80 nm, equiaxed TiC grains at the near surface (Figure 4-9a (I)), as measured using ImageJ; a transition zone of larger, ~ 30 - 110 nm sized TiC grains (II); a region of columnar grains of length ~ 330 - 450 nm and width ~ 90 - 140 nm (III); and intermediate sized TiC grains ~ 150 - 800 nm (IV) towards the coating/ substrate interface. Figure 4-9b shows a high magnification bright field image of a very fine grained near-surface region (I), and associated phase contrast image (Figure 4-9c) of grains at the surface with lattice spacing again consistent with the development of TiC (d_{111} = 0.246 nm; d_{220} = 0.154 nm). Figures 4-9d,e present high magnification annular dark field scanning TEM (ADF-STEM) images, showing a

transition zone region (I) to region (II) with interspersed with carbon deposits (Figure 4-9d), then a region of grains showing distinct columnar growth (region III) (Figure 4-9e).

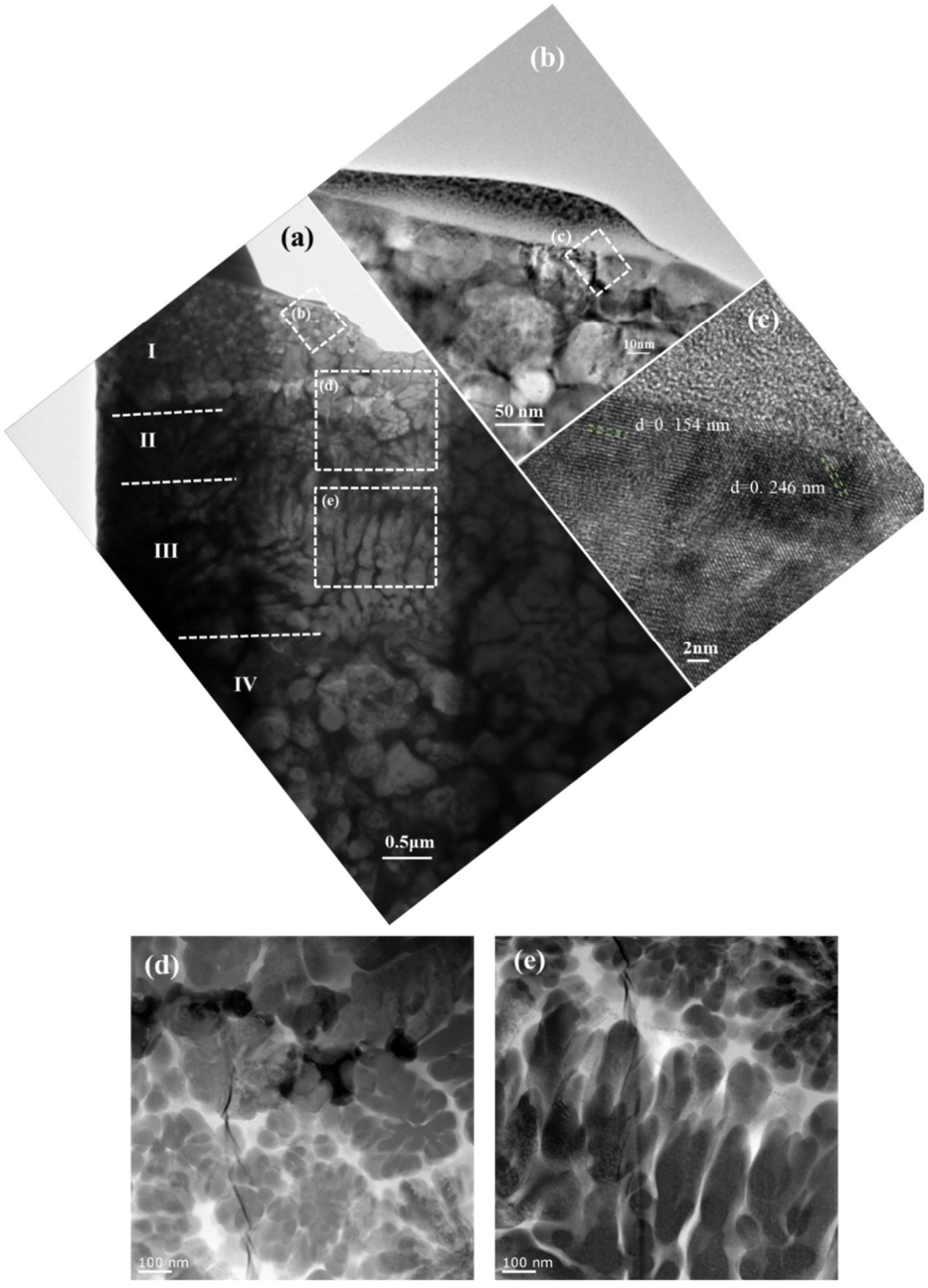

Figure 4-9 Cross-sectional TEM micrographs of an EDC layer processed under conditions of 10 A and 8 μs: (a) Bright field image, large field of view; (b,c) near surface region at increasing levels of magnification (boxed regions in each respective images); (d,e) high magnification dark field images of boxed regions showing transitional band and columnar growth microstructures

Application of the Scherrer equation to the XRD data (Figures 4-2a, 4-7 and 4-8), as determined using 111 diffraction peaks, indicated that the TiC grains from the starting tool electrode exhibited average grain sizes on the scale of ~ 130 nm, being much larger than the ~ 40 nm TiC average grain sizes within the coating, being supported by Figure 4-9a which demonstrates the development of ~ 40 nm sized grains near to the top surface, as sampled by XRD. This is consistent with the constituents of the melt pool being fully molten prior to solidification. Intermixing of workpiece material with TiC occurs during the melt pool lifetime.

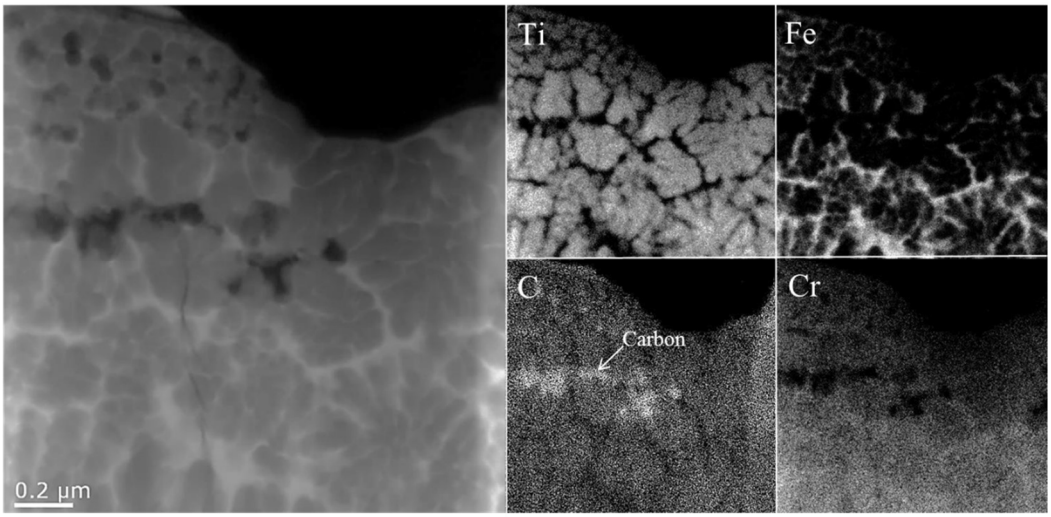

Figure 4-10 ADF-STEM image with associated EDS elemental maps showing the dispersion of Ti, Fe, C and Cr

Figure 4-10 provides more details of the near surface structure, with associated EDS chemical maps showing the distribution of elemental Ti, Fe, C and Cr, respectively, within this cermet. The data shows the phase separation of TiC grains within an Fe-rich matrix along with a cluster of C-rich deposits. Interestingly, there is also strong evidence for a fairly uniform distribution of Cr throughout the sample, slightly enhanced within the Fe matrix.

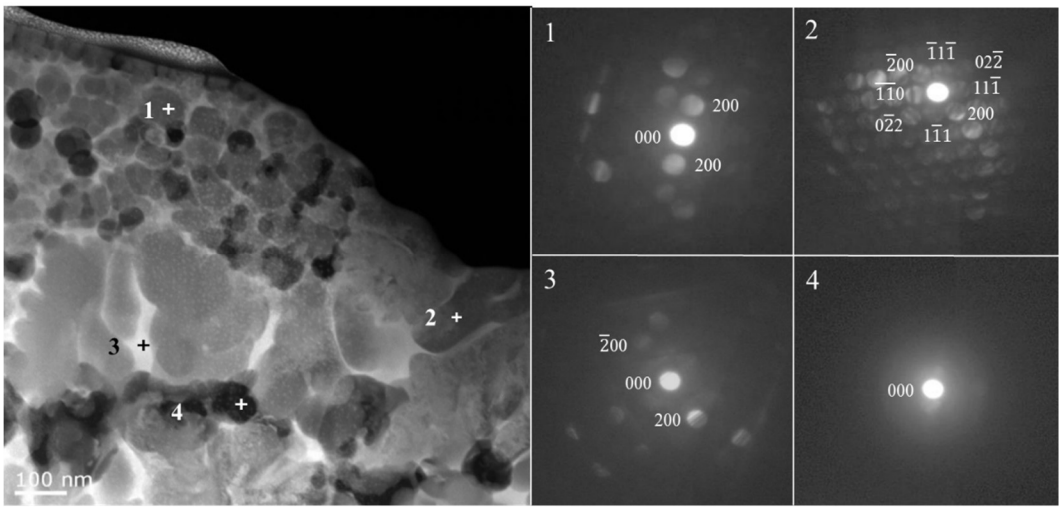

Figure 4-11 ADF-STEM image of the near surface grain structure; with associated CBED patterns from the specified locations consistent with (1, 2) TiC; (3) Fe and (4) amorphous C

Figure 4-11:1-4 presents an ADF-STEM image of the near surface grains with associated convergent beam electron diffraction (CBED) patterns consistent with the presence of fcc TiC grains ((1) systematic row and (2) close to <110> projection), within a matrix of iron ((3) systematic row), along with some localised clusters of amorphous C (4). The CBED patterns recorded with a highly converged probe, were used simply to establish which of the grains were crystalline or amorphous, with the composition of grains being established as TiC, Fe and C, as appropriate, using EDS (Figure 4-10).

4.3.4 Coating thickness

The investigation of mechanically polished and chemically etched coatings, in cross-sectional geometry, showed large variations in layer thickness, as a function of process conditions. For example, the SE image of Figure 4-12 shows the edge of a coated region of a sample processed under conditions of 6 A current and 8 μs pulse-on time.

The developed coating has replaced and fused with the substrate in an irregular fashion.

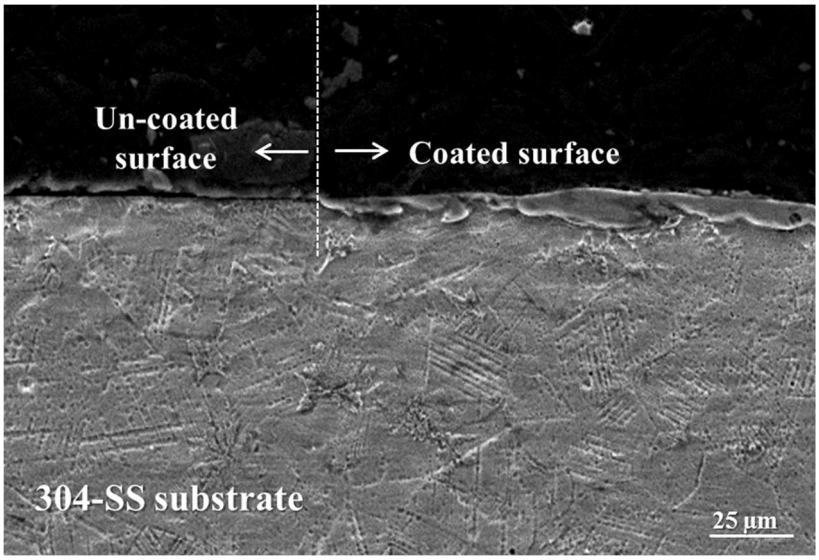

Figure 4-12 SE image of a coating, viewed in cross-section, EDC processed with 6 A current and 8 µs pulse-on time

Figures 4-13 and 4-14 shows optical microscope images and associated box plots for layer thickness, for the developed coatings, as a function of increasing current and pulse-on time, respectively. It is evident that the layers become thicker gradually (from ~ 7 to 10 µm) and more discontinuous as the current increases (from 2 to 19 A), whilst there is a much stronger increase in layer thickness (from ~ 3.6 to 34 µm) with increasing pulse-on time (from 2 to 64 µs).

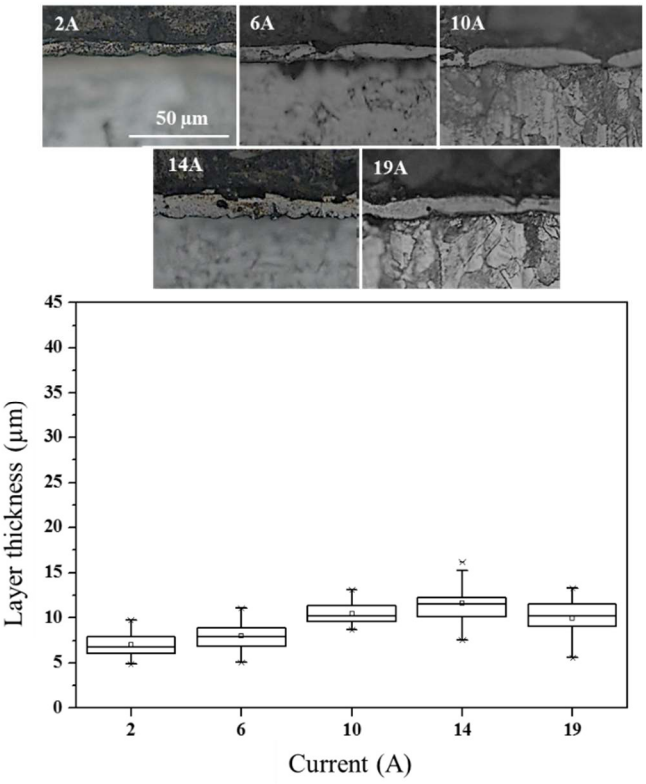

Figure 4-13 Variation of coating layer thickness (µm) as a function of current (A) and fixed pulse-on time of 8 µs (n=40)

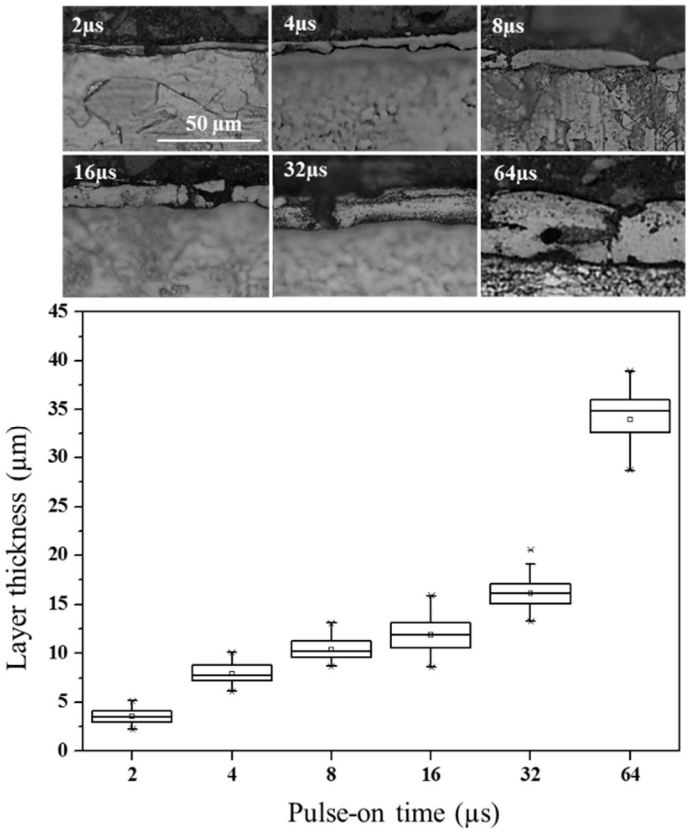

Figure 4-14 Variation of coating layer thickness (µm) as a function of pulse-on time (µs) and fixed current of 10 A (n=40)

4.3.5 Hardness

Figure 4-15 present bar graphs of Vickers micro-hardness for the coatings in cross-section geometry, and associated plots of Ti wt% values from EDS investigations of these samples in planar-view (with compositional data acquired from representative areas of ~ 0.24 mm^2 for each sample). It should be noted that indents of samples produced using 2 A current and 2 µs on-time, were too thin to provide reliable hardness data, and hence were omitted from the data set shown. It is evident that there is a direct correlation between hardness and Ti (and TiC by implication) content within the cermet. Increasing the discharge current led to a progressive increase in TiC deposition (Figure 4-15a), with consequent increase in tool electrode wear. These EDC processed layers exhibited hardness values ~ 4 - 8 times higher (from 6 to 19 A) than that of the stainless steel substrate (196 HV; σ = 16.8), demonstrating the ability of EDC processing to impart improved mechanical performance to the surface of austenitic stainless steel. However, an initial increase in hardness and Ti (TiC) content for increasing pulse-on time, up to 8 µs, was followed by a steady reduction in both hardness and TiC content for further pulse-on time increases. Coatings produced with 19 A current and 8 µs pulse-on time returned the highest mean value of hardness of ~ 1888 HV. It should be noted that some anomalous data points were observed during hardness testing, resulting in both high and low hardness results, attributable perhaps to extremely localised TiC deposits, *i.e.* inconsistent coating, and porosity, respectively.

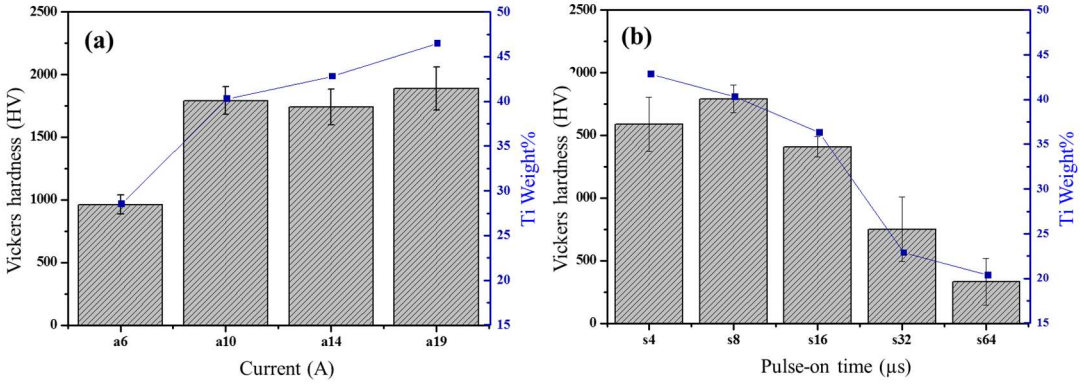

Figure 4-15 Vickers hardness and Ti wt% values, as a function of: a) current (A) and b) pulse-on time (µs); error bars are the standard deviations of 8 measurements

4.4 Comparison of EDC & EDM processed samples on 304-SS and HSS substrates

4.4.1 Microscopy of processed surfaces and coating cross-sections

Figures 4-16:a-d present SE micrographs of EDC TiC/Fe cermet coatings (processed under conditions of 10 A and 8 µs) and reference Cu EDM samples (again, processed under conditions of 10 A and 8 µs), on 304-SS and HSS substrates, respectively. The development of micro-cracks along with void formation was evident for all these processed samples. Average roughness values of ~ 1.3 µm and ~ 1.2 µm were returned for the cermet coated on 304-SS and HSS samples, respectively. Further, EDS analyses of the cermet coatings indicated Ti incorporations, *i.e.* corresponding to TiC transferred from the tool electrode, of ~ 39.4 wt% and ~ 29.3 wt% into the 304-SS and HSS, respectively. For comparison, 304-SS and HSS samples EDM processed using a conventional Cu electrode similarly exhibited distributed cracking and void formation (Figures 4-16b,d), with the delineation of final craters produced by the discharge process. In this case, the average surface roughness of processed Cu EDM 304-SS (~1.2 µm) was slightly lower than that of the processed HSS (~ 1.6 µm).

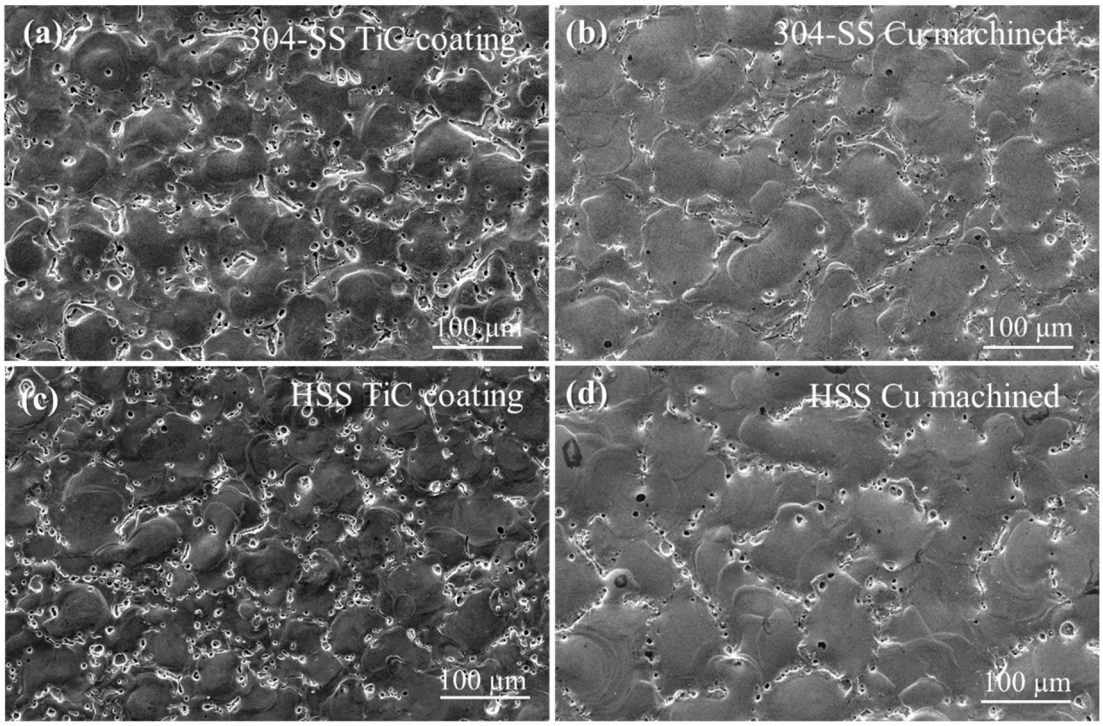

Figure 4-16 SE images of (a,c) EDC cermet coatings (10 A current and 8 µs pulse-on); and (b,d) EDM Cu reference samples (10 A current and 8 µs pulse-on), on (a,b) 304-SS; and (c,d) HSS substrates, respectively

Figure 4-17:a-d presents BSE images of the TiC/Fe cermet ED coating (10 A current and 8 µs pulse-on time) on a 304-SS substrate (cf. Figure 4-16a), viewed in cross-section, showing the development of an irregular, banded, composite microstructure. TiC grains appear dark in BSE imaging, indicative of the low, locally averaged, mean atomic number of TiC compared to Fe. The complicated microstructure varies as a function of depth into the coating (Figure 4-17b), reflecting the final cool-down sequence of the processed ED coating, with a mixture of equiaxed and banded columnar grains near the surface (Figure 4-17c) and coarse to finely graded equiaxed grains towards the coating/substrate interface (Figure 4-17d). The presence of ~ 21% Fe within the coating (as determined by EDS, see also Table 6-2) is indicative of the extent of intermixing of substrate and tool electrode material. The coating was also characterised by crack formations (*e.g.* Figure 4-17a, arrowed), and the presence

of some significantly larger TiC particles (*e.g.* Figure 4-17d, arrowed), being attributed to unmelted TiC, incorporated into the molten coating during processing.

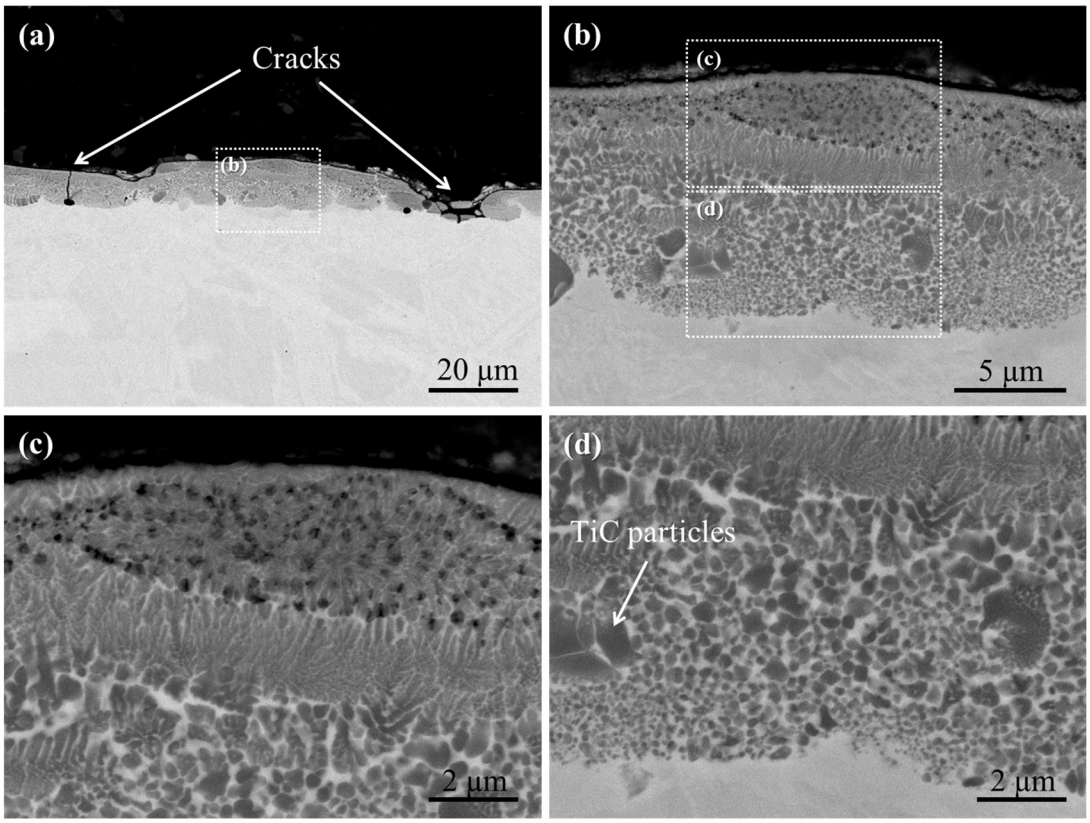

Figure 4-17 Cross-sectional BSE images of a TiC/Fe cermet EDC coating on 304-SS (TiC deposited under conditions of 10 A current and 8 µs pulse-on time), showing the development of a banded, composite microstructure. (a) Low magnification image with inset magnified in (b), and further magnified in (c,d)

Figure 4-18:a-d presents BSE images of the TiC/Fe cermet ED coating (10 A current and 8 µs pulse-on time) on the HSS substrate, showing the development of a similar, irregular, composite microstructure. Again, the microstructure varied with depth into the coating (Figure 4-18b), with local variations of equiaxed and columnar grains reflecting the cool-down sequence of the final intermixed molten layer (Figures 4-18c,d), with ~ 30% Fe within the coating in this instance (Table 6-2). The coating was again characterised by significant crack formations (*e.g.* Figure 4-18a, arrowed).

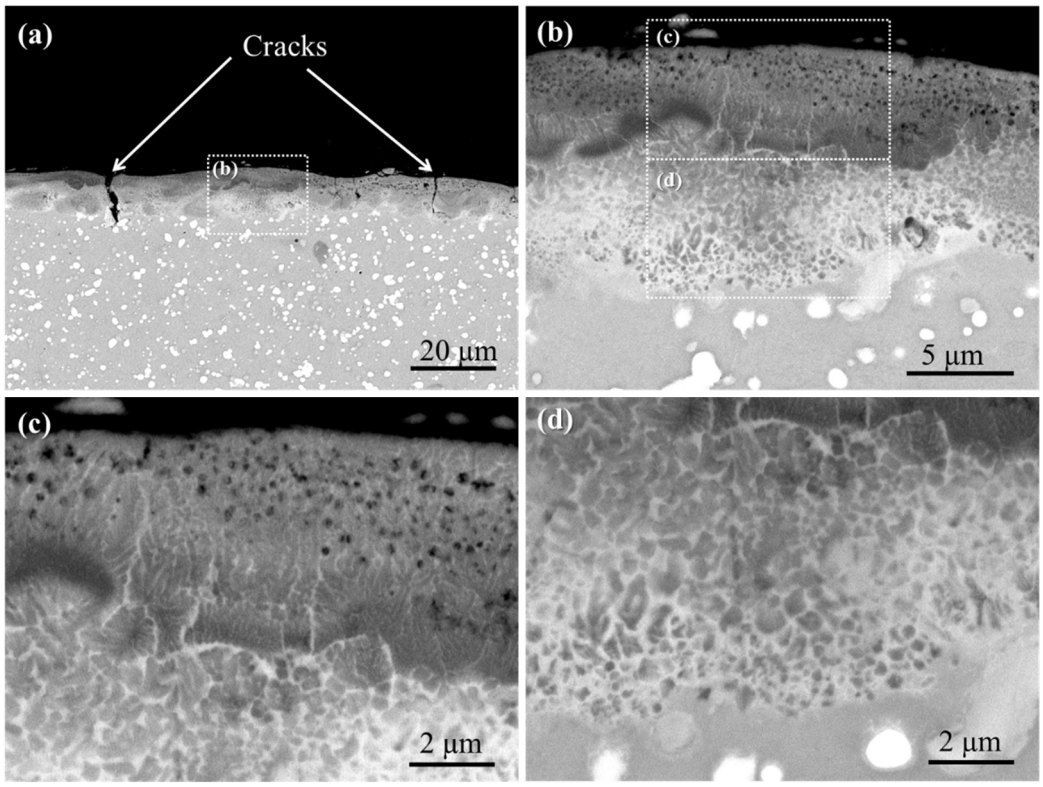

Figure 4-18 Cross-sectional BSE images of a TiC/Fe cermet ED coating on HSS (TiC deposited under conditions of 10 A current and 8 µs pulse-on time), showing the development of a similar, variable, composite microstructure. (a) Low magnification image with inset magnified in (b), and further magnified in (c,d)

Hardness data for TiC coatings (processed at 10 A current and 8 µs pulse-on time) on HSS (~ 2196 HV) were higher than those deposited on 304-SS (~ 1800 HV), reflecting the composite nature of the coatings combined with the low hardness of the as-polished 304-SS (~ 196 HV) as compare to the as-polished HSS (~ 733 HV). It should be noted that some irregular data points, with both high and low hardness values, were obtained during the tests, indicative of extremely localised TiC deposits, i.e. inconsistent coating and porosity (Figures 4-17 and 4-18, respectively).

4.4.2 Processed surface microstructures

Complementary XRD analyses were performed to appraise the crystal structures of the steel substrates, and the EDM and EDC processed samples (Figure 4-19).

Figure 4-19a presents XRD patterns for the as-polished 304-SS substrate, the as-deposited EDC TiC/Fe cermet coating (processed under conditions of 10 A and 8 µs), and a reference EDM surface processed using a Cu tool electrode (again, processed under conditions of 10 A and 8 µs). The diffraction pattern from the 304-SS substrate revealed peaks due to the dominant austenite γ-Fe phase with some martensite α`-Fe. Again, the difficulty of distinguishing between ferrite and martensite phases using the XRD technique is recognised, since both exhibit the same diffraction peaks [122]. The reference surface EDM machined using a Cu tool electrode again showed the dominance of austenite γ-Fe and Fe_3C along with some low intensity peaks due to martensite α′-Fe and Cr_3C_2. The XRD pattern for the developed EDC cermet coating exhibited six dominant peaks consistent with the presence of TiC, demonstrating conservation of TiC particles from the semi-sintered tool electrode into the workpiece surface, along with peaks due to austenite γ-Fe, with signatures of martensite α′-Fe, graphite, Cr_3C_2 and Fe_3C.

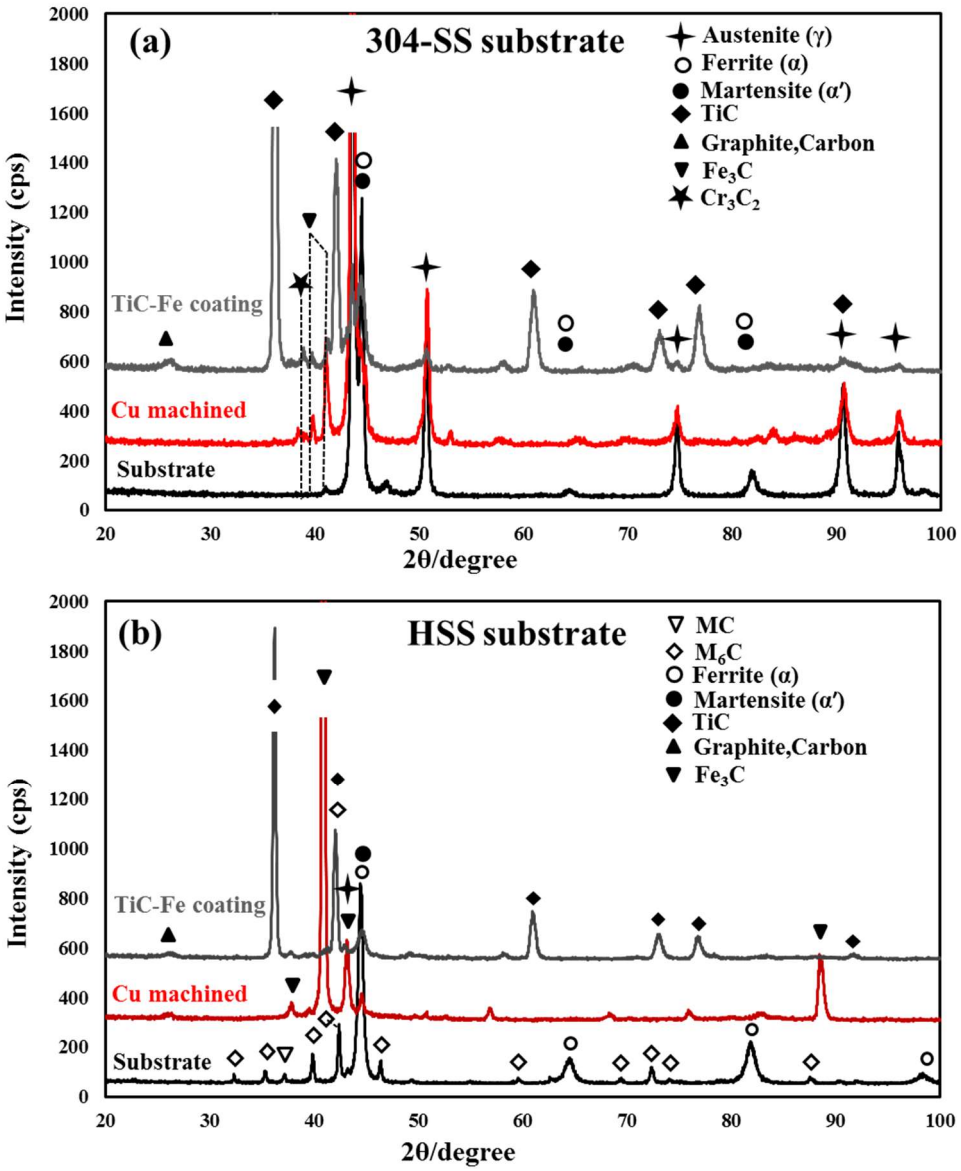

Figure 4-19 XRD patterns for ED processed TiC/Fe cermet coatings on: (a) 304-SS and (b) HSS substrates, along with a reference Cu machined surface

Figure 4-19b similarly presents XRD patterns for the as-polished HSS substrate, the as-developed EDC TiC/Fe cermet coating, and a reference Cu EDM machined surface. In this case, the HSS substrate comprised mainly ferrite α-Fe and M_6C carbide (Fe-Mo-C), with evidence of MC vanadium rich carbide (V-C) peaks. For the case of the reference surface EDM processed using a solid Cu electrode, XRD revealed the dominance of cementite Fe_3C, due to reaction between Fe from the substrate and cracked carbon from the dielectric (hydrocarbon) oil. Minor peaks attributable to

ferrite α-Fe phase or martensite α`-Fe were detected also. No Cu-based phases were detected. EDC samples prepared using the TiC-electrode exhibited dominant diffraction peaks due to the TiC phase, in addition to a smaller peak attributable to ferrite α-Fe or martensite α`-Fe. A minor peak attributable to graphite was also observed.

4.5 Discussion

The significant variation in the hardness of TiC/Fe nanostructured coatings, as a function of current and pulse-on time, emphasises the importance of EDC process control. Considerable variation in coating topography, composition and fine-scale structure has been revealed, depending on the amount of energy supplied to the surface. Each spark creates a localised melt pool which allows the fusion of TiC from the tool electrode with substrate material, which then rapidly cools and solidifies during the next pulse-off time.

The crater sizes, which ranged from ~ 41 to 96 and ~ 35 to 165 μm (Table 4-2), were found to be dependent on input energy which increases with increasing current and pulse-on time, respectively, consistent with related work [124]. All samples were processed for 60 minutes, with the total area of coating being 2 cm^2. The total number of sparks to cover the coated surface, assuming no overlapping, was determined by dividing the total coating area by the single crater area, equating to ~ 9.4 x 10^3 to 208 x 10^3 craters. The total number of sparks during processing was determined by dividing the total processing time (60 minutes) by the single discharge time (pulse-on, pulse-off and ignition delay time), yielding a total of ~ 8.6 x 10^6 to 10.1 x 10^6 sparks, equating to a total number of sparks of ~ 48 to 916 for each location (Table 4-3), as determined

by dividing the total number of sparks during processing by the total number of sparks to cover the surface.

These calculations covered the range of processing currents, on-times and off-time used here, in addition to an estimated value for the ignition delay time, taken as ~ 100 μs [125]. The key point is that every part of the workpiece surface experienced the repeated creation of many localised melt pools and solidification events, from this multiple sparking EDC process, to create a continuum cermet TiC/Fe coating. It should be noted that the SE images revealed the distribution of individual craters, corresponding to the final sequence of sparks as the plasma bombarded the workpiece surface [126] (Figures 4-4 and 4-5). It is considered that the clustered distribution of craters reflects pathways of least resistance to sparking, arising from localised difference in electrical conductivity of the substrate, but statistically this variability promotes uniform coverage of the workpiece surface.

Table 4-3 Estimate of the total number of sparks experienced by each location during the EDC process (1 h), emphasising that every location undergoes repeated melt pool formation and solidification, to create each continuum TiC/Fe cermet coating

	Current / A						Pulse-on time / μs					
	2	6	10	14	19		2	4	8	16	32	64
Total number of sparks to cover surface (x 10^3)	152	71	54	37	28		208	78	54	22	23	9.4
Total number of sparks during process (x 10^6)	9.9	9.9	9.9	9.9	9.9		10.1	10.0	9.9	9.7	9.3	8.6
Total number of sparks per location	65	140	185	267	358		48	128	185	435	409	916

Surfaces produced with the lowest current (2 A) or lowest pulse-on time (2 μs), *i.e.* low input energy, exhibited the lowest number of voids and cracks (Figures 4-4b and 4-5a). In particular, the size of the craters was found to increase with increasing current

and pulse-on time (Table 4-2), along with an increased tendency for void and crack formation [34], and a consequent increase, generally, in surface roughness. Again, this reflects the impact of increasing energy into the surface, combined with variations in the amount of Ti content retained within the coatings (Table 4-2 and Figure 4-15), and the consequences of rapid cool-down, with differential thermal contraction leading to coating disruption and crack formation [13], localised around crater edges. In addition, it is noted that there is a significant difference in the melting point of the coating and the substrate material, with the melting point of TiC (~ 3430 K) being slightly higher than the boiling point of iron (~ 3023 K), and hence Fe remains molten whilst TiC becomes recast during the initial stages of cermet solidification [42]. The associated effect of porosity formations (Figures 4-4 and 4-5) may be attributed to the expulsion of gas bubbles to the surface from molten material during solidification [127].

The significant variations in coating hardness (Figures 4-15a,b), as a function of increasing current and pulse-on time, may be attributed to variations in the Ti wt% (and hence TiC) content [33, 43], within the developed coatings (Figures 4-15a,b), rather than due to trends in the grain size. The lowest values of hardness were returned for conditions of low current, but even current conditions of 6 A produced a coating ~ 4 times harder than the substrate [43]. Maximum values for hardness were achieved using the highest processing current of 19 A, being ~ 8 times harder than the substrate. However, these layers showed the highest levels of cracking and void formation which are undesirable. Progression into the regime of higher pulse-on times, and even higher processing energy conditions, led to a reduction in coating hardness, attributable primarily to a reduction in the Ti (TiC) content, combined with increased carbon incorporation.

Figures 4-20a,b present plots of calculated energy associated with each set of processing conditions, as a function of increasing current and pulse-on time, respectively. Theoretical process energies were simply determined using the following equations:

$$E = P \times t \qquad (4\text{-}1)$$

$$P = V \times I \qquad (4\text{-}2)$$

Where E is electrical energy (Joule), P is power (Watt or Joule/second), t is time (second), in this case is the pulse-on time, and V and I are voltage and current, respectively.

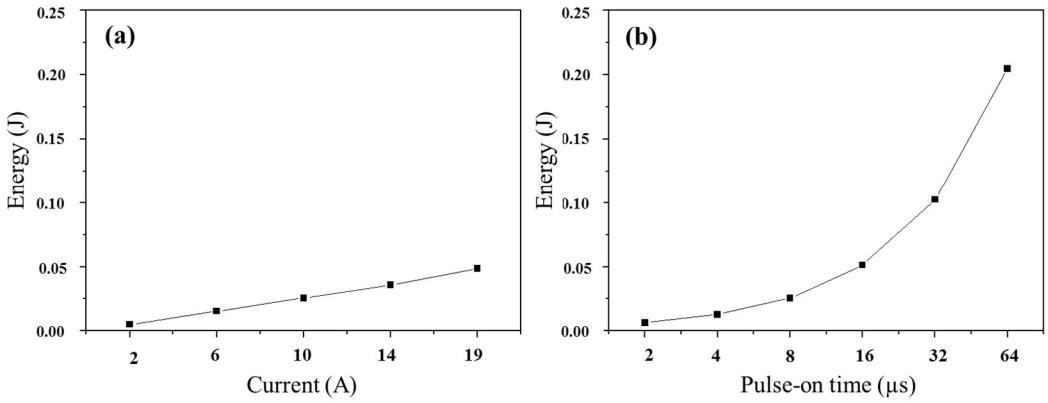

Figure 4-20 Calculated input energy as a function of: a) current (A); and b) pulse-on time (μs)

The suggestion, therefore, is that high energy conditions equate to a case of 'over-processing' and that reduced conditions of current and pulse-on time are desirable for optimised material functional properties, in this case hardness, free of the deleterious effects of cracking and void formation. In this context, it is recognised that the amount of transformed TiC can be defined by controlling the process parameters of discharge current and pulse-on time [42]. For the TiC/Fe system reported here, the data suggests preferred EDC process parameters towards 10 A current and 8 μs pulse-on time.

The characterisation data revealed a range of further interesting insights into the development of these cermet coatings. XRD analysis demonstrated the presence of predominantly austenite γ-Fe austenite and some martensite α`-Fe within the as-polished 304-SS substrate, and comparable levels of martensite compared to austenite within the cermet coatings, being indicative of the rapid cooing rates associated with the EDC process. Further, the XRD data demonstrated the TiC grains within the coating were significantly smaller than those within the tool electrode, consistent with the TiC material transported to the coating layer achieving a fully molten state prior to solidification. This description of the complexity of the cermet coating is reinforced by the TEM investigation of the sample processed under intermediate conditions of 10A and 8 μs, demonstrating the complex size distributions and aspect ratios of these nanostructured TiC grains within these coatings [35], reflecting the directions of solidification and grain growth during rapid cooling.

Figure 4-21 presents a schematic illustration of the resultant TiC/Fe ED coating produced under conditions of 10 A current and 8 μs pulse-on time, showing the development of a cermet coating with very fine equiaxed grains, with a transition towards columnar grains near the coating surface, and relatively coarse equiaxed grains towards the coating/substrate interface. Indeed, the fine details of the microstructures of the coatings, viewed in cross-sectional geometry, on both steel substrates (304-SS and HSS) (Figures 4-17 and 4-18) indicated that TiC precipitates from the Fe, Ti and C containing melt pool during the cool-down [128, 129]. The sizes and geometries of the TiC particles were variable, depending on depth into the coating, reflecting differences in the localised cool-down conditions.

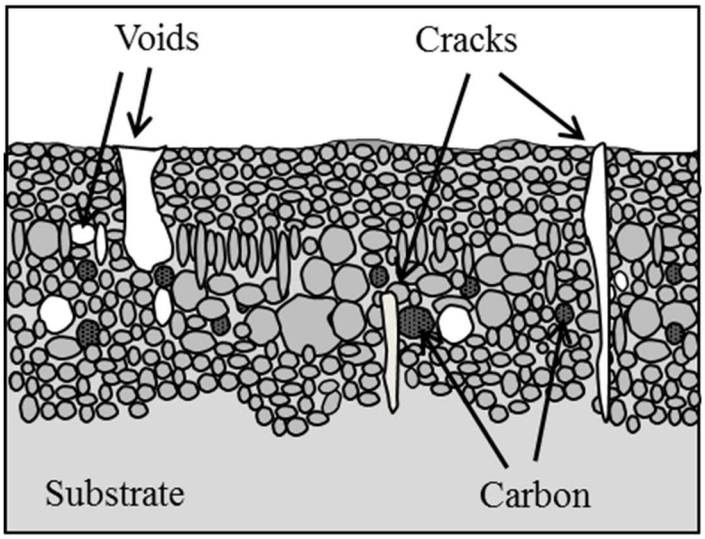

Figure 4-21 Schematic of the resultant TiC/Fe ED coating microstructure, under conditions of 10 A current and 8 µs pulse-on

The XRD and EDS data indicated a reduction in TiC content within the developed coatings, with increasing pulse-on time, and an associated increase in carbon content from the cracked dielectric oil under higher energy processing conditions. With reference to the binary Ti-C phase diagram (Figure 3-1), carbon concentrations between 10 - 19.3 wt% C constitute primary TiC during solidification, *i.e.* TiC is stable over a wide range of compositions. When the carbon content exceeds 19.3 wt%, graphite begins to form and this effect was seen here for the case of high energy processing conditions, with the formation of graphite (Figures 4-7 and 4-8) and small regions of amorphous carbon (Figures 4-10 and 4-11), based on XRD and TEM data, respectively. The small peaks in the XRD data, attributable to the presence of minor levels of Cr_3C_2 and Fe_3C, were at levels unlikely to affect the functional properties of these cermet coatings.

The TiC-rich particles (Figure 4-4b) identified on the processed surfaces under conditions of low current were attributed to partially melted TiC deposited directly from the tool electrode, also resulting in non-uniformity of TiC within the coating.

Conversely, the surface particles (Figure 4-6b) formed under high pulse-on conditions were found to be very C-rich and hence attributed to TiC particles alloyed with cracked C from the dielectric fluid.

It is noted that there was a trend of increasing cermet coating layer thickness with increasing input energy into the surface (Figures 4-13 and 4-14). This is consistent with the observation of increased recast layer thickness in EDM processed materials, with increasing current and pulse-on condition [26]. Further, it has been reported that increased pulse-on time results in both increased residual stress and recast layer thickness which can promote crack formation [130], consistent with the observations made here.

It is recognised that the processing conditions for the EDC technique will need to be optimised for any particular materials system and perhaps geometry. Nevertheless, there are a number of important trends emerging from this investigation, all of which point towards the benefits of low energy processing conditions, for a wide range of wear and corrosion resistant coating applications.

4.6 Summary

TiC/Fe cermets have been produced successfully on HSS and 304-SS substrates using the electrical discharge coating (EDC) process with a semi-sintered TiC tool electrode. The as-deposited coatings exhibited complex, TiC/Fe cermet microstructures, with a mixture of fine equiaxed and banded columnar grains near the surface, and coarse to finely graded equiaxed grains towards the coating/substrate interface, reflecting the final cool-down sequence of ED processing. The data indicate that TiC precipitates from the melt pool during the process of solidification, with coarser carbide likely to be primary TiC precipitates, whilst finer grains didn't have sufficient time for

substantial grain growth due to the effects of rapid cooling. A continuum cermet layer coverage was achieved following a sequence of repeated localised melt pool formations. Further, the data has demonstrated the variable hardness of these nanostructured EDC coatings, related primarily to variation in the TiC content within the developed coatings which contained complex intermixtures of TiC, austenite γ-Fe, martensite ά-Fe and graphite/amorphous carbon, along with trace levels of Cr_3C_2 and Fe_3C, reflecting input energy and the high cooling rates. It became evident that EDC coatings can become over-processed under conditions of high input energy, being characterised by increased levels of void formation and cracking around crater edges, along with reduced levels of TiC incorporation and increased levels of carbon from cracking of the dielectric oil. Hence, the suggestion is for the use of reduced energy conditions for processing, with preferred EDC process parameters for this particular materials system being 10 A current and 8 μs pulse-on time. Thereby promoting good levels of hardness and a surface finish with reduced levels of voids and cracks.

5 Modelling and characterisation of single spark interactions

5.1 Introduction

It is difficult to measure the energy distribution to the anode, cathode and dielectric fluid from the ED spark process, with temperature and cooling rate directly influencing microstructural development, and hence the physical properties of the modified surface. In this chapter, a 2D transient heat transfer model is developed to predict the amount of energy transferred into the workpiece during the EDC processing of cermet coatings, and validated via comparison with experimental observations as well as data in literature. 2D transient heat transfer principles are solved by the finite difference method and performed using MATLAB software. Interpolation, based on current and pulse-on time, allowed the plasma radius and Gaussian heat flux distribution into the workpiece to be predicted. In addition, the model allows for fundamental interactions between energy source and workpiece during EDC processing to be explored, with consideration of original coating/workpiece material properties enabling predictions of coating layer thicknesses and microstructural rearrangements to be made upon the associated rapid cooling phase.

The theoretical model for single discharge events during EDC processing is developed to include both the heating phase (pulse-on time) and the cooling phase (pulse-off time). The governing equations, with associated boundary conditions, for the heating source and plasma channel of the system are described initially. The program flow chart and gap condition measurements are then described, leading to model results with emphasis on the amount of energy transferred into the workpiece,

the heat distribution, coating layer thickness and cooling profile, correlated with the nano-scale microstructure development within an ED crater.

5.2 Process modelling and simulation

A simple and comprehensive model is now presented to help explain single spark interactions during ED processing. Energy is imparted into the workpiece from the plasma channel, with material on the scale of the plasma channel diameter experiencing a rapid heating and cooling phase, during pulse-on and pulse-off times, respectively.

5.2.1 Heating phase

5.2.1.1 Governing equations and boundary conditions

A two dimensional, axisymmetric, transient heat transfer model was developed, to facilitate improved understanding of electro-thermal heating for a single discharge incident upon a workpiece surface. The finite difference domain was defined with dimension 3 x 1.5 times the crater radius, in both the x and y directions, respectively; with a uniform square mesh of grid spacing $\Delta x = \Delta y = 0.5$ μm. Figure 5-1 illustrates the Gaussian heat distribution and interaction with the workpiece, along with the associated boundary conditions used for the analysis (see Appendix 2 for more details of boundary conditions). The initial temperature T_s of the workpiece is taken as ambient temperature; the material properties of the electrodes and dielectric are considered temperature-independent; and the time increment is set at $\Delta t = 10^{-8}$ s.

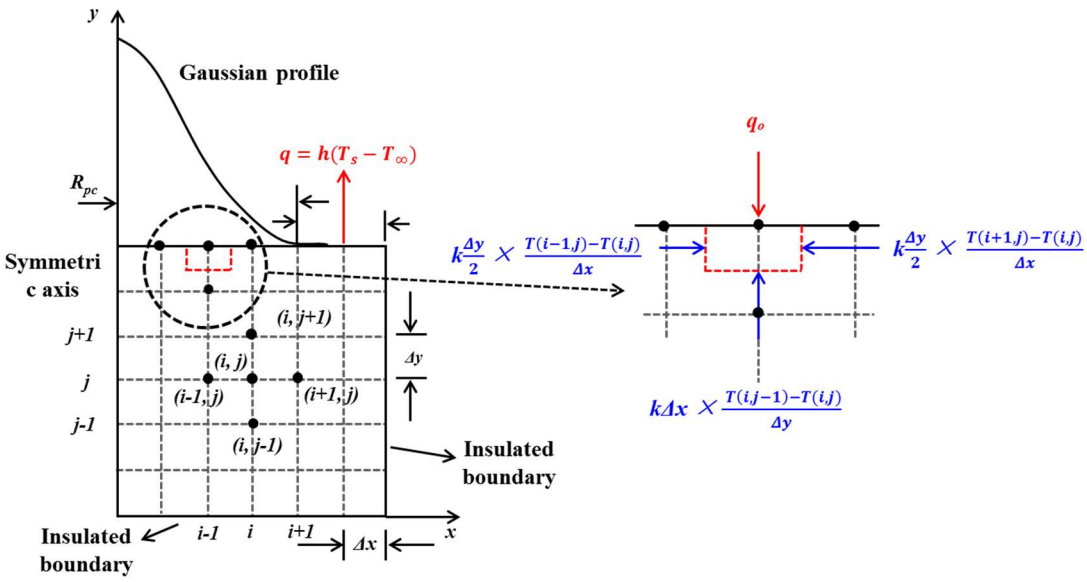

Figure 5-1 Gaussian profile heat source and boundary conditions with the workpiece, including interior node and expanded view of a top surface boundary node

Conduction without heat generation is considered the main mode of heat transfer between a plasma channel and workpiece, *e.g.* as shown by Kansal *et al.* [131] as well as Joshi and Pande [54], although some heat loss from the top surface of the workpiece is anticipated due to convective flow of the dielectric fluid, which is considered in more detail during the 'Cooling phase' (Section 5.2.2). For simplification, radiative heat losses are neglected here.

The governing Fourier heat conduction equation, taking into account the boundary conditions, is given by:

$$\frac{\partial^2 T}{\partial x^2} + \frac{\partial^2 T}{\partial y^2} + \frac{\partial^2 T}{\partial z^2} = \frac{1}{\alpha}\frac{\partial T}{\partial t} \qquad (5\text{-}1)$$

Where T (K) represents temperature, and x and y are Cartesian coordinates, used to represent radial distance from the centre of the crater, and distance below the specimen surface, respectively; t represents time (*i.e.* pulse-on time); and α represents thermal diffusivity (m^2/s), expressed as:

$$\alpha = \frac{k}{\rho c_p} \qquad (5\text{-}2)$$

Where $\boldsymbol{k}$ is thermal conductivity (W/m.K); ρ is density (kg/m^3); and $\boldsymbol{c_p}$ is the specific heat capacity (J/kg.K). When the temperature of the workpiece reaches a specified level during processing, some of the crater material melts and evaporates, whilst some of the tool electrode material becomes deposited on the workpiece surface which then re-solidifies. Latent heat is exchanged as a result of this phase transition and hence the term for thermal diffusivity $\boldsymbol{\alpha'}$ requires modification, and is used as in Zhang *et al.* [58]:

$$\boldsymbol{\alpha`} = \frac{\boldsymbol{k}}{\boldsymbol{\rho(c_{p+L_m/T_m)}}} \qquad (5\text{-}3)$$

Where $\boldsymbol{L_m}$ represents the latent heat of fusion (J/kg) and $\boldsymbol{T_m}$ is the melt temperature (K).

5.2.1.2 Heat source

The effective energy transferred into the workpiece is characteristic of the amount of energy available and the shape of the heat distribution profile. It is widely accepted that the plasma heat source during EDM processing approximates a Gaussian distribution, *e.g.* as has been approximated by Das *et al.* [51] and Zhang *et al.* [55] amongst others. The Gaussian distribution of heat flux is given by:

$$\boldsymbol{q(r) = q_0 e^{\left(-n\left(\frac{r}{R_{pc}}\right)^2\right)}} \qquad (5\text{-}4)$$

With maximum heat flux q_0 (W/m^2) given by:

$$\boldsymbol{q_0 = \frac{4.57\ F_v\ V\ I}{\pi R_{pc}^2}} \qquad (5\text{-}5)$$

Where r is radial distance from the centre of a single spark; R_{pc} is the plasma channel radius; F_v is the fraction of total energy transferred to the workpiece; and V and I are voltage and current, respectively. The exponent n used in equation (5-4) serves to define the Gaussian distribution. The heat flux profile becomes steep when $n < -4.5$ and becomes flat with any increase of n to a value approaching zero [73]. Further, Shen *et al.* [67] reported that the energy distribution was affected by the shape of the electrode, with enhanced energy distributed into the workpiece from a needle-shaped electrode. For the present work, based on the use of a flat electrode, a value of $n = -3$ was selected based on previous studies, for example from Somashekhar *et al.* [132], also in agreement with work of Tao *et al.* [133].

5.2.1.3 Plasma channel

With regard to the difficulties of measuring the plasma channel radius, as reported in literature (Section 2.4.3), and for consistency with other researchers, *e.g.* Das *et al.*[51] as well as the work of Tan and Yeo [53] and Erden [134], the plasma channel radius is assumed to be equal to the crater radius generated by the discharge. Accordingly, an interpolation approach, as a function of MATLAB software, was utilised to estimate the plasma channel radius, based on a wide range of crater measurements as a function of current and pulse-on time (Figure 5-2).

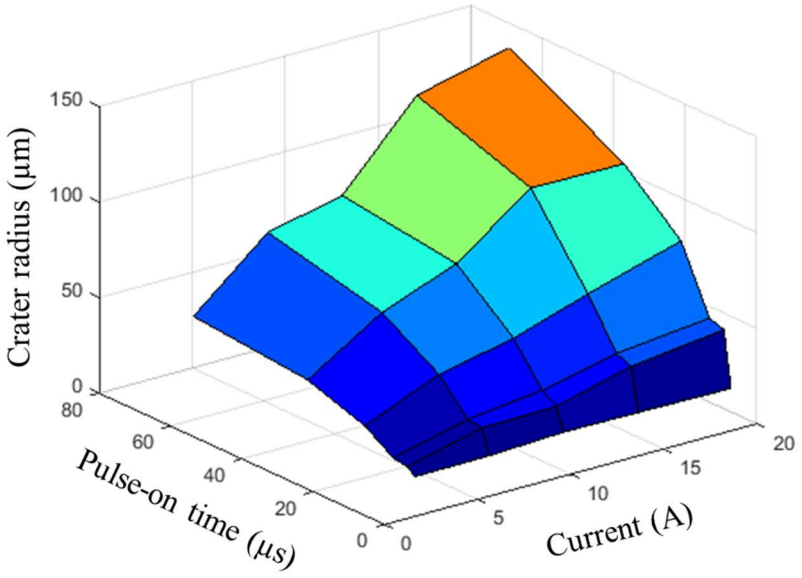

Figure 5-2 Crater radius as a function of current and pulse-on time obtained experimentally (Table 4-2)

5.2.2 Cooling phase

Immediately after the pulse-on time, the plasma channel collapses and is replaced by the dielectric fluid. This is accompanied by a sudden drop in pressure which results in the removal of some of the molten material in the form of debris. A cooling phase (pulse-off time) then proceeds allowing for molten material to cool-down and re-solidify, following renewed contact of the crater surface with the dielectric.

Convection boundary conditions may be applied to the surface through Newton's law of cooling:

$$\boldsymbol{q = h(T_s - T_\infty)} \qquad (5\text{-}6)$$

Where q (W/m^2) is the convection heat flux; T_s (K) is the surface temperature; T_∞ (K) is the dielectric fluid temperature; and h ($W/m^2.K$) is the convection heat transfer coefficient which is a function of fluid properties, geometry, surface roughness and the

fluid flow pattern [135]. In the present work, fluid flow over a flat plate is assumed to be uniform, at constant velocity (Figure 5-3), as given by:

$$\boldsymbol{h} = \frac{\boldsymbol{Nu_x}\, \boldsymbol{k}}{\boldsymbol{L}} \qquad (5\text{-}7)$$

Where L (m) is the workpiece length and $\boldsymbol{Nu_x}$ is the Nusselt number given by:

$$\boldsymbol{N_{ux}} = \boldsymbol{0.644 Re_x^{0.5} Pr^{0.33}} \qquad (5\text{-}8)$$

Where: $$\boldsymbol{Re_L} = \frac{\boldsymbol{\rho\, u_\infty L}}{\mu} \qquad (5\text{-}9)$$

And: $$\boldsymbol{Pr} = \frac{\mu\, \boldsymbol{c_p}}{\boldsymbol{k}} \qquad (5\text{-}10)$$

Where *Re* is the Reynolds number and *Pr* is the Prandtl number, respectively, $\boldsymbol{u_\infty}$ is the velocity of the fluid (m^2/s) and μ is the dynamic viscosity of the fluid (kg/m.s). For laminar flow, it is required that $Re < 5x10^5$ and $0.6 \leq Pr \leq 50$ [135].

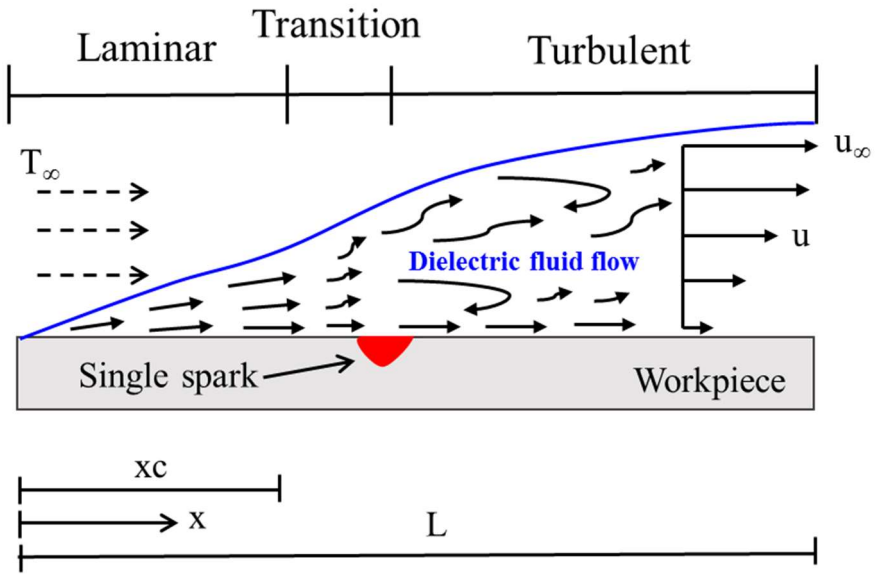

Figure 5-3 Schematic illustrations of fluid flow over a flat plate

5.2.3 Workpiece and tool electrode material properties

In this numerical simulation the material properties of the electrodes were set as input values, with Table 5-1 summarising the properties of the 304-SS workpiece and the TiC tool electrode, respectively.

Table 5-1 Material properties of the workpiece and tool electrode (Granta CES 2009 EduPack data base software)

	Density (kg/m^3)	Thermal conductivity (W/m.K)	Specific heat capacity (J/kg.K)	Latent heat of fusion (J/kg)	Melting point (K)
304-SS	7,905	15	510	272,500	1,698
TiC	4,910	21.5	5,565	1,160,000	3,478

5.2.4 Program flow chart

Figure 5-4 presents a flowchart for this 2D transient heat transfer model, with the program code performed using MATLAB (see Appendix 3 for heating and cooling phase MATLAB code), drawing on the approaches of Xia *et al.* [66] and Zhang *et al.* [58], by comparing experimentally determined with theoretically calculated temperature and crater radii, respectively, to estimate the effective heat transfer into the workpiece during EDC. This approach allows the percentage of energy transferred to the workpiece to be estimated, to be between 0 and 1, stepwise 0.01. Furthermore, the present model allows the workpiece material to be replaced with expressions for a 50:50 composite, based on both workpiece and tool electrode material properties, when every node on the workpiece under the influence of a spark reaches the melting point. In addition, the model is capable of calculating the rate of cooling of each melt pool, produced by a single spark event, which allows for grain size within the coating layer (crater) to be predicted.

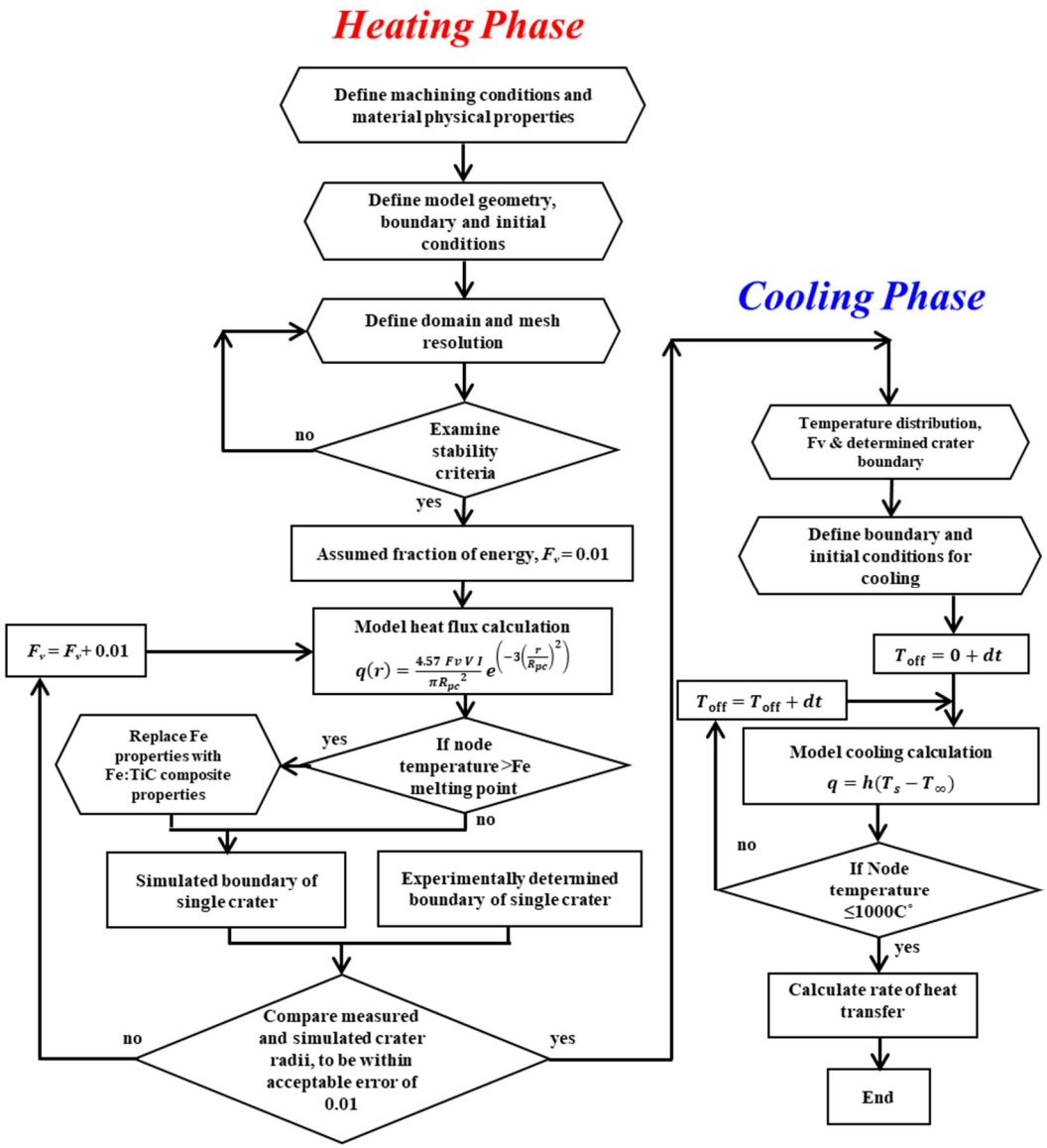

Figure 5-4 Process flow, highlighting the 2D transient heat transfer model

5.3 Results

5.3.1 Gap voltage measurement

The gap voltage was measured experimentally for each set of processing parameters. Figure 5-5 presents examples of open gap voltage waveforms, as measured under three different discharge conditions (constant current of 10 A: and 8, 32 and 64 µs pulse-on times), illustrating details of the rapidly changing voltage (12.5 ns sample interval and

80 Mega samples per second (MS/s) sampling rate). In each case, a capacitor charges until it reaches the discharge voltage, then the voltage drops suddenly to a steady state value at which point discharge occurs, and this value is maintained for the whole duration of the discharge, then decreases when the discharge ceases. The gap voltage was observed to vary in the range 25 - 35 V, for variable conditions of current (2 to 19 A, for a fixed pulse-on time of 8 µs); and variable conditions of pulse-on times (2 to 16 µs, for a fixed current of 10 A). Accordingly, a value of 30 V was used as the gap voltage in the modelling, for the case of these processing parameters. However, it was observed that the gap voltage decreased significantly, with increasing discharge pulse-on times of 32 µs and 64 µs, necessitating adjustment to the modelling voltage to 23 V and 18 V, respectively, in these cases. Furthermore, it was observed that the agitation delay time for discharge varied, for each set of processing parameters.

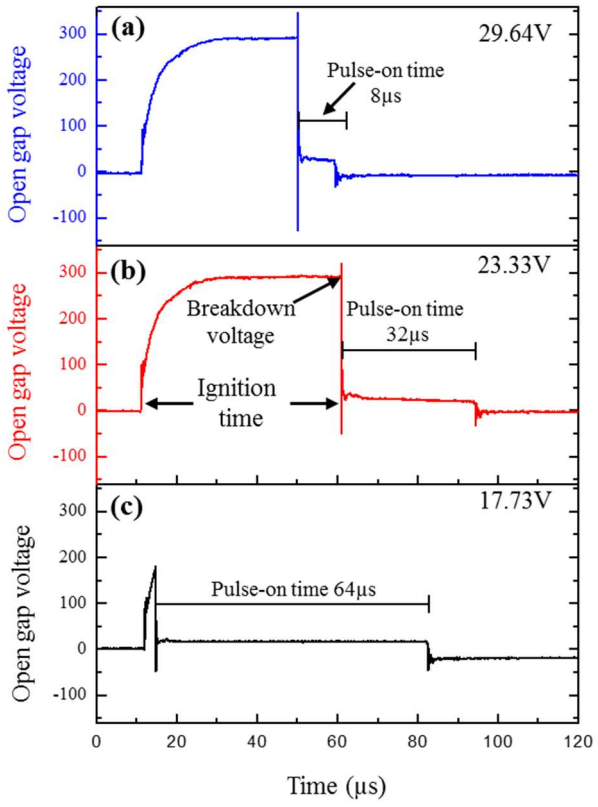

Figure 5-5 Waveforms associated with EDC coatings produced using a TiC tool electrode and a 304 stainless steel workpiece, with negative polarity for pulse-on times of: a) 8 µs, b) 32 µs and c) 64 µs (fixed 10 A current)

5.3.2 Code validity and fraction of energy transferred to the workpiece

Figures 5-6 and 5-7 presents a comparison of the fraction of energy transferred to the workpiece during EDC processing, as predicted by the present model (red lines), based on estimates for F_v obtained during EDM processing, as reported by Singh [64] (blue lines) and Shabgard and Akhbari [136] (black lines), as a function of increasing current and pulse-on time. The energy distribution ratio into the workpiece varied between 17% and 23% with increasing current (fixed pulse on-time of 8 μs), whilst a significant increase in the amount of energy transferred to the workpiece, up to ~ 50% was associated with an increase in pulse-on time (fixed current of 10 A). The high increase in fraction of energy transferred, for pulse on conditions of 32 and 64 μs, might be attributed to the drop in gap voltages, to 23 and 18 V, respectively. Overall, the values of F_v are in good general agreement with previous reports such as Singh [64] and Shabgard and Akhbari [136], but are slightly higher, which probably reflects the differences in the EDC mechanisms of surface modification, as workpiece material is replaced/alloyed with tool electrode material, being distinct from material removal during EDM processing. It is also acknowledged that the current work uses a reverse polarity with an anode workpiece, as distinct from a cathodic workpiece as used in the work referenced. The disparity in energy balance between polarity types may contribute the difference in results shown (Figures 5-6 and 5-7). Similarly, Shen *et al.* [67] reported that polarity has a significant effect on the energy distribution, with more energy transferred into the anode than into the cathode workpiece.

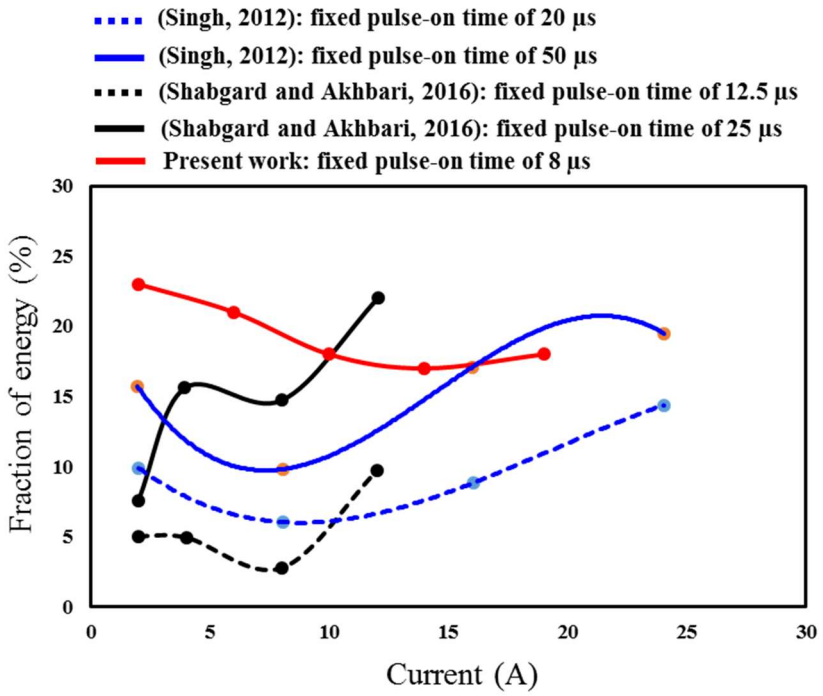

Figure 5-6 Fraction of energy transferred to the workpiece as function of increasing current, compared to literature (Singh, 2012 [64]) and (Shabgard and Akhbari, 2016 [136])

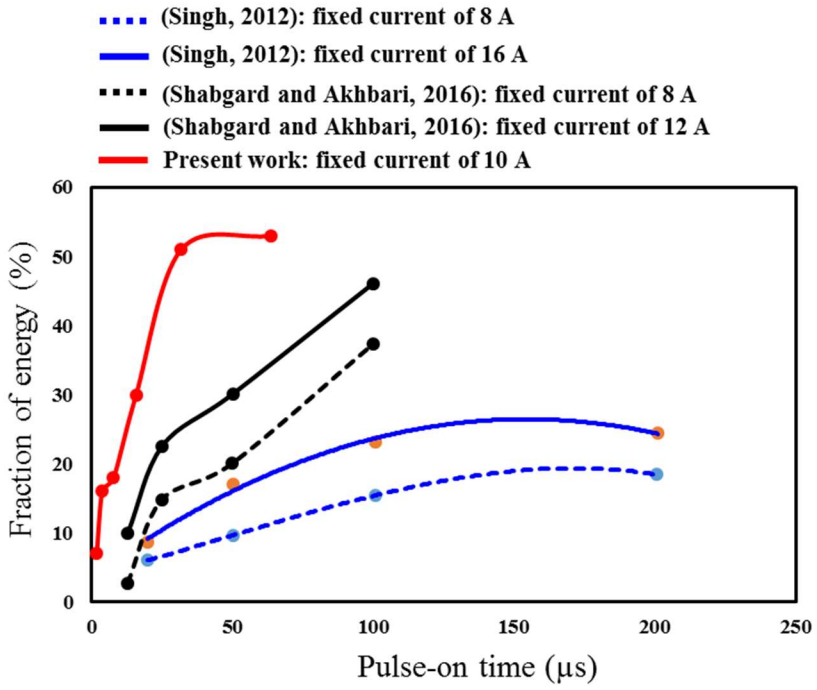

Figure 5-7 Fraction of energy transferred to the workpiece as function of increasing pulse-on time, compared to literature (Singh, 2012 [64]) and (Shabgard and Akhbari, 2016 [136])

5.3.3 Heat distribution

Simulated results for temperature distribution into the workpiece, as a consequence of single spark events, as a function of increasing current and pulse-on time, are shown in Figure 5-8. The minimum temperature attained was determined to be ~ 13,000 K under low energy processing parameters (*i.e.* 2 A / 8 μs and 10 A / 2 μs). With increasing current (4 to 19 A, for fixed pulse-on time of 8 μs), the temperature was found to vary between ~ 17.5 x 10^3 - 20 x 10^3 K; whilst for increasing pulse-on time (8 to 64 μs, for a fixed current of 10 A), temperatures of ~ 20 x 10^3 K reducing to ~ 16 x 10^3 K were achieved.

The highest temperature established at the centre gradually decreased with distance from the origin (dotted white line (Figure 5-8)), reflecting the Gaussian distribution of the heat flux equation. Hence, maximum energy was transferred at the centre, with decreasing power density towards the periphery. The dashed white line represents the consequent boundary of molten material with the bulk substrate. It is considered that the neighbouring workpiece surface that does not interact directly with the plasma channel is largely unaffected, due to short pulse-on time, and hence does not change significantly in temperature.

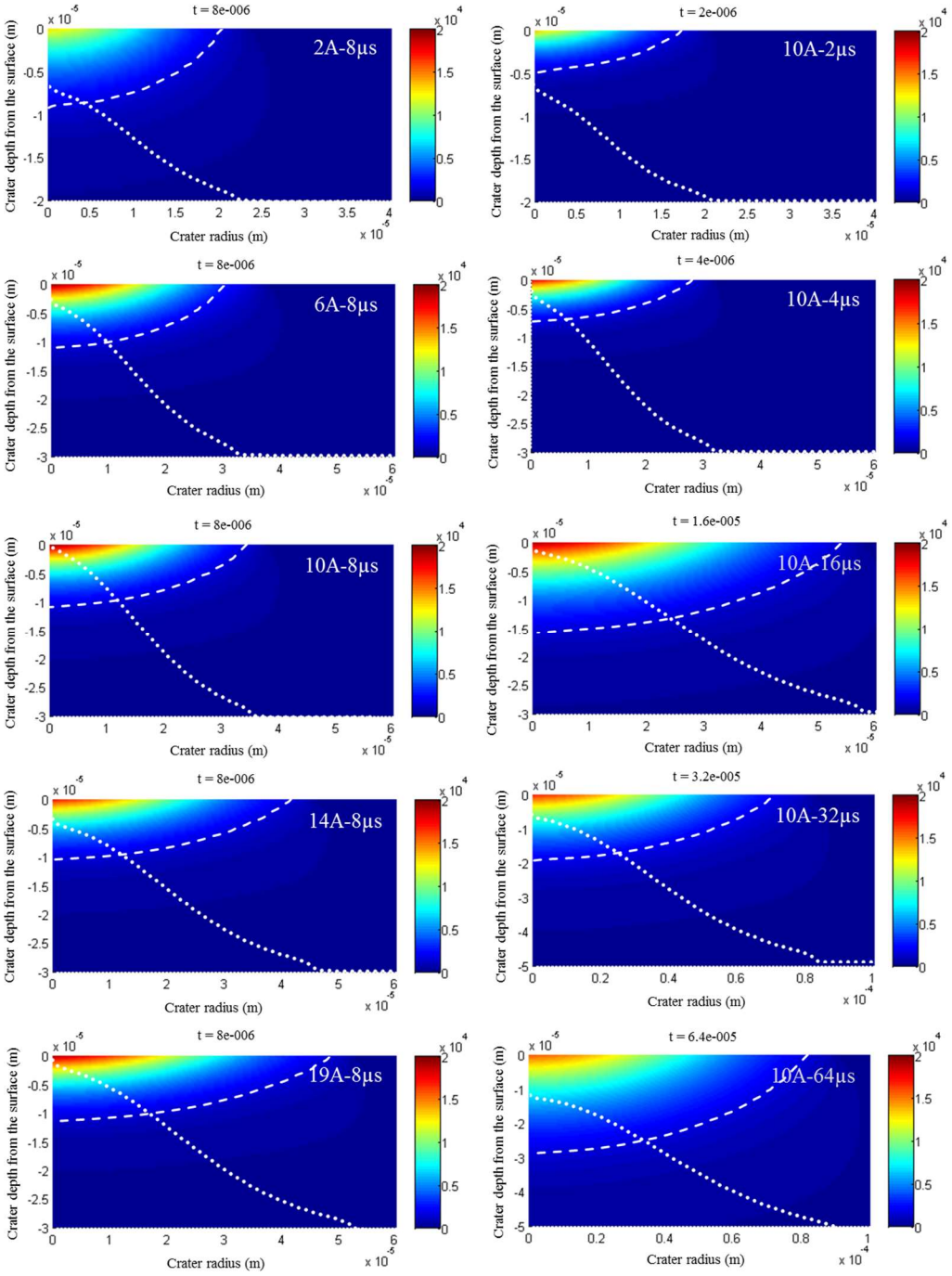

Figure 5-8 MATLAB simulations showing heat distribution into the workpiece at the end of the 'pulse-on' stage; along with the temperature distribution across the top surface (dotted white line) and the boundary of molten material with the bulk substrate (dashed white line)

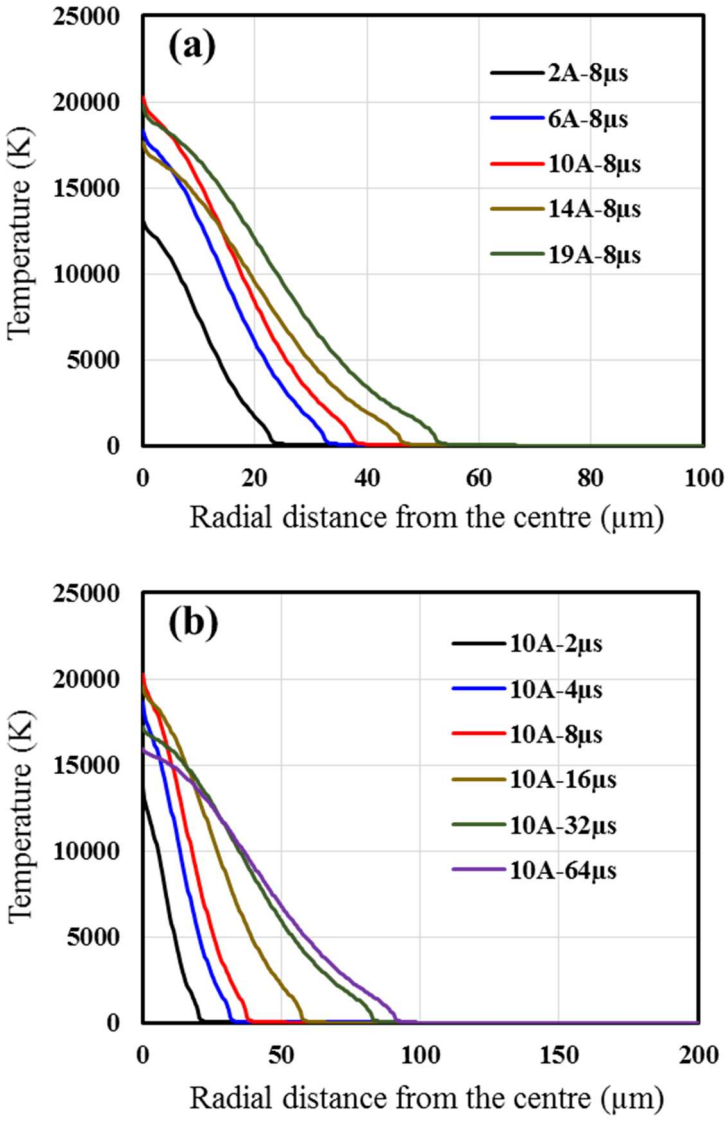

Figure 5-9 Radial temperature profiles along the top surface of the workpiece as functions of: a) increasing current; and b) pulse-on time

Figures 5-9a,b (extracted from Figure 5-8) present simulated temperature profiles across the top surface of the workpiece as a function of current and pulse-on time, respectively, demonstrating increases in the size of the heat affected region with increasing the current and pulse-on time, however, maximum temperature does not have the same trend, reflecting the increasing size of the plasma channel. A similar effect was reported by Xie *et al.* [52] for EDM simulations of Ti-alloys.

5.3.4 Crater diameter

Representative craters for each set of processing parameters were identified using SEM (Figure 5-10) with sizes reported based on an average of 30 measurements, as determined using ImageJ, Table 5-2. The edges of individual craters produced by discrete spark events could be readily identified. Overlapping craters and craters created from abnormal discharges were discounted. Average crater sizes ranged from 41 to 96 μm with increasing current from 2 to 19 A (fixed pulse on-time of 8 μs); and from 35 to 165 μm with increases in the pulse-on time from 2 to 64 μs (fixed current of 10 A), which reflects the general trend of increasing input energy (Figure 4-20).

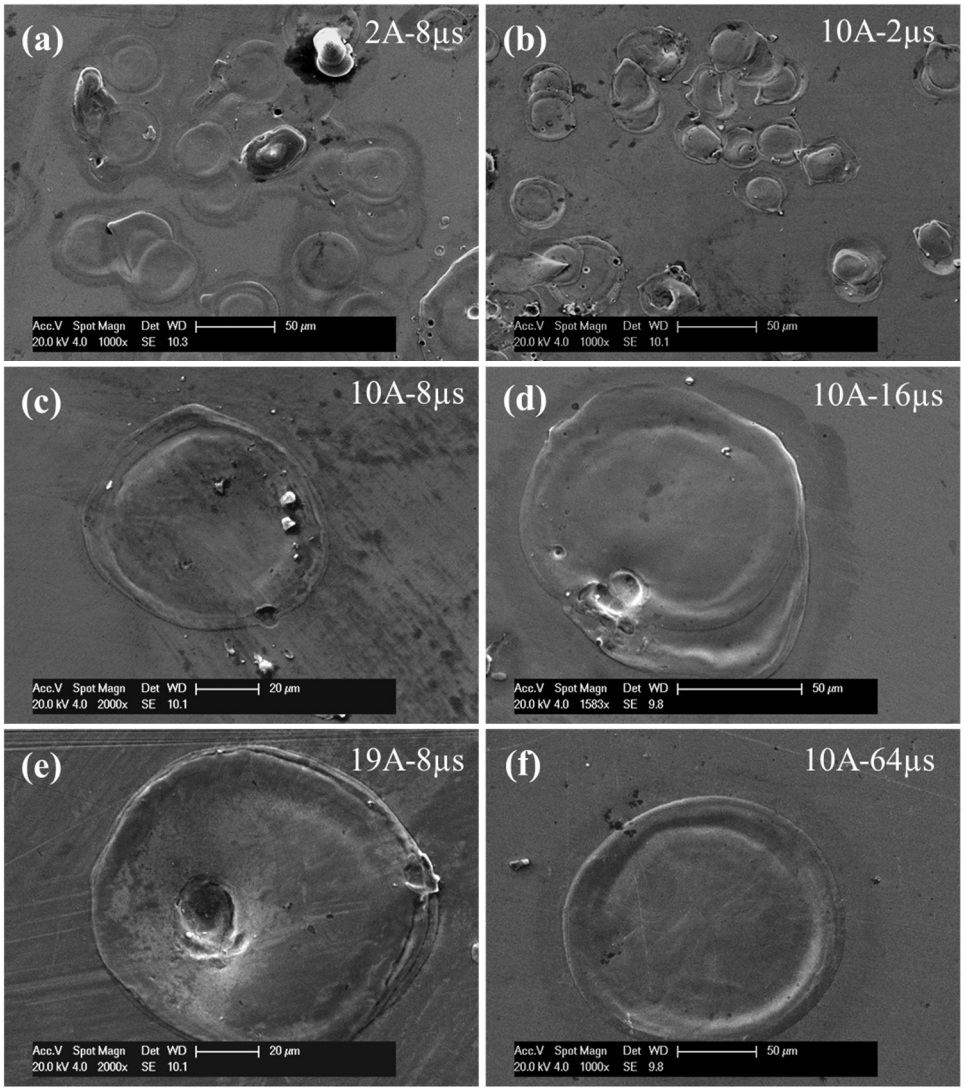

Figure 5-10 Plan view SE images of craters created from single spark events, at the start of template coating. Average crater sizes increased with increasing discharge energy

Table 5-2 Average crater sizes (n = 30) as a function of processing conditions

	Current / A						**Pulse-on time / µs**					
	2	6	10	14	19		2	4	8	16	32	64
Mean crater size / µm	41	60	69	83	96		35	57	69	107	151	165
σ	*4.3*	*4.7*	*5.0*	*8.6*	*8.7*		*5.6*	*11.8*	*5.7*	*7.8*	*14.3*	*16.5*

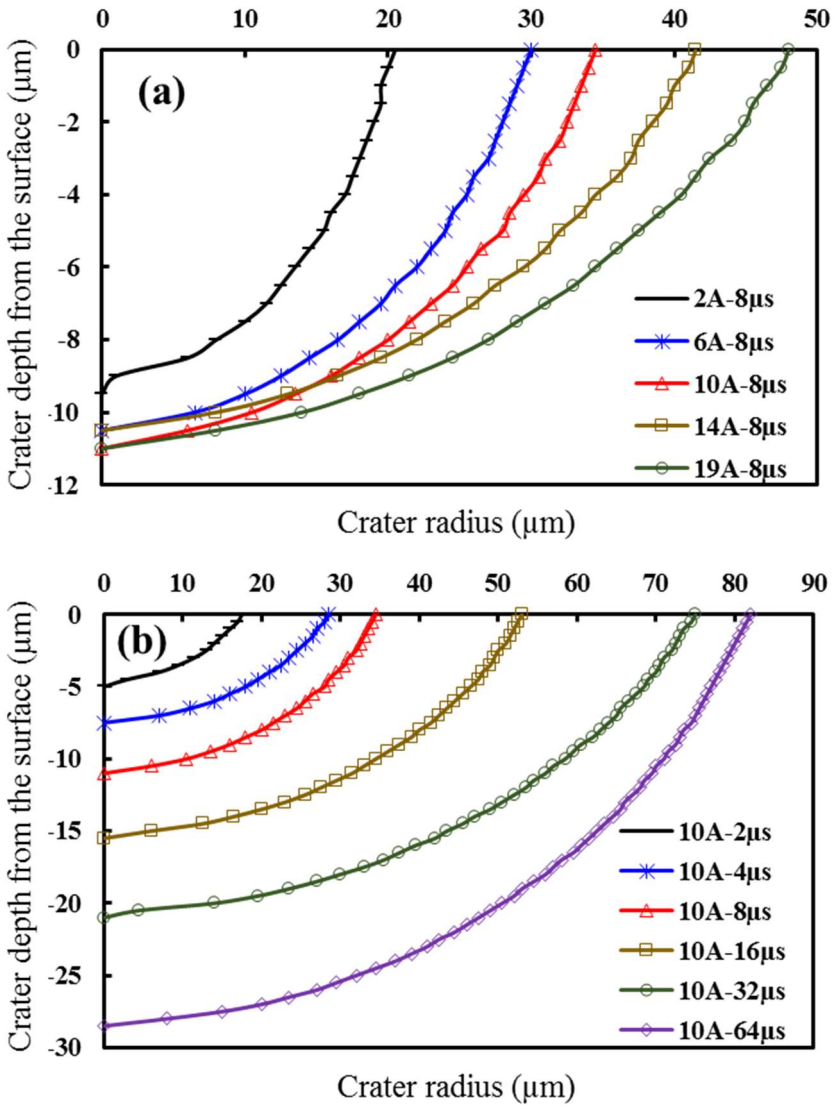

Figure 5-11 Simulated crater boundaries into the workpiece as a function of increasing a) current; and b) pulse-on time

Simulated crater profiles, delineating the boundary between the melt pool and the bulk workpiece, as a function of current and pulse-on time, are presented in Figures 5-11a,b (extracted from Figure 5-8). The crater diameter was predicted to increase significantly with increasing current (for fixed pulse on time of 8 µs), but without significant change in melt pool depth (Figure 5-11a); whilst increasing the pulse-on time (for fixed current of 10A) resulted in an increase in both crater width and depth (Figure 5-11b) [137].

5.3.5 TiC distribution and cermet layer thickness

Figure 5-12 presents representative high magnification BSE images of EDC processed samples in cross-section geometry, providing detailed insight into the microstructural development of the coatings, confirming the formation of a metal matrix composite (MMC) of variable TiC/Fe composition, as a function of processing conditions (cf. Figures 4-9, 4-10 and 4-17). Localised compositions, as determined by EDS, are summarised in Table 5-3 (Figures 5-12b (1-3) and 5-12e (4-6)). Regions of enhanced TiC (Figures 5-12b,e (arrowed)), originating from the tool electrode, appear dark (locally averaged composition) within such BSE images, due to the lower atomic number of Ti compared to Fe. Coatings produced under the low energy conditions of 2 A (8 µs) and 10 A (2µs) showed a non-uniform distribution of TiC throughout the coating (Figures 5-12a,b), with a high amount of Ti ~ 39 wt% in region 2 compared to a low amount of Ti ~ 6 wt% in region 1 (Figure 5-12b and Table 5-3), reflecting a lower level of intermixing between workpiece and transferred tool electrode material. Coatings produced under conditions of increasing current (10 - 19 A for a fixed pulse-on time of 8 µs) exhibited a higher amount and more regular distribution of TiC throughout the coating, but with a much more complicated, intermixed microstructure (Figures 5-12c,e,g), being attributable to the electrode condition, the complexities of the melting mechanism, material re-deposition and cool-down process.

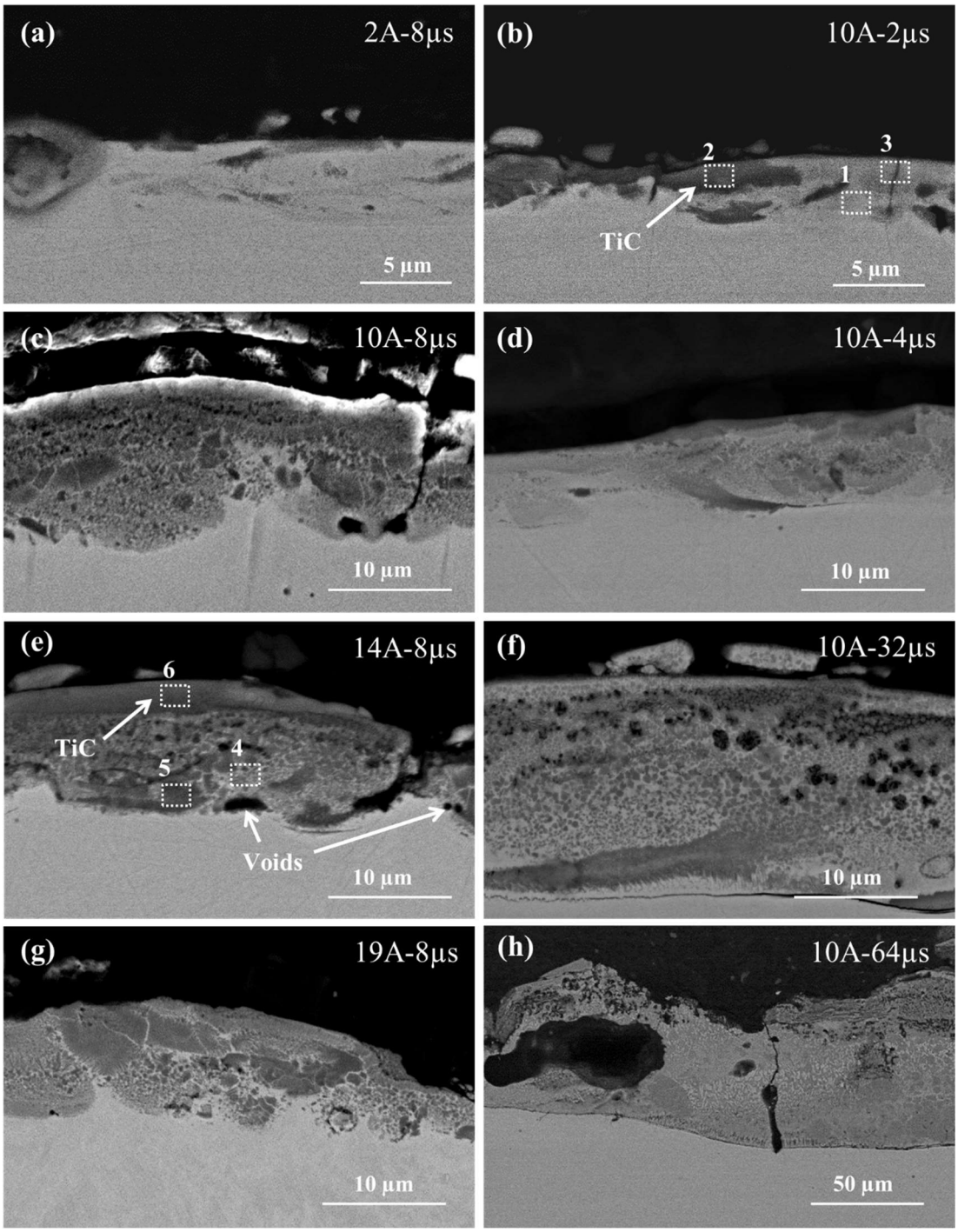

Figure 5-12 SE images of EDC processed coatings, viewed in cross-section: (a,c,e,g) for fixed pulse-on time of 8 µs as a function of increasing current; and (b,d,f,h) for fixed current of 10 A as a function of increasing pulse-on time. (b:1-3; and e:4-6) Representative regions for localised composition, determined by EDS, as summarised in Table 5-3.

Table 5-3 Localised cermet coating compositions as determined by EDS (Figures 5-12b,e)

	Element (wt%)					Element (wt%)			
Fig 5-12b Region	**Ti**	**Fe**	**C**	**Cr**	***Fig 5-12e Region***	**Ti**	**Fe**	**C**	**Cr**
1	6.17	61.75	13.29	14.62	***4***	32.19	35.81	18.73	10.17
2	38.77	11.63	33.60	7.72	***5***	37.53	25.06	17.78	8.96
3	21.42	40.64	27.59	7.48	***6***	56.79	7.13	32.27	3.81

Simulations of crater formation from single spark events during EDM processing provide information on material removal rate and the thickness of the recast layer, to help refine the process. Similarly, simulations of single spark events during EDC processing, as performed here, provide for improved understanding of crater development and the layer formation process, in terms of resultant microstructure and thickness. Figure 5-13 presents a comparison of simulated crater depths from single spark events, with experimentally determined EDC layer thicknesses (after 60 minutes of processing, corresponding to the overlap of ~ 185 spark events per location (Table 4-3), as a function of increasing current and pulse-on time. The key point being that there is a strong correlation between crater depth and developed coating thickness, consistent with EDC being a sequential replacement process for near surface material. A slight increase in simulated crater depth with increasing current (2 - 10 A) was returned (Figure 5-13a), reflecting a fairly consistent fraction of energy into the workpiece (Figure 5-6); whilst increasing the pulse-on time led to a significant increase in crater depth, commensurate with an increase in layer thickness (Figure 5-13b), reflecting the increased energy imparted to the workpiece (Figure 5-7). It is noted that crater depth and layer thickness followed a very similar trend with increasing pulse-on times from 2 to 16 μs, whilst there was a higher discrepancy between simulated and experimentally determined values for longer pulse-on times of 32 and 64 μs, reflecting a greater variation in crater sizes under higher energy processing conditions.

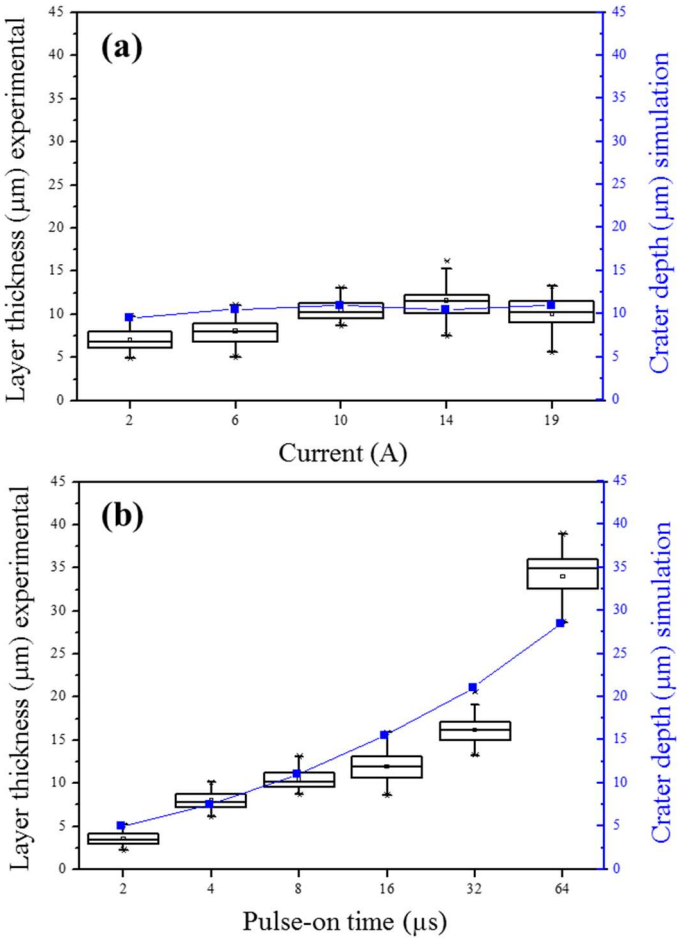

Figure 5-13 Comparison of simulated crater depth from a single spark event with experimentally determined EDC layer thicknesses, as function of increasing current and pulse-on time

5.3.6 Cooling phase and coating microstructure development

Figures 5-14 and 5-15 present more detailed BSE images of the Fe/TiC cermet coatings, produced under conditions of 8 and 64 µs (fixed current of 10 A), respectively, in order to illustrate the variability of the fine scale microstructure. For the former (10A, 8 µs), the microstructure comprised a band of very fine grained material at the surface (Figure 5-14b Region I); a thin, transitional region of columnar grains (Figure 5-14c Region II); a band of equiaxed, coarser TiC grains within the Fe matrix (Figure 5-14c Region III); and another band of very fine grained material next to the coating/substrate interface (Figure 5-14d Region IV). The development of this microstructure was attributed to localised differential cooling rates, as determined by

heat flow back into the dielectric oil and into the substrate, on the time scale of an individual discharge.

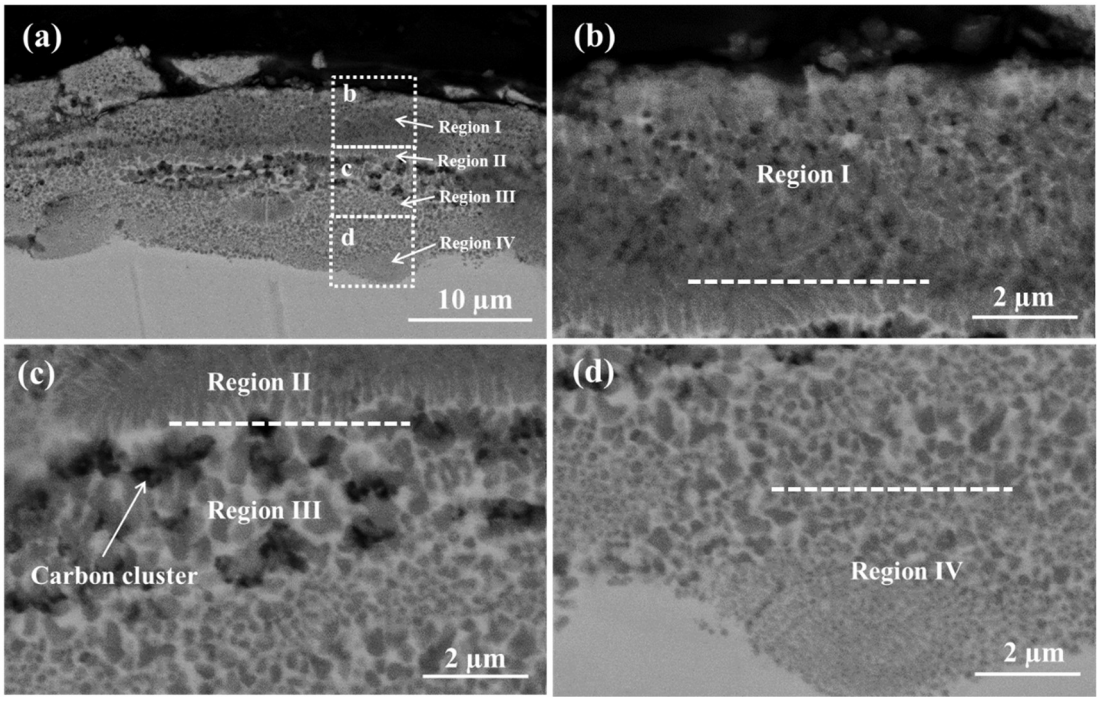

Figure 5-14 BSE images of the developed cermet coating microstructures in cross-section geometry, processed under conditions of: a-d) 10 A current and 8 µs pulse-on time

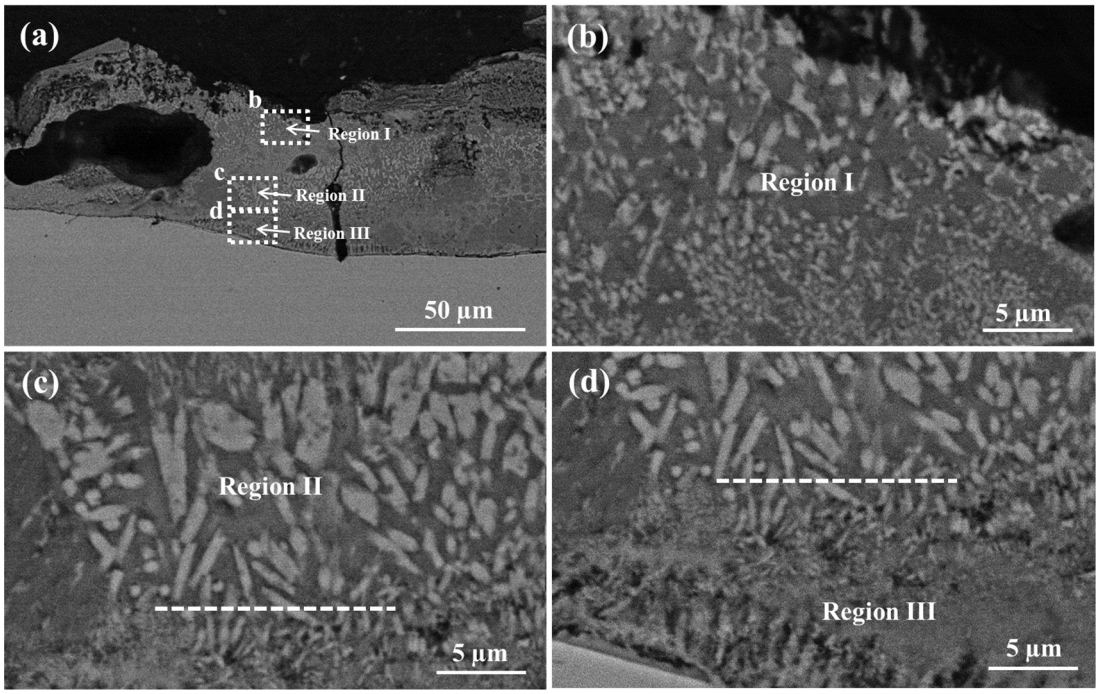

Figure 5-15 BSE images of the developed cermet coating microstructures in cross-section geometry, processed under conditions of: a-d) 10 A current and 64 µs pulse-on time

The latter (10A, 64 μs) similarly showed the development of a banded microstructure with generally larger grain sizes, reflecting the increased pulse-on time and energy into the system, and the consequent longer time taken for cooling and recrystallisation. In this case, the near surface region was characterised by relatively large grains (Figure 5-15b Region I); an inner banded structure of columnar grains (Figure 5-15c Region II); and a dendritic structure next to the coating/substrate interface (Figure 5-15d Region III) [138]. Increased thickness of the coating layer was associated with increased levels of cracking through the coating and at the coating/substrate interference (Figures 5-12h and 5-15a).

Figures 5-16a,b present the average rate of change of temperature at the surface of a single cermet crater centre, as a function of increasing current (for a fixed pulse-on time of 8 μs) and increasing pulse-on time (for a fixed current of 10 A), respectively. The rate of heat transfer varied for these sample sets, with the highest value of ~ 6.8 x 10^8 K/s returned for samples produced under conditions of low pulse-on time of 2μs (10 A); whilst a long pulse-on time of 64 μs (10 A), or an increase in current (> 10 A), were associated with lower values of cooling rate. Since the flow of dielectric fluid was maintained constant, this variation in heat flow was attributed to differences in the melt pool volume and its initial temperature after the pulse-on time.

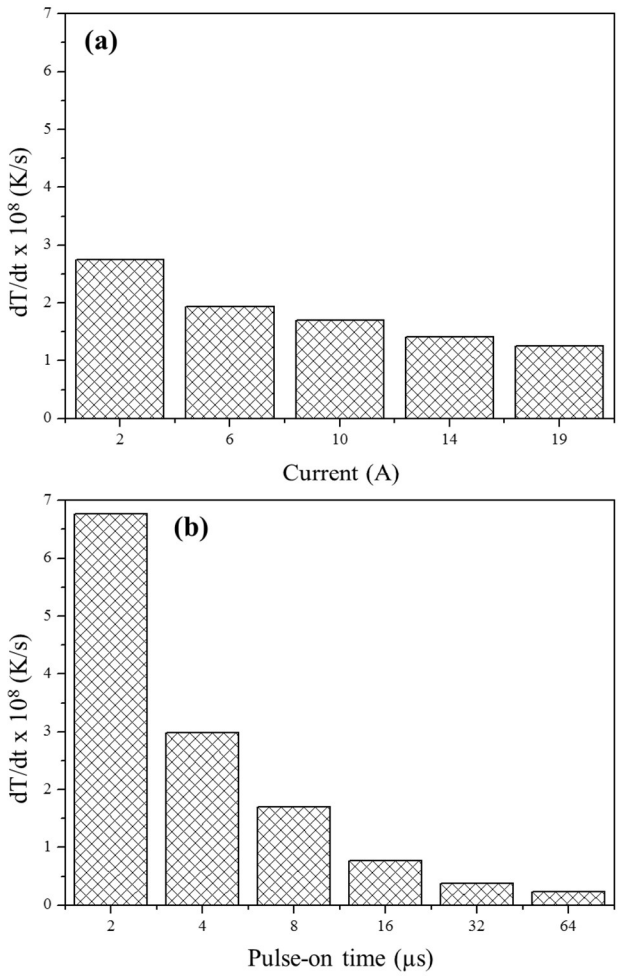

Figure 5-16 Average surface simulated cooling rate for a single TiC crater deposit as a function of: a) Current (fixed pulse-on time of 8 µs) and b) Pulse-on time (fixed current of 10 A)

To better understand the microstructural formation processes of both individual craters and layer cermet coatings comprising many sequentially deposited craters, temperature profiles at different depths into a crater, as a function of increasing time, where calculated. Figure 5-17 shows a depiction of the microstructure generated within a crater processed under conditions of 10 A current and 8 µs pulse-on time (Figures 5-12c and 5-14:a-d), alongside temperature-time simulation with each curve representing a node located at different depths (1 µm pitch) into the centre of the crater; *i.e.* from the oil-flow/surface interface to the melt/solid (crater/workpiece) interface. It is noted that the temperature of the near surface molten material decreased sharply,

reducing to ~ 4 x 10^3 K within ~ 10 µs of the end of the pulse-on time, followed by a lower cooling rate. The resultant banded microstructure within the crater is defined by the competing heat transfer processes, with rapid cooling of near surface material governed by convection within the flowing dielectric oil, whilst initial gentle heating combined with slightly slower cooling rates in the vicinity of the melt/solid interface (~ 3 µm from the bottom of the crater) are governed by conduction into the substrate. Hence, it is evident that the cooling phase has two distinct stages, with rapid non-uniform cooling within the first ~ 10 - 20 µs leading up to the onset of TiC crystallisation (~ 3.16 - 3.25) x 10^3 K, followed by a second more uniform stage of heat loss up to ~ 100 µs, leading up to the onset of Fe matrix solidification (~ 1.4 - 1.45) x 10^3 K.

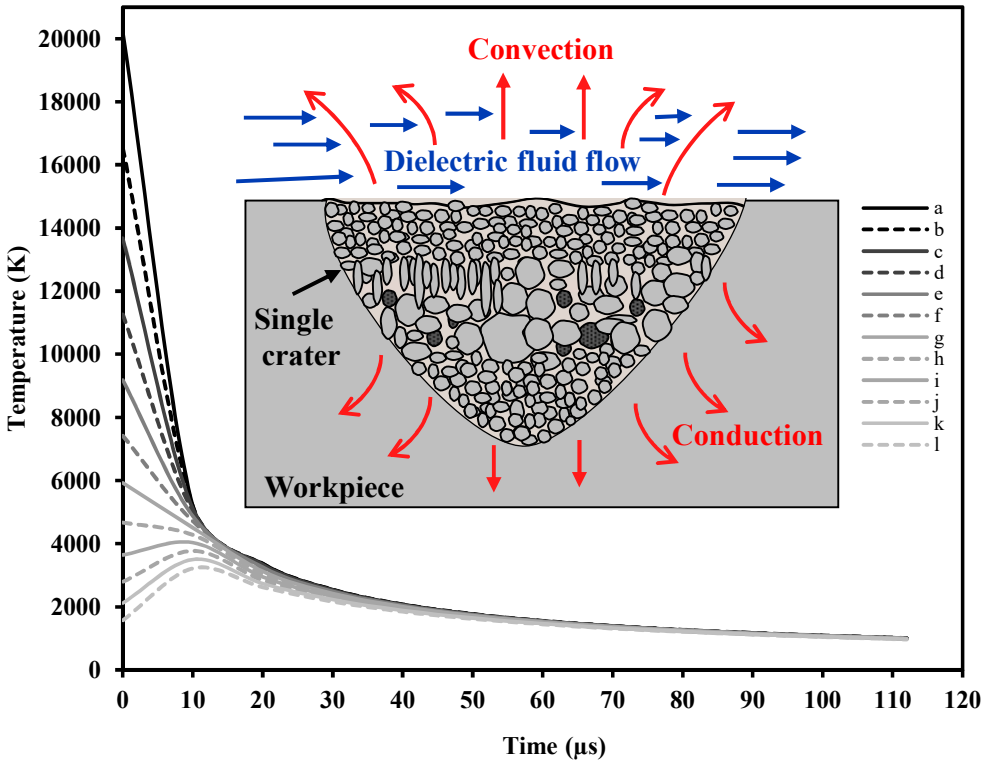

Figure 5-17 Cooling profiles as a function of increasing time (pulse-off), with each line representing a node located at the crater centre (a-l) from the oil-flow/surface interface to the melt/solid interface, with 1 µm pitch

5.3.7 Cross-section TEM of single crater

In order to gain improved understanding of the composition and structure of EDC coatings, single craters produced using a TiC electrode and 304-SS substrate, under conditions of 10 A current and 8 µs pulse-on time for ~ 30 second, were investigated using SEM and TEM. For example, Figure 5-18 presents complementary SE and BSE images of localised craters and deposits on a 304-SS substrate.

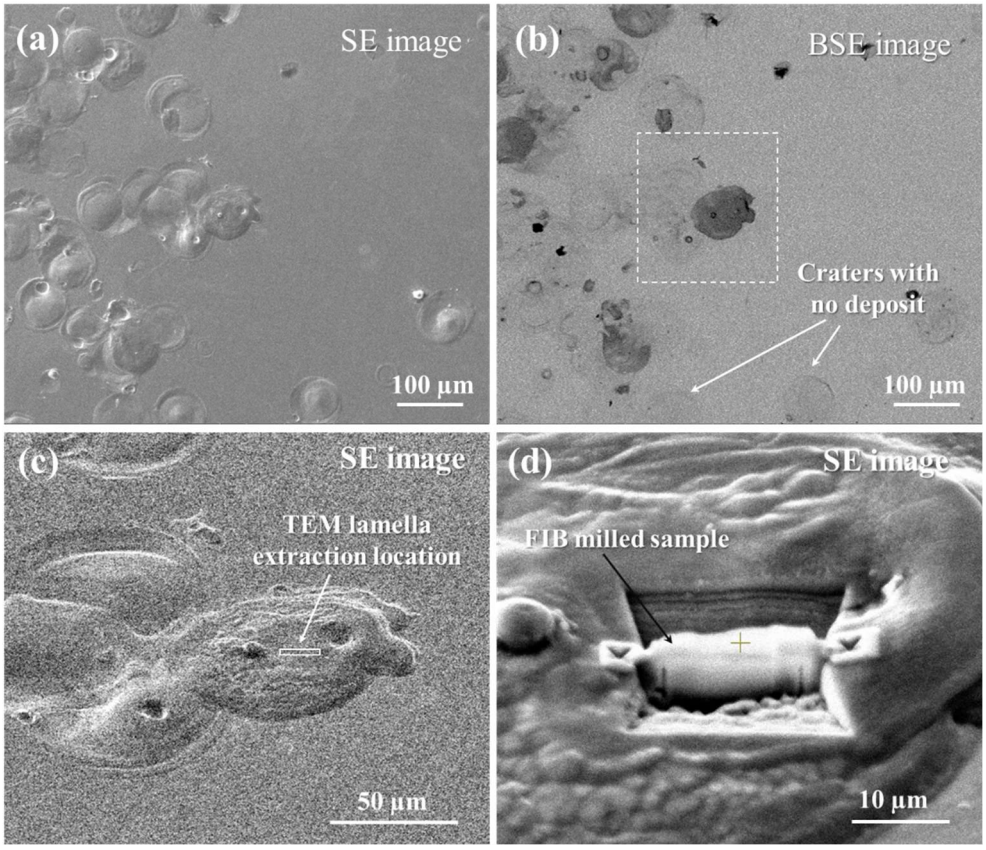

Figure 5-18 Single deposit sample used for TEM sectioning: (a,b) SE and BSE images showing individual craters/deposits, EDC processed on 304-SS; (c) magnified SE image of the boxed region in (b) showing location selected for sectioning; (d) SE image of FIB milled, electron transparent sample foil (arrowed).

The BSE image of Figure 5-18b, in particular, reveals compositional variations with dark regions corresponding to material with low, locally averaged atomic number, commensurate with the presence of localised tool electrode TiC deposits within the stainless steel. The effects of many discharges which did not result in deposition in the

vicinity of this deposit can be seen also, in the form of craters exhibiting similar BSE brightness levels to that of the substrate (Figure 5-18b, arrowed). Figure 5-18c shows the location selected for FIB lift-out, corresponding to the deposit highlighted within the boxed region of Figure 5-18b. The site was coated with a protective layer of Pt, prior to FIB milling using Ga+ ions at 30 kV with sequential reduction of ion beam current density to define an electron transparent membrane (~10 × 6 μm), free of surface amorphisation artefacts, for observation in cross-section in the TEM. A sub-section of the TEM lamella, was ion beam polished to < 100 nm thickness for improved electron transparency.

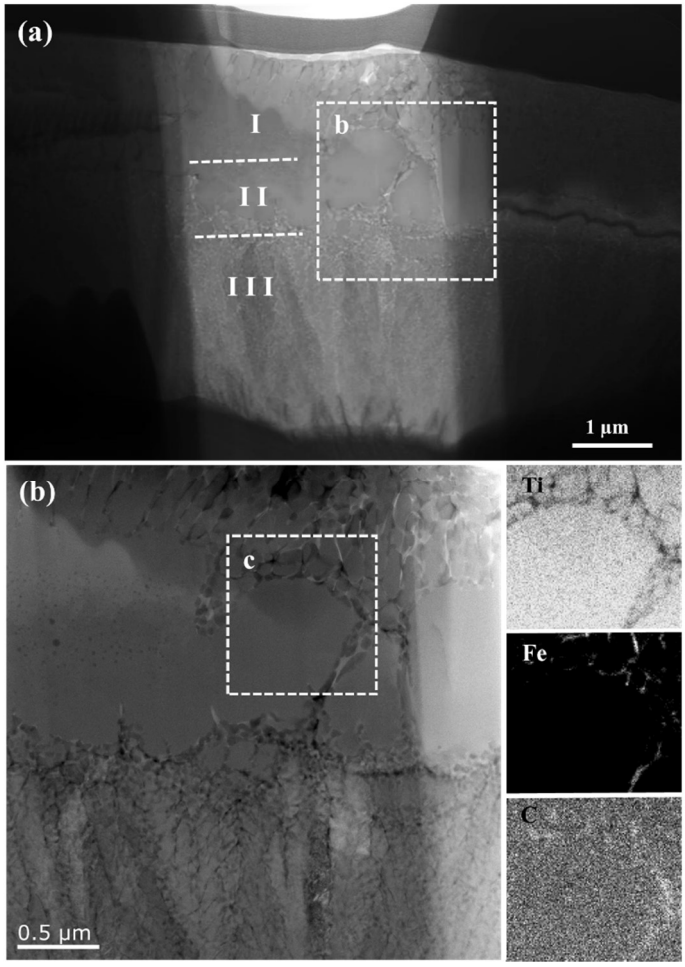

Figure 5-19 (a,b) Cross-sectional TEM micrographs of a single EDC deposit processed under conditions of 10 A and 8μs; and (c) associated EDS maps for Ti, Fe and C

Figure 5-19a presents a BF-STEM image of this deposit showing the presence of three distinct bands of material; *i.e.* a near surface region (I) of 50 - 200 nm sized grains with slight preferred orientation; a thicker banded region (II) of much larger ~ 1 - 2 μm sized grains; then a narrow transition zone of small, 50 - 200 nm sized equiaxed grains into a further distribution (III) of ~ 1 μm long columnar grains towards the deposit/substrate interface, intermixed with some finer grains. Figure 5-19b present a dark-field scanning transition electron microscopy (DF-STEM) image highlighting the fine scale structural variations across regions I, II & III of Figure 5-19a, with associated EDS maps Figure 5-19b (boxed region c) confirming a distribution of Fe and enhanced levels of C surrounding the TiC grains. This is consistent with the phase separation of TiC and Fe from the melt upon rapid cooling to form the cermet.

5.4 Discussion

The fraction of total discharge energy transferred to the workpiece is an important factor determining temperature distribution within the modified layer; the modelling of which allows for prediction of the developed microstructure and correlation with layer mechanical properties. The fraction of energy transferred to the workpiece, F_v, is defined ultimately by the discharge voltage, current and pulse-on time. Figure 5-6 illustrated that an increase in current, from 2 to 19 A, for a fixed pulse-on time of 8 μs, has a low impact on F_v, and this is attributed to the instability of the heat source. Under conditions of short pulse-on time, discharge occurs at very high frequency, resulting in inadequate time for conduction of energy and hence insignificant impact of current [136]. Conversely, Figure 5-7 illustrates increasing F_v to the workpiece with increasing pulse-on time from 2 to 64 μs (for a fixed current of 10 A), being attributable to the effects of a relatively steady heat source with sufficient time for conduction. No

significant change in F_v at high pulse-on times of ~ 32 - 64 μs occurs (Figure 5-7, red line) because additional energy supply is lost to maintain the plasma channel, and hence energy transfer to the workpiece becomes limited [64]. Singh and Shukla [50] reported similarly that a further increase in pulse-on time does not give significant erosion during EDM, with additional energy supplied being lost to maintain the plasma channel.

It is evident that values for F_v, predicted using the current model, are close to the experimental EDC data and in good agreement with other studies, including [64] and [136] (Figures 5-6 and 5-7), reflecting the incorporation of real processing conditions, such as the Gaussian distribution of the heat source, along with latent heat of fusion and the cermet material properties. However, it is noted that the modelling of EDC processes returns slightly higher values [64, 136] for F_v, as compared to EDM. This is attributed to the difference between coating and machining processes, with EDC acting to replace and intermix near surface material rather than remove material, with a decrease in the heat carried away by debris leading to an increase of heat conducted into the workpiece [65].

Further, the modelling of crater depth (Figure 5-13) showed good agreement with experimental data for the overall EDC layer thickness. The increase in crater depth with increasing pulse-on time (Figure 5-13b) is related directly to increasing F_v and correlates with the depth of initially formed craters from single spark events, being attributable to the more effective transfer of heat into the bulk. Small variations between the simulated crater depths and layer thicknesses for conditions of high pulse-on time (32 - 64 μs) is attributed to the high variability of crater sizes (Table 5-2), attributed to fluctuating average gap voltages. Hence, crater dimensions are dependent

primarily upon heat input during discharge and the time required to create each melt pool.

The EDC processing conditions of 10 A and 8 μs produced colonies of very fine grained equiaxed TiC within an Fe matrix near the coating surface and close to the melt pool/substrate interface, along with an intermediate band of larger equiaxed and columnar grains containing segregated clusters of carbon (Figures 4-9, 4-17 and 5-14), being characteristic of a very rapid cooling process and indicative of the initiation of crystallisation at both the surface and the melt pool/substrate interface. During the pulse-on time, TiC particles from the tool electrode melt and fuse with the workpiece melt pool, whilst the process of solidification starts at the end of the discharge. The TiC melting point is higher than that of Fe and hence it is anticipated that TiC particles develop in advance of Fe matrix formation. Subtle variations in localised grain sizes simply reflect variations in localised composition and heat flow, mediated by conduction into the substrate and convection into the dielectric oil.

This description of ED coating development is consistent with the predictions of the simulations based on heat transfer into the workpiece. A steep drop in temperature was predicted for the near surface of the melt pool, to ~ 4 x 10^3 K, during the first ~10 μs (Figure 5-17), which is still above the melting point of TiC. At the same time a gradual rise in temperature was predicted in the vicinity of the melt pool/substrate interference. Thereafter, a more generalised, homogeneous cooling process occurred, resulting in the onset of the solidification process.

Lower average values for the cooling rate were predicted for samples produced under conditions of high pulse-on time of 64 μs (Figure 5-16b), consistent with the development of more dendritic TiC/Fe cermet morphologies observed at the melt pool/substrate interface (Figures 5-15:a-d), being consistent with high thermal input

energy and a relatively low cooling rate in this case [139], whilst columnar grained structures were again found in the middle of this coating.

The SEM (*e.g.* BSE image Figure 5-18b) and TEM (Figure 5-19) data indicate a variability of TiC deposition during a single discharge, with many sparking events not leading to TiC deposition, and some to TiC-rich deposits. It is considered that the deposit is solid prior to the next localised spark and melt pool formation event, which leads to progressive incorporation and intermixing of more substrate and tool electrode material into the developing coating. The single TiC-rich deposits here contained a ~ 2 wt% contribution of Fe at the surface, whilst the continuum TiC/Fe cermet coating contained ~ 21 wt% Fe Table 6-2. Hence, the dilution effect from repeated sparking suggests that time of processing is a critical EDC processing parameter.

5.5 Summary

A theoretical model has been developed to predict the amount of energy transferred into the workpiece during the EDC processing of cermet coatings. 2D transient heat transfer principles solved by the finite difference method enabled coating thicknesses and microstructures to be predicted and validated against previously reported literature and experimental observations. The modelling demonstrated that the fraction of energy imparted into the workpiece from each spark event is a critical consideration for ED processing and varies as a function of process conditions. The effective amount of energy transferred to the workpiece was predicted to vary between 17% and 23% for increasing current from 2 to 19 A (for a fixed pulse-on time 8 μs); and between 7% and 53% for increasing pulse-on time from 2 to 64 μs (for fixed current of 10 A). A maximum value of F_v was attained for the highest pulse-on time of 64 μs.

Estimates for crater depth from the modelling compared well with experimentally determined values for coating thickness, except for the case of high pulse-on times where there was more variability, but generally, crater sizes (layer thicknesses) increased as the amount of energy transferred to the workpiece increased. Further, the predictions for heat transfer and cooling rate of the melt pool compared well with experimental observations for the developed cermet microstructures, as a function of processing conditions. In particular, intermediate processing conditions of 10 A and 8 μs were associated with the development of complex, banded, fine-grained microstructures, reflecting differences in localised cooling rates and the competing pathways for heat conduction into the substrate and convection within the dielectric fluid. Increasing the pulse-on time was characterised by a propensity towards grain growth, reflecting the higher energies imparted into the coatings and slower cooling rates.

6 Laser surface melt processing and tribological behaviour of EDC TiC/Fe cermet coatings

6.1 Introduction

As-deposited EDC coatings are characterised generally by the poor integrity of their surfaces, being symptomatic of material surfaces processed by EDM. In particular, there is concern that the wear performance of ED processed coatings is likely to be affected strongly by the integrity of the surface, *i.e.* porosity, cracks and surface roughness. One suggested approach to address this issue is to laser re-melt the coating.

In this chapter, as-deposited TiC/Fe ED coatings, subjected to laser melting treatments to eliminate defects at the EDC surface, are investigated, with emphasis on microstructure development as a function of laser power. A systematic study of the wear performance of TiC/Fe cermet coatings, as compared to a reference EDM surface and a polished substrate, on two different types of steel substrate was performed. An EDM surface machined using a Cu electrode under identical conditions provided a baseline for isolating the effects of TiC addition because it resulted the same surface topography as the TiC/Fe ED coating with the development of cracking and void formation (Figure 4-16), and exhibited almost the same surface roughness. Laser surface melting as a post treatment of the coating under two loading conditions is also described (Table 6-1).

The specific wear rate and the wear scar development are investigated, and correlated with the near surface microstructure of the TiC/Fe EDC, to appraise the suitability of such laser surface melting (LSM) modification processes, to produce wear resistance coatings. Comparison is made with reference to the wear properties of EDM surfaces, prepared using a conventional Cu electrode.

Table 6-1 Summary of the reciprocating ball-on-flat wear tests, to be investigated

Workpiece material	Process	Wear test conditions (load (N) & reciprocating cycles)
304-SS substrate & HSS substrate	as-polished substrate	10 N & 35,000 cycles
		50 N & 10,000 cycles
	as-deposited TiC/Fe EDC	10 N & 35,000 cycles
		50 N & 10,000 cycles
	reference Cu EDM	10 N & 35,000 cycles
		50 N & 10,000 cycles
	LSM (240W & 280W)	10 N & 35,000 cycles
		50 N & 10,000 cycles

6.2 Laser surface melting (LSM) of EDC TiC/Fe coatings

6.2.1 Surface topography of as-deposited and LSM processed coatings

LSM was performed on the as-deposited ED coatings, in order to homogenise the surface. Figures 6-1:a-f present SE images of the as-deposited and laser processed TiC/Fe cermet coatings (on both substrate types, 304-SS and HSS, using preferred EDC parameters of 10 A current and 8 μs pulse-on time), demonstrating the development of much smoother surfaces under laser conditions of both 240W and 280W, with significant reduction in the density of pores and cracks due to reflow of the molten surface (Figures 6-1:c-f), compared to the as-deposited coatings (Figures 6-1a,b).

For the case of the HSS substrate, laser treatment at 240 W removed cracks and voids associated with the original ED coating process, but new, relatively large cracks were found to develop (Figure 6-1d, arrowed). This morphology was distinct from that of laser processed ED coatings on 304-SS (Figure 6-1c) which yielded surfaces entirely free of cracking. The presence and absence of cracks for these LSM processed

cermet coated HSS and 304-SS was attributed to the effects of differential thermal expansion/contraction, combined with high cooling rates.

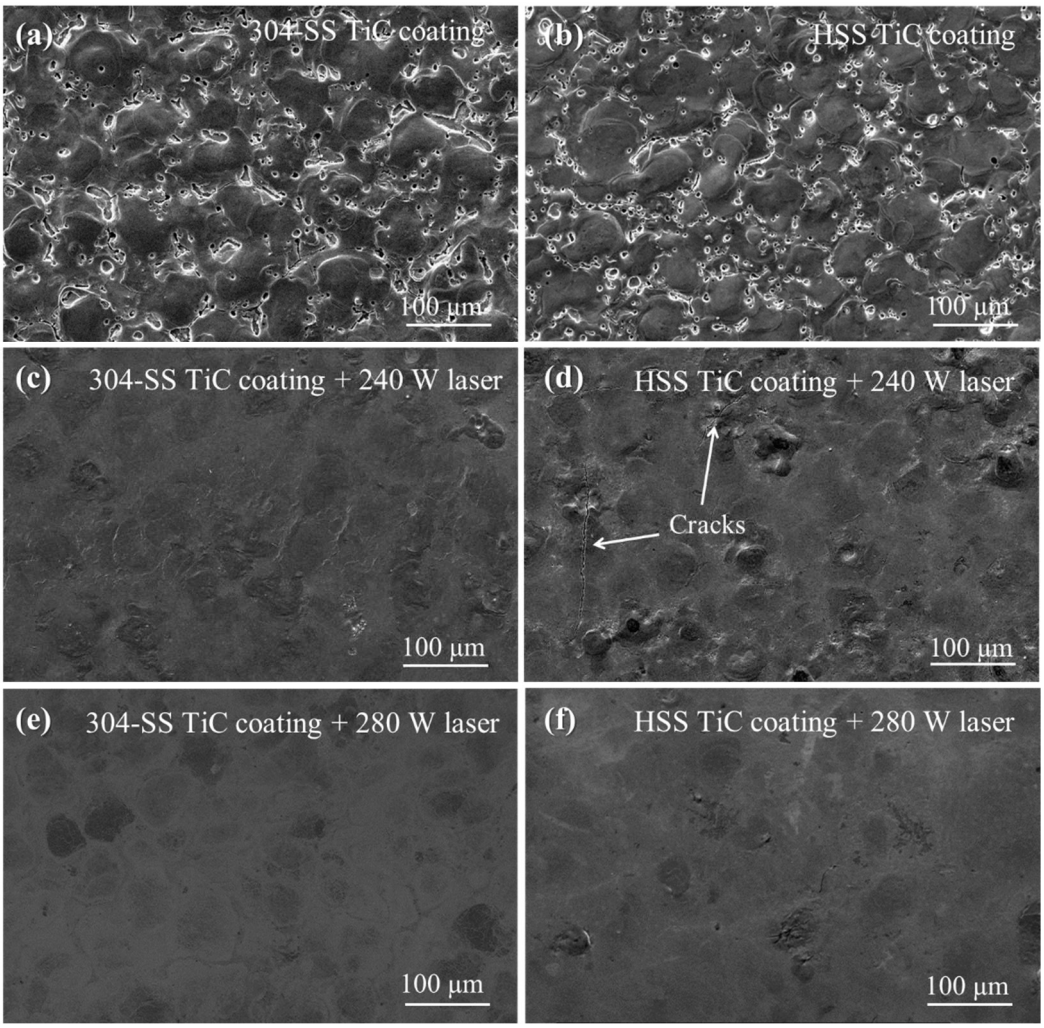

Figure 6-1 SE images of (a,b) as-deposted TiC/Fe on 304-SS and HSS, (c-f) laser surface treated TiC/Fe cermet coatings on: (c,e) 304-SS and (d,f) HSS substrates, as a function of power: (c,d) 240 W and (e,f) 280 W, respectively (1600 mm/minute scan speed; Ar environment)

EDS area analyses (Table 6-2) indicated that laser processing at 240 W acted to reduce significantly the levels of Ti (TiC) incorporation for both cermet coated 304-SS and HSS samples (from ~ 39 wt% down to ~ 26 wt% and from ~ 29 wt% down to ~ 21 wt%, respectively). Further, laser processing under conditions of 280 W acted to reduce average Ti (TiC) incorporations down to ~ 18 wt% and ~ 15 wt%, respectively.

This effect may be attributed to the evaporation and dilution of TiC within the substrate.

Table 6-2 TiC/Fe cermet coating compositions before and after LSM treatment, based on EDS area analyses

	Ti Wt%	C Wt%	Fe Wt%	Roughness Ra (µm)		Ti Wt%	C Wt%	Fe Wt%	Roughness Ra (µm)
cermet / 304-SS	39.4	31.3	21.1	1.3	**cermet / HSS**	29.3	27.4	30.1	1.2
cermet / 304-SS; 240 W LSM	25.6	16.1	40.4	0.3	**cermet / HSS; 240 W LSM**	20.8	18.1	41.8	0.4
cermet / 304-SS; 280 W LSM	18.1	19.8	43.6	0.4	**cermet / HSS; 280 W LSM**	15.0	18.7	48.0	0.6

6.2.2 Microstructure of as-deposited and LSM processed coatings

Figure 6-2 presents low and high-magnification BSE images, in cross-sectional geometry, of as-deposited TiC/Fe cermets on 304-SS, and LSM processed coatings under conditions of 240 and 280 W, respectively. Voids and crack formations have been eliminated, for both laser powers (Figures 6-2c,e), compared to the original ED cermet coated samples (Figure 6-2a).

The LSM processed coatings were characterised by flatter surfaces (Ra ~ 0.3 µm and 0.4 µm for processing conditions of 240 W and 280 W, respectively, compared to Ra ~ 1.3 µm for the as-deposited coatings (Tables 6-2)) and a significant increase in grain size (Figures 6-2d,f compared to Figure 6-2b), being attributed to an increased melt lifetime, providing for the movement of molten material to in-fill the cracks and voids. The grain structures yielded after laser processing were dendritic in nature, similar to that of laser melted TiC [140].

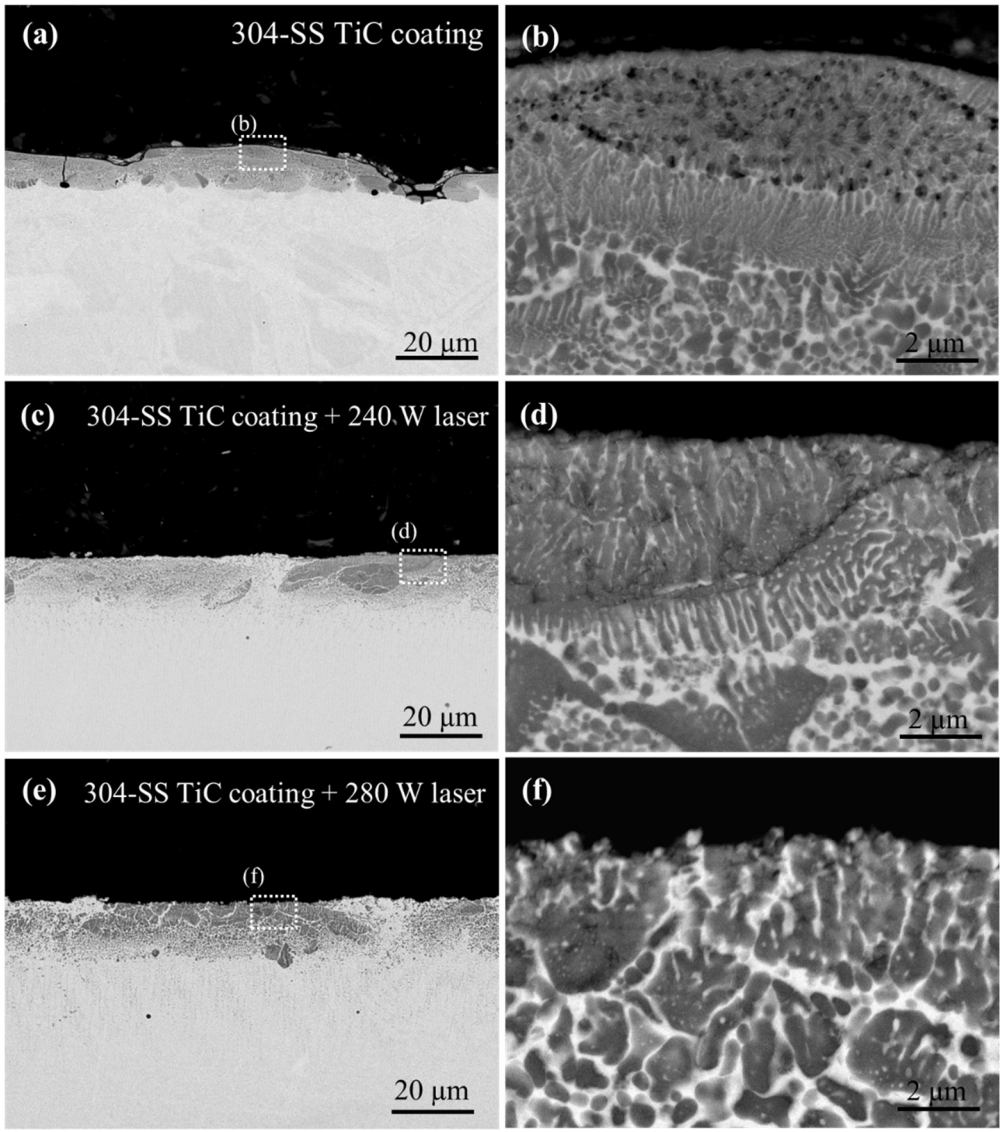

Figure 6-2 High resolution cross-sectional BSE images of: (a,b) as-deposted TiC/Fe on 304-SS; and laser surface treated TiC/Fe cermet coatings as a function of power: (c,d) 240 W and (e,f) 280 W, respectively (1600 mm/minute scan speed; Ar environment)

Figure 6-3 presents low and high-magnification BSE images, in cross-sectional geometry, of as deposited TiC/Fe cermets on HSS, and LSM processed coatings as a function of laser powers of 240 and 280 W, respectively. Again, voids and crack formations were eliminated, for both laser powers (Figure 6-3c,e), as compared with the original ED cermet coated samples (Figure 6-3a).

The microstructure of the HSS substrate consisted mainly of carbides of various sizes and shapes within an iron matrix (Figure 6-3a), and identified by XRD as ferrite

α-Fe, M_6C carbide (Fe-Mo-C) and MC vanadium rich carbide (V-C) (Figure 4-3b). LSM processing acted to dissolve these carbides with the resultant melt zone consisting of a cellular dendritic structure, for both laser powers of 240 and 280 W (Figure 6-3c) and (Figure 6-3e), respectively. A small laser melted zone was observed for the coating processed under 240 W laser power (Figure 6-3c) as compare to the 280 W laser power (Figure 6-3e). These observations are consistent with previous work on the laser melting of HSS [141].

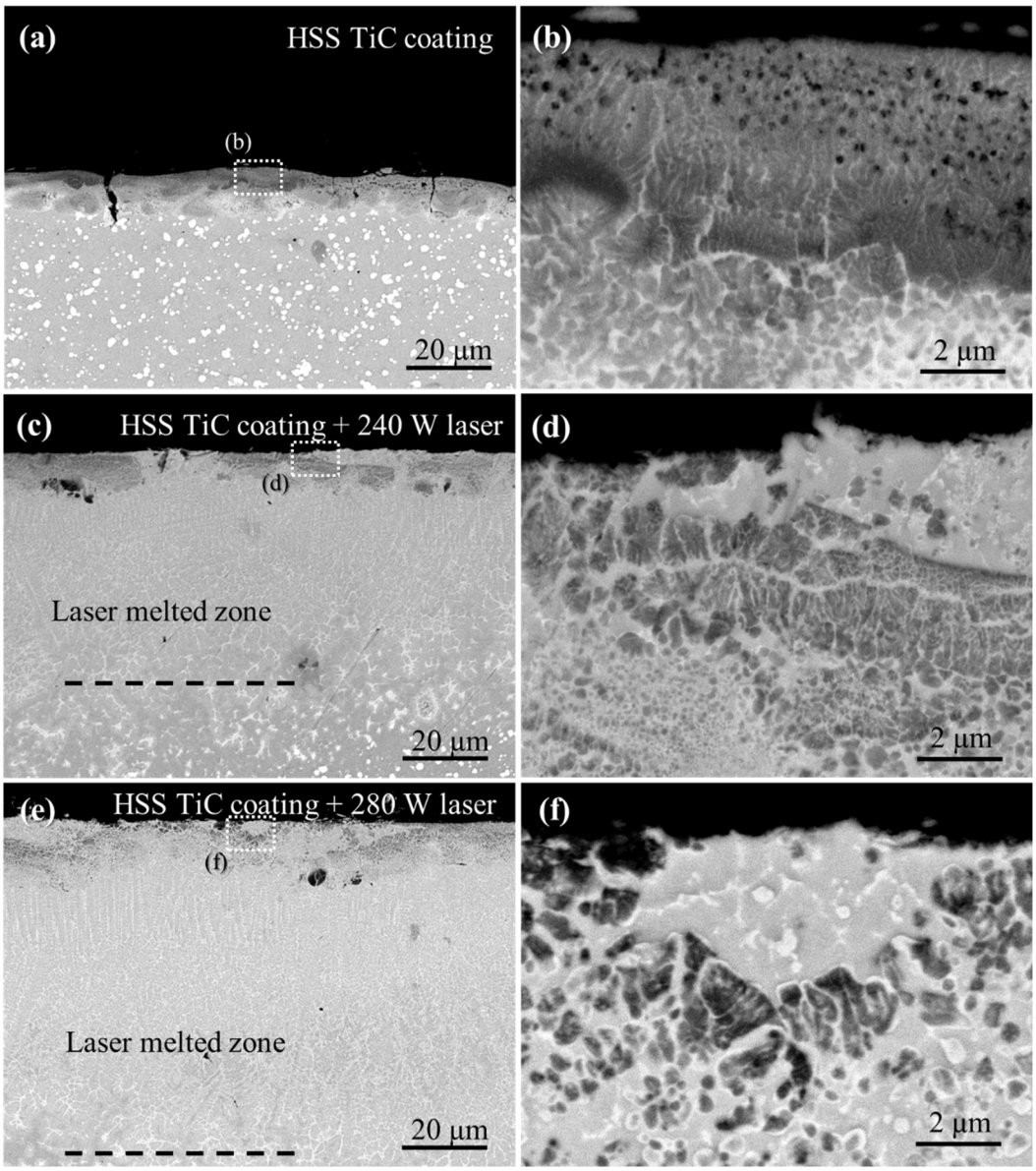

Figure 6-3 High resolution cross-sectional BSE images of (a,b) as-deposted TiC/Fe on HSS; and laser surface treated TiC/Fe cermet coatings, as a function of power: (c,d) 240 W and (e,f) 280 W, respectively (1600 mm/minute scan speed; Ar environment)

6.2.3 Crystal structure of LSM processed coatings

Figures 6-4a,b present XRD patterns for LSM processed TiC/Fe coatings on 304-SS and HSS, under process conditions of 240 W and 280 W, respectively, compared to the as-deposited coatings. The XRD data consists of peaks attributable to both the TiC electrode and the substrates. The coating on both substrate types mainly exhibited six dominant peaks consistent with the presence of TiC (Section 4.4.2).

It is noted that there was an increase in the peak intensity with increasing laser power, for fcc TiC_{111}, TiC_{200} and TiC_{222} lattice planes at $2\theta \sim 35.9^{\circ}$, 41.7° and 76.1°, respectively, indicative of the development of some preferred orientation. Similarly, there was the suggestion for some slight preferred orientation for γ-Fe_{200} ($2\theta \sim 50.7^{\circ}$) for LSM processed coatings on 304-SS, as compared to the substrate (Figure 6-4a). There was also evidence for the presence of some extra peaks attributable to γ-Fe within the LSM processed cermet coatings on HSS (Figure 6-4b), similar to the reports of fcc structure development within laser re-melted HSS [141].

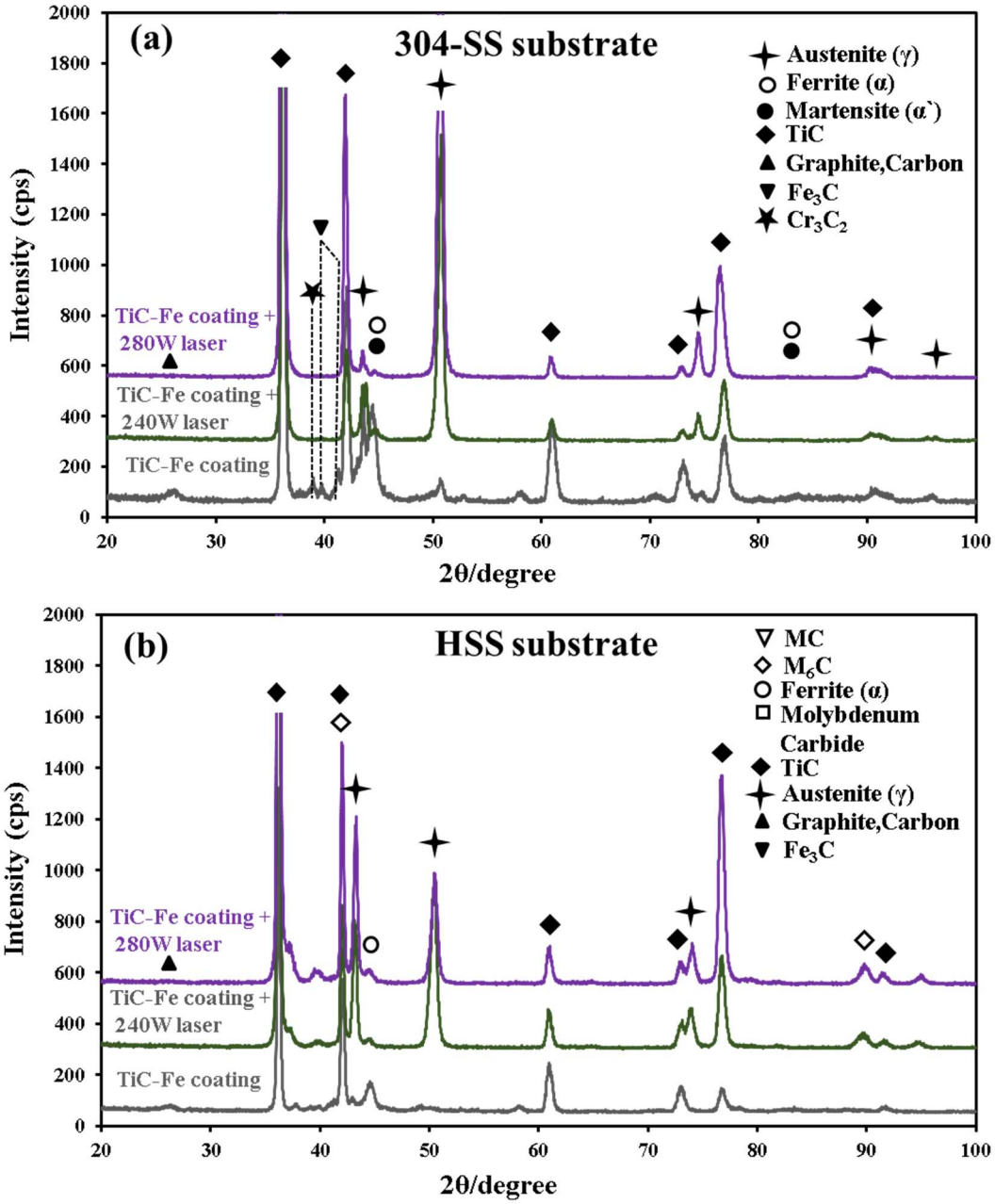

Figure 6-4 XRD patterns for as-deposited TiC/Fe on (a) 304-SS; and (b) HSS; and LSM processed under conditions of 240 and 280 W, respectively (1600 mm/minute scan speed; Ar environment)

6.3 Reciprocating wear testing of EDC TiC/Fe coated and EDM processed steel surfaces

6.3.1 Specific wear rates and wear scar profiles

As-processed TiC/Fe cermet coatings, on both substrate types, were wear tested using a dry sliding reciprocating technique, under conditions of 10 N and 50 N for 35,000 and 10,000 reciprocating cycles, respectively. Specific wear rates (Figure 6-5) were determined from the cross-sectional profiles of the wear tracks.

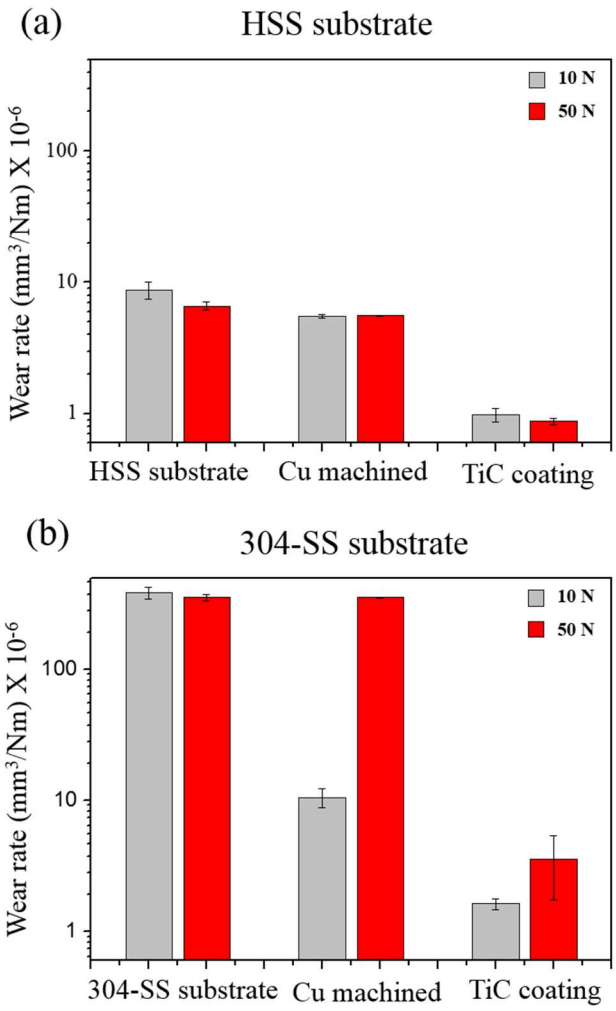

Figure 6-5 Specific wear rates (logarithmic scale) for samples based on: a) HSS and b) 304-SS substrates (as-polished substrate; EDM Cu reference surface; and EDC TiC/Fe cermet coating) under loads of 10 N and 50 N, respectively

The wear rate for the TiC/Fe cermet coated HSS sample was approximately an order of magnitude lower than that of the as-polished HSS substrate, under loads of both 10 and 50 N (Figures 6-5a). Further, the wear rate of the cermet coated 304-SS, outperformed the as-polished substrate by approximately two orders of magnitude (Figures 6-5b), again demonstrating that the EDC coating provides significant tribological benefit, under both loading conditions. Even though the 304-SS substrate benefits more than the HSS, in practical terms, from the EDC process, the absolute wear rate of the coating on 304-SS was slightly higher (~ 2 - 4 Times) than that on HSS, indicating a combined effect of coating and substrate on the wear mechanism. It is noted that the reference Cu EDM machined HSS surface yielded no significant improvements in wear behaviour, compared to the as-polished substrate, for both loading conditions (Figure 6-5a), whilst interestingly the Cu EDM machined 304-SS sample yielded an order of magnitude improvement in specific wear rate under loading conditions of 10 N, but no improvement under conditions of 50 N (Figure 6-5b).

Figures 6-6 and 6-7 present cross-sectional profiles of the wear tracks for the as-polished substrates, EDM Cu reference samples, and EDC TiC/Fe cermet samples, on HSS and 304-SS, under conditions of 10 and 50 N, respectively. It is interesting to note that as-polished 304-SS substrate showed very wide and deep wear tracks under both loading condition (Figures 6-7a,b), which were replicated following EDM Cu processing under a 50 N load (Figure 6-7b), whilst the wear profiles were much shallower under a reduced load of 10 N (Figure 6-7a). Conversely, better wear resistance was shown by the as-polished HSS substrates, although very similar wear profiles were returned following EDM Cu processing, for both loading conditions of 10 and 50 N (Figures 6-6a,b). Most importantly and in all cases, however, the TiC/Fe cermet coating showed much shallower, narrow wear track profiles (Figures 6-6 and

6-7 (grey lines)), indicative of small amounts of material removal and vastly superior wear resistance in comparison with the as-polished substrate and Cu machined surfaces.

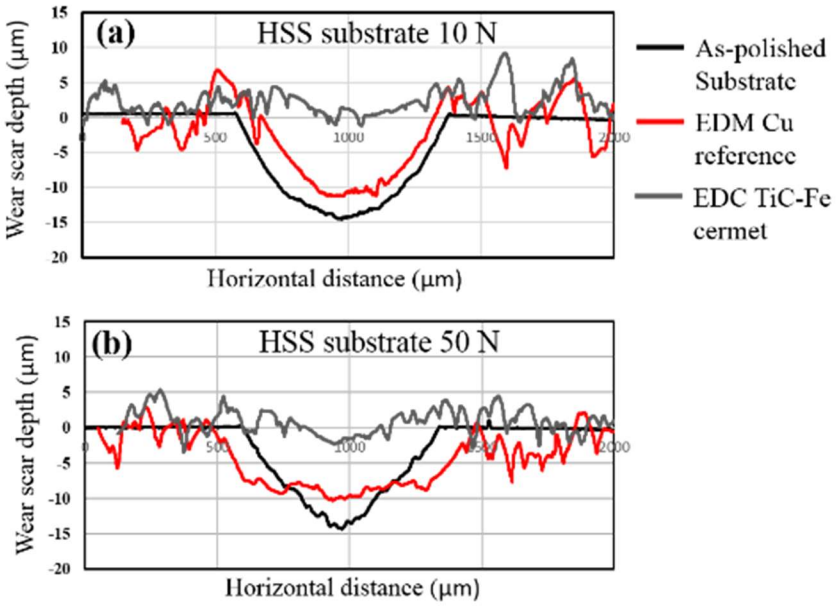

Figure 6-6 Cross-sectional wear scars profiles for the as-polished substrates, EDM Cu reference samples, and EDC TiC/Fe cermet on HSS samples under conditions of a) 10 and b) 50 N, respectively

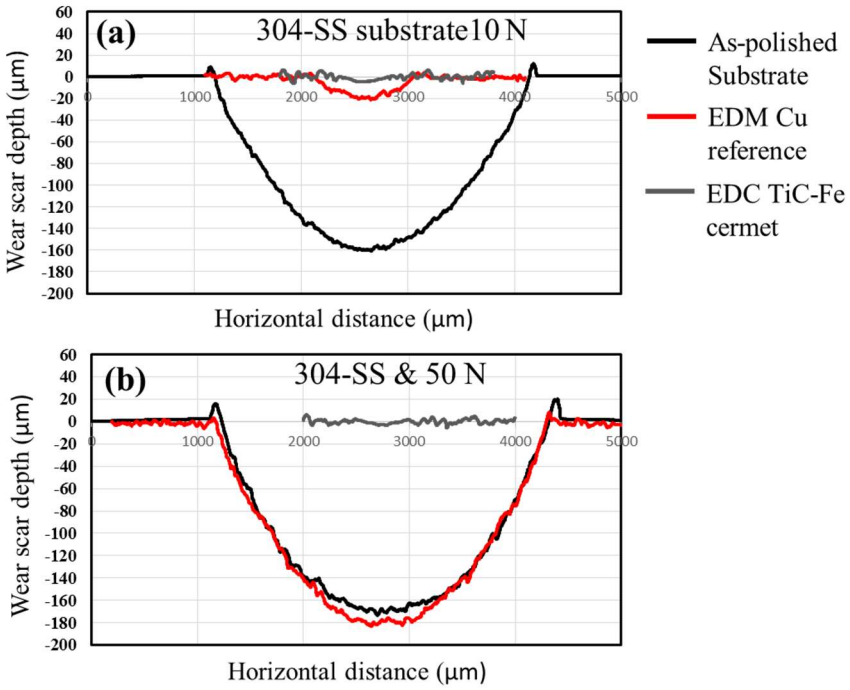

Figure 6-7 Cross-sectional wear scars profiles for the as-polished substrates, EDM Cu reference samples, and EDC TiC/Fe cermet on 304-SS samples under conditions of a) 10 and b) 50 N, respectively

6.3.2 Wear scar characterisation

Low and representative high magnification SEM imaging of the wear scars was performed, in order to gain improved understanding of the wear mechanisms of these processed samples. Figure 6-8 presents mixed secondary electron (SE) and backscattered electron (BSE) images of the wear track (Figure 6-8a) and highlighted details (Figures 6-8b,c) of as-polished HSS, under conditions of 10 N load. The surface showed a uniform wear track, with parallel scratches along the sliding direction (Figure 6-8c), combined with accumulated wear debris at the ends of the reciprocating track [9], being indicative of abrasive wear [142, 143]. Further, EDS analyses of the wear debris indicated enhanced levels of oxidation (O ~ 16.4 wt% and 30.0 wt%; Figure 6-8b, Regions II and III, respectively), as compared to the as-polished substrate (O ~ 1.43 wt%; (Figure 6-8b Region I)).

The development of a cermet coating leads to an increase in the hardness of the near surface modified layer (Figure 4-15), resulting in enhanced wear resistance of the substrate. For example, Figure 6-9 illustrates a wear track (Figure 6-9a) and associated details (Figures 6-9b,c) of the cermet coating on HSS under 10 N loading. In this case, the wear track shows a uniform, smooth surface, although some cracks and voids associated with the as-developed EDC coating can still be distinguished (Figures 6-9b,c). There was no evidence for fracture or grain pull out on the wear track, with some debris present in the initial EDC cracks (Figure 6-10).

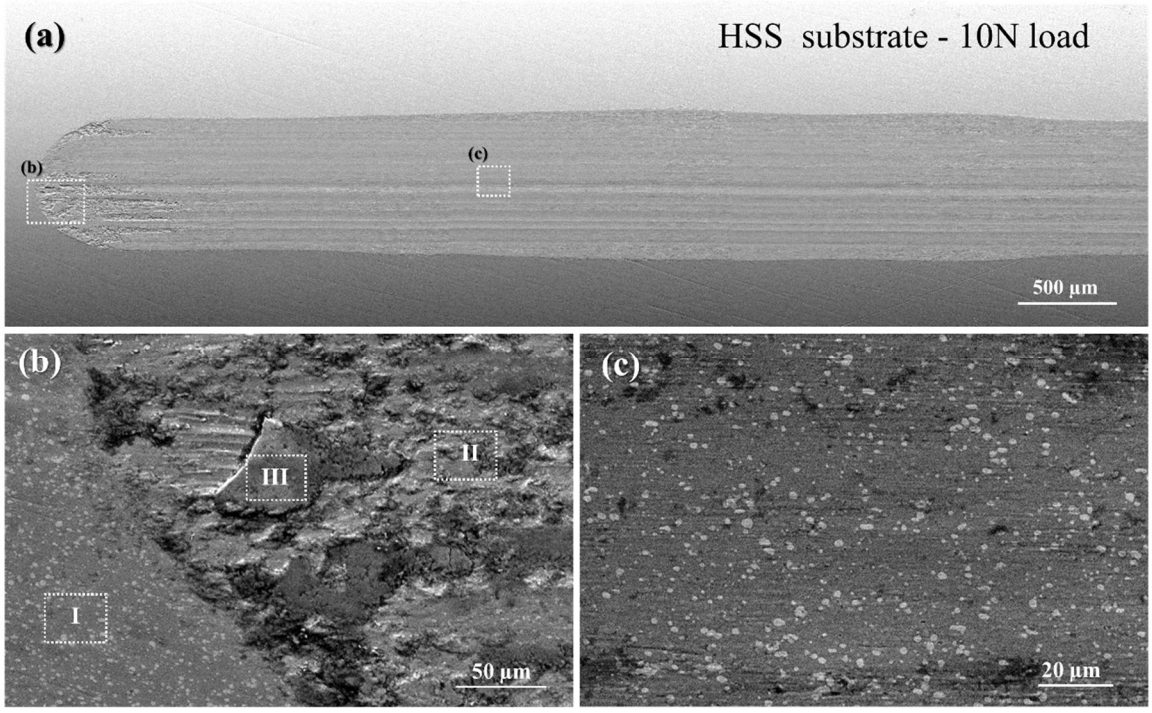

Figure 6-8 Low magnification SEM images showing: (a) the extent of a wear scar (mixed SE & BSE image); and (b,c) representative details of a wear scar on an as-polished HSS substrate, under loading conditions of 10 N, indicative of abrasive wear

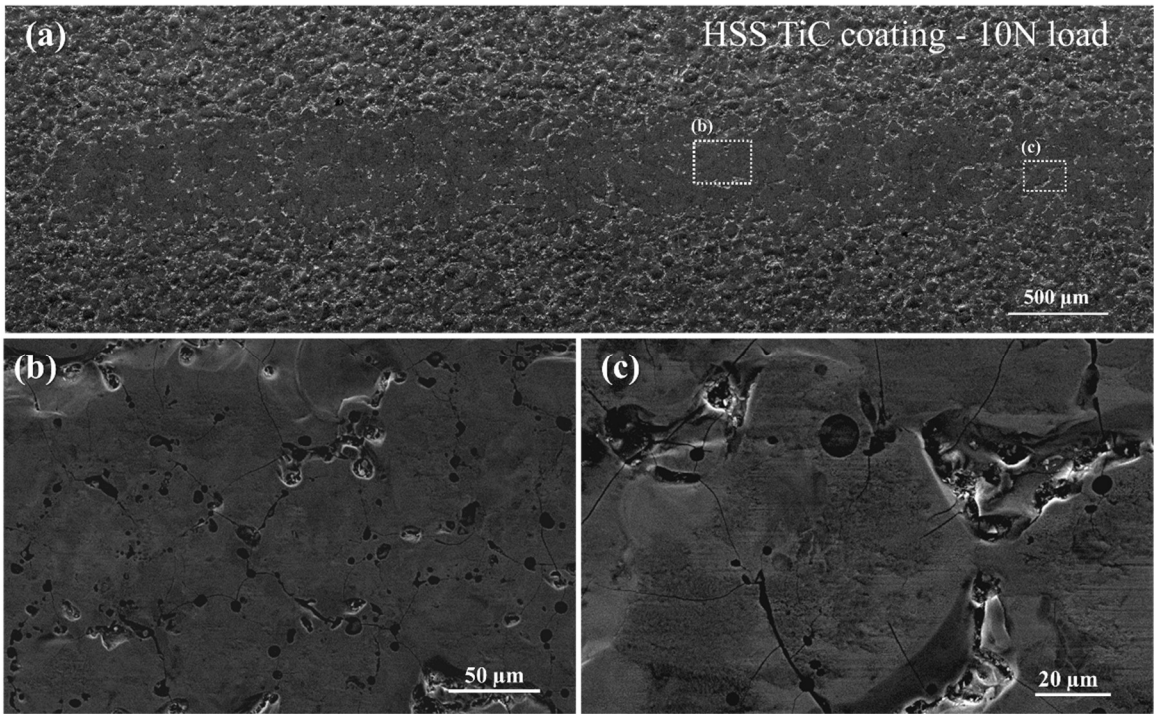

Figure 6-9 Low magnification SE images showing: (a) the extent of a wear scar; and (b,c) representative details of a wear scar on a cermet coated HSS sample, under loading conditions of 10 N, indicative of greatly improved wear performance

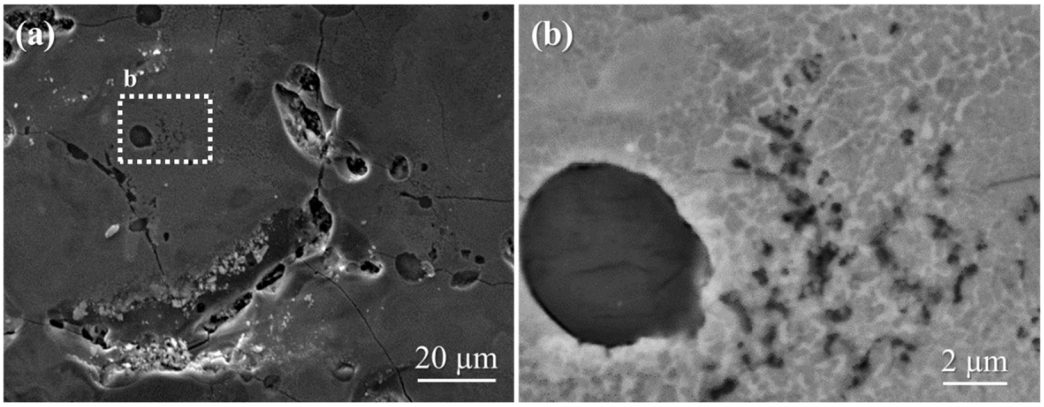

Figure 6-10 a) SE and b) BSE images of TiC/Fe coated HSS, under loading conditions of 10 N

For completeness, Figures 6-11 and 6-12 present high magnification SE images of the wear track details on HSS and 304-SS substrates, under conditions of 10 N and 50 N loading, respectively, as compared to the as-polished substrates, the EDM Cu reference samples, and the ED processed TiC/Fe cermet coatings (see Appendix 4 for more details of SE images of the wear track and highlighted details).

The as-polished 304-SS (Figure 6-11b) under 10 N loading showed evidence of a more severe wear regime, compared to HSS (Figure 6-11a), with regions of embedded wear particles, indicative of adhesive wear [144, 145]. However, the wear tracks on both cermet coated HSS and 304-SS substrates under low loading conditions showed very similar, improved wear morphologies (Figures 6-11e,f), with the development of more uniform, smooth wear surfaces, again with cracking and voids from the initial EDC coating. Intriguingly, the HSS reference sample, EDM processed with a Cu electrode, under 10 N loading, generally showed a smooth surface, along with some localised regions of high oxygen levels, indicative of oxidation (Figure 6-11c). Conversely, the 304-SS sample, EDM Cu processed, revealed a different wear mechanism including abrasive grooves as well as delamination (Figure 6-11d), again suggesting an adhesive mode of wear. Further, some cracks and voids associated with

the initial EDM process were evident for both substrates (Figures 6-11c,d), along with debris accumulated near the wear track ends.

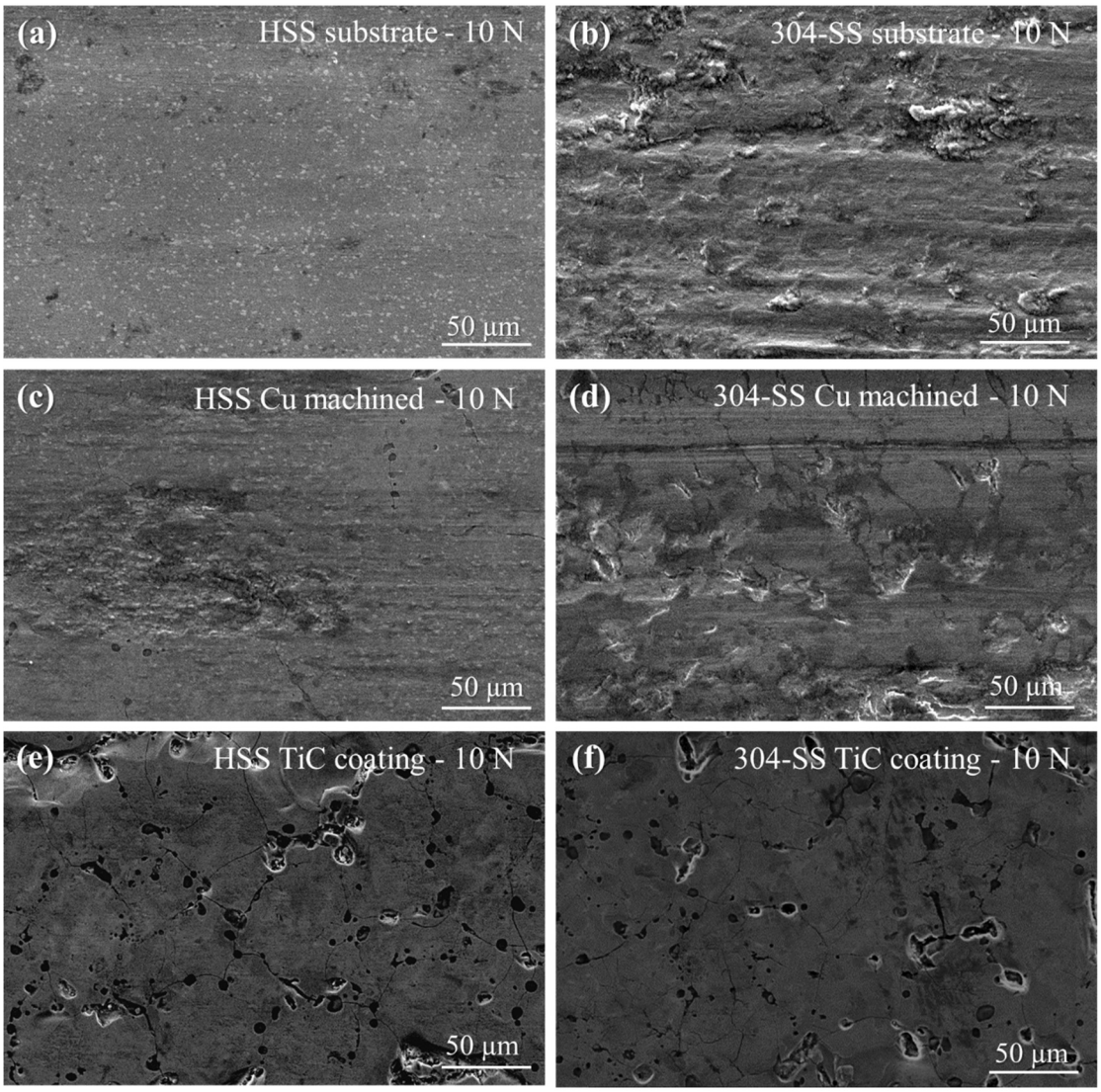

Figure 6-11 High magnification SE images of wear tracks of: (a,c,e) HSS; and (b,d,f) 304-SS, under conditions of 10 N loading. (a,b) as-polished substrates; (c,d) EDM Cu reference samples; and (e,f) EDC cermet coatings

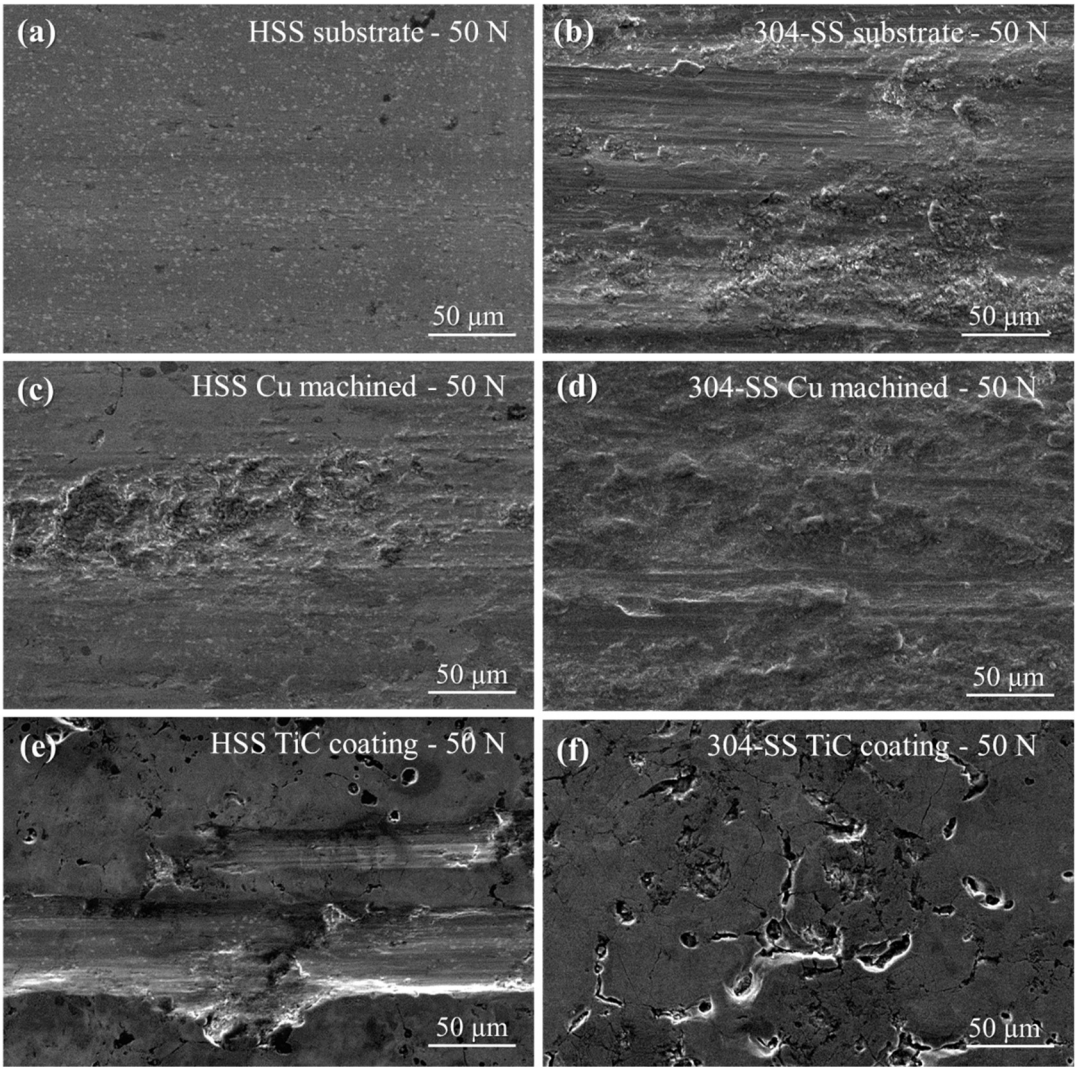

Figure 6-12 High magnification SE images of wear tracks of: (a,c,e) HSS; and (b,d,f) 304-SS, under conditions of 50 N loading. (a,b) as-polished substrates; (c,d) EDM Cu reference samples; and (e,f) ED cermet coatings

Figures 6-12a,b illustrate wear surfaces of the as-polished HSS and 304-SS substrates under the higher loading condition of 50 N, respectively, demonstrating the same morphologies of the samples under 10 N loading, indicative of the same wear mechanism.

The EDM Cu HSS surface under 50 N loading comprised a mixture of morphologies, including both rough and smooth regions, illustrative of abrasive wear. Conversely, the EDM Cu 304-SS surface exhibited more severe wear, with the dominance of adhesive wear along with some abrasive wear, EDS analysis of the wear

surface again indicated enhanced levels of oxidation, up to ~ 20.7 wt%. Both cermet coated HSS and 304-SS substrates under 50 N loading (Figures 6-12e,f) (Figures 6-13 and 6-14) showed improved wear performance compared to the as-polished substrates, but exhibited different wear regimes as compared to 10N load condition (cf. Figures 6-11e,f). Wear tracks on the cermet coated HSS under 50 N load exhibited sharp abrasive grooves concentrated in the middle of the wear track for almost the entire length of the wear tracks (Figure 6-13a). Figures 6-13b,c show details of sharp abrasive grooves and some embedded debris in this case, characteristic of brittle fracture/grain pull-out. Lower levels of oxidation were found to be associated with these worn surfaces (Figures 6-13b,c; regions I and II; O ~ 4.6 wt% and 4.3 wt%, respectively).

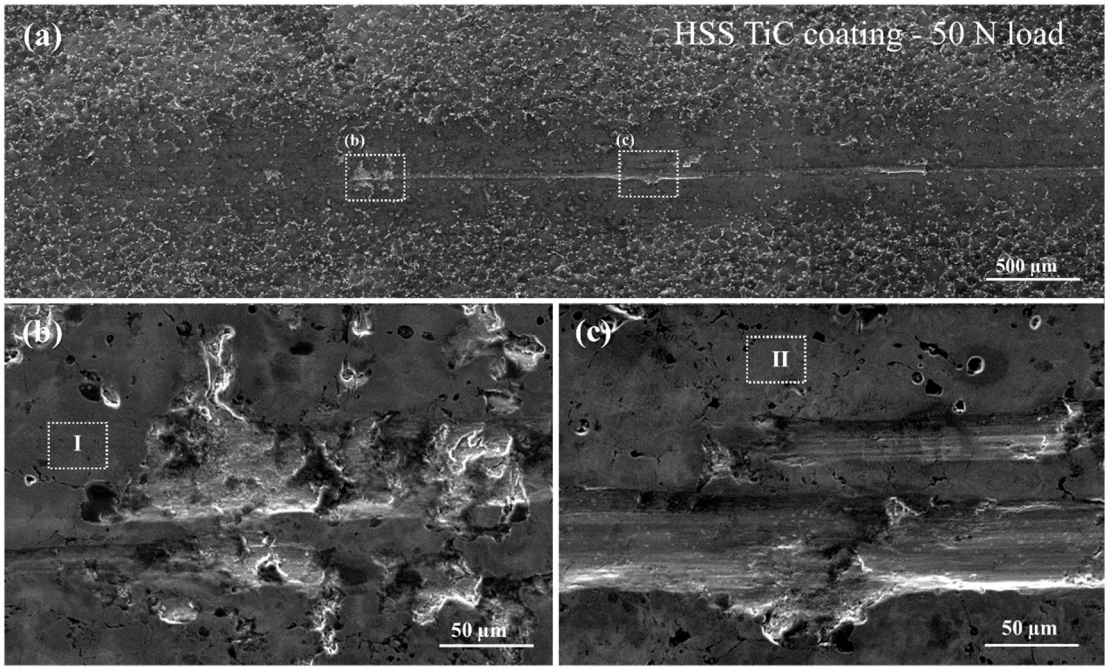

Figure 6-13 Low magnification SE images showing (a) the extent and (b,c) representative details of a wear scar on a cermet coated HSS sample, under loading conditions of 50 N, again indicative a greatly improved wear performance

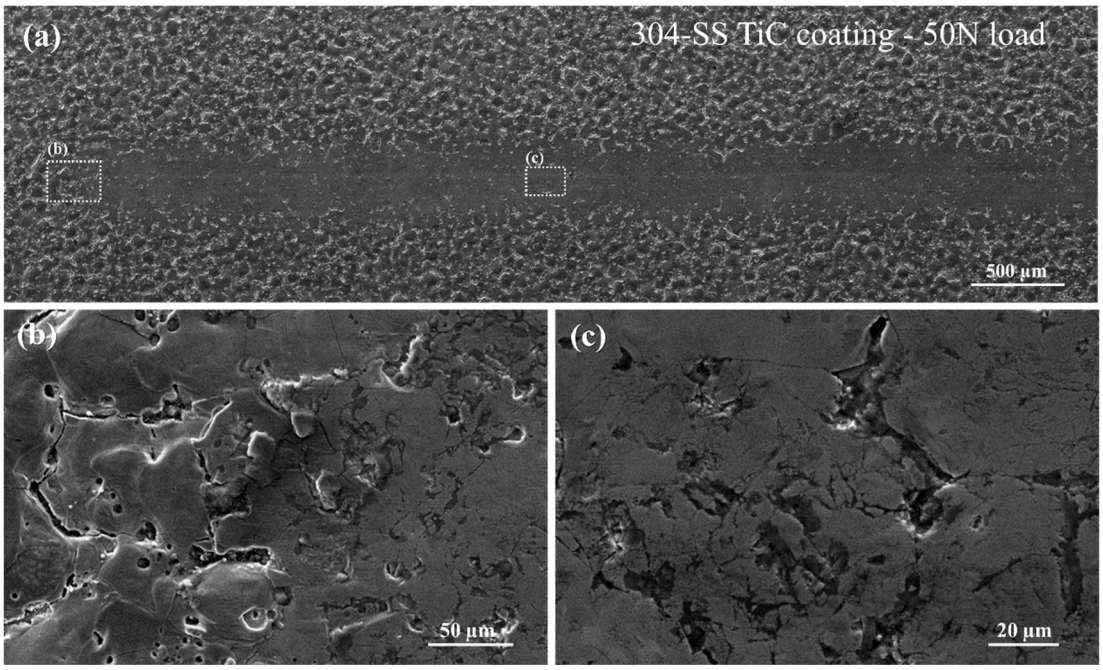

Figure 6-14 Low magnification SE images showing: (a) the extent; and (b,c) representative details of a wear scar on cermet coated 304-SS, under loading conditions of 50 N, again indicative a greatly improved wear performance

Figure 6-14 presents a wear scar and highlighted details of cermet coated 304-SS under 50 N of loading. The wear track showed evidence of fracture and pull-out of material, with the surface exhibiting newly developed regions of cracking and micro-cracking (Figures 6-14b,c), distinct from those remnant from the EDC processing, along with some debris at the ends of the wear tracks.

6.3.3 Counterbody wear rate

The specific wear rates of the counterbodies for all the wear tests are summarised in Figure 6-15. In the case of all tests using 304-SS substrates (Figure 6-15b), the counterbody wear rates reflected very closely the trend of the coating wear rate, albeit ~ 1 order of magnitude lower. This lower wear rate may be explained by the use of a harder, more wear resistant alpha-alumina counterbody. Additionally, the trend for increased sample wear rate with increased load matches the wear rate trend for the counterbodies.

Figure 6-15a present the counterbody wear rate of the HSS-based samples, interestingly the TiC coating on HSS yielded a slightly higher value of 5.0 x 10^{-7} mm^3/Nm counterbody wear rate compared to that of the TiC coating on 304-SS of 3.9 x 10^{-7} mm^3/Nm. This is despite the notably lower coating wear rate when using a HSS substrate compared to the 304-SS. This phenomenon may be explained by the observed three-body abrasion which is thought to have taken place in samples based on HSS substrates, as evidenced by the existence of a sharp abrasive groove in the centre of the wear track on TiC/HSS. Such a phenomenon resulting in localised wear on the coating, but not significantly increasing overall wear across the track, is likely to exacerbate counterbody wear. Complementary optical microscope images of typical wear scars, observed on balls after testing against the cermet coatings on both substrates, under low and high loading conditions, are shown in Figure 6-16.

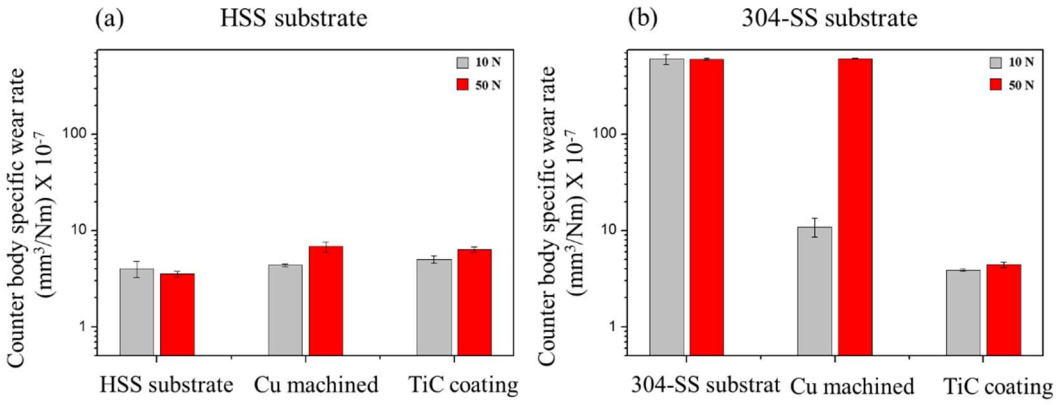

Figure 6-15 Specific wear rates of the counterbody Al_2O_3 ball after sliding test against TiC/Fe cermet coating on a) HSS and b) 304-SS, both under loading conditions of 10 and 50 N

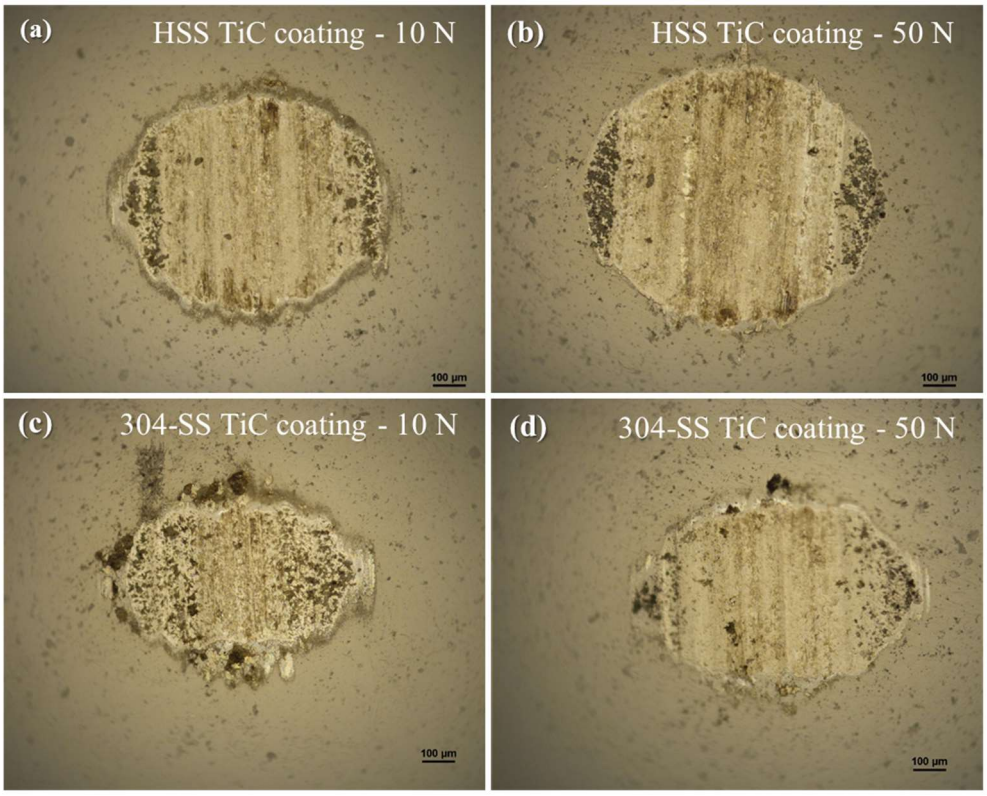

Figure 6-16 Optical microscope images of Al_2O_3 ball wear scars, after sliding wear testing against TiC/Fe cermet coatings on: (a,b) HSS; and (c,d) 304-SS, both under conditions of (a,c) 10 N and (b,d) 50 N

Figure 6-17 presents SE images of an Al_2O_3 ball, before and after sliding against a cermet TiC/Fe ED coating on HSS (under condition of 10 A current and 8 µs pulse-on time). The un-worn Al_2O_3 ball exhibits micro-voids, whilst EDS analyses confirmed that the ball consisted of only Al and O (Figure 6-17a). Pitting and abrasive wear is seen on the ball used to wear test the cermet coating on HSS (Figure 6-17b), with EDS analyses of the worn surface indicating transfer of coating material during testing and the generation of a tribolayer [88, 146].

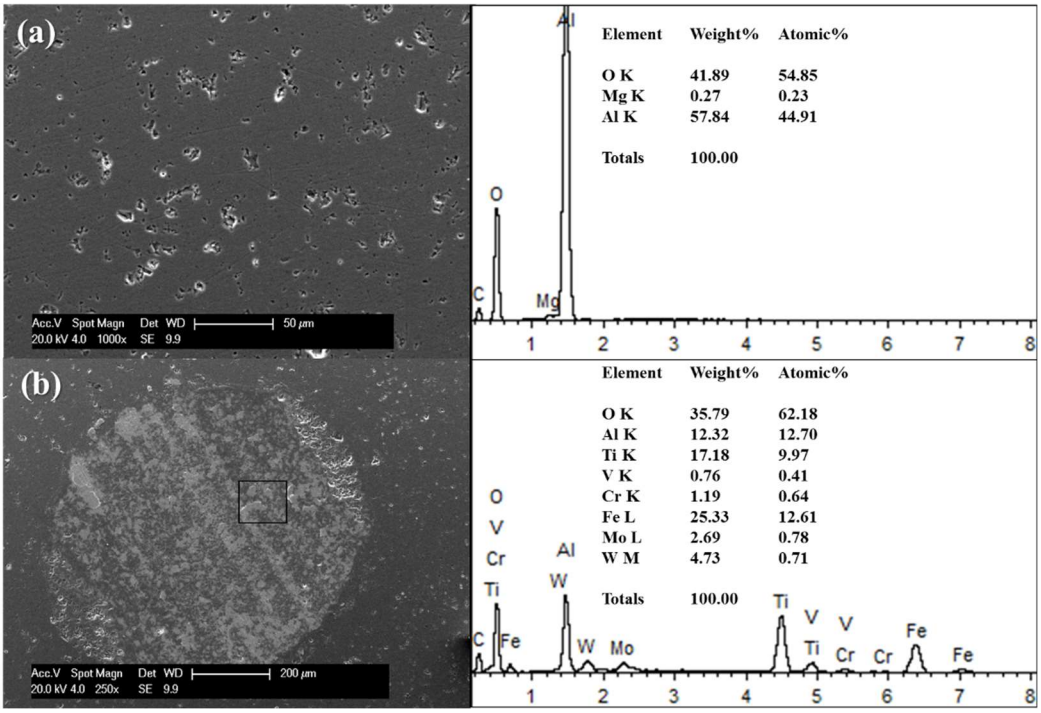

Figure 6-17 SE images and associated EDS analyses of: (a) a new Al_2O_3 ball; and (b) a ball after sliding testing against a TiC/Fe cermet coating on HSS

6.3.4 Coefficient of friction (CoF)

Figures 6-18 and 6-19 present time dependent coefficient of friction (CoF) profiles, recorded during wear testing, for the as-polished substrates, the EDM Cu machined surfaces and the TiC/Fe cermet coatings, under conditions of 10 N and 50 N loading. The cermet coated samples, in all cases, yielded lower CoF values, as compared to the as-polished and EDM Cu processed samples. CoF values for cermet coated HSS and 304-SS, once established, under loading conditions of 10 N and 50 N, varied between ~ 0.2 and ~ 0.6. For example, Figure 6-18a shows the CoF profile for cermet coated HSS under 10 N load, with gradual increase to ~ 0.4 after ~ 160 minutes, at which point steady state friction was achieved. A different onset to the profile was observed for the case of cermet coated HSS under 50 N load (Figure 6-18b), with rapid increase of the CoF to ~ 0.7 before dropping to < 0.1, within the first few seconds, as the wear profile initiated. A steep increase in CoF to ~ 0.5 after ~ 15 minutes occurred, as the

wear profile became established and thereafter maintained. Conversely, Figure 6-19a presents associated CoF profiles for cermet coated 304-SS, under 10 N loading, demonstrating very low CoF values from the outset, up to a steady state value of ~ 0.3. A more gradual increase in the CoF profile was returned for cermet coated 304-SS under 50 N loading, throughout the duration of the test, reaching a value of ~ 0.55.

The CoF of as-polished HSS, under conditions of 10 N and 50 N loading (Figures 6-18a,b), showed initial rapid increase, as the contact area became established, followed by steady state friction of value ~ 0.7 and ~ 0.8, respectively. The CoF of the as-polished 304-SS substrate, under 10 N (Figure 6-19a), showed similar, initial behaviour, but was noticeably more erratic, returning higher friction values after the initial run-in period. For the case of the 304-SS substrate under 50 N (Figure 6-19b), a more steady increase in CoF was observed, reaching a value of ~ 1.2 by the end of the test.

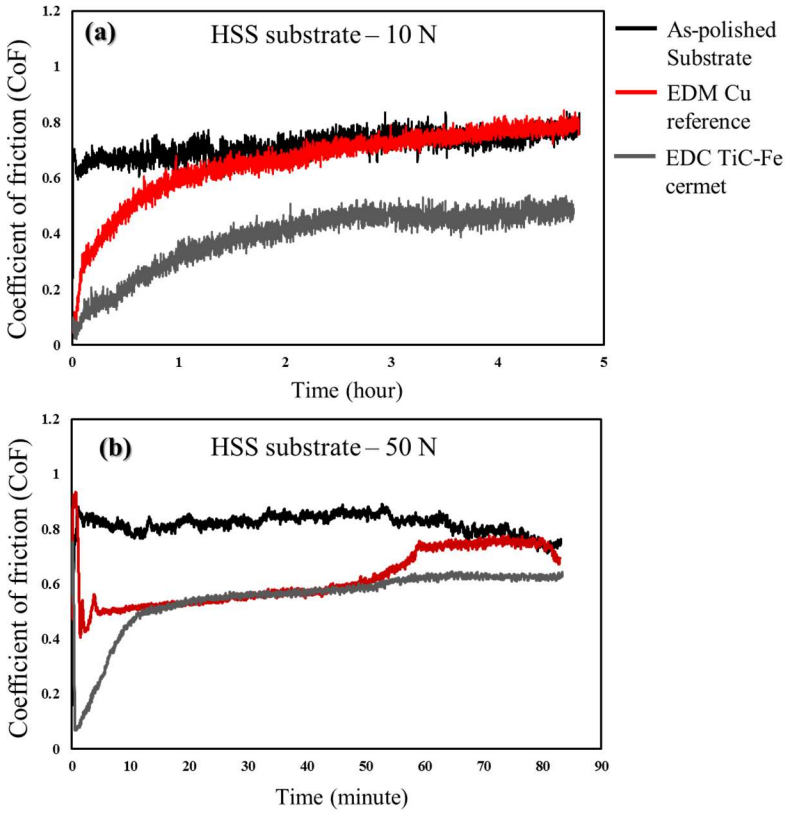

Figure 6-18 Time dependent CoF profiles for as-polished substrates, EDM Cu reference samples, and EDC TiC/Fe cermets on HSS, under conditions of: (a) 10 N; and (b) 50 N, respectively

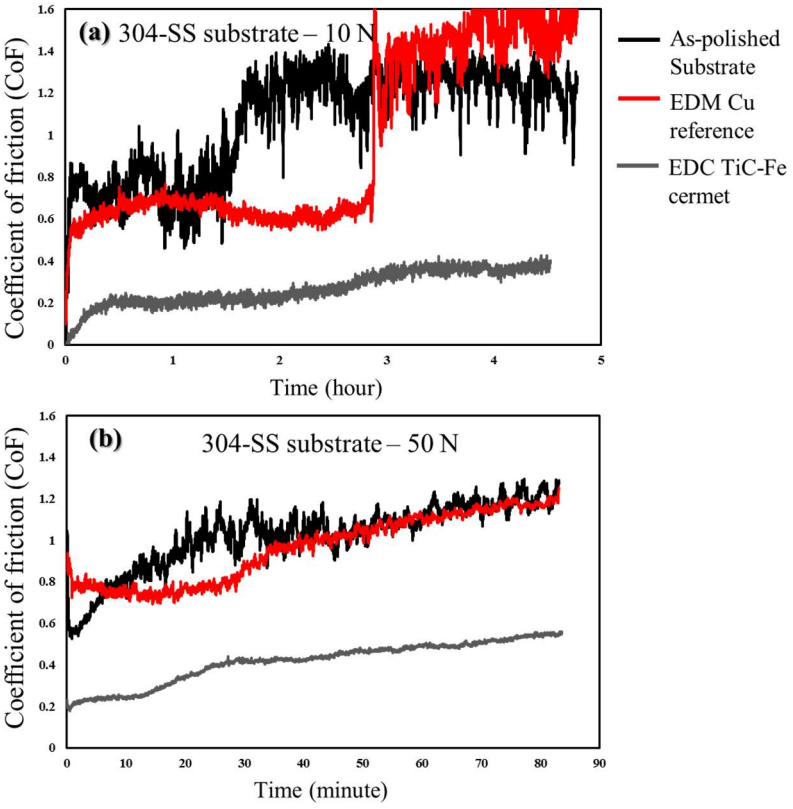

Figure 6-19 Time dependent CoF profiles for as-polished substrates, EDM Cu reference samples, and EDC TiC/Fe cermets on 304-SS, under conditions of: (a) 10 N; and (b) 50 N, respectively

For comparison, the CoF profiles for EDM Cu processed samples all tended to show intermediate performance, between that of the as-polished and cermet coated samples during the early stages of wear, becoming similar to the as-polished samples by the end of testing.

For the case of the Cu processed HSS under 10 N load (Figure 6-18a), a rapid climb of the CoF to mimic the profile of the as-polished substrate after ~ 90 minutes occurred. When the load was raised to 50 N, the Cu processed sample, after an initial rapid process of stabilisation, mimicked the performance of cermet coated HSS for about ~ 60 minutes, before a process of degradation, following the profile of the as-polished substrate (Figure 6-18b). The CoF profiles for Cu processed 304-SS showed similar profiles to that of the as-polished substrate, under both loading conditions. However, under 10 N loading (Figure 6-19a), a noticeable discontinuity in the CoF profiles occurred at ~ 1.5 h and ~ 3 h, for the as-polished and Cu processed samples, respectively (Figure 6-19a).

It is emphasised that the CoF profiles were similar for all repeat tests, with some minor variations, as expected, being attributable to localised surface variations and differing contact behaviour with the wear media.

6.4 Reciprocating wear testing of LSM processed EDC TiC/Fe

6.4.1 Specific wear rates

Figure 6-20 presents a specific wear rate data for cermet coated HSS and 304-SS, laser processed at 240 W and 280 W, under identical loading conditions of 10 N and 50 N, for comparison with as-coated samples (as previously described).

Slight improvement in wear rate was returned for the cermet coated HSS under high loading conditions, however the wear rate for HSS under low loading conditions was slightly degraded. Further, the wear rate for all laser processed coatings on 304-SS increased (up to two orders of magnitude) with increasing laser power. For the coating on HSS substrate, the mean wear rate of 0.56 x 10^{-6} mm^3/Nm was returned for the 280 W processed coating using a 50 N load, as compared to 0.64 x 10^{-6} mm^3/Nm and 0.87 x 10^{-6} mm^3/Nm for the 240 W and untreated coatings, respectively.

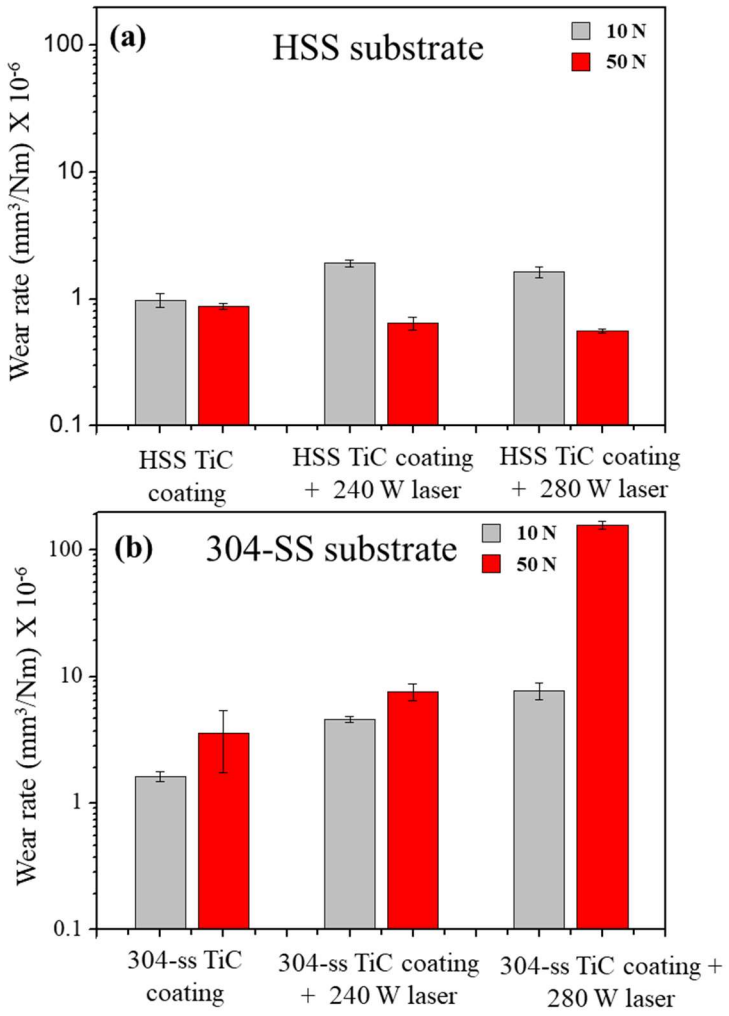

Figure 6-20 Specific wear rates of as-deposited and laser treated TiC/Fe cermet coatings as a function of power, 240 W and 280 W, under loading conditions of 10 N and 50 N on: (a) HSS and (b) 304-SS substrates, respectively

6.4.2 Wear scar characterisation

Figure 6-21 presents SE images of wear track details for 240 W and 280 W laser processed cermet coatings on HSS under loading conditions of 10 N and 50 N (see Appendix 5 for more details of SE images of the wear track and highlighted details), showing no significant differences in surface topography, with some scratch along the surface . However, the sharp grooves and brittle fracture associated with wear scars on as-coated HSS under 50 N loading (Figures 6-12e and 6-13:a-c) are absent from the laser treated samples, demonstrating the benefit of laser processing for the homogenisation of cermet coated HSS and improved wear performance under high loading conditions.

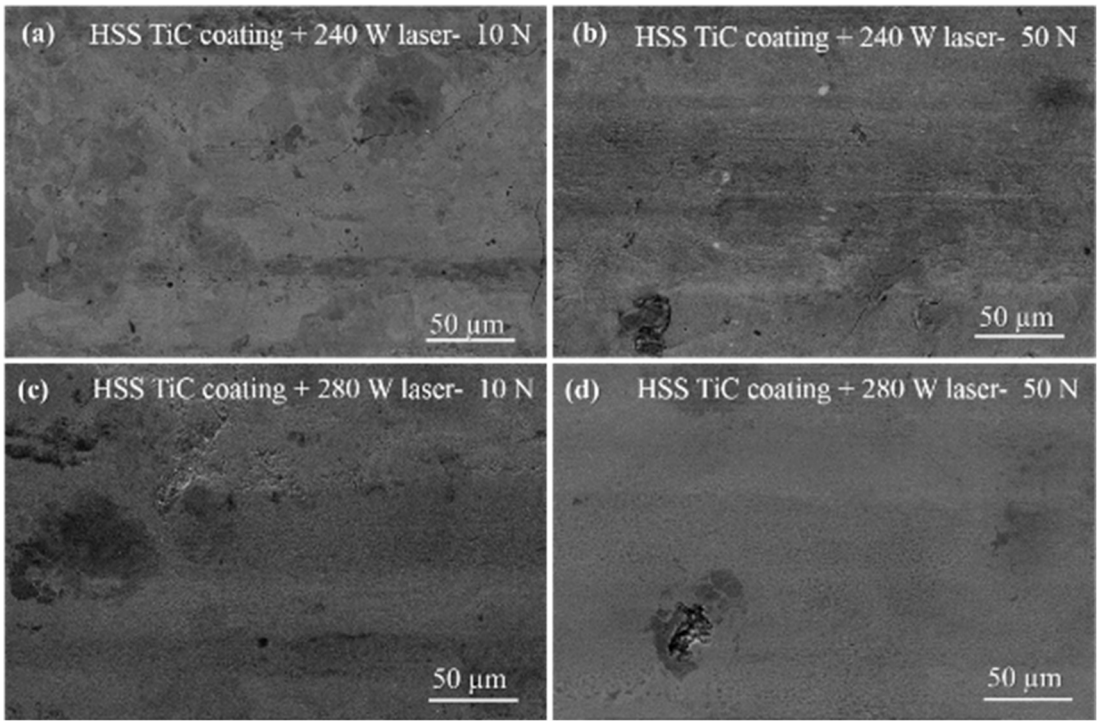

Figure 6-21 SE micrographs of wear scar details following: (a,b) 240 W and (c,d) 280 W laser surface treatment of TiC/Fe cermet coated HSS under loading conditions of: (a,c) 10 N; and (b,d) 50N, respectively (1600 mm/minute scan speed; Ar environment)

Figure 6-22 presents SE images of wear track details of 240 W and 280 W laser processed cermet coatings on 304-SS under loading conditions of 10 N and 50 N (see

Appendix 5 for more details of SE images of the wear track and highlighted details), showing smooth and uniform wear scars representative of the majority of tracks on these cermets processed under 240 W laser power and 10 N normal load (Figure 6-22a). Under high loading conditions, the surfaces exhibited abrasive grooves characteristic of more severe wear (Figure 6-22b). Indeed, for laser processed cermet coated 304-SS, the wear tracks in all cases showed abrasive grooves characteristic of more severe wear. Further, cermet coatings laser processed at 280 W laser power also showed an abrasive wear mode under low loading conditions(Figure 6-22c), and the coating was removed entirely under 50 N loading conditions(Figure 6-22d). Hence, LSM processing is considered not beneficial for cermet coatings on more ductile steel substrates.

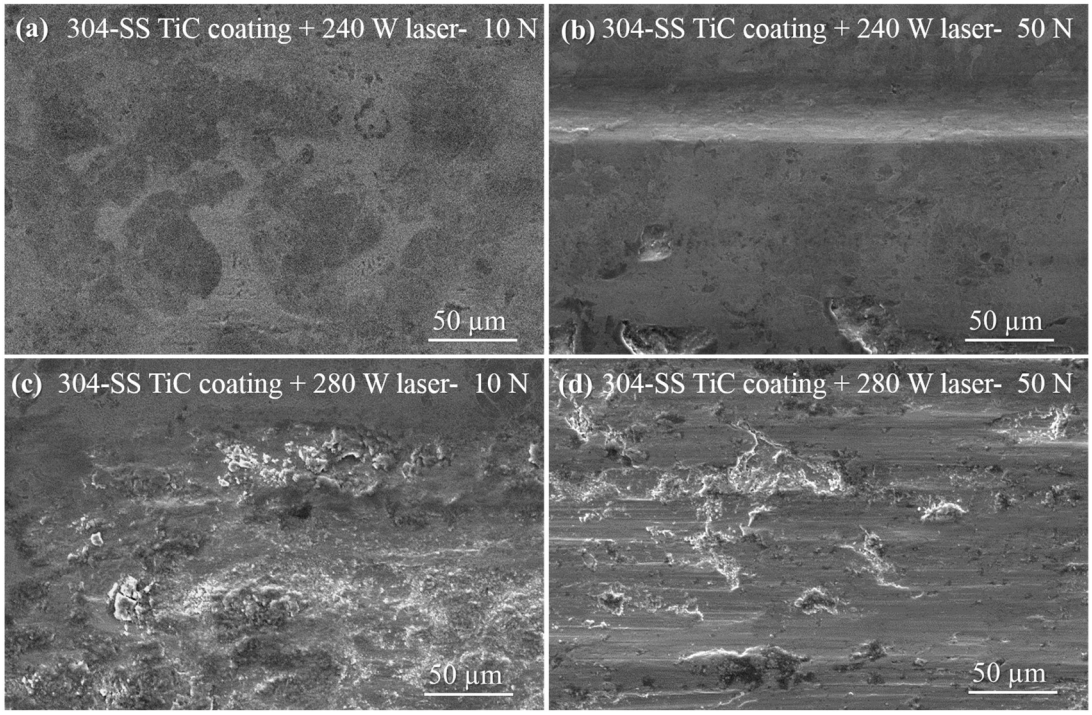

Figure 6-22 SE micrographs of wear scar details following: (a,b) 240 W and (c,d) 280 W laser surface treatment of TiC/Fe cermet coated 304-SS under loading conditions of: (a,c) 10 N; and (b,d) 50 N, respectively (1600 mm/minute scan speed; Ar environment)

6.4.3 Coefficient of friction (CoF)

Figure 6-23 shows CoF profiles yielded by wear tests on cermet coated HSS samples, LSM processed at 240 W and 280 W, under loading conditions of 10 N and 50 N, showing no significant change in CoF for laser processed samples, as compared to as-coated HSS. However, an increase in laser power resulted in an increase of the CoF for laser processed coatings on 304-SS (Figure 6-24). This can be explained by the high CoF of the as-polished 304-SS (Figure 6-19: black line), and hence its sensitivity to a decrease in the amount of TiC present within the coating with increasing laser power (Table 6-2).

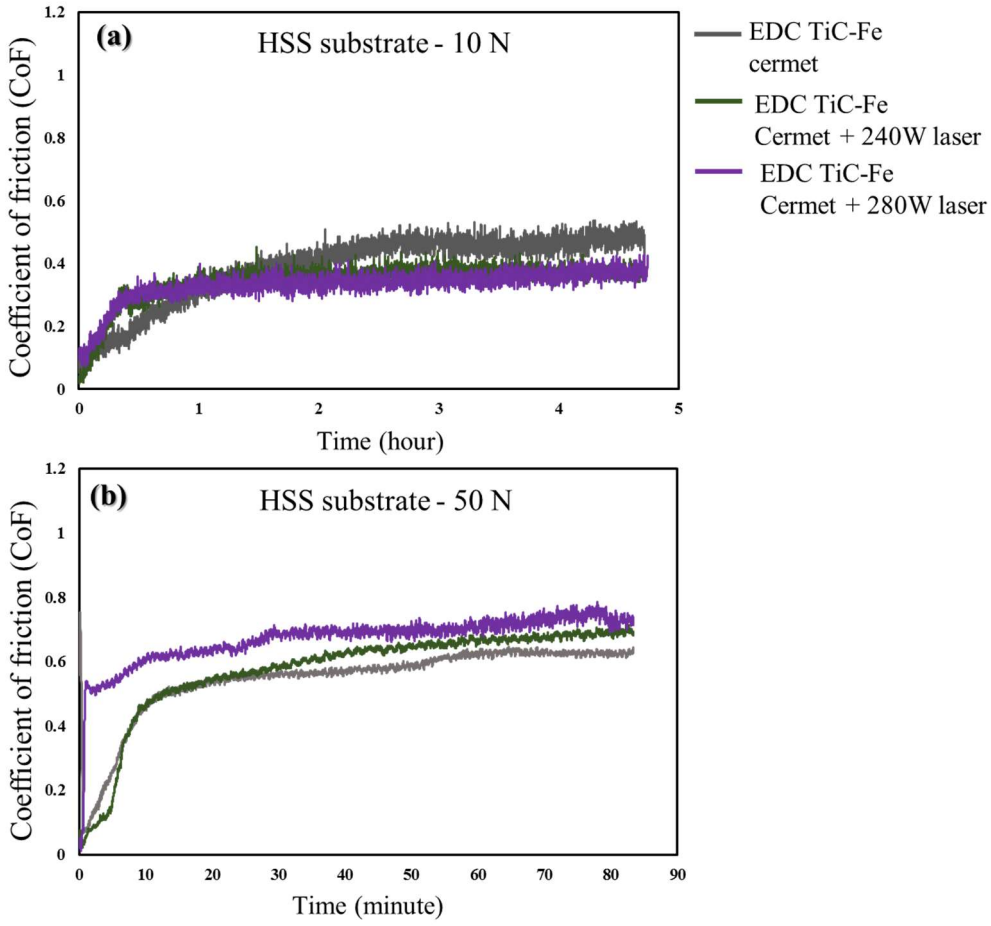

Figure 6-23 Time dependent CoF profiles for as-deposited and LSM treated TiC/Fe cermet coatings on HSS, as a function of power, 240 W and 280 W, under loading conditions of a) 10 N and b) 50 N

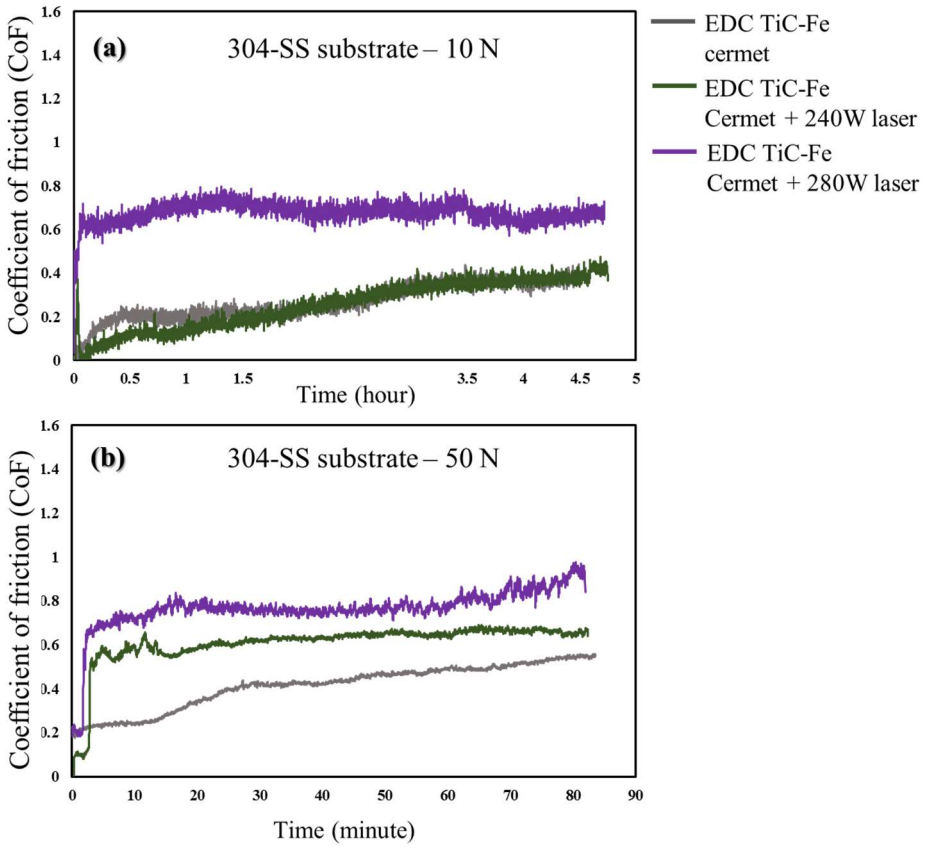

Figure 6-24 Time dependent CoF profiles for as-deposited and laser treated TiC/Fe cermet coatings on 304-SS, as a function of power, 240 W and 280 W, under loading conditions of: (a) 10 N and (b) 50 N

6.5 Discussion

This study has shown that EDC TiC/Fe cermet coatings on two different steels can yield dry sliding wear resistances up to two orders of magnitude greater than that of the substrate alone (Figure 6-5), with the variability of specific wear rates reflecting the respective morphologies of the coatings, substrates and loading conditions applied. The lowest wear rate was returned for coated HSS samples under 50 N loading (Figure 6-5a), whilst best improvement in wear resistance, compared to the as-polished substrate, was shown for coated 304-SS samples under 10 N loading (Figure 6-5b).

It is interesting to note that the wear rate of cermet coated 304-SS was approximately twice that of coated HSS under loading conditions of 10 N. However,

the wear mechanism appeared to be the same for both cermet coated steels under 10 N load, with the production of smooth, wear tracks, mediated by a mechanical polishing mechanism (Figures 6-11e,f) and schematic illustration in Figures 6-25a,c [146]. Further, under conditions of 50 N loading, the wear rate of cermet coated 304-SS was approximately four times that of coated HSS, but with a degradation of wear rate for the 304-SS sample, as compared with a slight improvement in wear rate for the HSS sample, respectively, reflecting a difference in the wear mechanism under conditions of higher loading. This point is particularly notable, given the level of TiC present in the coating on 304-SS (Ti 39 wt%) was significantly higher than that for coated HSS (29 wt%) (Table 6-2)). Hence, it is evident that the substrate has a strong influence on the wear performance of cermet coated steels.

The dependence of wear behaviour on coating/substrate properties may be explained with reference to the microstructures and properties of the TiC/Fe coatings and the steel substrates. The fine details of the microstructures of the coatings on both steel substrates investigated in this study are shown in cross-section in Figures 4-17 and 4-18. It is recognised that these TiC-based coatings comprise a complex intermix of a Fe-based matrix with TiC grains, of varying sizes and geometries, depending on depth into the coating (Figures 4-9, 4-17 and 4-18). Hence, it is logical that the final mechanical properties of the coating comprise those of the individual TiC and Fe phases. Particularly given the much poorer wear behaviour of pure 304-SS compared to HSS, the poorer wear behaviour of TiC coated 304-SS can be explained generally by the much lower hardness of 304-SS (196 HV; σ = 16.8) in comparison to that of HSS (733 HV; σ = 94), hence imparting poorer wear properties to the developed coating. It is recognised that TiC coatings on 304-SS exhibited hardness values of ~1800 HV, as compared to ~ 2196 HV for coatings on HSS, when processed under

conditions of 10 A current and 8 μs pulse on time. When considering this hardness level, the contribution of matrix material from a much softer steel (~ 196 HV compared to ~ 733 HV for HSS), is likely to provide significant impact on the mean coating mechanical properties, and hence wear behaviour. The pervasive nature of the substrate as a matrix for the coating, as evidenced by the highly composite nature of the coatings on both substrate types (as shown in Figures 4-17 and 4-18, respectively) also supports the suggestion that substrate properties contribute significantly to the developed coating performance.

However, the contribution of a second mechanism to wear behaviour under high loading condition of 50 N cannot be ruled out, *i.e.* deflection of the coating, caused by deformation of the underlying, substrate, in turn leading to an increase in wear rate [6]. Hence, as in this case, a softer substrate (in this case 304-SS) would contribute to an increased coating wear rate as illustrate in Figures 6-25c,d.

The TiC/Fe coatings on HSS, under 50 N loading, exhibited signs of fracture and grain pull-out (Figure 6-13), with the wear tracks comprising long, sharp, abrasive grooves, indicative of either debris trapped between the counterbody and substrate, or debris adhered to the counterbody. This phenomenon, typical of an abrasive wear mechanism, is well understood with entrapped, hard/sharp, relatively large, ceramic particles acting as abrasive particles or moving indents, causing scratching [9, 13, 90] (Figure 6-25b). This wear mechanism differs from that of cermet coated 304-SS, under 50 N loading, which showed a reduction in wear performance. The prevalence of some pull-out of material and crack formation in this case is indicative of deformation of the underlying, softer substrate (Figure 6-14), resulting in deflection of the coating, in turn leading to an increase in wear rate [6] (Figure 6-25d).

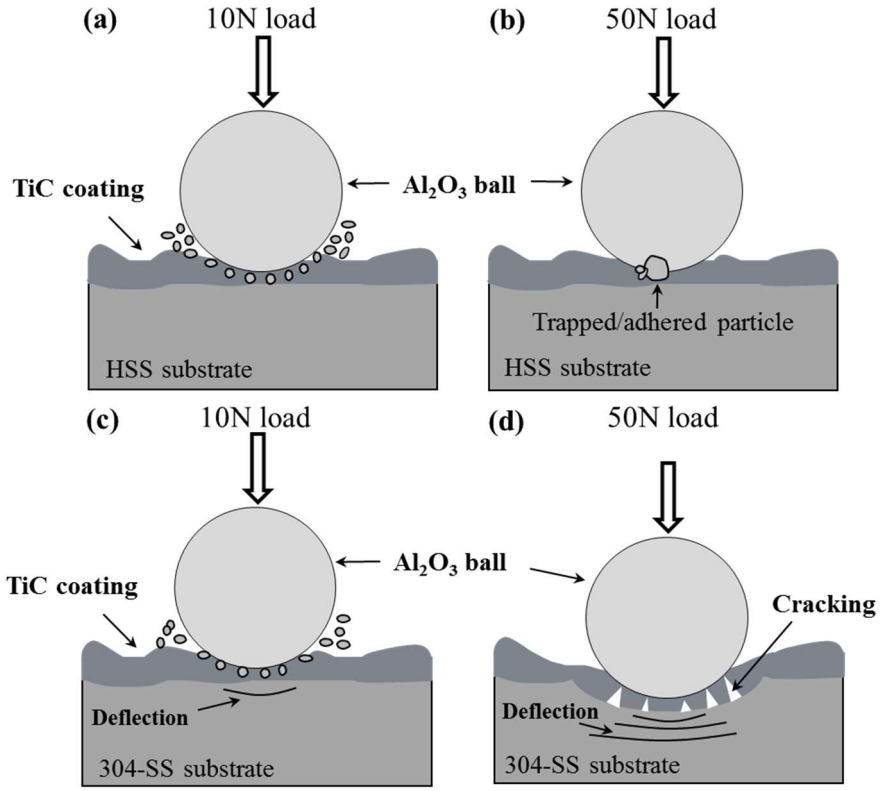

Figure 6-25 Schematic illustrations of the wear mechanisms of TiC/Fe cermet coated: (a,b) HSS and (c,d) 304-SS, under conditions of 10 N and 50 N loading, respectively

It is noted that the specific wear rates of these ED TiC/Fe cermet coated steels, produced using a semi-sintered TiC tool electrode (~ 0.9 - 1 x 10^{-6} mm^3/Nm on HSS and ~ 1.6 - 3.6 x 10^{-6} mm^3/Nm on 304-SS, under 10 N and 50 N loads, respectively), are significantly lower than those reported for TiC-based coatings produced using a semi-sintered Ti tool electrode, with and without graphite mixed dielectric fluid (*i.e.* 5.8 - 8 x 10^{-6} mm^3/Nm and 24.6 - 150 x 10^{-6} mm^3/Nm, under 20 N and 50 N loads, respectively), on $45^{\#}$ carbon steel, based on wear tests of 15 minutes duration using a 5 mm Si_3N_4 ball at room temperature [45]. This demonstrates that the direct ED production of TiC/Fe using a TiC tool electrode provides for coatings with enhanced wear resistance compared to cermet coatings produced via the in situ reaction of Ti with C.

Compared to other coating methods, the range of specific wear rates observed using EDC here from a semi-sintered TiC electrode is broadly consistent with other TiC thin coating systems. For example, magnetron sputtered nanocrystalline TiC/amorphous C composite thin film coatings yielded wear rates of ~ 2 - 4 x 10^{-6} mm^3/Nm at room temperature for coatings in the range of 0.5 < C/Ti < 1.5 wt% ratio, under 1 and 5 N loading conditions [90]. In addition, comparison can be made with the same cermet material system under identical reciprocating ball-on-flat geometry, to the present work. For example, Onuoha *et al.* [147] report a variable specific wear rate for TiC-304L stainless steel composites prepared by melt infiltration of ~ 4 - 24 x 10^{-7} mm^3/Nm, when worn against 6.35 mm diameter WC-Co balls for a load range of 20 - 80 N.

It is also interesting to note that EDC processing imparts superior wear resistance to steels, as compared with EDM processed surfaces using a reference Cu tool electrode. EDM surfaces subjected to wear testing under identical conditions yielded similar wear rates to those of the as-polished substrates (Figure 6-5), with the exception of processed 304-SS under 10 N loading which showed an order of magnitude improvement in specific wear rate. This latter observation was attributed to some hardening of the sample near surface upon crystallisation following EDM processing, combined with the formation of iron carbide Fe_3C during the process, due to reaction of Fe from the substrate and cracked carbon from the dielectric, as confirmed by XRD (Figure 4-19a) [28], thereby increasing the effective wear resistance of the sample compared to the as-polished 304-SS. No additional benefit was imparted by EDM into the HSS given its initial, higher wear resistance.

An additional processing step of laser surface treatment was used in order to improve the surface morphology of the EDC TiC/Fe coatings, whilst seeking to

maintain wear performance. Under laser power conditions of 280 W, cracking and porosity were almost eliminated from the coating surfaces for both substrate types.

However, with regard to the wear performance of laser processed ED coatings on HSS, a minimal reduction in wear rate was returned only for the higher loading condition of 50 N, with a slight increase in wear rate under 10 N (Figure 6-20a). The reason for improvement in wear performance under higher loading may be attributed to surface homogenisation (Figure 6-1) and the removal of asperities which would otherwise induce stress concentrations and localised fracture (Figure 6-13). Conversely, diminished wear performance under the lower loading conditions of 10 N may be attributed to a reduction in the Ti wt% content of the coating, as a consequence of LSM processing (Table 6-2), which would act to reduce hardness (Figure 4-15b).

Intriguingly, for the case of laser processed TiC/Fe coatings on 304-SS, the wear rate degraded significantly in all cases (Figure 6-20b). This phenomenon may be explained with reference to the initial wear properties of the softer 304-SS, coupled with a reduction of the Ti wt% content of the coating, from ~ 39 wt% (as-deposited), to ~ 25 wt% (240 W laser power) and ~ 18 wt% (280 W laser power), respectively (Table 6-2). Further, the BSE images of laser processed samples Figures 6-2d,f indicated an increase in coating grain size (compared to as deposited Figure 6-2b), as a consequence of laser treatment, indicative of a slower cooling rate during the process of recrystallisation, which might also contribute to a reduction of coating mechanical properties and hence wear performance. Accordingly, LSM processing of EDC cermet layers acts to lower the ceramic content, being diluted with the base metal, such that wear performance then becomes dominated by the properties of the substrate.

6.6 Summary

TiC/Fe cermets have been produced successfully on HSS and 304-SS substrates using the EDC process with a semi-sintered TiC tool electrode. The as-deposited coatings exhibited complex, TiC/Fe cermet microstructures, with a mixture of equiaxed and banded columnar grains near the surface, and coarse to finely graded equiaxed grains towards the coating/substrate interface, reflecting the final cool-down sequence of ED processing. The cermet coatings on HSS and 304-SS yielded wear rates, under dry sliding conditions, one and two orders of magnitude lower than those of the as-polished substrates. In particular, wear performance was found to be dependent strongly on substrate type, with coatings on HSS being ~ 2 - 4 times more wear resistant than those on 304-SS. The variability of wear rate was attributed to a combination of factors, being dependent on the morphology of the cermet coatings combined with the mechanical properties of the substrate. An additional processing step of laser surface treatment was used to homogenise the ED cermet coatings, with conditions of 280 W laser power eliminating successfully all cracking and porosity characteristic of the as-deposited coatings. However, laser processing was associated with a general increase in wear rate for all samples, with the exception of HSS under high loading conditions. This effect was attributed to a dilution of the amount of TiC within the cermet coatings, following laser processing, combined with an increase in grain size. Improvement of the wear rate of laser treated, cermet coated HSS, under conditions of high loading, was attributed to the avoidance of abrasive wear mechanisms following homogenisation of the coating.

7 Discussion

7.1 Introduction

EDC is a surface modification process used to produce a hard coating on the workpiece surface, using a powder metallurgy (PM) tool electrode and/or by adding powder suspended in a dielectric fluid. The EDC process exploits the sparking principle, being an adaptation of EDM, to deposit a significant amount of tool electrode material onto complex shapes and uneven workpiece surfaces, with negative tool polarity promoting material deposition [21], as part of an integrated manufacturing process. The high temperatures associated with the sparking process allow a wide range of difficult to process materials to be deposited, including ceramics.

The main aim of this thesis has been to investigate the effects of ED processing parameters on the development of TiC/Fe cermet coatings, whilst developing improved understanding of the EDC process at the fundamental level. Detailed consideration has been given to the effects of process conditions of current and pulse on time, on the elemental distribution and microstructural development of coatings, correlated with their mechanical properties and tribological behaviour. In addition, the modelling of single spark events provided for better understanding of the principles of material deposition. The LSM processing of as-deposited ED coatings was also investigated, to improve the surface integrity of ED processed surfaces.

7.2 Surface topography and microstructure

TiC/Fe cermet coatings were produced successfully on HSS and 304-SS substrates, using the EDC process, utilising a semi-sintered TiC tool electrode. The surface uniformity and quality of the ED coating were strongly related to the discharge parameters of current and pulse-on time [21]. Surfaces produced with low input energy, such as low current (2 A) or low pulse-on time (2 μs), exhibited the lowest number of voids and cracks (Figures 4-4b and 4-5a). Increasing current and/or pulse-on time resulted in increased cracking and void formation [34], reflecting the impact of increasing input energy, along with Ti content variations within the coatings, and the consequences of a rapid cooling rate. TiC/Fe ED coatings on 304-SS and HSS substrates, deposited under conditions of 10 A and 8 μs, exhibited a similar surface topography with almost similar roughness values of ~ 1.3 μm and ~ 1.2 μm, respectively.

Figures 4-17 and 4-18 demonstrated that the coatings were indeed a metal matrix ceramic composite, containing a dispersion of TiC and Fe, with a mixture of equiaxed and banded columnar grains near the surface, and coarse to finely graded equiaxed grains towards the coating/substrate interface, reflecting the final cool-down sequence of ED processing. Figure 4-10 presented an ADF-STEM image of the coating, again created under conditions of 10 A current and 8 μs pulse-on time, along with associated EDS elemental maps, showing distinct TiC grains within an Fe-based matrix, confirming again that the developed coatings were indeed cermets. Uniform carbon distributions throughout the crystalline regions of the coatings, along with localised, enhanced concentrations attributable to amorphous inter-granular carbon, were also observed (Figure 4-10, arrowed).

Coatings produced under the low energy conditions of 2 A / 8 µs and 10 A / 2 µs showed highly non-uniform distributions of TiC (Figures 5-12a and b, respectively), reflecting a lower level of intermixing between material transferred from the tool electrode and the workpiece material. Increasing the current to 10 and 19 A, at a fixed pulse-on time of 8 µs, led to higher amounts and more regular distributions of TiC throughout the coatings, reflecting the development of a complex microstructure (Figures 5-12c,e,g), being attributed to the electrode condition and the complexity of sequential melting and deposition mechanisms, during multiple discharges events.

High-resolution transmission electron microscopy (HRTEM) imaging (Figure 4-9) provided detailed insights into the nanostructured TiC reinforcing layer on 304-SS. More recently, a similar observation of a developing nano-structure for the recast layer of EDM Fe-Al-Mn alloys was reported [35]. Further, Murray *et al*. [36] reported on significant tool electrode material deposition, with grains down to 3 nm diameter within the recast layer during EDM of single-crystal Si, processed using a 150 µm diameter tungsten tool electrode. The application of the XRD Scherrer equation indicated average TiC grain sizes within the cermet coatings investigated here to be ~40 nm, being significantly smaller than the average ~ 130 nm grain sizes of the TiC starting material, which supports the suggestion of the melt pool being fully molten prior to solidification, and that tool electrode and workpiece material intermixing occurs during the melt pool lifetime.

The as-deposited TiC/Fe cermet coatings on 304-SS exhibited dominant diffraction peaks from the TiC phase, with the indication of some slight preferred orientation, in addition to smaller peaks attributed to austenite γ-Fe, martensite α′-Fe, chromium carbide Cr_3C_2, cementite Fe_3C and amorphous carbon (Figures 4-7, 4-8 and 4-19a), whilst showing increased dominance of TiC with increasing current at fixed pulse-on

time (Figure 4-7), combined with the development of higher levels of coating crystallinity.

It is considered that excess C in the system may originate from the dielectric oil, in combination with C from substrate, contributing to the development of trace levels of Fe_3C and Cr_3C_2 identified. The diffusion and reaction of C with molten iron to form iron carbide is a commonly reported phase present within EDM steels [148]. Similarly, Gill and Kumar [28] reported on the presence of Fe_3C and W_3C on hot die steel H11 after ED processing with a Cu-W powder metallurgy tool electrode. Similarly, as-deposited coatings on HSS substrates comprised mainly TiC, in addition to smaller peaks attributable to ferrite α-Fe or martensite α′-Fe, along with a signature for austenite γ-Fe.

7.3 Coating hardness

EDC TiC/Fe layers exhibited high hardness value, ~ 4 - 8 times higher than the 304-SS substrate (196 HV; $\sigma = 16.8$), with increasing current from 6 A to 19 A, for fixed pulse-on time. This was attributed to the significant increase in TiC deposition with increasing discharge current (Figure 4-15a), with consequent increase in the wear of the tool electrode, in combination with the more uniform TiC distribution with increasing current (Figures 5-12c,e,g). Increased pulse-on time, from 2 μs up to 8 μs at a fixed current of 10 A led to an increase in hardness, followed by a steady reduction in hardness for further increases in pulse-on time (Figure 4-15b). The same behaviour of hardness value as a function of pulse-on time was report by Wang *et al.* [1] (Figure 2-10). A significant variations in coating hardness as a function of processing parameters may attributed to Ti wt% variations within the coatings (Figures 4-15a,b) [33, 43]. Another reason for hardness reduction with increasing pulse-on time is the

increase in grain size with increase input energy to the system and the low cooling rate of ~ 0.24 x 10^8 K/s under 64 µs pulse-on time as compared to the highest cooling rate returned for samples produced under conditions of low pulse-on time of 2 µs and fixed current at 10 A, of ~ 6.8 x 10^8 K/s, predicted by the model (Section 5.3.6; Figure 5-16 b), and the consequent longer time taken for cooling and recrystallization. For example, samples processed with a long pulse-on time of 64 µs at 10 A current exhibited larger grain sizes, columnar grains and a more dendritic structure (Figures 5-15:a-d). The anomalous hardness points observed during testing, *i.e.* high hardness, were attributed to localised TiC deposits (Figure 4-17d, arrowed), whilst low hardness was probably related to the presence of cracks and voids within the coating.

The preferred TiC/Fe EDC parameters on 304-SS and HSS (10 A current and 8 µs pulse-on time) produced coatings with hardness values of ~ 1800 HV and ~ 2196 HV, respectively, broadly consistent with other reported EDC TiC-based coatings. For example, Wang *et al.* [1] reported ~ 2000 HV for TiC coatings on carbon steel produced using a Ti green compact tool electrode under conditions of 4.3 A current and 8 µs pulse-on time. Further, Hwang *et al.* [43] reported ~ 1710 HV hardness values for a Ni workpiece processed using a multi-layered Ti/graphite tool electrode, under conditions of 12 A current and 80 µs pulse-on time. Similarly, Ueno *et al.* [46] reported ~ 2000 HV hardness values for coatings processed using a TiC sintered tool electrode under 25 A current and 8 µs pulse-on time.

The preferred EDC process parameters for the present TiC-based cermet materials system is suggested to be under low energy conditions, such as 10 A current and 8 µs pulse-on time, in order to produce coatings with good levels of hardness and an acceptable surface finish with low levels of voids and cracks.

7.4 Modelling of single spark event

The EDC processing technique is known to involve a complex mechanism of localised melting of the workpiece material, on the scale of individual discharges, along with material removal, material deposition from the tool electrode and intermixing within the near surface of the workpiece. However, the development of the EDC processing technique has been limited by a lack of detailed understanding the interaction of input energy with the processed material, and hence the composition and structure of the resultant coatings.

The amount of energy transferred to the workpiece is an important factor, affecting crater formation and the microstructural development of the near surface modified layers. The 2D transient heat transfer model presented, using finite difference methods, provided estimates for the effective value of F_v, combined with predictions for microstructural arrangements upon ED coating, as a function of processing conditions. The predicted F_v value varied between 17% and 23% for increasing current from 2 to 19 A at fixed pulse-on time 8 μs; and between 7% and 53% for increasing pulse-on time from 2 to 64 μs at a fixed current of 10 A (Figures 5-6 and 5-7). A maximum value for F_v was attained for the highest pulse-on time of 64 μs (Figure 5-7). This is consistent with the observation of previous work of determine the energy transfer to the workpiece during EDM processing, as reported by Singh [64] and Shabgard and Akhbari [136], with slightly higher values reflecting the differences in ED coating mechanisms of alloying and replacing the electrode material with workpiece material, rather than removing material during the EDM process, demonstrating that electrode polarity may affect the energy distribution [67].

Single crater event simulation during EDM processing provided information on material removal rate and the recast layer, and hence provided insights to improve the

control of this machining process. Similarly, the simulation of single spark events during EDC helped to explain the process of coating formation, in terms of thickness and resultant microstructure. By comparing experimental layer thicknesses and simulated crater depths (Figure 5-13), a good correlation was found with a slight increase in simulated crater depth with increasing current (2 - 10 A), whilst increasing pulse-on times led to increased simulated crater depths and experimentally measured layer thicknesses. This may be explained by an increase in the effective amount of energy transferred to the workpiece with increasing pulse-on time (Figure 5-7). This observation is true for both experimental and simulated crater radii (Figures 5-11a,b).

The predictions of heat transfer and cooling profiles along the crater depth of the melt pool for deposited craters processed under conditions of 10 A current and 8 µs pulse-on time (Figure 5-17) showed a sharp decrease of surface temperature from ~20,000 K to ~ 4,000 K within 10 µs of the off-time, in the first 3 µm of crater depth. This behaviour of rapid cooling is probably imposed by convection within the flowing dielectric fluid at the oil-flow/surface interface, followed by a lower cooling rate. Conversely, the initial slight increases in temperature, accompanied by slower cooling rates in the vicinity of the melt pool/solid substrate interface within ~ 3 µm from the bottom of the crater, are governed by conduction into the bulk substrate. Hence, the cooling phase has two distinct phases, with the first ~ 10 - 20 µs exhibiting rapid non-uniform cooling, leading up to the onset of TiC crystallisation (~ 3.16 - 3.25) x 10^3 K, followed by a second regime up to ~ 100 µs with more uniform cooling, leading to the onset of Fe matrix solidification (~ 1.4 - 1.45) x 10^3 K.

7.5 Formation mechanism of TiC/Fe composite coatings

Based on these experimental observations and numerical simulations of single crater deposition, the mechanisms for initial TiC cermet formation may be partitioned into three steps (Figure 7-1).

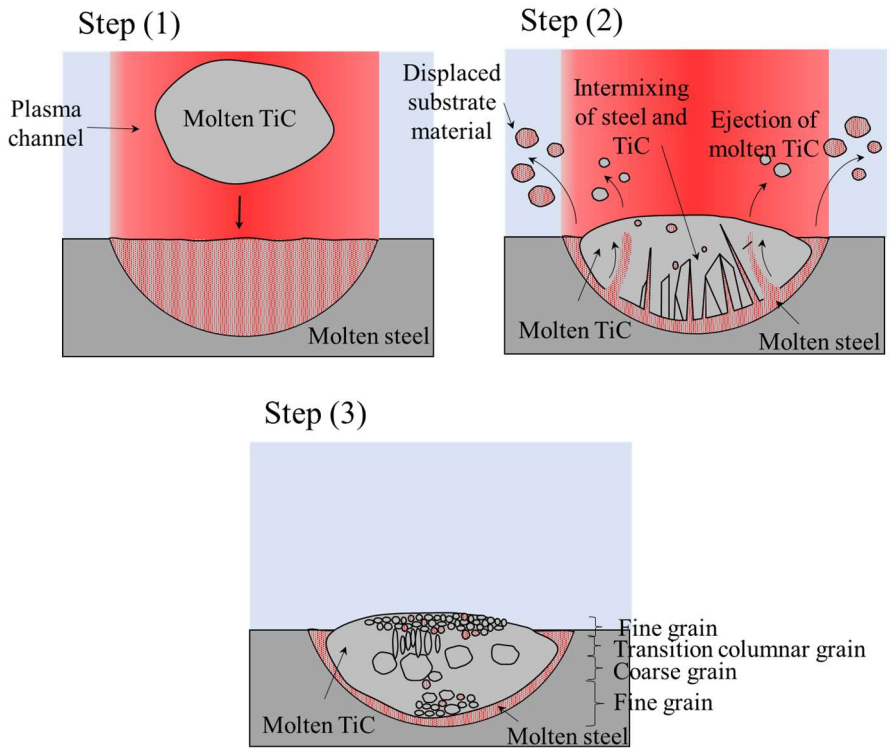

Figure 7-1 Depiction of initial TiC deposition/metal intermixing during the ED coating process

During Step 1, molten TiC is transferred and fuses with the melt pool created at the workpiece surface beneath the plasma channel during the pulse-on time. Step 2 relates to dissolution of the TiC from the tool electrode within the workpiece material during the melt pool lifetime. Step three, during the pulse-off time, it is recognised that TiC starts to precipitates before the Fe phase, given that the melting point of TiC is much higher than that of 304-SS. The concept of phase separation and precipitation of TiC during cermet microstructure development for TiC/Fe ED coatings may be explained

further with reference to the Fe-Ti-C ternary phase diagram [149]. Figure 7-2a presents liquidus surface projections for the ternary Fe-Ti-C phase diagram, whilst Figure 7-2b presents details of the projection surface for the Fe-rich corner [128].

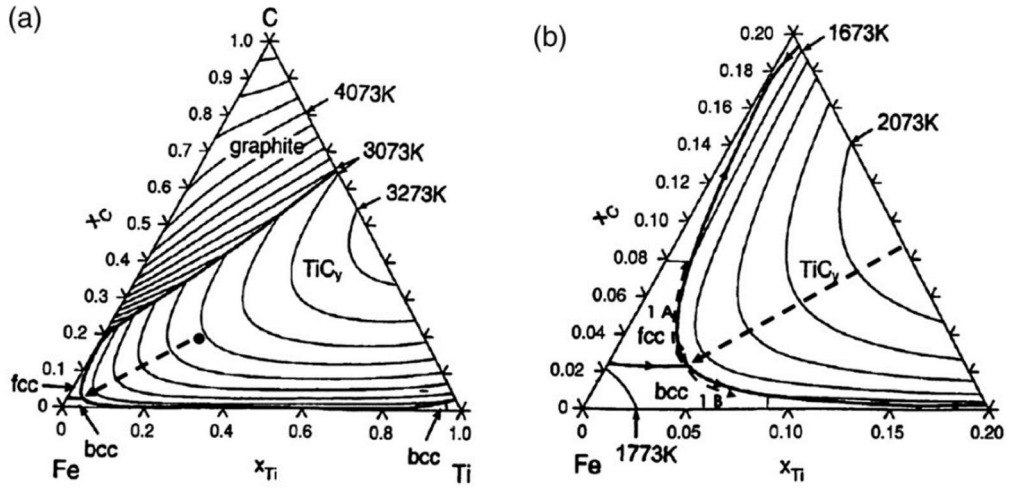

Figure 7-2 Liquidus projections for the Fe-Ti-C ternary system a) over whole composition range; and b) the Fe-rich corner [128]

Solidification would depend on the specific composition and temperature of the melt pool. For example, a mixture with carbon-rich composition allows for solidification path 1A (Figure 7-2b), whilst for a low-carbon mixture with more Ti, the solidification path follows 1B (Figure 7-2b). Solidification path 1A, for the case here, shares similarities with the Fe-C binary phase diagram, with the formation of austenite γ-Fe solid solution dendrites and associated formation of graphite or Fe_3C [128].

The modelled cooling profile then explains the solidification process (Figure 5-17), with a rapid cooling rate near the top surface governed by convection within the flowing dielectric, resulting in an equiaxed, very fine-grained microstructure (Figures 4-9a Region I , 4-9b , 4-17b,c and 5-14b Region I), reflecting a quenching process, followed by a transition towards columnar grains (Figures 4-9 Region III, 4-17b,c and 5-14c Region II). A slightly lower cooling rate, promoted by conduction into the

substrate, produced a relatively equiaxed coarse-grained, and fine-grained microstructure toward the coating/substrate interface (Figures 4-17d, 5-14c Region III and 5-14d Region IV), respectively. This mechanism is particularly valid for the TiC/Fe system, given the lack of solubility of Fe in TiC.

To understand the continuum development of TiC/Fe cermet ED coatings, one should consider the total number of sparks per location during processing (Table 4-3). For example, the favourable processing conditions of 10 A current and 8 μs pulse-on time experienced ~ 200 sparks per location during the whole processing time. This number was estimated by dividing the total number of sparks during the process by the total number of craters need to cover the surface. It is recognised that material movement and intermixing of tool electrode and workpiece material is constrained by the lifetime of the melt pool and hence, it is considered that the deposit is solid prior to the next localised spark and melt pool formation event, which leads to progressive incorporation of more substrate and tool electrode material into the developing coating, by a repetition of intermixing and rapid solidification processes. However, when combined with many sparking events which do not lead to TiC deposition (Figure 5-18b), but simply localised re-melting of the coating, this leads to a net dilution effect, *i.e.* promoted by sparking events without TiC incorporation. Hence, the sequence of many localised melt pool formation and solidification events results ultimately in the formation of the TiC/Fe cermet, whilst the range of TiC grain sizes and banded structures within the developed continuum cermet coating reflects simply the progression of solidification as a function of the localised cooling rate. Hence, it is considered unlikely that EDC can be used to create pure coatings, and that the dilution of developing coatings with substrate material is inevitable.

7.6 Wear behaviour of TiC/Fe cermet ED coatings

The TiC/Fe cermet ED coatings on two different substrate types (produced under favourable processing parameters 10A and 8 μs pulse-on time) were subjected to a study to investigate the surface tribological properties. The tests were performed using a reciprocating ball-on-flat geometry, with an Al_2O_3 counterface ball, under two loading conditions of 10 N and 50 N for 35,000 and 10,000 reciprocating cycles, respectively.

The data showed that TiC/Fe ED coatings can yield dry sliding wear resistance values up to two orders of magnitude greater than that of the steel substrates (Figure 6-5). Given the initial, poor wear resistance of 304-SS in comparison to HSS, the wear rate of TiC/HSS showed a much greater relative reduction in specific wear rate, compared to TiC/304-SS. The variability of specific wear rates reflects the microstructural development of these TiC/Fe cermet coatings and the loading conditions. The wear rate of TiC/304-SS was approximately twice that of TiC/HSS, under 10 N loading conditions. Despite this, the wear mechanism appeared to be the same for both samples, based on a mechanical polishing mechanism, as evidenced by the development of smooth wear track surfaces (Figures 6-11e,f). This mechanism has been observed for other TiC-based cermets [146].

At 50 N load, the difference in wear rate increased to a factor of four (Figure 6-5), but with a degradation of wear rate for TiC/304-SS, as compared with a slight improvement in wear rate for TiC/HSS, respectively, reflecting a difference in the wear mechanism under conditions of higher loading. This difference was particularly notable, as the level of Ti and C present in the TiC coating on 304-SS was in fact higher than that on HSS (39 wt% Ti compared to 29 wt%) (Table 6-2). Hence, the substrate has a strong influence on the wear properties of the coating.

TiC coatings on HSS, under 50 N loading conditions, exhibited evidence of fracture and grain pull-out (Figure 6-13), with the wear tracks containing long sharp abrasive grooves, typical of an abrasive mechanism involving either material trapped between counterbody and substrate, or material adhered to the counterbody. This phenomenon is well understood and the existence of entrapped, hard/sharp, ceramic particles can act like abrasive particles or a moving indent, causing scratching [9, 13, 90]. Conversely, the wear mechanism of cermet coated 304-SS differs from that of coated HSS, under 50 N loading conditions, with a reduction in wear performance. The surface exhibited crack formations, with a prevalence for some pull-out of material (Figure 6-14). This disparity is perhaps explained by deformation of the underlying substrate, which is particularly evident for softer substrate materials during the wear of thin harder coatings. In this case, particularly under higher loads, the substrate deforms during wear, resulting in deflection of the coating and the formation of cracks, leading to an increase in wear rate [6].

The developed microstructure of TiC/Fe cermet coatings also helps to explain the dependence of wear behaviour on the coating/substrate material properties. Figure 4-17 and 4-18 showed the cross-sectional microstructures of TiC-based coatings on 304-SS and HSS substrates, respectively. Based on these images, it is understood that TiC-based coatings on steel substrates comprise a complex, intermixed structure, with a Fe-based matrix and TiC grains of varying sizes and geometries depending on depth into the coating. Hence, it is logical that the final mechanical properties of the coatings reflect the dispersion of these TiC and Fe phases. Particularly, given the much poorer wear behaviour of pure 304-SS compared to HSS (Figure 6-5), the lower wear behaviour of TiC/304-SS as compared to TiC/HSS is attributable ultimately to the poor wear properties of the 304-SS within and beneath the coating.

The TiC/Fe coating on 304-SS exhibited a significantly low CoF of ~ 0.3, for both loading conditions of 10 and 50 N, as compared to coated HSS with a CoF of ~ 0.55 (Figures 6-18 and 6-19, respectively). Again, this is attributed mainly to the higher TiC content within the coating on 304-SS (Table 6-2).

To investigate the influence of the EDM process on wear behaviour, a simple reference surface machined using a conventional Cu electrode, under otherwise identical conditions to those used to produce TiC/Fe coatings, was also subjected to wear testing. This reference surface yielded similar wear rates to that of the substrate, except in the case of the 10 N wear test on 304-SS. In this case the wear rate on the Cu machined surface was more than an order of magnitude lower than that on the substrate only. This may be explained by the hardening of the sample after recrystallization during EDM, thereby increasing the wear resistance of the material significantly compared to the initial poor wear resistance of 304-SS, combined with the formation of Fe_3C as confirmed by XRD (Figure 4-19a). This phenomenon is not significant in the case of HSS, given the already initially much higher wear resistance of the substrate.

7.7 Laser processed TiC/Fe cermet ED coating

Laser surface treatment was used to densify the surface morphology of TiC-based ED coatings on both steel substrate types (Figure 6-1). At 240 W laser power, some cracking was evident for coatings on HSS, whilst at 280 W, cracking and porosity were almost eliminated from the surfaces of coatings on both substrates (304-SS and HSS). Based on cross-sectional imaging of the as-deposited and LSM treated surfaces on both substrates (Figures 6-2 and 6-3, respectively), this cracking typically extended from the coating/substrate interface up to the coating surface. The laser processed TiC

coating on 304-SS at 240 W yielded a surface entirely free of cracking. The presence of cracks for the case of the TiC/HSS substrate, and its absence for the case of TiC/304-SS, may be explained by the notable difference in thermal expansion coefficient for the two substrates, and hence cermet matrix materials.

Regarding the wear behaviour of LSM processed TiC/Fe cermet coatings on HSS, interestingly, a minimal reduction in wear rate was obtained for the laser processed sample at the higher load of 50 N (Figure 6-20). This was attributed to the homogenisation of the surface after laser treatment (Figure 6-1), *i.e.* the removal of asperities which would otherwise cause stress concentrations and localised fracture. The wear rate increased slightly for both laser parameters at 10 N load, and this may be explained by a reduction in the TiC level within the coating after laser processing, (Table 6-2), attributable to the evaporation and/or dilution of TiC within the substrate material.

For the case of laser treated TiC/Fe coatings on 304-SS, these samples exhibited a significant increase in wear rate for both laser treatment conditions. This substantial worsening of wear properties may be explained by the poorer initial wear properties of 304-SS and hence its sensitivity to the amount of TiC present within the coating. As shown in Table 6-2, the weight % of Ti reduced from ~ 39% in the untreated coating, to ~ 25% and then ~ 18%, for laser powers of 240 and 280 W, respectively. Additionally, increased grain sizes, as seen in BSE images (Figure 6-2) after LSM treatment, indicative of slower cooling rates, may also contribute to a reduction in mechanical properties, and hence degradation of wear performance.

In summary, the key point of the EDC method is its ability to process difficult materials, regardless of their mechanical properties, such as ceramics. EDC may be used to apply localised coatings, or for surface modification, without the need for

complicated equipment. It may also be used with conformal surfaces. These advantages have resulted in its developing use with materials with high mechanical properties for precision components, for example of interest to the industrial, aerospace and medical implant industries.

8 Conclusions and Future work

8.1 General conclusions

EDC is a surface modification process, being an adaptation of EDM. It provides for the deposition of functionally significant amounts of material onto complex surfaces, as part of an integrated manufacturing process to produce a high-value components, using a semi-sintered tool electrode.

This thesis has reported on the development of the EDC process, through improved understanding of the principles of materials deposition, microstructure development and the functional properties of ED coatings, as assessed using a range of characterisation techniques. In particular, the process-mapping of TiC/Fe ED cermet coatings on 304-SS, as a function of increasing current (2 - 19 A) and pulse-on time (2 - 64 μs), proved to be an appropriate system for the appraisal of EDC processing phenomena. A 2D transient heat transfer (finite difference method) model was developed and used to estimate the effective amount of energy transferred to the workpiece during single spark events, allowing for fundamental interactions between energy source and workpiece to be investigated. Based on considerations of the starting tool electrode and workpiece material properties, predictions for coating layer thicknesses and associated nano-scale microstructural developments during the rapid cooling phase could be made, in turn providing valuable insights into the generic principles of ED coating formation. Selective laser melting of as-deposited ED coatings proved an effective solution for the inherent EDC problem of surface defects. In particular, the wear performance of ED processed TiC/Fe cermet coatings, on two different types of steel, using two different loading conditions, with and without post-deposition laser melting, was investigated and correlated with near surface

microstructure, in turn providing insights towards process optimisation. A summary of the main outcomes of the experiment work now follows:

TiC/Fe cermets have been produced successfully on 304-SS and HSS substrates using the EDC process with a sacrificial semi-sintered TiC tool electrode. The coating microstructure of as-deposited TiC/Fe cermet coating on the 304-SS comprised a mixture of TiC and austenite γ-Fe, along with signatures attributable to low levels of Cr_3C_2, Fe_3C and amorphous carbon. As-deposited coatings on HSS exhibited a dominance of TiC along with ferrite or martensite α′-Fe, and trace levels austenite γ-Fe.

The continuum cermet layer reflects a sequence of repeated localised melt pool formation and solidification of intermixed TiC, originating from the tool electrode, with substrate material, resulting in complex, TiC/Fe cermet microstructures, with a mixture of equiaxed and banded columnar grains near the surface, and coarse to finely graded equiaxed grains towards the coating/substrate interface, reflecting the final cool-down sequence of ED processing.

The data demonstrate variable hardness of these nanostructured cermet coatings, reflecting variations in the TiC content as a function of processing parameters (current and pulse-on time). It is evident that the ED coatings can become over-processed, being characterised by increased levels of void formation and cracking around crater edges under conditions of high input energy. Further increase in pulse-on time results in reduced levels of TiC incorporation, along with increased carbon levels from cracking of the dielectric oil. Hence, the suggestion is for the use of reduced energy conditions to obtain favourable coating properties, along with good levels of hardness and better surface finish (*i.e.* reduced levels of voids, cracks and low roughness).

Hence, favourable processing conditions for this materials system was selected to be 10 A and 8 μs current and pulse-on time, respectively.

A theoretical model was developed for the coating process, and used to demonstrate that the fraction of energy imparted into the workpiece from each spark event requires critical consideration for EDC, and that different fractions of energy value for different ED process conditions should be considered. The model showed that the effective amount of energy transferred to the workpiece varied between 17% and 23% for increasing current from 2A to 19A at fixed pulse-on time 8μs; whilst an increase in pulse-on time from 2μs to 64μs at fixed current of 10A led to an increase in F_v from 7% to 53%. The maximum value of F_v energy attained corresponded to the highest pulse duration of 64 μs.

The temperature distribution determined within an individual crater exhibited the highest temperature in the crater centre and decreased gradually in the radial direction, reflecting the Gaussian distribution of the heat flux equation. The lowering of temperature was affected strongly by the surface in contact with the flowing dielectric fluid, providing for high convection heat transfer. The model estimated crater depth values commensurate with the range of EDC layer thicknesses measured experimentally, except for the case of high pulse-on times where there was more variability. In general, layer thicknesses increased with the increasing amounts of energy transferred to the workpiece.

The solidification of the melt pool, with initial high cooling rates, was characteristic of a quenching process. The size and shape of the resultant grains varied within the coating layer, also being attributable to an effect of cooling rate. The thermal model calculation for temperature distribution into the melt pool, as a function of cooling time, correlated well with the microstructural development within the ED cermet

coatings, as a function of processing conditions. In particular, the favourable processing conditions of 10 A current and 8 μs pulse-on time were found to be associated with the development of a complex banded nanoscale microstructure, reflecting differences in localised cooling rates and heat transfer modes, *i.e.* convection within the flowing dielectric fluid due to surface/oil interaction, and conduction into the substrate. Increasing the pulse-on time was characterised by a propensity towards the development of large grains and more columnar growth, as compared to samples produced at the lower pulse-on time 8 μs, reflecting a high input of thermal energy and a comparatively low cooling rate.

With regard to the tribological properties of ED coatings, the wear tests were performed using a linear reciprocating ball-on-flat geometry, under dry sliding conditions. The TiC/Fe coatings on both steel substrates (HSS and 304-SS) yielded specific wear rates up to two orders of magnitude lower than those of the substrate only. It is recognised that the wear performance of the coatings is highly dependent on substrate type, with coatings on HSS exhibiting wear resistance ~ 2 - 4 times higher than that on 304-SS, again reflecting the metal matrix composite nature of the coatings, with differences in hardness and wear performance reflecting the respective substrates. The effects of deformation of an underlying soft substrate is also suggested to contribute to an increase in wear rate.

Laser surface treatments using conditions of 240 W and 280 W laser power were used successfully to improve the surface properties, by eliminating cracks and porosity characteristic of as-deposited TiC ED coatings. Processing under conditions of 280 W, in particular, was found to eliminate these defects entirely, while 240 W left some remaining. However, the wear rate was found to increase after LSM treatment for all samples, except coatings on HSS under 50 N load. The increase in wear rate was

attributed to a significant reduction in the TiC level within the coatings, after laser treatment, due to evaporation and dilution effects. Particularly for the case of coatings on 304-SS, for which the mechanical properties are highly reliant on a high level of TiC within the coating. An increase in grain size after laser treatment may also contribute to the worsening of the wear properties. The improvement in performance for coatings on HSS under 50 N may be explained by the avoidance of third body abrasive mechanisms, which took place for the as-deposited samples.

EDC has received attention, given its potential advantages to consecutively machine material while depositing a coating in the same process, without need for further apparatus or post-processing. In particular, the process takes advantage of the ability of EDM to create complex shapes using an inverted form tool electrode, and hence a coating process can be applied easily to complex components. Since EDC is capable of producing coatings from hard, high melting point materials such as ceramics, which may be difficult to process by other means, the technique has excellent potential for the production of hard-wearing coatings, to enhance the lifetime of components. This work has opened up the possibility to extend the ED model to include different material types and dielectric media, being essential for the development of new process methodologies.

8.2 Future work

Based on the finding of this work, some broad areas for further investigation have been identified.

During EDC, material is supplied simply from a sacrificial, semi-sintered tool electrode. A comprehensive characterisation of TiC/Fe ED coatings was reported on in chapter 4, giving a fundamental perspective of the material deposition, elemental

distribution and microstructural development, within the coating. Hence, there is great scope for the investigation of other “hard to process” materials for tool electrode and workpiece, depending on the specific application.

The post-process surface treatments described in chapter 6 showed the potential of LSM, as applied to TiC/Fe coatings, to address the inherent problem of poor surface properties of as-processed ED coatings. The morphological features of cracks and porosity, typical of EDC surfaces, were reduced, but the LSM process affected the fatigue performance of the processed coatings, due to stress concentration effects. In particular, cracks are considered instrumental in the initiation stage of fatigue failure. Roughness, porosity and surface cracking is also related to a worsening of corrosion behaviour, as a consequence of an increase in the area susceptible to chemical attack. Hence, it is suggested that combined fatigue and corrosion testing should be performed on ED coated surfaces in the future.

It has been reported that pulsed electron beam (PEB) irradiation surface treatments acts to improve EDM processed surfaces. Hence, it is suggested also to investigate PEB and LSM processed ED surfaces.

Further work can be done also to extend the simulation of single spark interactions during ED processing, as presented in chapter 5. Considering should be given to the effect of multi-spark interactions, to broaden knowledge of the microstructural development within continuum coating layers. The modelling work would also support investigations into the ED processing of new materials, as part of the strategy to optimise processing conditions for any combination of tool electrode and workpiece.

References

1. Wang, Z.L., Y. Fang, P.N. Wu, W.S. Zhao, and K. Cheng, Surface modification process by electrical discharge machining with a Ti powder green compact electrode. Journal of Materials Processing Technology, 2002. **129**(1–3): p. 139-142.

2. Furutania, K., A. Saneto, H. Takezawa, N. Mohri, and H. Miyake, Accretion of titanium carbide by electrical discharge machining with powder suspended in working fluid. Precision Engineering, 2001. **25**(2): p. 138-144.

3. Lin, Y.-C., L.-R. Hwang, C.-H. Cheng, and P.-L. Su, Effects of electrical discharge energy on machining performance and bending strength of cemented tungsten carbides. Journal of Materials Processing Technology, 2008. **206**(1): p. 491-499.

4. Singh, S., S. Maheshwari, and P. Pandey, Some investigations into the electric discharge machining of hardened tool steel using different electrode materials. Journal of Materials Processing Technology, 2004. **149**(1): p. 272-277.

5. Podgornik, B., M. Sedlaček, M. Čekada, S. Jacobson, and B. Zajec, Impact of fracture toughness on surface properties of PVD coated cold work tool steel. Surface and Coatings Technology, 2015. **277**: p. 144-150.

6. Holmberg, K. and A. Matthews. (2009), Coatings Tribology: Properties, Mechanisms, Techniques and Applications in Surface Engineering. 2nd. Amsterdam, The Netherlands: Elsevier Science, p. 7-21, 53-60 & 142-162.

7. Creighton, J. and P. Ho. (2001). Introduction to chemical vapor deposition (CVD). Ohio: ASM International, p.1-10.

8. Shanaghi, A., A.R.S. Rouhaghdam, S. Ahangarani, and P.K. Chu, Effect of plasma CVD operating temperature on nanomechanical properties of TiC nanostructured coating investigated by atomic force microscopy. Materials Research Bulletin, 2012. **47**(9): p. 2200-2205.

9. Azadi, M., A.S. Rouhaghdam, S. Ahangarani, and H.H. Mofidi, Mechanical behavior of TiN/TiC multilayer coatings fabricated by plasma assisted chemical vapor deposition on AISI H13 hot work tool steel. Surface and Coatings Technology, 2014. **245**: p. 156-166.

10. Wolfe, D.E. and J. Singh, Titanium carbide coatings deposited by reactive ion beam-assisted, electron beam–physical vapor deposition. Surface and Coatings Technology, 2000. **124**(2): p. 142-153.

11. Jakubéczyová, D., P. Hvizdoš, and M. Selecká, Investigation of thin layers deposited by two PVD techniques on high speed steel produced by powder metallurgy. Applied Surface Science, 2012. **258**(12): p. 5105-5110.

12. Zalnezhad, E., A.A. Sarhan, and M. Hamdi, Optimizing the PVD TiN thin film coating's parameters on aerospace AL7075-T6 alloy for higher coating hardness and adhesion with better tribological properties of the coating surface. The International Journal of Advanced Manufacturing Technology, 2013. **64**(1-4): p. 281-290.

13. Arun, I., M. Duraiselvam, V. Senthilkumar, R. Narayanasamy, and V. Anandakrishnan, Synthesis of electric discharge alloyed nickel–tungsten coating on tool steel and its tribological studies. Materials & Design, 2014. **63**: p. 257-262.

14. Pouraliakbar, H., G. Khalaj, L. Gomidželović, M.-J. Khalaj, and M. Nazerfakhari, Duplex ceramic coating produced by low temperature thermo-reactive deposition and diffusion on the cold work tool steel substrate: Thermodynamics, kinetics and modeling. Ceramics International, 2015.

15. Jameson, E.C.(2001). Electrical discharge machining. Dearborn, Michigan: Society of Manufacturing Engineers, p.1-7.

16. Kunieda, M., B. Lauwers, K. Rajurkar, and B. Schumacher, Advancing EDM through fundamental insight into the process. CIRP Annals-Manufacturing Technology, 2005. **54**(2): p. 64-87.

17. El-Hofy, H.A.-G.(2013). Fundamentals of machining processes: conventional and nonconventional processes. 2nd. Broken Sound Parkway, CRC press, p.385-398.

18. Schumacher, B.M., After 60 years of EDM the discharge process remains still disputed. Journal of Materials Processing Technology, 2004. **149**(1): p. 376-381.

19. DiBitonto, D.D., P.T. Eubank, M.R. Patel, and M.A. Barrufet, Theoretical models of the electrical discharge machining process. I. A simple cathode erosion model. Journal of Applied Physics, 1989. **66**(9): p. 4095-4103.

20. Yeo, S., W. Kurnia, and P. Tan, Electro-thermal modelling of anode and cathode in micro-EDM. Journal of Physics D: Applied Physics, 2007. **40**(8): p. 2513-2521.

21. Chen, H.-J., K.-L. Wu, and B.-H. Yan, Characteristics of Al alloy surface after EDC with sintered Ti electrode and TiN powder additive. The International Journal of Advanced Manufacturing Technology, 2014. **72**(1-4): p. 319-332.

22. Luo, Y., The dependence of interspace discharge transitivity upon the gap debris in precision electrodischarge machining. Journal of Materials Processing Technology, 1997. **68**(2): p. 121-131.

23. Kunieda, M. and Takanobu, N., Factor determining discharge location in EDM. IJEM, 1998. **3**: p. 53.

24. Mohri, N., N. Saito, Y. Tsunekawa, and N. Kinoshita, Metal surface modification by electrical discharge machining with composite electrode. CIRP Annals-Manufacturing Technology, 1993. **42**(1): p. 219-222.

25. Simão, J., D. Aspinwall, F. El-Menshawy, and K. Meadows, Surface alloying using PM composite electrode materials when electrical discharge texturing hardened AISI D2. Journal of Materials Processing Technology, 2002. **127**(2): p. 211-216.

26. Chen, Y.-F., H.-M. Chow, Y.-C. Lin, and C.-T. Lin, Surface modification using semi-sintered electrodes on electrical discharge machining. The International Journal of Advanced Manufacturing Technology, 2008. **36**(5-6): p. 490-500.

27. Ho, S.K., D.K. Aspinwall, and W. Voice, Use of powder metallurgy (PM) compacted electrodes for electrical discharge surface alloying/modification of Ti–6Al–4V alloy. Journal of Materials Processing Technology, 2007. **191**(1–3): p. 123-126.

28. Gill, A.S. and S. Kumar, Surface alloying of H11 die steel by tungsten using EDM process. The International Journal of Advanced Manufacturing Technology, 2015. **78**(9-12): p. 1585-1593.

29. Xiao, H., X. Jie, Z. Zeng, and G. Li, Titanium carbonitride coating by pulsed electrical discharge in an aqueous solution of ethanolamine. Surface and Coatings Technology, 2014. **258**: p. 1006-1010.

30. Kumar, S., R. Singh, T.P. Singh, and B.L. Sethi, Surface modification by electrical discharge machining: A review. Journal of Materials Processing Technology, 2009. **209**(8): p. 3675-3687.

31. Batish, A., A. Bhattacharya, V. Singla, and G. Singh, Study of material transfer mechanism in die steels using powder mixed electric discharge machining. Materials and Manufacturing Processes, 2012. **27**(4): p. 449-456.

32. Yih-Fong, T. and C. Fu-Chen, Investigation into some surface characteristics of electrical discharge machined SKD-11 using powder-suspension dielectric oil. Journal of Materials Processing Technology, 2005. **170**(1): p. 385-391.

33. Janmanee, P. and A. Muttamara, Surface modification of tungsten carbide by electrical discharge coating (EDC) using a titanium powder suspension. Applied Surface Science, 2012. **258**(19): p. 7255-7265.

34. Chen, S.-L., M.-H. Lin, G.-X. Huang, and C.-C. Wang, Research of the recast layer on implant surface modified by micro-current electrical discharge machining using deionized water mixed with titanium powder as dielectric solvent. Applied Surface Science, 2014. **311**: p. 47-53.

35. Chen, S.-L., M.-H. Lin, C.-C. Chen, and K.-L. Ou, Effect of electro-discharging on formation of biocompatible layer on implant surface. Journal of Alloys and Compounds, 2008. **456**(1): p. 413-418.

36. Murray, J., M. Fay, M. Kunieda, and A. Clare, TEM study on the electrical discharge machined surface of single-crystal silicon. Journal of Materials Processing Technology, 2013. **213**(5): p. 801-809.

37. Gnanavel, C., R. Saravanan, M. Chandrasekaran, and R. Pugazhenthi. Restructured review on Electrical Discharge Machining-A state of the art. in IOP Conference Series: Materials Science and Engineering. 2017. **183**(1): P.01201.

38. Kansal, H., S. Singh, and P. Kumar, Parametric optimization of powder mixed electrical discharge machining by response surface methodology. Journal of Materials Processing Technology, 2005. **169**(3): p. 427-436.

39. Liu, Q., Q. Zhang, M. Zhang, and J. Zhang, Review of size effects in micro electrical discharge machining. Precision Engineering, 2016. **44**: p. 29-40.

40. Simao, J., H.G. Lee, D.K. Aspinwall, R.C. Dewes, and E.M. Aspinwall, Workpiece surface modification using electrical discharge machining. International Journal of Machine Tools and Manufacture, 2003. **43**(2): p. 121-128.

41. Kumar, S. and U. Batra, Surface modification of die steel materials by EDM method using tungsten powder-mixed dielectric. Journal of Manufacturing Processes, 2012. **14**(1): p. 35-40.

42. Furutani, K., H. Sato, and M. Suzuki, Influence of electrical conditions on performance of electrical discharge machining with powder suspended in working oil for titanium carbide deposition process. The International Journal of Advanced Manufacturing Technology, 2009. **40**(11-12): p. 1093-1101.

43. Hwang, Y.-L., C.-L. Kuo, and S.-F. Hwang, The coating of TiC layer on the surface of nickel by electric discharge coating (EDC) with a multi-layer electrode. Journal of Materials Processing Technology, 2010. **210**(4): p. 642-652.

44. Suzuki, T. and S. Kobayashi, Mechanisms of TiC layer formation on high speed steel by a single pulse in electrical discharge machining. Electrochimica Acta, 2013. **114**(0): p. 844-850.

45. Xie, Z., Y. Mai, W. Lian, S. He, and X. Jie, Titanium carbide coating with enhanced tribological properties obtained by EDC using partially sintered titanium electrodes and graphite powder mixed dielectric. Surface and Coatings Technology, 2016. **300**: p. 50-57.

46. Ueno, M., N. Fujita, Y. Kimura, and N. Nakata, Evaluation of coating and wear characteristics of roll surface coated with TiC by electrical discharge coating. Journal of Materials Processing Technology, 2016. **236**: p. 9-15.

47. Kanemaru, M., S. Sorimachi, S. Ibuka, and S. Ishii, Single bubble generated by a pulsed discharge in liquids as a plasma microreactor. Plasma Sources Science and Technology, 2011. **20**(3): p. 034007.

48. Yeo, S., W. Kurnia, and P. Tan, Critical assessment and numerical comparison of electro-thermal models in EDM. Journal of Materials Processing Technology, 2008. **203**(1): p. 241-251.

49. Singh, S. and A. Bhardwaj, Review to EDM by using water and powder-mixed dielectric fluid. Journal of Minerals and Materials Characterization and Engineering, 2011. **10**(02): p. 199-230.

50. Singh, H. and D. Shukla, Optimizing electric discharge machining parameters for tungsten-carbide utilizing thermo-mathematical modelling. International Journal of Thermal Sciences, 2012. **59**: p. 161-175.

51. Das, S., M. Klotz, and F. Klocke, EDM simulation: finite element-based calculation of deformation, microstructure and residual stresses. Journal of Materials Processing Technology, 2003. **142**(2): p. 434-451.

52. Xie, B.-c., Y.-k. Wang, Z.-l. Wang, and W.-s. Zhao, Numerical simulation of titanium alloy machining in electric discharge machining process. Transactions of Nonferrous Metals Society of China, 2011. **21**: p. s434-s439.

53. Tan, P. and S. Yeo, Modelling of overlapping craters in micro-electrical discharge machining. Journal of Physics D: Applied Physics, 2008. **41**(20): p. 205302.

54. Joshi, S. and S. Pande, Thermo-physical modeling of die-sinking EDM process. Journal of Manufacturing Processes, 2010. **12**(1): p. 45-56.

55. Zhang, Y., Y. Liu, Y. Shen, Z. Li, R. Ji, and F. Wang, A new method of investigation the characteristic of the heat flux of EDM plasma. Procedia CIRP, 2013. **6**: p. 450-455.

56. Shao, B. and K.P. Rajurkar, Modelling of the Crater Formation in Micro-EDM. Procedia CIRP, 2015. **33**: p. 377-382.

57. Tang, J. and X. Yang, A novel thermo-hydraulic coupling model to investigate the crater formation in electrical discharge machining. Journal of Physics D: Applied Physics, 2017. **50**(36): p. 365301.

58. Zhang, Y., Y. Liu, Y. Shen, Z. Li, R. Ji, and B. Cai, A novel method of determining energy distribution and plasma diameter of EDM. International Journal of Heat and Mass Transfer, 2014. **75**: p. 425-432.

59. Snoeys, R. and F. Van Dijck, Investigation of electro discharge machining operations by means of thermo-mathematical model. CIRP Annals, 1971. **20**(1): p. 35-37.

60. Van Dijck, F. and W. Dutre, Heat conduction model for the calculation of the volume of molten metal in electric discharges. Journal of Physics D: Applied Physics, 1974. **7**(6): p. 899.

61. Beck, J.V., Large time solutions for temperatures in a semi-infinite body with a disk heat source. International Journal of Heat and Mass Transfer, 1981. **24**(1): p. 155-164.

62. Jilani, S.T. and P. Pandey, Analysis and modelling of EDM parameters. Precision Engineering, 1982. **4**(4): p. 215-221.

63. Eubank, P.T., M.R. Patel, M.A. Barrufet, and B. Bozkurt, Theoretical models of the electrical discharge machining process. III. The variable mass, cylindrical plasma model. Journal of Applied Physics, 1993. **73**(11): p. 7900-7909.

64. Singh, H., Experimental study of distribution of energy during EDM process for utilization in thermal models. International Journal of Heat and Mass Transfer, 2012. **55**(19): p. 5053-5064.

65. Okada, A., Y. Uno, and I. Okajima, Energy Distrihution in Electrical Discharge Machining with Graphite Electrode. Memoirs of The Faculty of Engineering, 2000. **34**(1-2): p. 19-26.

66. Xia, H., M. Kunieda, and N. Nishiwaki, Removal amount difference between anode and cathode in EDM process. International Journal of Electrical Machining, 1996. **1**: p. 45-52.

67. Shen, Y., Y. Liu, Y. Zhang, B. Tan, R. Ji, B. Cai, and C. Zheng, Determining the energy distribution during electric discharge machining of Ti–6Al–4V. The International Journal of Advanced Manufacturing Technology, 2014. **70**(1-4): p. 11-17.

68. Schulze, H.-P., R. Herms, H. Juhr, W. Schaetzing, and G. Wollenberg, Comparison of measured and simulated crater morphology for EDM. Journal of Materials Processing Technology, 2004. **149**(1): p. 316-322.

69. Descoeudres, A., C. Hollenstein, G. Wälder, and R. Perez, Time-resolved imaging and spatially-resolved spectroscopy of electrical discharge machining plasma. Journal of Physics D: Applied Physics, 2005. **38**(22): p. 4066.

70. Natsu, W., M. Shimoyamada, and M. Kunieda, Study on expansion process of EDM arc plasma. JSME International Journal Series C Mechanical Systems, Machine Elements and Manufacturing, 2006. **49**(2): p. 600-605.

71. Kojima, A., W. Natsu, and M. Kunieda, Spectroscopic measurement of arc plasma diameter in EDM. CIRP Annals-Manufacturing Technology, 2008. **57**(1): p. 203-207.

72. Revaz, B., G. Witz, and R. Flükiger, Properties of the plasma channel in liquid discharges inferred from cathode local temperature measurements. Journal of Applied Physics, 2005. **98**(11): p. 113305.

73. Izquierdo, B., J. Sanchez, S. Plaza, I. Pombo, and N. Ortega, A numerical model of the EDM process considering the effect of multiple discharges. International Journal of Machine Tools and Manufacture, 2009. **49**(3): p. 220-229.

74. Ikai, T. and K. Hashigushi. Heat input for crater formation in EDM. in Proceedings of the International Symposium for Electro-Machining-ISEM XI, EPFL. 1995: P.163-170.

75. Buckley, D.H. (181). Surface effects in adhesion, friction, wear, and lubrication. Vol. 5. Amsterdam: Elsevier, p.444-445.

76. Holmberg, K., H. Ronkainen, A. Laukkanen, and K. Wallin, Friction and wear of coated surfaces—scales, modelling and simulation of tribomechanisms. Surface and Coatings Technology, 2007. **202**(4): p. 1034-1049.

77. Mair, L., T. Stolarski, R. Vowles, and C. Lloyd, Wear: mechanisms, manifestations and measurement. Report of a workshop. Journal of Dentistry, 1996. **24**(1-2): p. 141-148.

78. Dwivedi, D., Adhesive wear behaviour of cast aluminium–silicon alloys: overview. Materials & Design (1980-2015), 2010. **31**(5): p. 2517-2531.

79. Eyre, T., Wear characteristics of metals. Tribology International, 1976. **9**(5): p. 203-212.

80. Zum Gahr, K.-H., Wear by hard particles. Tribology International, 1998. **31**(10): p. 587-596.

81. Blau, P.J., Fifty years of research on the wear of metals. Tribology International, 1997. **30**(5): p. 321-331.

82. Holmberg, K., A. Matthews, and H. Ronkainen, Coatings tribology—contact mechanisms and surface design. Tribology International, 1998. **31**(1): p. 107-120.

83. Archard, J. and W. Hirst. The wear of metals under unlubricated conditions. in Proceedings of the Royal Society of London A: Mathematical, Physical and Engineering Sciences. 1956. **236**(1206): p.397-410.

84. An, J., W. Sun, and X. Niu, Dry Sliding Wear Behavior and a Proposed Criterion for Mild to Severe Wear Transition of Mg–3Al–0.4 Si–0.1 Zn Alloy. Tribology Letters, 2017. **65**(3): p. 98.

85. Li, X., Q. Zhang, Y. Zhou, J. Liu, K. Chen, and S. Wang, Mild and Severe Wear of Titanium Alloys. Tribology Letters, 2016. **61**(2): p. 14.

86. Wang, S., L. Wang, Y. Zhao, Y. Sun, and Z. Yang, Mild-to-severe wear transition and transition region of oxidative wear in steels. Wear, 2013. **306**(1): p. 311-320.

87. Lim, S., M. Ashby, and J. Brunton, Wear-rate transitions and their relationship to wear mechanisms. Acta Metallurgica, 1987. **35**(6): p. 1343-1348.

88. Rasool, G. and M. Stack, Wear maps for TiC composite based coatings deposited on 303 stainless steel. Tribology International, 2014. **74**: p. 93-102.

89. Md Idriss, A., M. Maleque, I. Yaacob, R. Nasir, S. Mridha, and T. Baker, Microstructural aspects of wear behaviour of TiC coated low alloy steel. Materials Science and Technology, 2016. **32**(4): p. 303-307.

90. Souček, P., T. Schmidtová, V. Buršíková, P. Vašina, Y. Pei, J.T.M. De Hosson, O. Caha, V. Peřina, R. Mikšová, and P. Malinský, Tribological properties of nc-TiC/aC: H coatings prepared by magnetron sputtering at low and high ion

bombardment of the growing film. Surface and Coatings Technology, 2014. **241**: p. 64-73.

91. Stewart, T.L. and K.P. Plucknett, The sliding wear of TiC and Ti (C, N) cermets prepared with a stoichiometric Ni 3 Al binder. Wear, 2014. **318**(1): p. 153-167.

92. Onuoha, C.C., C. Jin, Z.N. Farhat, G.J. Kipouros, and K.P. Plucknett, The effects of TiC grain size and steel binder content on the reciprocating wear behaviour of TiC-316L stainless steel cermets. Wear, 2016. **350**: p. 116-129.

93. Tijo, D. and M. Masanta, Mechanical performance of in-situ TiC-TiB2 composite coating deposited on Ti-6A1-4V alloy by powder suspension electro-discharge coating process. Surface & Coatings Technology, 2017. **328**: p. 192-203.

94. Zeng, Z.-y., H.-q. Xiao, X.-h. Jie, and Y.-m. Zhang, Friction and wear behaviors of TiCN coating based on electrical discharge coating. Transactions of Nonferrous Metals Society of China, 2015. **25**(11): p. 3716-3722.

95. Zhu, H., K. Dong, H. Wang, J. Huang, J. Li, and Z. Xie, Reaction mechanisms of the TiC/Fe composite fabricated by exothermic dispersion from Fe–Ti–C element system. Powder Technology, 2013. **246**: p. 456-461.

96. Rajabi, A., M.J. Ghazali, J. Syarif, and A. Daud, Development and application of tool wear: A review of the characterization of TiC-based cermets with different binders. Chemical Engineering Journal, 2014. **255**: p. 445-452.

97. Tijo, D., S. Kumari, and M. Masanta, Hard and wear resistance TiC-composite coating on AISI 1020 steel using powder metallurgy tool by electro-discharge coating process. Journal of the Brazilian Society of Mechanical Sciences and Engineering, 2017: p. 1-16.

98. Sova, A., S. Grigoriev, A. Okunkova, and I. Smurov, Cold spray deposition of 316L stainless steel coatings on aluminium surface with following laser post-treatment. Surface and Coatings Technology, 2013. **235**: p. 283-289.

99. Afzal, M., A.N. Khan, T.B. Mahmud, T. Khan, and M. Ajmal, Effect of laser melting on plasma sprayed WC-12wt.% Co coatings. Surface and Coatings Technology, 2015. **266**: p. 22-30.

100. Ciubotariu, C.-R., D. Frunzăverde, G. Mărginean, V.-A. Șerban, and A.-V. Bîrdeanu, Optimization of the laser remelting process for HVOF-sprayed Stellite 6 wear resistant coatings. Optics & Laser Technology, 2016. **77**: p. 98-103.

101. Abbas, N.M., D.G. Solomon, and M.F. Bahari, A review on current research trends in electrical discharge machining (EDM). International Journal of Machine Tools and Manufacture, 2007. **47**(7): p. 1214-1228.

102. Umar, Z., R. Rawat, K. Tan, A. Kumar, R. Ahmad, T. Hussain, C. Kloc, Z. Chen, L. Shen, and Z. Zhang, Hard TiC x/SiC/aC: H nanocomposite thin films using pulsed high energy density plasma focus device. Nuclear Instruments and

Methods in Physics Research Section B: Beam Interactions with Materials and Atoms, 2013. **301**: p. 53-61.

103. Emamian, A., S.F. Corbin, and A. Khajepour, The effect of powder composition on the morphology of in situ TiC composite coating deposited by Laser-Assisted Powder Deposition (LAPD). Applied Surface Science, 2012. **261**: p. 201-208.

104. Yasuoka, M., P. Wang, and R.-i. Murakami, Comparison of the mechanical performance of cutting tools coated by either a TiC x N 1− x single-layer or a TiC/TiC 0.5 N 0.5/TiN multilayer using the hollow cathode discharge ion plating method. Surface and Coatings Technology, 2012. **206**(8): p. 2168-2172.

105. Metals Handbook. (1973). Metallography, structures and phase diagrams. Vol 8. American Society for Metals, Novelty, OH.

106. Bhushan, B. and B.K. Gupta. (1991). Handbook of tribology: materials, coatings, and surface treatments. McGraw-Hill, New York.

107. Krauss, G. (2015). Steels - Processing, Structure, and Performance. 2nd. Materials Par, OH: ASM International, p. 497.

108. ASM Handbook. (1994). Surface Engineering. Vol. 5. United State of America: ASM International, p.1988.

109. Gill, S.S., J. Singh, R. Singh, and H. Singh, Effect of cryogenic treatment on AISI M2 high speed steel: metallurgical and mechanical characterization. Journal of Materials Engineering and Performance, 2012. **21**(7): p. 1320-1326.

110. Cho, I.S., A. Amanov, and J.D. Kim, The effects of AlCrN coating, surface modification and their combination on the tribological properties of high speed steel under dry conditions. Tribology International, 2015. **81**: p. 61-72.

111. Sun, G., K. Wang, R. Zhou, A. Feng, and W. Zhang, Effect of different heat-treatment temperatures on the laser cladded M3: 2 high-speed steel. Materials & Design, 2015. **65**: p. 606-616.

112. Lu, L., L. Hou, J. Zhang, H. Wang, H. Cui, J. Huang, Y. Zhang, and J. Zhang, Improved the microstructures and properties of M3: 2 high-speed steel by spray forming and niobium alloying. Materials Characterization, 2016. **117**: p. 1-8.

113. Abdul Aleem, B., M. Hashmi, and B. Yilbas, Laser surface treatment of high-speed steel: presence of TiC particles at the surface. Surface and Interface Analysis, 2012. **44**(2): p. 150-155.

114. Mesquita, R.A. (2016). Tool Steels: Properties and Performance. Boca Raton London New York: CRC Press, p. 62 &228.

115. Garg, R., K. Singh, A. Sachdeva, V.S. Sharma, K. Ojha, and S. Singh, Review of research work in sinking EDM and WEDM on metal matrix composite materials. The International Journal of Advanced Manufacturing Technology, 2010. **50**(5-8): p. 611-624.

116. Lin, C., J. Lin, and T. Ko, Optimisation of the EDM process based on the orthogonal array with fuzzy logic and grey relational analysis method. The International Journal of Advanced Manufacturing Technology, 2002. **19**(4): p. 271-277.

117. Ion, J. (2005). Laser processing of engineering materials: principles, procedure and industrial application. Linacre House, Jordan Hill, Oxford: Elsevier Butterworth-Heinemann, p. 111-113.

118. Du, B., S.R. Paital, and N.B. Dahotre, Synthesis of TiB 2–TiC/Fe nano-composite coating by laser surface engineering. Optics & Laser Technology, 2013. **45**: p. 647-653.

119. Davinci, M.A., N. Parthasarathi, U. Borah, and S.K. Albert, Effect of the tracing speed and span on roughness parameters determined by stylus type equipment. Measurement, 2014. **48**: p. 368-377.

120. Callister, W. D., & Rethwisch, D. G., Materials science and engineering: an introduction. John Wiley & Sons. Inc.–New York, USA, 2007.

121. Williams, D. and Carter C. (1996). Transmission electron microscopy. 1-Basics. New York: Plenum Press, p. 133-146.

122. Varez, A., B. Levenfeld, J. Torralba, G. Matula, and L. Dobrzanski, Sintering in different atmospheres of T15 and M2 high speed steels produced by a modified metal injection moulding process. Materials Science and Engineering: A, 2004. **366**(2): p. 318-324.

123. Kain, V., K. Chandra, K. Adhe, and P. De, Effect of cold work on low-temperature sensitization behaviour of austenitic stainless steels. Journal of Nuclear Materials, 2004. **334**(2): p. 115-132.

124. Govindan, P., A. Gupta, S.S. Joshi, A. Malshe, and K.P. Rajurkar, Single-spark analysis of removal phenomenon in magnetic field assisted dry EDM. Journal of Materials Processing Technology, 2013. **213**(7): p. 1048-1058.

125. Morimoto, K. and M. Kunieda, Sinking EDM simulation by determining discharge locations based on discharge delay time. CIRP Annals-Manufacturing Technology, 2009. **58**(1): p. 221-224.

126. Li, G.L., X.H. Jie, and W. Luo. Preparation of (Ti, Al) C Ceramic Coating on Carbon Steel by Electrical Discharge Coating and its Properties Research. in Key Engineering Materials. 2012. **531**: p. 108-113.

127. Guu, Y., AFM surface imaging of AISI D2 tool steel machined by the EDM process. Applied Surface Science, 2005. **242**(3): p. 245-250.

128. Emamian, A., S.F. Corbin, and A. Khajepour, Effect of laser cladding process parameters on clad quality and in-situ formed microstructure of Fe–TiC composite coatings. Surface and Coatings Technology, 2010. **205**(7): p. 2007-2015.

129. AlMangour, B., D. Grzesiak, T. Borkar, and J.-M. Yang, Densification behavior, microstructural evolution, and mechanical properties of TiC/316L stainless steel nanocomposites fabricated by selective laser melting. Materials & Design, 2018. **138**: p. 119-128.

130. Lee, H.-T. and T.Y. Tai, Relationship between EDM parameters and surface crack formation. Journal of Materials Processing Technology, 2003. **142**(3): p. 676-683.

131. Kansal, H., S. Singh, and P. Kumar, Numerical simulation of powder mixed electric discharge machining (PMEDM) using finite element method. Mathematical and Computer Modelling, 2008. **47**(11): p. 1217-1237.

132. Somashekhar, K., S. Panda, J. Mathew, and N. Ramachandran, Numerical simulation of micro-EDM model with multi-spark. The International Journal of Advanced Manufacturing Technology, 2015. **76**(1-4): p. 83-90.

133. Tao, J., J. Ni, and A.J. Shih, Modeling of the anode crater formation in electrical discharge machining. Journal of Manufacturing Science and Engineering, 2012. **134**(1): p. 011002.

134. Erden, A., Effect of materials on the mechanism of electric discharge machining (EDM). Journal of Engineering Materials and Technology, 1983. **105**(2): p. 132-138.

135. Theodore, L. (2011). Heat transfer applications for the practicing engineer. Vol. 7. Hoboken New Jersey: John Wiley & Sons, Inc, p. 141-146.

136. Shabgard, M. and S. Akhbari, An inverse heat conduction method to determine the energy transferred to the workpiece in EDM process. The International Journal of Advanced Manufacturing Technology, 2016. **83**(5-8): p. 1037-1045.

137. Maradia, U., C. Hollenstein, and K. Wegener, Temporal characteristics of the pulsed electric discharges in small gaps filled with hydrocarbon oil. Journal of Physics D: Applied Physics, 2015. **48**(5): p. 055202.

138. Zhitnyak, I., N. Gloushankova, E. Levashov, and D. Shtansky, Structural transformations in TiC-CaO-Ti3PO (x)-(Ag2Ca) electrodes and biocompatible TiCaPCO (N)-(Ag) coatings during pulsed electrospark deposition. Surface & Coatings Technology, 2016. **302**: p. 327-335.

139. Sahoo, C.K., L. Soni, and M. Masanta, Evaluation of microstructure and mechanical properties of TiC/TiC-steel composite coating produced by gas tungsten arc (GTA) coating process. Surface and Coatings Technology, 2016. **307**: p. 17-27.

140. Gu, D., Y.-C. Hagedorn, W. Meiners, K. Wissenbach, and R. Poprawe, Nanocrystalline TiC reinforced Ti matrix bulk-form nanocomposites by Selective Laser Melting (SLM): Densification, growth mechanism and wear behavior. Composites Science and Technology, 2011. **71**(13): p. 1612-1620.

141. Benyounis, K.Y., O.M. Fakron, and J.H. Abboud, Rapid solidification of M2 high-speed steel by laser melting. Materials & Design, 2009. **30**(3): p. 674-678.

142. Yoon, K., S. Cho, S. Kim, M. Yoon, and S. Yang, Wear mechanism of TiN-coated high-speed steel during sliding. Wear, 1993. **170**(1): p. 101-108.

143. Telasang, G., J.D. Majumdar, G. Padmanabham, and I. Manna, Wear and corrosion behavior of laser surface engineered AISI H13 hot working tool steel. Surface and Coatings Technology, 2015. **261**: p. 69-78.

144. Sun, Y., Sliding wear behaviour of surface mechanical attrition treated AISI 304 stainless steel. Tribology International, 2013. **57**: p. 67-75.

145. Hsu, C.-H., K.-H. Huang, and Y.-H. Lin, Microstructure and wear performance of arc-deposited Ti–N–O coatings on AISI 304 stainless steel. Wear, 2013. **306**(1): p. 97-102.

146. Jin, C., C.C. Onuoha, Z.N. Farhat, G.J. Kipouros, and K. Plucknett, Microstructural damage following reciprocating wear of TiC-stainless steel cermets. Tribology International, 2017. **105**: p. 201-218.

147. Onuoha, C.C., G.J. Kipouros, Z.N. Farhat, and K.P. Plucknett, The reciprocating wear behaviour of TiC–304L stainless steel composites prepared by melt infiltration. Wear, 2013. **303**(1): p. 321-333.

148. Cabanillas, E., J. Desimoni, G. Punte, and R. Mercader, Formation of carbides by electro-discharge machining of alpha iron. Materials Science and Engineering: A, 2000. **276**(1-2): p. 133-140.

149. Emamian, A., S.F. Corbin, and A. Khajepour, In-situ deposition of metal matrix composite in Fe-Ti-C system using laser cladding process, in Metal, Ceramic and Polymeric Composites for Various Uses. 2011: p. 33-60.

150. Incropera, F.P., D.P. DeWitt, T.L. Bergman, and A.S. Lavine. (2006). Introduction to Heat Transfer. 6th. New Jersey: John Wiley & Sons, Inc, p. 214-215 & 302-204.

151. Bejan, A. and A.D. Kraus. (2003). Heat Transfer Handbook. New Jersey: John Wiley & Sons, Inc, p. 237.

Appendix 1 TEM image of 304-SS

A complementary TEM image of the 304-SS sample prepared using conventional mechanical sectioning.

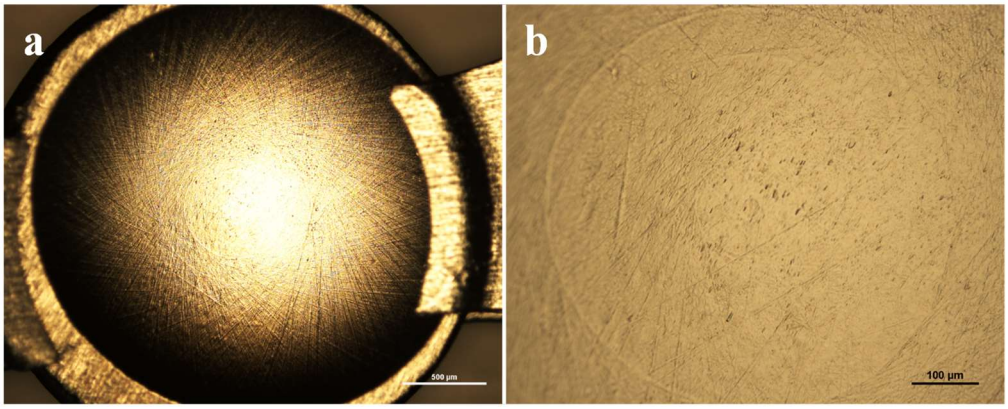

Figure A1-1 Optical microscopy image of the 3mm disc after dimpling doun to ~30 µm thickness

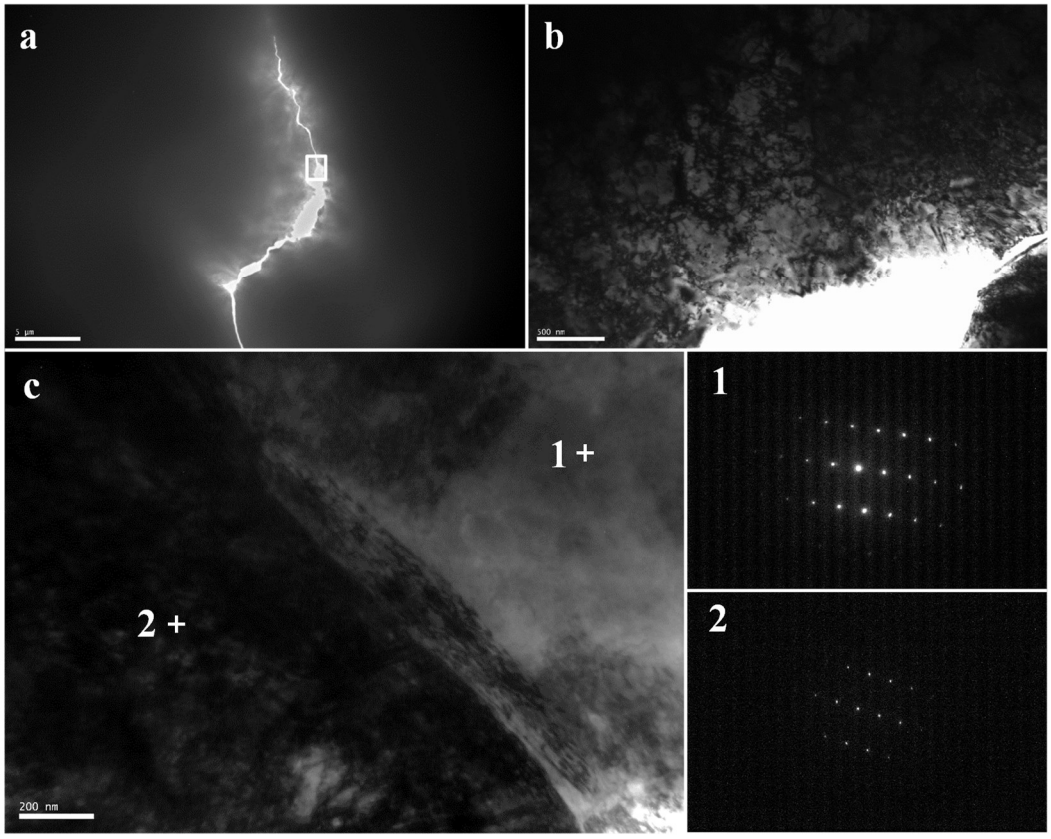

Figure A1-2 TEM image of a,b) a small hole appeared in the middle of the disc, c) a represented two grain with in the 304-SS substrate with associated CBED patterns from the specified locations consistent with (1) fcc close to <310> projection and (2) fcc close to <001> or bcc close to <112> projection

Appendix 2 Heat transfer equations

Heat transfer equations and boundary conditions of the single spark inter action model (Chapter 5).

Interior nodes

Figure 5-1 illustrates the Gaussian heat distribution and interaction with the workpiece surface along with the associated boundary conditions used for the analysis. The model is considered a two dimensional system under transient heat condition and no internal heat generation, therefore, the governing Fourier heat conduction equation can be written as:

$$\frac{\partial^2 T}{\partial x^2} + \frac{\partial^2 T}{\partial y^2} = \frac{1}{\alpha}\frac{\partial T}{\partial t} \qquad \text{(A-1)}$$

The central difference approximation can be used to obtain a finite difference form of this equation. The approximation of first order differentiation at (m+$\frac{1}{2}$, n) and (m-$\frac{1}{2}$, n) expressed as:

$$\frac{\partial T}{\partial x}\Big|_{(m+1/2,n)} \approx \frac{T_{m+1,n} - T_{m,n}}{\Delta x} \qquad \text{(A-2)}$$

$$\frac{\partial T}{\partial x}\Big|_{(m-1/2,n)} \approx \frac{T_{m,n} - T_{m-1,n}}{\Delta x} \qquad \text{(A-3)}$$

The subscripts of (m and n) are used to design the (x and y) location of the discrete nodal point. The approximation of second order differentiation for the x direction at m,n expressed as:

$$\frac{\partial^2 T}{\partial x^2}\Big|_{(m,n)} \approx \frac{T_{m+1,n}+T_{m-1,n}-2T_{m,n}}{\Delta x^2} \qquad \text{(A-4)}$$

Similarly for the y direction:

$$\frac{\partial^2 T}{\partial y^2}\Big|_{(m,n)} \approx \frac{T_{m,n+1}+T_{m,n-1}-2T_{m,n}}{\Delta y^2} \qquad \text{(A-5)}$$

In transient heat mode the problem must be discretized in time in addition to discretization in space, therefore, the integer p in introduce where:

$$t = p\,\Delta t \qquad \text{(A-6)}$$

And the finite difference approximation to the time derivative in equation A-1 is expressed as:

$$\frac{\partial T}{\partial t}\Big|_{(m,n)} \approx \frac{T_{m,n}^{p+1}-T_{m,n}^{p}}{\Delta t} \qquad \text{(A-7)}$$

The superscript p is used to denote the time dependence of temperature T and the time derivative is expressed in term of the temperature difference associated with new (p + 1) and previous (p) time, hence the calculation must be performed at successive time separated by the interval Δt. By substituting equations A-4, A-5 and A-7 into equation A-1, the explicit form with Δx = Δy of the finite difference equation for the interior node is written as [150]:

$$T_{m,n}^{p+1} = F_{\circ}(T_{m+1,n}^{p} + T_{m-1,n}^{p} + T_{m,n+1}^{p} + T_{m,n-1}^{p}) + (1 - 4F_{\circ})T_{m,n}^{p} \qquad \text{(A-8)}$$

Where $F_\circ$ is the Fourier number (dimensionless) and express as:

$$\boldsymbol{F_\circ = \frac{\alpha\,\Delta t}{\Delta x^2}} \qquad \text{(A-9)}$$

The accuracy of the finite difference solution can be improved by decreasing the value of Δx, Δy and Δt, consequently the interior nodal point must be increase with decrease of Δx and Δy. The undesirable future of the explicit method is the not unconditionally stable, and therefore, the chosen of Δx must be maintained below a certain limit which depends on the Δt and other parameters in the system. Therefore, the stability criterion for the interior node and two dimension node is $(1\text{-}4F_\circ) \geq o$, or $F_\circ \leq \frac{1}{4}$.

Top surface nodes (conduction)

The top surface of the workpiece is undergone to conduction heat transfer between a plasma channel and underneath the workpiece surface and convective heat flow with the dielectric fluid (Figure 5-1), the near surface node has been assigned a thickness equal to half of that of interior node. The general form of the energy balance during time interval Δt is expressed as:

$$\sum \dot{\boldsymbol{Q}}_{\boldsymbol{in}} + \dot{\boldsymbol{E}}_{\boldsymbol{gen}} = \dot{\boldsymbol{E}}_{\boldsymbol{es}} \qquad \text{(A-10)}$$

Where $\dot{\boldsymbol{Q}}_{\boldsymbol{in}}$ (W) is the rate of energy transfer into the control volume, $\dot{\boldsymbol{E}}_{\boldsymbol{gen}}$ (W) is the rate of energy generation in this case is zero and $\dot{\boldsymbol{E}}_{\boldsymbol{es}}$ (W) is the rate of increase the energy stored within the control volume.

Or can be expressed as:

$$\Delta t \sum \dot{\boldsymbol{Q}}_{\boldsymbol{in}} + \Delta t\, \dot{\boldsymbol{E}}_{\boldsymbol{gen}} = \Delta \dot{\boldsymbol{E}}_{\boldsymbol{es}} \qquad \text{(A-11)}$$

Where:

$$\Delta \dot{\boldsymbol{E}}_{\boldsymbol{es}} = \boldsymbol{\rho}\, \boldsymbol{V}_{\boldsymbol{element}}\, \boldsymbol{c}_{\boldsymbol{p}}\, \Delta \boldsymbol{T} \qquad \text{(A-12)}$$

Therefore:

$$\sum \dot{\boldsymbol{Q}}_{\boldsymbol{in}} + \Delta \boldsymbol{t}\, \dot{\boldsymbol{E}}_{\boldsymbol{gen}} = \boldsymbol{\rho}\, \boldsymbol{V}_{\boldsymbol{element}}\, \boldsymbol{c}_{\boldsymbol{p}}\, \frac{\Delta \boldsymbol{T}}{\Delta \boldsymbol{t}} \qquad \text{(A-13)}$$

In finite difference form:

$$\sum \dot{\boldsymbol{Q}}_{\boldsymbol{in}} + \Delta t\, \dot{\boldsymbol{E}}_{\boldsymbol{gen}} = \boldsymbol{\rho}\, \boldsymbol{V}_{\boldsymbol{element}}\, \boldsymbol{c}_{\boldsymbol{p}}\, \frac{\boldsymbol{T}_{\boldsymbol{m,n}}^{\boldsymbol{p+1}} - \boldsymbol{T}_{\boldsymbol{m,n}}^{\boldsymbol{p}}}{\Delta \boldsymbol{t}} \qquad \text{(A-14)}$$

The rate heat flow by conduction through a solid expressed as:

$$\boldsymbol{q} = -\boldsymbol{kA}\frac{\boldsymbol{dt}}{\boldsymbol{dn}} \qquad \text{(A-15)}$$

The finite difference approximation in x direction can be written as:

$$\boldsymbol{q}_{\boldsymbol{x}} = \boldsymbol{k}\, \frac{\Delta \boldsymbol{y}}{\boldsymbol{2}}\, \frac{\boldsymbol{T}_{\boldsymbol{m-1,n}} - \boldsymbol{T}_{\boldsymbol{m,n}}}{\Delta \boldsymbol{x}} \qquad \text{(A-16)}$$

$$q_x = k \frac{\Delta y}{2} \frac{T_{m+1,n} - T_{m,n}}{\Delta x} \qquad \text{(A-17)}$$

And in y direction can be written as:

$$q_y = k \Delta x \frac{T_{m,n-1} - T_{m,n}}{\Delta y} \qquad \text{(A-18)}$$

Substituting equations A-16, A-17, A-18 and the main heat flux into equation A-13 can obtain:

$$q_{m,n} + k \frac{\Delta y}{2} \frac{T_{m-1,n} - T_{m,n}}{\Delta x} + k \frac{\Delta y}{2} \frac{T_{m+1,n} - T_{m,n}}{\Delta x} + k \Delta x \frac{T_{m,n-1} - T_{m,n}}{\Delta y} = \rho \ c_p \Delta x \frac{\Delta y}{2} \frac{T_{m,n}^{p+1} - T_{m,n}^{p}}{\Delta t} \qquad \text{(A-19)}$$

With square mesh Δx=Δy the final finite difference form for the node on the surface under the plasma channel (conduction mode) can be written as:

$$T_{m,n}^{p+1} = \left(1 - 4F_\circ\right) T_{m,n}^{p} + F_\circ \left(2T_{m,n-1}^{p} + T_{m-1,n}^{p} + T_{m+1,n}^{p}\right) + 2F_\circ \, q_{m,n} \frac{\Delta x}{k} \qquad \text{(A-20)}$$

Top surface nodes (convection)

The rate heat flow by convection can be found using Newten equation:

$$\boldsymbol{q = h(T_s - T_\infty)} \qquad \text{(A-21)}$$

Substituting equations A-16 , A-17, A18 and A-19 into equation A-13 we obtain the final finite difference form for the node on the surface that contact with the dielectric fluid (convection mode) , the stability criterion for the surface with convection mode is $\boldsymbol{F_\circ}$ (2+Bi) ≤ $\boldsymbol{\frac{1}{2}}$, and can be written as [151]:

$$\boldsymbol{T^{p+1}_{m,n} = F_\circ(2T^p_{m-1,n} + T^p_{m,n+1} + T^p_{m,n-1} + 2Bi\, T_\infty) + (1 - 4F_\circ - 2Bi\, F_\circ)\, T^p_{m,n}} \qquad \text{(A-22)}$$

Corner nodes (conduction and convection)

For the external corner with conduction:

$$\boldsymbol{T^{p+1}_{m,n} = \left(1 - 3F_\circ\right) T^p_{m,n} + F_\circ\left(T^p_{m+1,n} + 2T^p_{m,n-1}\right) + 2F_\circ\, q\, \frac{\Delta x}{k}} \qquad \text{(A-23)}$$

For the external corner with convection with $\boldsymbol{F_\circ}$ (1+Bi) ≤ $\boldsymbol{\frac{1}{4}}$:

$$\boldsymbol{T^{p+1}_{m,n} = 2F_\circ(T^p_{m-1,n} + T^p_{m,n-1} + 2Bi\, T_\infty) + (1 - 4F_\circ - 4Bi\, F_\circ)\, T^p_{m,n}} \qquad \text{(A-24)}$$

Appendix 3 MATLAB code

The MATLAB Code of numerical simulation (Chapter 5).

Heating phase

The code present in this section is an example of the numerical simulation of the heating phase of single crater event of the EDC coating process using TiC tool electrode and 304-SS substrate at 10 A current and 8 µs pulse-on time.

```
clear all
close all
clc
tic
%Input Data Samer
rr = 34.5e-6;%input('Enter the experimental radius value micrometre*e-6= ');
hh =10.4e-6;%input('Enter the experimental depth value micrometre*e-6 = ');
Iav=10;%input('Enter the current value in amps = '); % %input applied
tonn=8e-6 ; %input('Enter the pulse-on value in microsecond *e-6  = ');
V1=30;%input('Enter discharge voltage value in (V) = ');

%Properties Data
MP1=1698; %melting point of 304-SS (K)
MP2= 3478; %melting point of TiC
kST=15; % thermal conductivity of 304-SS (W/m.k)
kTiC=18.25;  % thermal conductivity of TiC+304-SS (W/m.k)
q1=7905;% density of 304-SS (kg/m^3)
q2=6407.5;%density of TiC+304-SS (kg/m^3)
cp1=510;% specific heat of 304-SS (J/kg.k)
cp2=533.25;% specific heat of TiC+304-SS (J/kg.k)
lm1= 272500; %latent heat of fusion of 304-SS (J/Kg)
lm2= 716250;% latent heat of fusion of TiC+304-SS (J/Kg)

%surface domain
R=rr*3;
Y=R/2;
dx = 0.5e-6; %mesh resolution in meters
dt=1e-8;
r = 0:dx:R; %total distance in x direction (it will divide the vector and
give the value of R)
y = 0:dx:Y; %total distance in y direction  (it will divide the vector and
give the value of y)

T=0:dt:tonn;  %total pulse on
 [R_plot,Y_plot]=meshgrid(r,y);
```

```
%surface criteria for heating
 alfa1=kST/(q1*(cp1+(lm1/MP1)));%thermal diffusivity of 304-SS (m^2/s)
 alfa2=kTiC/(q2*(cp2+(lm2/MP2)));%thermal diffusivity of TiC (m^2/s)
 F011 = (alfa1*dt)/(dx^2); %Fourier number for the 304-SS case
 F012 = (alfa2*dt)/(dx^2); %Fourier number for the TiC case
             if F011 <= 0.25 %   criterion for mesh grid used in the program
(conduction)
                 disp('surface node criterion met for heating 1')
             if F012 <= 0.25 %   criterion for mesh grid used in the program
(conduction)
                 disp('surface node criterion met for heating 2')
k=[kST, kTiC]; %thermal conductivity of 304-SS (W/m.k)
F0=[F011, F012];

%surface criteria for cooling
Tliquid= 293;% liquid temperature
h=1750; %heat transfer coefficient of free oil W/m2.K
alfa11=(kST/(q1*cp1));%thermal diffusivity of 304-SS (m^2/s)
 alfa22=(kTiC/(q2*cp2));%thermal diffusivity of TiC (m^2/s)
 F011 = (alfa11*dt)/(dx^2); %Fourier number for the 304-SS case
 F022= (alfa22*dt)/(dx^2); %Fourier number for the TiC case
Bi1=((h*dx)/kST);%
Bi2= ((h*dx)/kTiC);%
if  F011*(2+Bi1) <= 0.5 %   criterion for mesh grid used in the program
(conduction)
                 disp('surface node criterion met for cooling 1')
if  F011*(1+Bi1) <= 0.25 %   criterion for mesh grid used in the program
(conduction)
                 disp('surface node criterion met for cooling 11')
if F022*(1+Bi2) <= 0.25 %   criterion for mesh grid used in the program
(conduction)
                 disp('surface node criterion met for cooling 2')
if F022*(2+Bi2) <= 0.5 %   criterion for mesh grid used in the program
(conduction)
                 disp('surface node criterion met for cooling 22')
%frame=0;%for movie

%start calculation
 Fv1=0;
mxl = 0;
myl = 0;
des1 = 0; % initial condition not satisfied
des2 = 0; % initial condition not satisfied
des=and(des1,des2);

%Mesh Generation
m = length (r); %number of rows in mesh
n = length (y); %number of columns in mesh
ton= length  (T);
```

```
%Interpolation
current=[ 2,  2,  2,  2,  2,  2;
          6,  6,  6,  6,  6,  6;
         10, 10, 10, 10, 10, 10;
         14, 14, 14, 14, 14, 14;
         19, 19, 19, 19, 19, 19];

time=[ 2, 4, 8, 16, 32, 64;
       2, 4, 8, 16, 32, 64;
       2, 4, 8, 16, 32, 64;
       2, 4, 8, 16, 32, 64;
       2, 4, 8, 16, 32, 64];

radius=[18.0732, 21.5322, 22.6500, 32.6450, 42.9050, 48.6950;
        18.4500, 31.3950, 32.3500, 48.8850, 67.7100, 82.0500;
        20.3000, 32.000, 37.000, 57.4000, 82.6500, 90.7500;
        19.9800, 42.3350, 45.8000, 70.0250, 137.6750,132.6050;
        19.4550, 48.4650, 51.000, 84.5900, 111.1350, 144.5250];

current_q=Iav;
time_q=tonn*1e6;
radius_q =griddata(current,time,radius,current_q,time_q);

%for the convection on the surface
%rcp=(((7.5e-6)*(Iav^0.37)*(((tonn*1e6)^0.4))))
rcp=(radius_q)*1e-6
Rcp = 0:dx:rcp; %total distance in x direction (it will divide the vector
and give the value of Rcp)
rcpNP=length(Rcp);

while (des1==0)&&(des2==0)&&(Fv1<=1)
Fv1 = Fv1+0.01;
A=ones(n,m);
tempstart=A*Tliquid;
TempOld =tempstart; %mesh of m rows, n columns, at uniform temperature Ti;
TempNew=zeros(n,m);
for l=2:ton

    for j = 1:n
        for i = 1:m
            if TempNew(j,i) > MP1
                k1 = k(2);F01=F0(2);
               else
                k1 =k(1);F01=F0(1);
            end
                if (i==1)&&(j==1)
                    TempNew(j,i)=((1-
(3*F01))*TempOld(1,1))+(F01*((2*TempOld(1,2))+TempOld(2,1)))+((2*F01*(dx/k1)
*((4.57*Fv1*V1*Iav)/(pi*((rcp)^2))))*(exp(-3*((r(i)/(rcp))^2)))); %top left
corner symmetric
```

```
                    elseif (j==1)&&(i==m)
                            TempNew(j,i)=(((1-(4*F011)-
(4*Bi1*F01))*(TempOld(1,m)))+((2*(F01)*(((TempOld(1,m-
1)))+(TempOld(2,m))+(2*Bi1*Tliquid))))); %top right corner convection
                        elseif (j==n)&&(i==1)
                            TempNew(j,i)=((1-
(3*F01))*TempOld(n,1))+(F01*((2*TempOld(n,2))+TempOld(n-1,1)));   %down left
corner insulated
                            elseif (j==n)&&(i==m)
                                 TempNew(j,i)=((1-
(3*F01))*TempOld(n,m))+(F01*((2*TempOld(n,m-1))+TempOld(n-1,m))); %down
right corner insulated
                                elseif (j==1)&&(i>=2)&&(i<=(rcpNP))
                                    TempNew(j,i)=((1-
(4*F01))*TempOld(1,i))+(F01*(2*TempOld(2,i)+TempOld(1,i+1)+TempOld(1,i-
1)))+((2*F01*(dx/k1)*((4.57*Fv1*V1*Iav)/(pi*((rcp)^2))))*(exp(-
3*((r(i)/(rcp))^2))));   %top surface conduction
                                    elseif (j==1)&&(i>rcpNP)&&(i<=(m-1))
                                      TempNew(j,i)=((1-(4*F011)-
(2*Bi1*F01))*TempOld(1,i))+(F01*(((2*TempOld(2,i)))+(TempOld(1,i+1))+(TempOl
d(1,i-1))+(2*Bi1*Tliquid)));%top surface convection


                                    elseif (j==n)&&(i>=2)&&(i<=(m-1))
                                        TempNew(j,i)=((1-
(4*F01))*TempOld(n,i))+(F01*(2*TempOld(n-1,i)+TempOld(n,i+1)+TempOld(n,i-
1)));   %bottom surface insulated
                                        elseif (j>=2)&&(j<=(n-1))&&(i==m)
                                            TempNew(j,i)=((1-
(4*F01))*TempOld(j,m))+(F01*(2*TempOld(j,m-1)+TempOld(j+1,m)+TempOld(j-
1,m)));%right right surface insulated
                                            elseif (j>=2)&&(j<=(n-
1))&&(i==1)
                                                TempNew(j,i)=((1-
(4*F01))*TempOld(j,1))+(F01*(2*TempOld(j,2)+TempOld(j+1,1)+TempOld(j-1,1)));
%left surface symmetric
                else
                    TempNew(j,i)=((1-
(4*F01))*TempOld(j,i))+(F01*(TempOld(j+1,i)+TempOld(j-
1,i)+TempOld(j,i+1)+TempOld(j,i-1)));  %interior node
                end
            end
    end

    TempOld=TempNew;%program repeats another iteration using new temp
distribution
    surf(R_plot,-Y_plot,TempNew);  axis tight; axis equal;
title(['T=',num2str(T(l))]);  view(2), colorbar;  shading interp
    axis([0 4E-5 -2E-5 0]);
```

```
     xlabel('Crater radius (m)')
     ylabel('Crater depth from the surface (m)')
%      pause(0.01)
      drawnow;
% frame=frame+1;% for movie
% fig1=figure(1); % for movie
% mov2(frame)=getframe(fig1);   %for movie
end
% movie2avi(mov2, 'Video_11.avi', 'compression', 'None','fps',4);%for
convert movie file to AVI media player
mx = 0;
my = 0;
    for iOJ=1:m
        if TempNew(1,iOJ)>=MP1
            mx=mx+1;
        end
    end
    for kOJ=1:n
        if TempNew(kOJ,1)>=MP1
            my=my+1;
        end
    end
mxl = mx*dx;
myl = my*dx;

fractureenergy=Fv1

     if (mxl>=0.99*rr) %&& (myl>=0.97*hh)
          des1 = 1;
          des2 = 1;
     end
    des=and(des1,des2);
    ddd = [des des1 des2]
    mxl;
    radius= mxl*1e6
    myl;
    thickness=myl*1e6
     cratervolume=(((pi*  (mxl^2)*myl)/8))+((pi*(myl^3))/6)*1e18


end
             end
             end
             end
             end
             end
             end

  save('Last_Temp.mat','mxl','mx','myl','my','TempNew')
```

```
%draw the crater boundary
     g=0;
     for j=1:n
         for i=1:m
             if TempNew(j,i)<=MP1
                 g=g+1;
                 if i==1%
                      xx(g)=R_plot(j,i+0);%
                      yy(g)=Y_plot(j,i);%
                     break%
                 end
                 xx(g)=R_plot(j,i+0);
                 yy(g)=Y_plot(j,i);
                 break
             end
          end
          if TempNew(j,1)<=MP1
              break
         end
     end
      yy(end)=yy(end-0);
       figure
        plot (xx,-yy)
        xlabel('Crater radious (m)')
        ylabel('Crater depth from the surface (m)')
     xxx=xx';
     yyy=-yy';

save('crater_geometry.mat','xx','yy','radius','thickness','fractureenergy','
cratervolume','xxx','yyy')

 toc
```

Cooling phase

The code present in this section is an example of the numerical simulation of the cooling phase of single crater event of the EDC coating process using TiC tool electrode and 304-SS substrate at 10 A current and 8 µs pulse-on time.

```
clear all
clc
tic
rr = 34.5e-6;%input('Enter the experimental radius value micrometre*e-6= ');
hh =10.4e-6;%input('Enter the experimental depth value micrometre*e-6 = ');
R=rr*3;
Y=R/2;
dx =0.5e-6; %mesh resolution in meters
dt=1e-8;
r = 0:dx:R; %total distance in x direction (it will divide the vector and
give the value of R)
y = 0:dx:Y; %total distance in y direction  (it will divide the vector and
give the value of y)
 load('Last_Temp.mat');
% surf(R_plot,-Y_plot,TempNew);  axis tight; axis equal; view(2), colorbar;
shading interp

 [R_plot,Y_plot]=meshgrid(r,y);
%  figure
%  surf(R,-Y,A);  axis tight; axis equal; view(2), colorbar;  shading interp

%Properties Data
 h=1750;       %heat transfer coefficent of free oil  W/m2.K
timeoff=(256*5)*1e-6;          %       ;
T=0:dt:timeoff;  %total pulse on
Tliquid= 293;% liquid temperature
toff= length  (T);
kST=15; % thermal conductivity of 304-SS (W/m.k)
kTiC=18.25;  % thermal conductivity of TiC (W/m.k)
q1=7905;  % density of 304-SS (kg/m^3)
q2=6407.5;  %density of TiC (kg/m^3)
cp1=510;  % specific heat of 304-SS (J/kg.k)
cp2=533.25;  % specific heat of TiC (J/kg.k)
lm1= 272500; %latent heat of fusion of 304-SS
lm2= 716250;% latent heat of fusion of TiC
MP1=1698; %melting point of  304 ST.ST (K)
MP2= 3478; %melting point of TiC
alfa1=(kST/(q1*cp1));%thermal diffusivity of 304-SS (m^2/s)
alfa2=(kTiC/(q2*cp2));%thermal diffusivity of TiC (m^2/s)
F01 = (alfa1*dt)/(dx^2); %Fourier number for the 304-SS case
F02= (alfa2*dt)/(dx^2); %Fourier number for the TiC case
```

```
Bi1=((h*dx)/kST);%
Bi2= ((h*dx)/kTiC);%
if  F01*(2+Bi1) <= 0.5 %   criterion for mesh grid used in the program
(conduction)
                disp('surface node criterion met for cooling 1')
if  F01*(1+Bi1) <= 0.25 %   criterion for mesh grid used in the program
(conduction)
                disp('surface node criterion met for cooling 11')
if F02*(1+Bi2) <= 0.25 %   criterion for mesh grid used in the program
(conduction)
                disp('surface node criterion met for cooling 2')
if F02*(2+Bi2) <= 0.5 %   criterion for mesh grid used in the program
(conduction)
                disp('surface node criterion met for cooling 22')

m = length (r); %number of rows in mesh
n = length (y); %number of columns in mesh
toff= length  (T);
TempOldcooling =TempNew; %bring the final heat distribution
TempNewcooling=ones(n,m);
%
mxl;
myl;
Mx1=0:dx:mxl;
Mx1NP=length (Mx1);
My1=0:dx:myl;
My1NP=length (My1);
%
des1=0;des3=zeros(n,1);
des1;
% frame=0;% for video
for l=2:toff
if (des1==1)

  break
end
  for kk=1:n
    if TempOldcooling(kk,1)<=1000
    des3(kk,1) = 1;
    else des3(kk,1)=0;
    end
  end

des1=fix(sum(des3)/max(size(des3)));
    des=des1;
    ddd = [des des1];
    T(l);
    for j = 1:n
        for i = 1:m
```

```
                if (j==1)&&(i==1)
                    TempNewcooling(j,i)=(((1-(4*F02)-
(4*Bi2*F02))*(TempOldcooling(1,1)))+((2*(F02)*(((TempOldcooling(1,2)))+(Temp
Oldcooling(2,1))+(2*Bi2*Tliquid))))); %top left corner convection
                    elseif (j==1)&&(i==m)
                        TempNewcooling(j,i)=(((1-(4*F02)-
(4*Bi2*F02))*(TempOldcooling(1,m)))+((2*(F02)*(((TempOldcooling(1,m-
1)))+(TempOldcooling(2,m))+(2*Bi1*Tliquid))))); %top right corner convection
                        elseif (j==n)&&(i==1)
                            TempNewcooling(j,i)=Tliquid;%((1-
(3*F01))*TempOldcooling(n,1))+(F01*((2*TempOldcooling(n,2))+TempOldcooling(n
-1,1)));   %down left corner symetric
                            elseif (j==n)&&(i==m)
                                TempNewcooling(j,i)=Tliquid; %down right
corner fixed
                                elseif (j==1)&&(i>=2)&&(i<=(Mx1NP))
                                    TempNewcooling(j,i)=((1-(4*F02)-
(2*Bi2*F02))*TempOldcooling(1,i))+(F02*(((2*TempOldcooling(2,i)))+(TempOldco
oling(1,i+1))+(TempOldcooling(1,i-1))+(2*Bi2*Tliquid)));   %top surface TiC
convection
                                     elseif (j==1)&&(i>=(Mx1NP))&&(i<=(m-1))
                                    TempNewcooling(j,i)=((1-(4*F01)-
(2*Bi1*F01))*TempOldcooling(1,i))+(F01*(((2*TempOldcooling(2,i)))+(TempOldco
oling(1,i+1))+(TempOldcooling(1,i-1))+(2*Bi1*Tliquid)));   %top surface 304
convection
                                    elseif (j==n)&&(i>=2)&&(i<=(m-1))
                                        TempNewcooling(j,i)=Tliquid;
%bottom surface fixed
                                        elseif (j>=2)&&(j<=(n-1))&&(i==m)

TempNewcooling(j,i)=Tliquid;%right right surface fixed
                                            elseif
(j>=2)&&(j<=(My1NP))&&(i==1)
                                                TempNewcooling(j,i)=((1-
(4*F02))*TempOldcooling(j,1))+(F02*(2*TempOldcooling(j,2)+TempOldcooling(j+1
,1)+TempOldcooling(j-1,1))); %left surface TiC symmetric
                                                  elseif
(j>=(My1NP))&&(j<=(n-1))&&(i==1)
                                                   TempNewcooling(j,i)=((1-
(4*F01))*TempOldcooling(j,1))+(F01*(2*TempOldcooling(j,2)+TempOldcooling(j+1
,1)+TempOldcooling(j-1,1))); %left surface 304 symmetric
                  elseif    (j>=2)&&(j<=(My1NP))&&(i>=2)&&(i<=(Mx1NP))
               TempNewcooling(j,i)=((1-
(4*F02))*TempOldcooling(j,i))+(F02*(TempOldcooling(j+1,i)+TempOldcooling(j-
1,i)+TempOldcooling(j,i+1)+TempOldcooling(j,i-1)));  %interior TiC node
                else %(j>=(My1NP))&&(j<=(n-1))&&(i>=(Mx1NP))&&(i<=(m-1))
                    TempNewcooling(j,i)=((1-
(4*F01))*TempOldcooling(j,i))+(F01*(TempOldcooling(j+1,i)+TempOldcooling(j-
1,i)+TempOldcooling(j,i+1)+TempOldcooling(j,i-1)));  %interior 304 node
                end

       end
    end
```

```
    TempOldcooling=TempNewcooling;%program repeats another iteration using
new temp distribution

%frame=frame+1;for video
figure(1)
surf(R_plot,-Y_plot,TempNewcooling);  axis tight; axis equal;
title(['T=',num2str(T(l))]);  view(2), colorbar;  shading interp

     xlabel('Crater radious (m)')
     ylabel('Crater depth from the surface (m)')
%      pause(0.01)
     % drawnow;

% fig1=figure(1);                          %  for video
% mov2(frame)=getframe(fig1);
end
end
end
end
end
 %movie2avi(mov2, 'Video_11.avi', 'compression', 'None','fps',4); %for
 %vedio

% for calculation the cooling rate
Time=T(l);
AA=TempNew(:,1);
TEMPTEMP= TempNewcooling(:,1);
coolingrate=(-1*((log((TEMPTEMP-Tliquid)./(AA-Tliquid)))./Time) );
save('cooling-rate.mat','coolingrate')

% for drawing the cooling rate vs melting depth
depth=1:n;
melteddepth=(depth*dx)-dx;
figure (2)
plot (melteddepth,coolingrate)
   xlabel('crater depth from the surface (m)')
   ylabel('cooling rate (K/ms)')
xxx=melteddepth';
yyy=coolingrate;
save('cooling.mat','Time','xxx','yyy')
toc
```

Appendix 4 SE images of the wear tracks

A details of SE images of the wear track and highlighted details for the samples investigated in the thesis (Chapter 6).

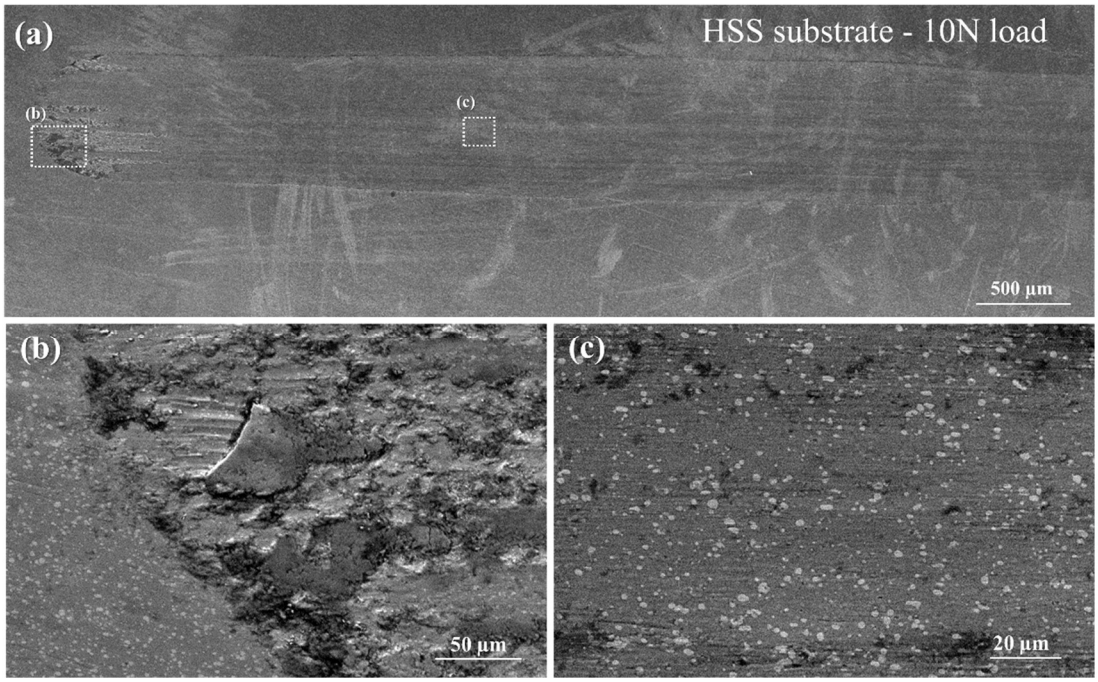

Figure A4-1 Low magnification SE images showing (a) the extent and (b,c) representative details of a wear scar on an as-polished HSS substrate under loading conditions of 10 N

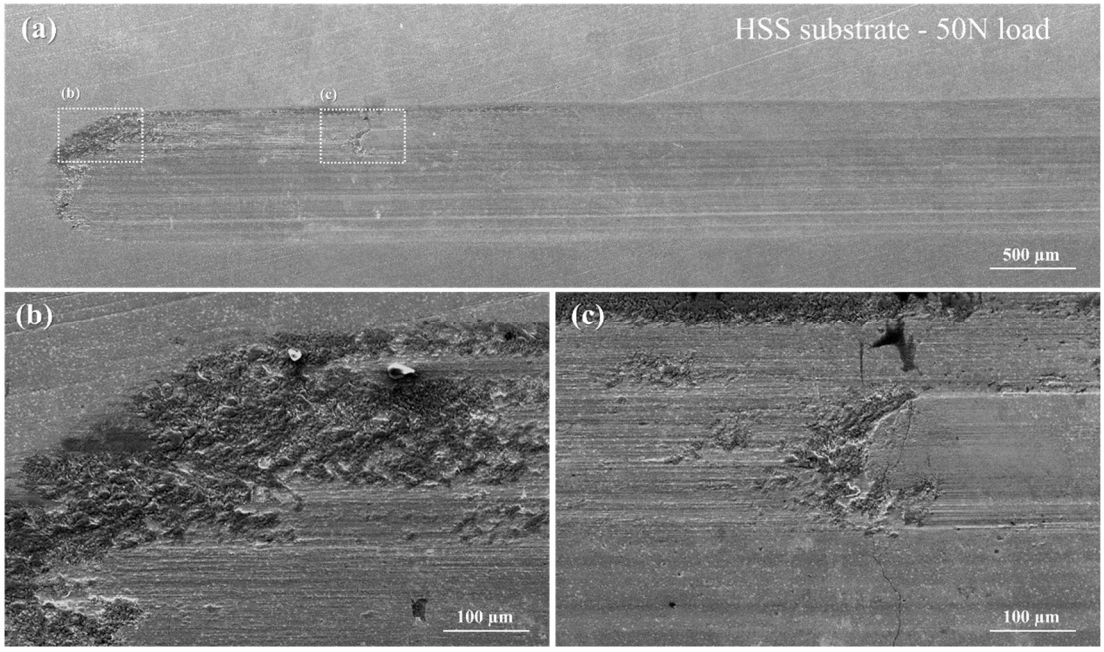

Figure A4-2 Low magnification SE images showing (a) the extent and (b,c) representative details of a wear scar on an as-polished HSS substrate under loading conditions of 50 N

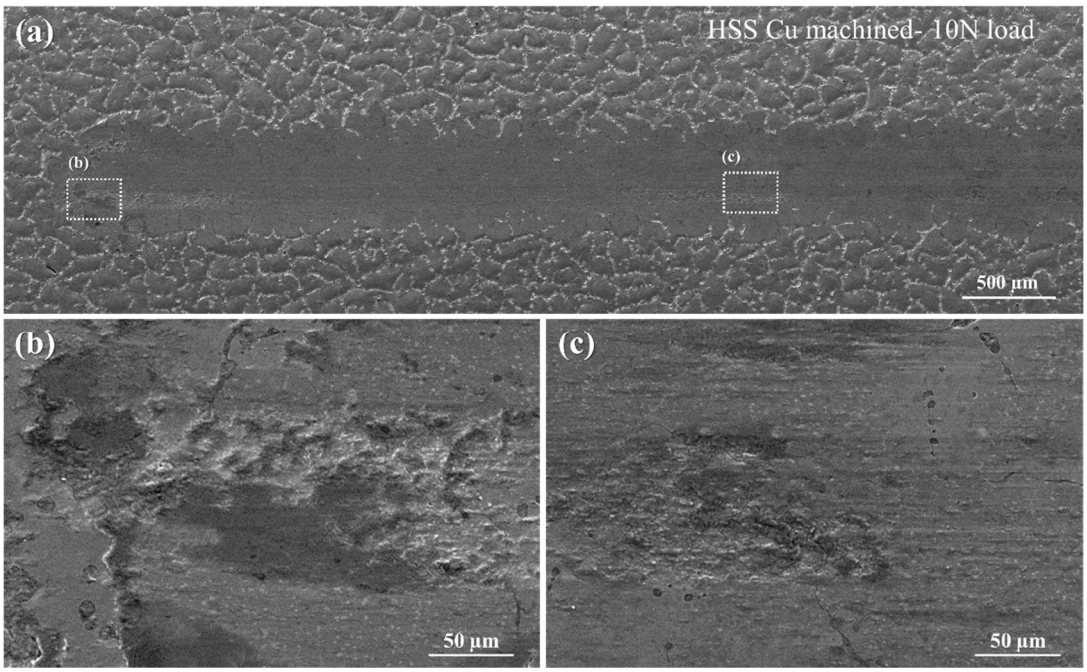

Figure A4-3 Low magnification SE images showing (a) the extent and (b,c) representative details of a wear scar on HSS Cu machined under loading conditions of 10 N

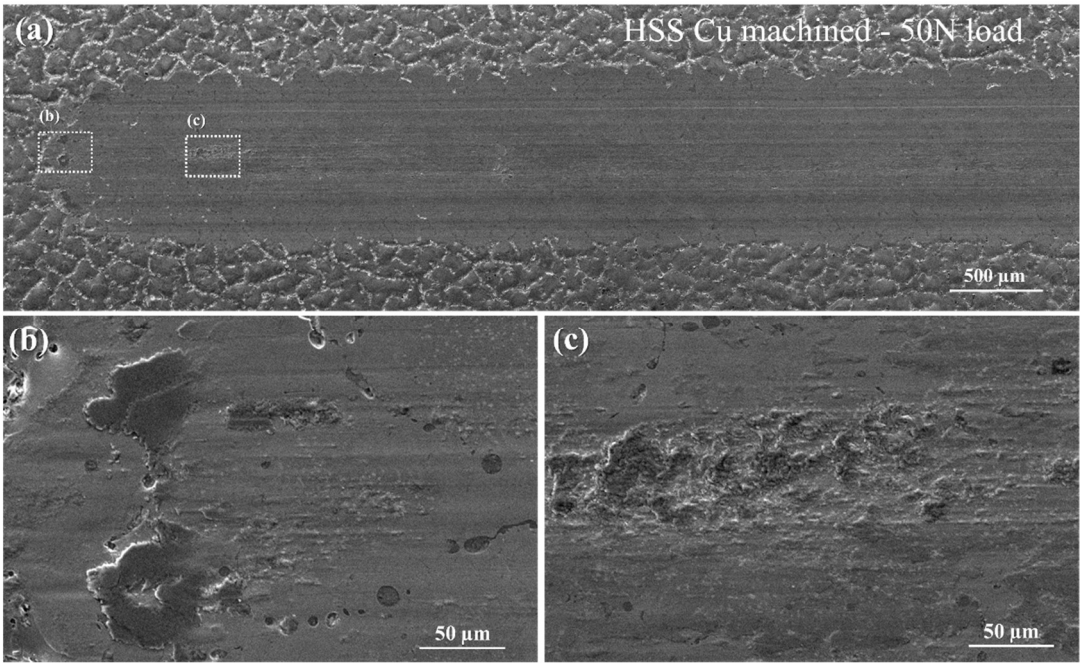

Figure A4-4 Low magnification SE images showing (a) the extent and (b,c) representative details of a wear scar on HSS Cu machined under loading conditions of 50 N

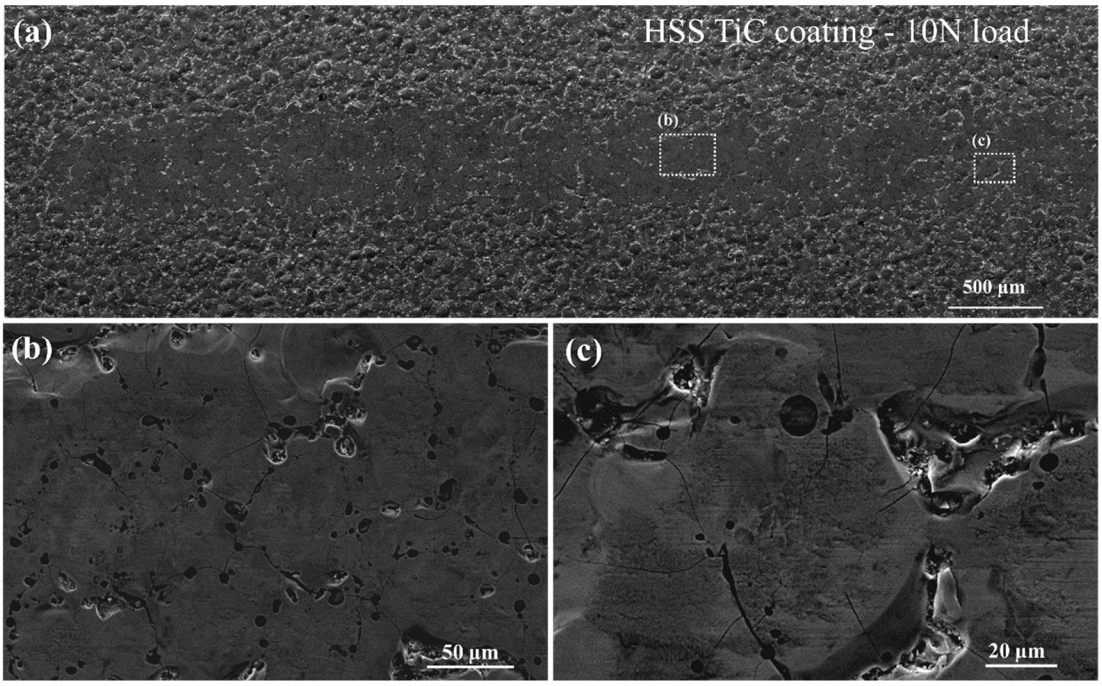

Figure A4-5 Low magnification SE images showing: (a) the extent and (b,c) representative details of a wear scar on a cermet coated HSS sample, under loading conditions of 10 N

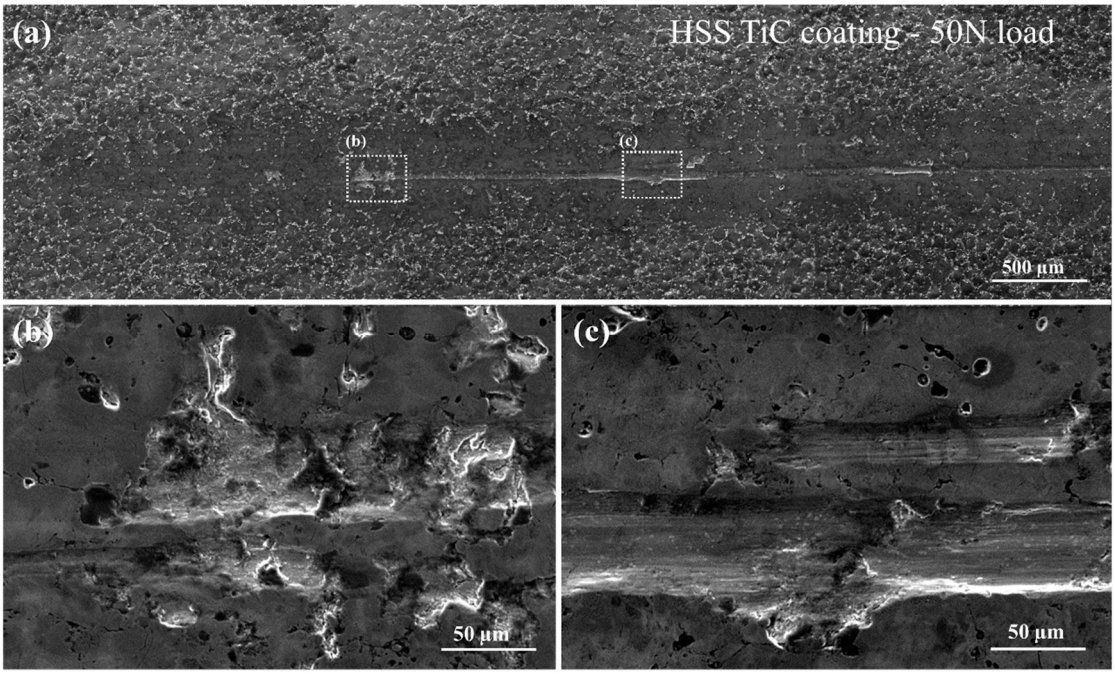

Figure A4-6 Low magnification SE images showing (a) the extent and (b,c) representative details of a wear scar on a cermet coated HSS sample, under loading conditions of 50 N

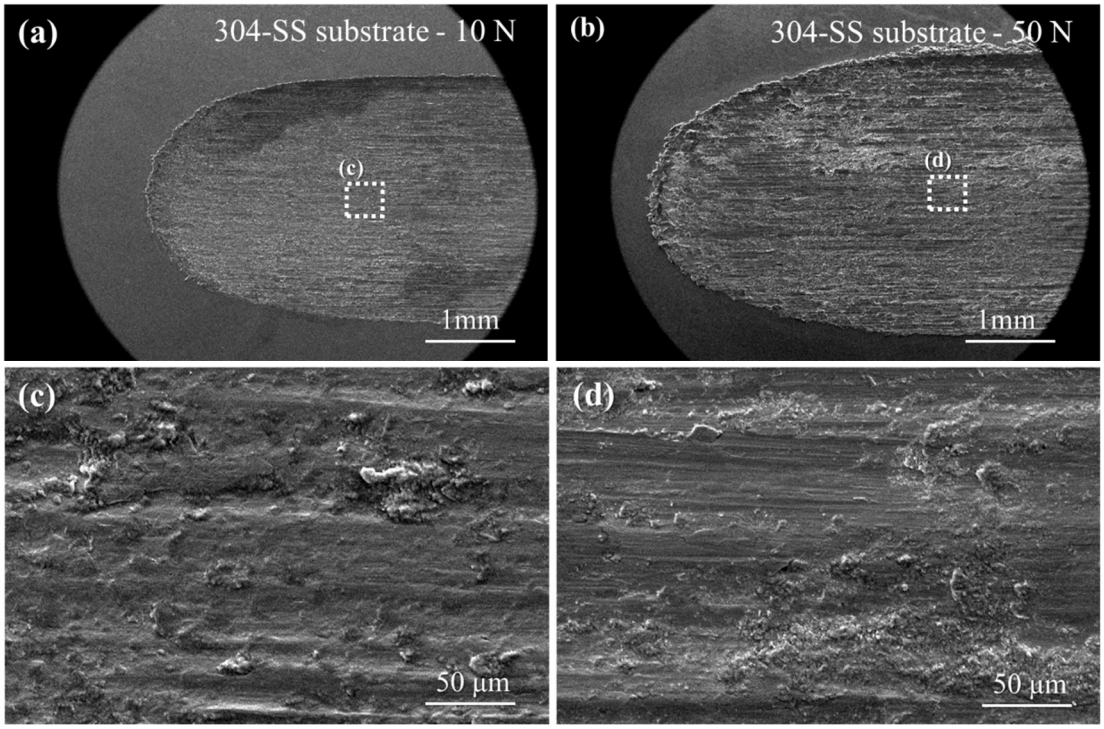

Figure A4-7 SE images of (a,b) low magnification of the as-polished 304-SS substrate under loading conditions of 10 & 50 N and (c,d) representative details of a wear scar on an as-polished 304-SS substrate under loading conditions of 10 & 50 N

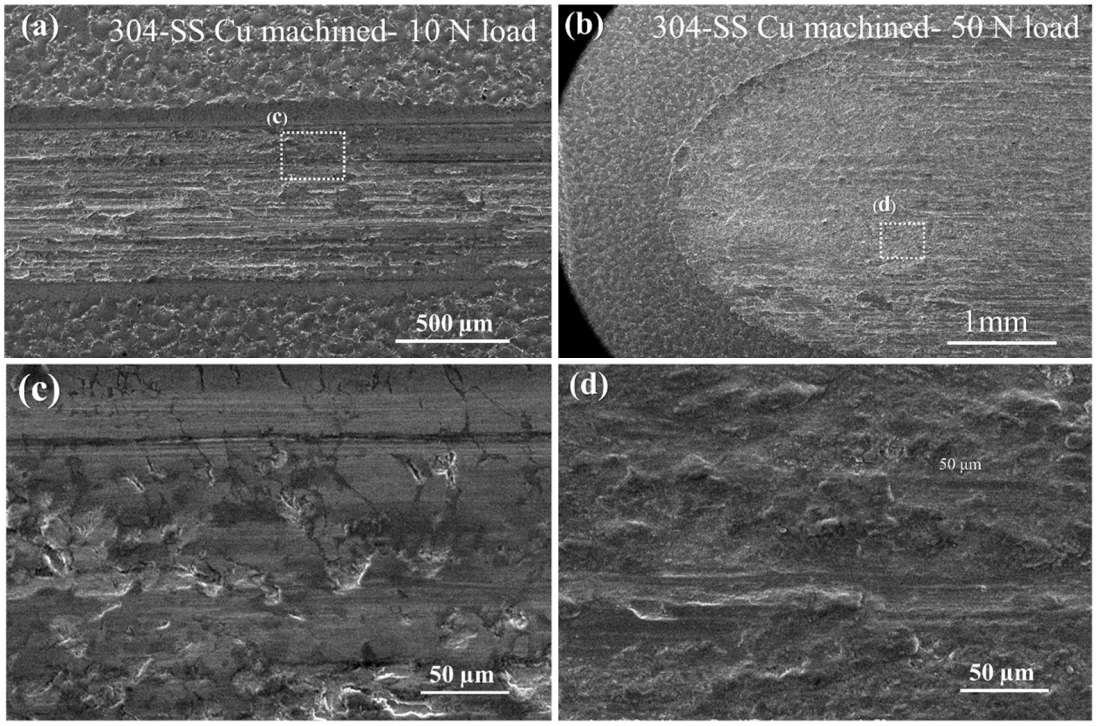

Figure A4-8 SE images of (a,b) low magnification of the 304-SS Cu machined under loading conditions of 10 & 50 N and (c,d) representative details of a wear scar on 304-SS Cu machined under loading conditions of 10 & 50 N

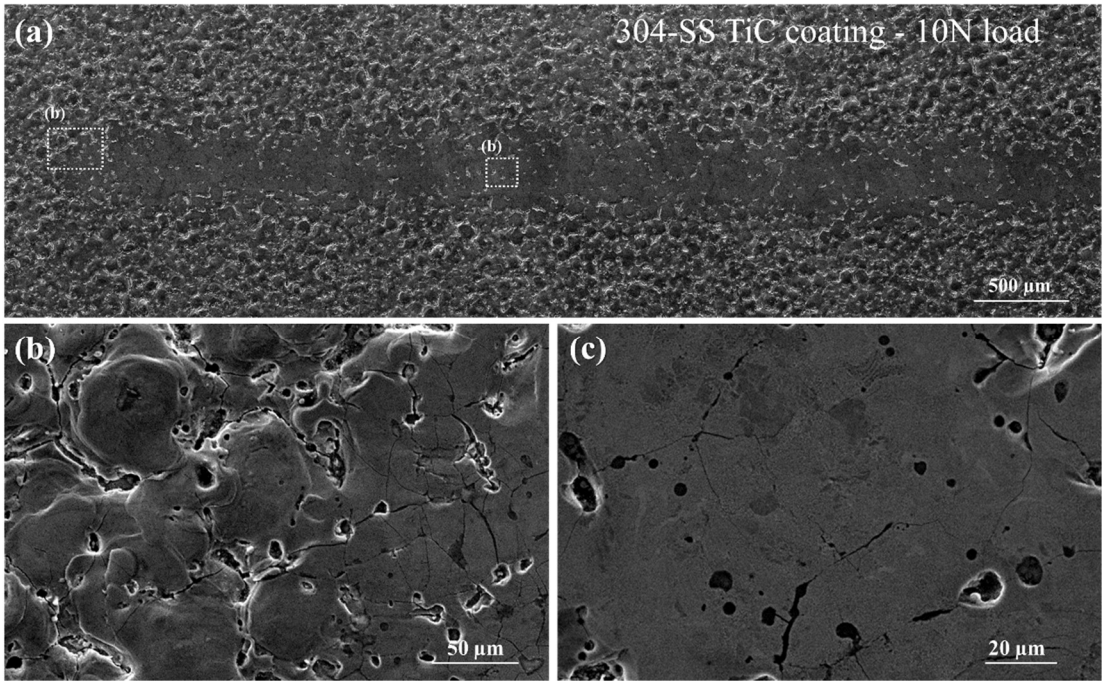

Figure A4-9 Low magnification SE images showing (a) the extent and (b,c) representative details of a wear scar on a cermet coated 304-SS sample, under loading conditions of 10 N

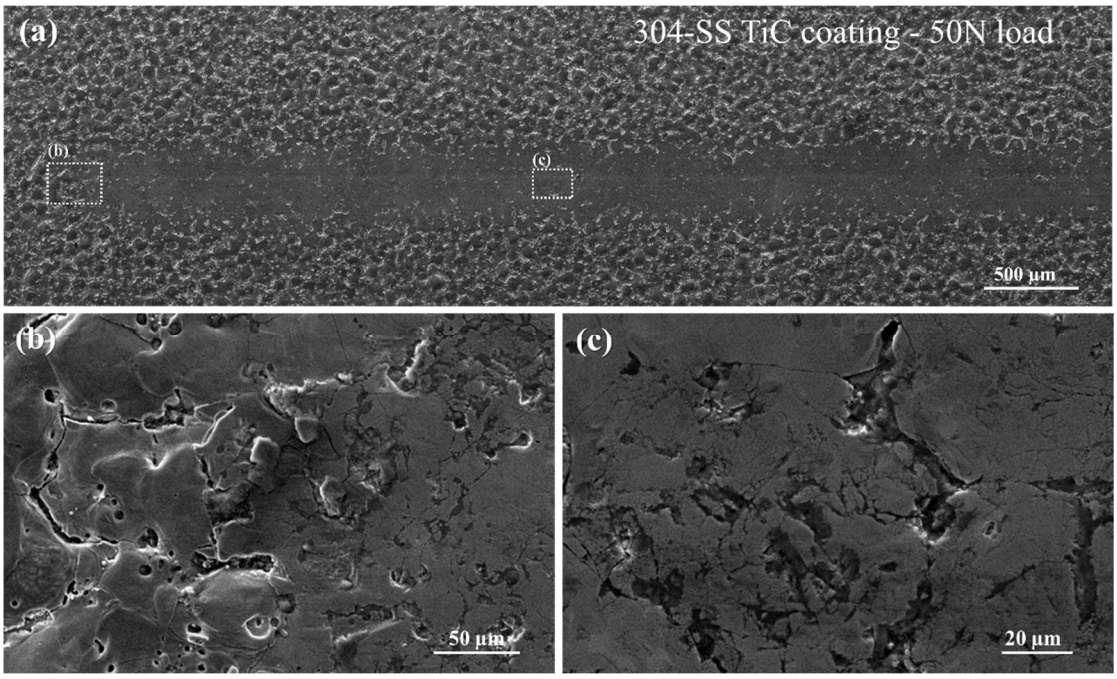

Figure A4-10 Low magnification SE images showing (a) the extent and (b,c) representative details of a wear scar on a cermet coated 304-SS sample, under loading conditions of 50 N

Appendix 5 SE images of the LSM wear track

A details of SE images of the wear track and highlighted details for the laser processed samples investigated in the thesis (Chapter 6).

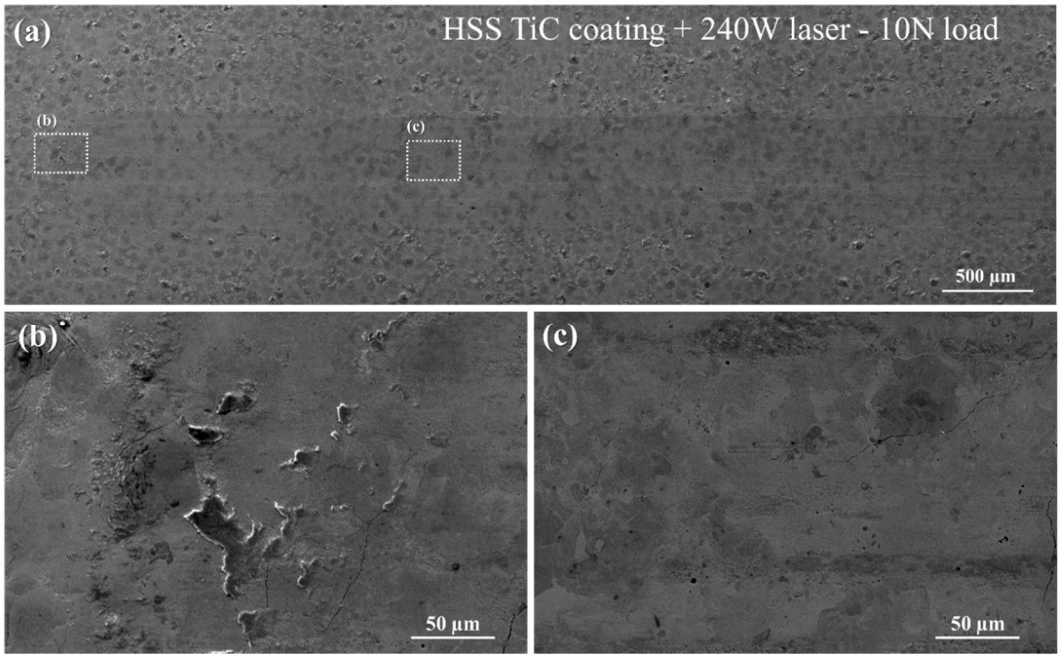

Figure A5-1 Low magnification SE images showing (a) the extent and (b,c) representative details of a wear scar on a cermet coated HSS and processed with 240 W laser , under loading conditions of 10 N

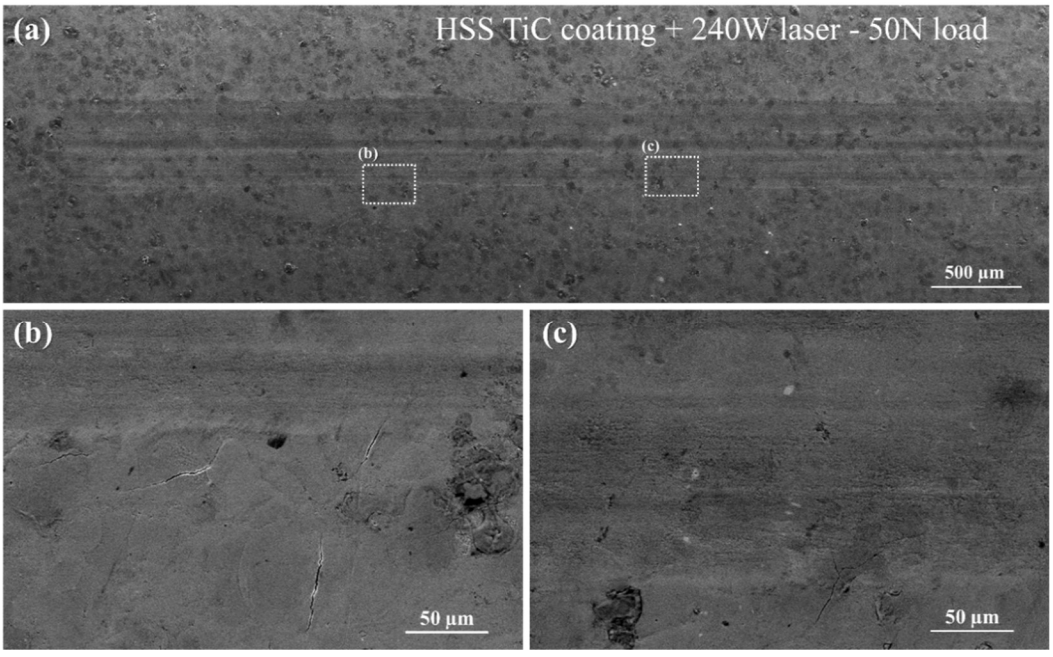

Figure A5-2 Low magnification SE images showing (a) the extent and (b,c) representative details of a wear scar on a cermet coated HSS and processed with 240 W laser , under loading conditions of 50 N

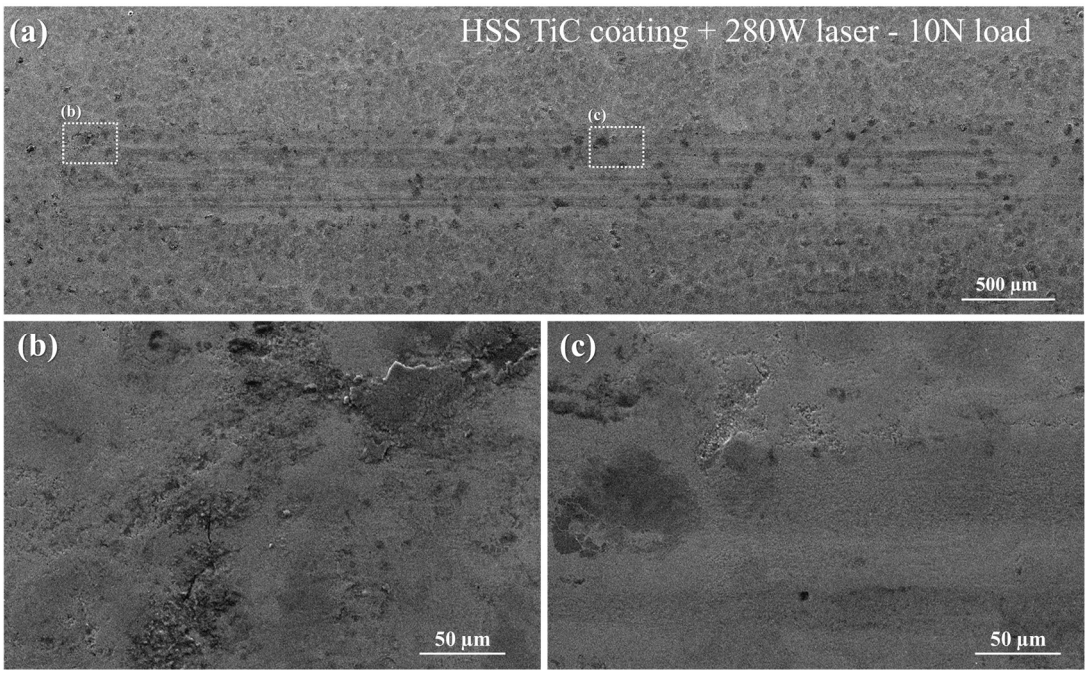

Figure A5-3 Low magnification SE images showing (a) the extent and (b,c) representative details of a wear scar on a cermet coated HSS and processed with 280 W laser , under loading conditions of 10 N

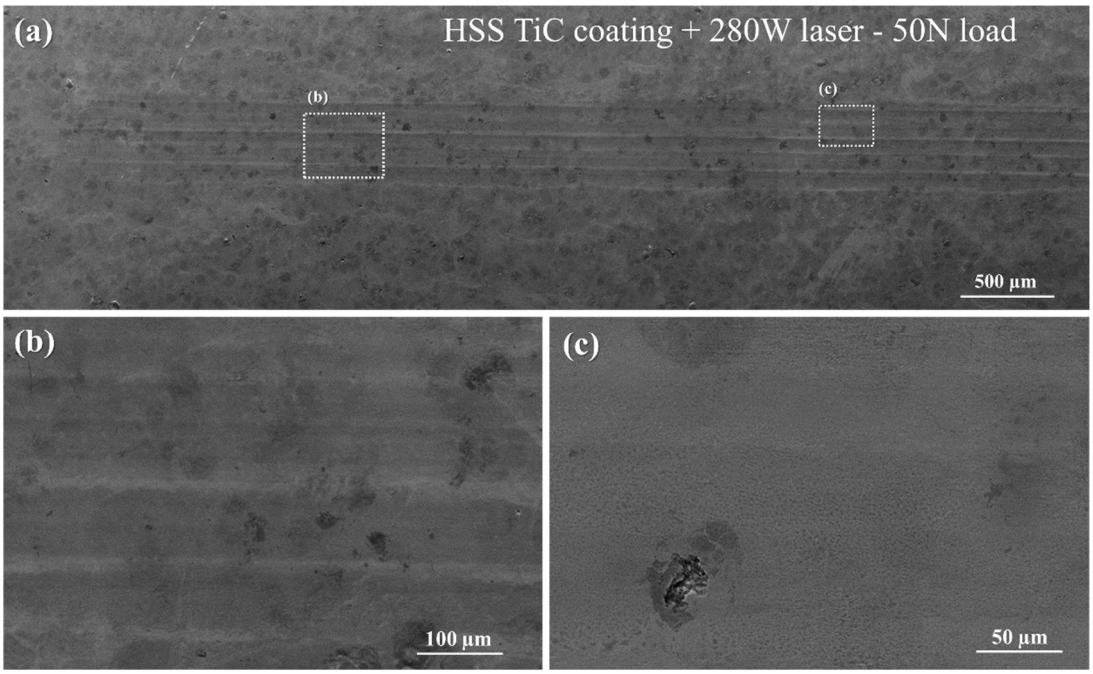

Figure A5-4 Low magnification SE images showing (a) the extent and (b,c) representative details of a wear scar on a cermet coated HSS and processed with 280 W laser , under loading conditions of 50 N

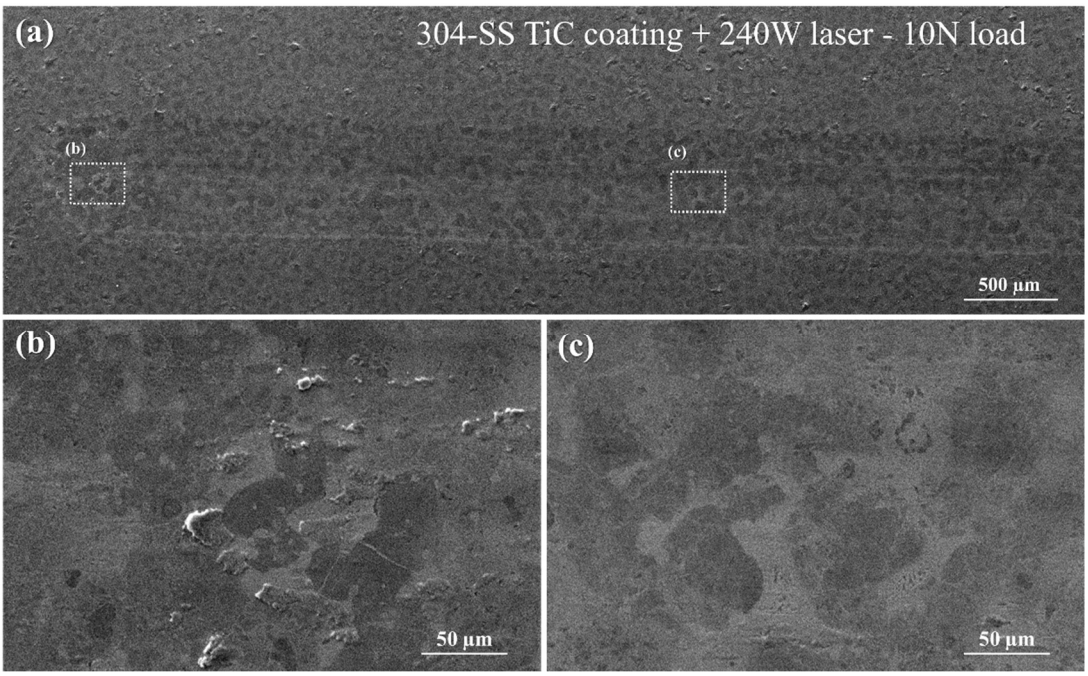

Figure A5-5 Low magnification SE images showing (a) the extent and (b,c) representative details of a wear scar on a cermet coated 304-SS and processed with 240 W laser , under loading conditions of 10 N

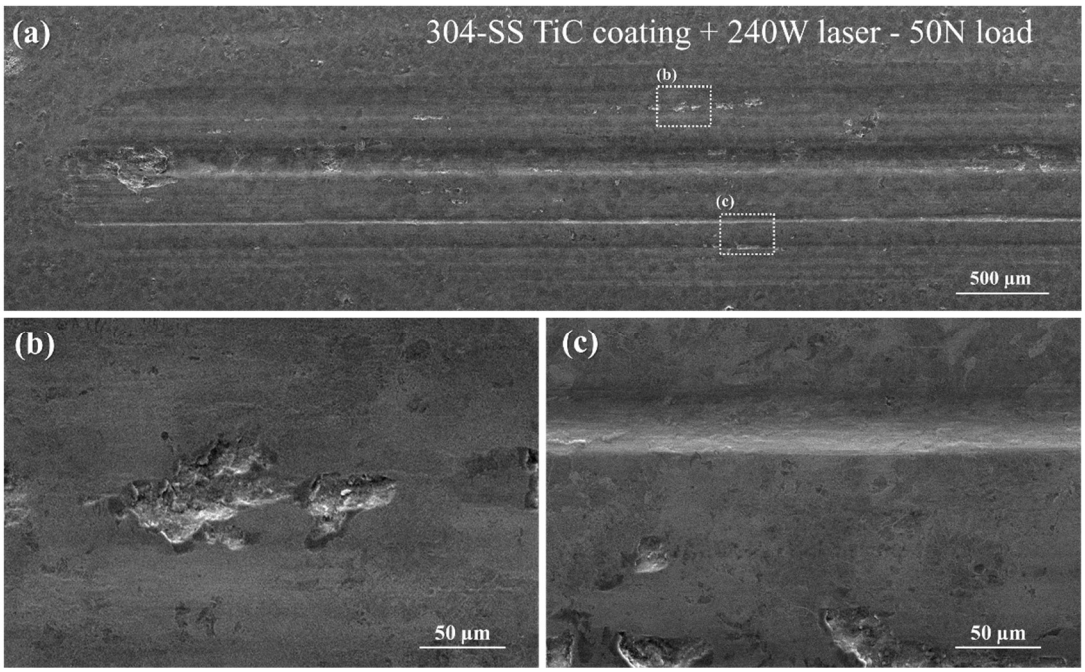

Figure A5-6 Low magnification SE images showing (a) the extent and (b,c) representative details of a wear scar on a cermet coated 304-SS and processed with 240 W laser , under loading conditions of 50 N

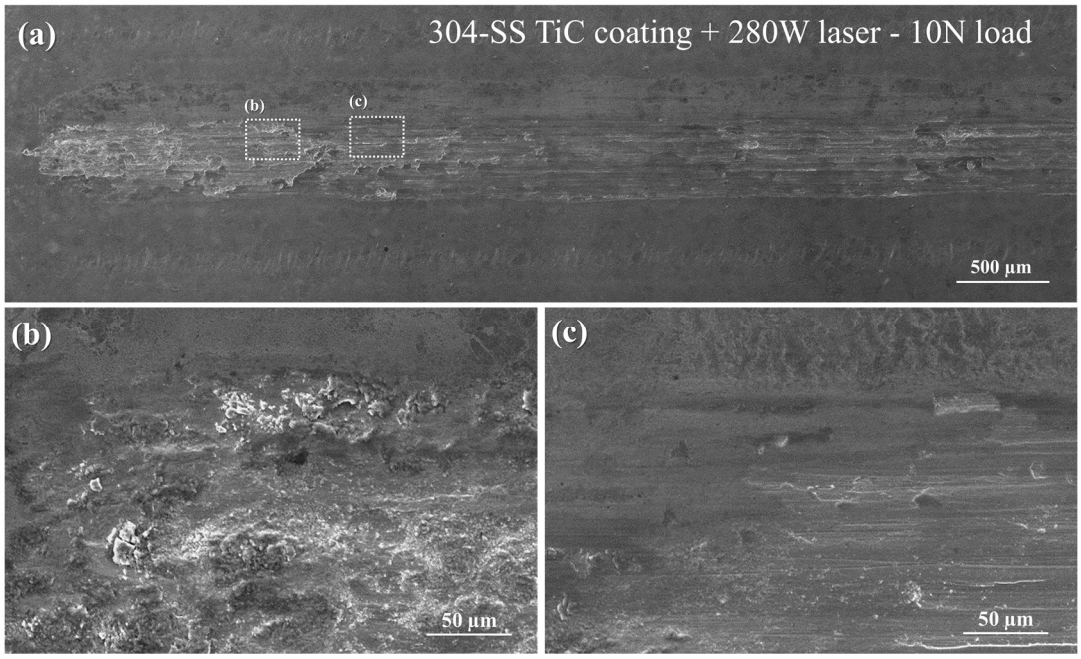

Figure A5-7 Low magnification SE images showing (a) the extent and (b,c) representative details of a wear scar on a cermet coated 304-SS and processed with 280 W laser , under loading conditions of 10 N

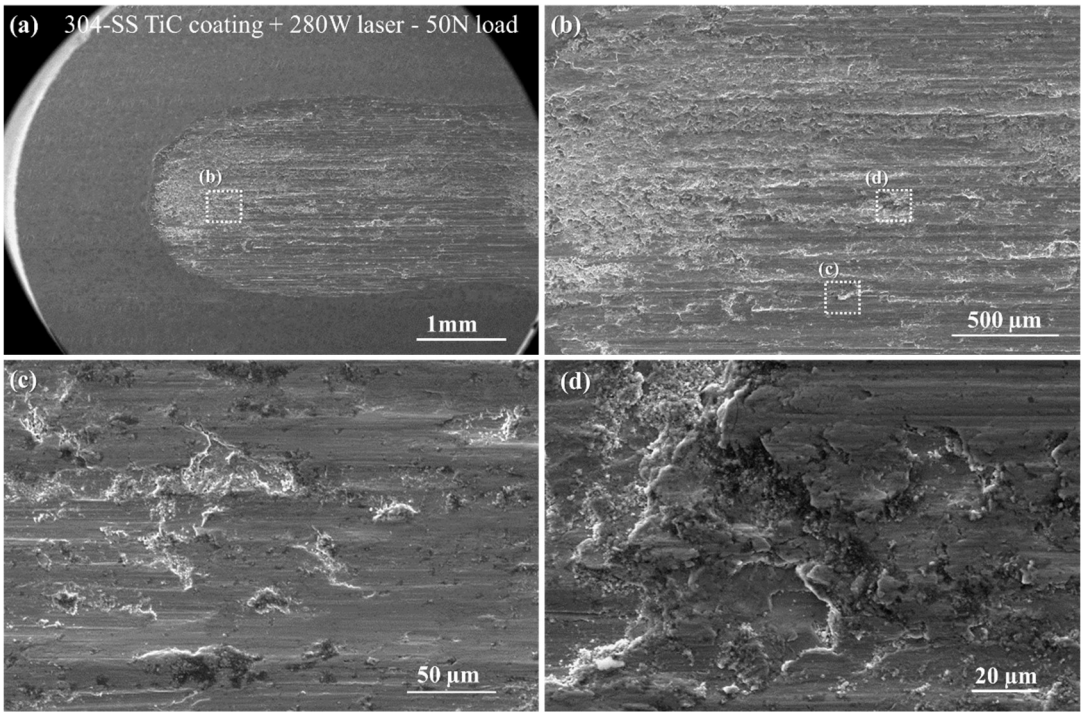

Figure A5-8 Low magnification SE images showing (a) the extent and (b,c,d) representative details of a wear scar on a cermet coated 304-SS and processed with 280 W laser , under loading conditions of 50 N